AFOSR·TR· 90-0078

AD-A217 752

STRENGTH AND MICROSTRUCTURE OF CERAMICS

BRIAN R. LAWN

Ceramics Division
National Institute of Standards and Technology
Gaithersburg, MD 20899

With C.J. Alpert, S.J. Bennison, H.M. Chan, S-J. Cho, R.F. Cook,
C.J. Fairbanks, M.P. Harmer, B.J. Hockey, D.B. Marshall,
S. Lathabai, Y-W. Mai, P.L. Swanson

Final Technical Report
FY 87-89

for

Air Force Office of Scientific Research
Bolling Air Force Base
Washington, DC 20332

November 1989

90 02 06 245

REPORT DOCUMENTATION PAGE

Form Approved
OMB No. 0704-0188

1. AGENCY USE ONLY (Leave blank)	2. REPORT DATE	3. REPORT TYPE AND DATES COVERED
	November 1989	Final Report - 87-89

4. TITLE AND SUBTITLE

"Strength and Microstructure of Ceramics"

5. FUNDING NUMBERS

2306/A2

6. AUTHOR(S)

B. R. Lawn

7. PERFORMING ORGANIZATION NAME(S) AND ADDRESS(ES)

National Institute of Standards & Technology
Ceramics Division, Building 223, Room A347
Gaithersburg, MD 20899

8. PERFORMING ORGANIZATION REPORT NUMBER

AFOSR-ISSA-87-0034
AFOSR-ISSA-88-0005

9. SPONSORING/MONITORING AGENCY NAME(S) AND ADDRESS(ES)

Air Force Office of Scientific Research
Bolling Air Force Base
Washington, D. C. 20332

10. SPONSORING/MONITORING AGENCY REPORT NUMBER

AFOSR-TR· 90-0013

11. SUPPLEMENTARY NOTES

12a. DISTRIBUTION/AVAILABILITY STATEMENT

Unlimited

12b. DISTRIBUTION CODE

13. ABSTRACT (Maximum 200 words)

Results of a study program on the toughness properties of monophase ceramics are summarized. In situ observations of crack propagation in alumina and other monophase ceramics show crack interface bridging to be the principal source of increasing toughness with crack size, i.e. R-curve behavior. Fracture mechanics models describing this behavior, in the particular context of strength, are developed. Results of strengths tests confirming the essential predictions of the theory are presented. Results of wear and fatigue tests are also described. The model has strong implications concerning the controlled processing of ceramics for optimum toughness and strength properties.

14. SUBJECT TERMS		15. NUMBER OF PAGES
Ceramics, Alumina, Toughening, Mechanical Properties. R-curve behavior, Fracture mechanics		100
		16. PRICE CODE

17. SECURITY CLASSIFICATION OF REPORT	18. SECURITY CLASSIFICATION OF THIS PAGE	19. SECURITY CLASSIFICATION OF ABSTRACT	20. LIMITATION OF ABSTRACT
Unclassified	Unclassified	Unclassified	Unlimited

STRENGTH AND MICROSTRUCTURE OF CERAMICS

INTRODUCTION

APPENDED PUBLICATIONS

1. "Crack-Interface Grain Bridging as a Fracture Resistance Mechanism in Ceramics: I. Experimental Study on Alumina"
P.L. Swanson, C.J. Fairbanks, B.R. Lawn, Y-W Mai and B.J. Hockey
J. Am Ceram. Soc. 70 279 (1987).

2. "Crack-Interface Grain Bridging as a Fracture Resistance Mechanism in Ceramics: II. Theoretical Fracture Mechanics Model"
Y-W Mai and B.R. Lawn
J. Am. Ceram. Soc. 70 289 (1987).

3. "Crack Resistance by Interfacial Bridging: Its Role in Determining Strength Characteristics"
R.F. Cook, C.J. Fairbanks, B.R. Lawn and Y-W. Mai
J. Mater. Research 2 345 (1987).

4. "Microstructural Effects on Grinding of Alumina and Glass-Ceramics"
D.B. Marshall, B.R. Lawn and R.F. Cook
J. Am. Ceram. Soc. 70 C-139 (1987).

5. "Toughness and Flaw Response in Non-Transforming Ceramics: Implications for NDE"
B.R. Lawn and C.J. Fairbanks
Review of Progress in Quantitative NDE, D.O. Thompson and D.E. Chimenti, eds., Plenum, New York, Vol. 6B, p. 1023, 1987.

6. "Indentation Deformation and Fracture of Sapphire"
H.M. Chan and B.R. Lawn
J. Am. Ceram. Soc. 71 29 (1988).

7. "Temperature Dependence of Hardness of Alumina-Based Ceramics"
C.J. Alpert, H.M. Chan, S.J. Bennison and B.R. Lawn
J. Am. Ceram. Soc. 71 C-371 (1988).

8. "Crack-Interface Traction: A Fracture Resistance Mechanism in Brittle Polycrystals"
P.L. Swanson
Advances in Ceramics, American Ceramic Society, Vol. 22, p. 135, 1988.

9. "Effect of Heat Treatment on Crack-Resistance Curves in a Liquid-Phase-Sintered Alumina"
S.J. Bennison, H.M. Chan and B.R. Lawn
J. Am. Ceram. Soc. 72 677 (1989).

10. "Flaw Tolerance in Ceramics With Rising Crack-Resistance Characteristics"
S.J. Bennison and B.R. Lawn
J. Mater. Sci. 24 3169 (1989).

11. "Role of Interfacial Grain-Bridging Sliding Friction in the Crack-Resistance and Strength Properties of Nontransforming Ceramics"
S.J. Bennison and B.R. Lawn
Acta Metall., in press.

12. "Fatigue Limits in Noncyclic Loading of Ceramics With Crack-Resistance Curves"
S. Lathabai and B.R. Lawn
J. Mater. Sci., in press.

13. "Cyclic Fatigue Behavior of an Alumina Ceramic With Crack-Resistance Curves"
S. Lathabai, Y-W. Mai and B.R. Lawn
J. Am. Ceram. Soc. 72 1760 (1989).

14. "Grain-size and R-Curve Effects in the Abrasive Wear of Alumina"
S-J. Cho, B.J. Hockey, B.R. Lawn and S.J. Bennison
J. Am. Ceram. Soc. 72 1249 (1989).

15. "A History in the Role of MgO in the Sintering of α-Al$_2$O$_3$"
S.J. Bennison and M.P. Harmer
Ceramics Transactions, American Ceramic Society, Vol. 7, 1989.

INTRODUCTION

This research program has been directed toward basic research into the role of microstructure in the toughness and strength properties of ceramics, in particular ceramics that are characterized by R-curve behavior, i.e. an increasing toughness characteristic with crack extension. The R-curve is now known to be pronounced in monophase ceramics with coarse microstructures, and is crucial to the utility of multiphase ceramic composites. It is important to understand the subtle interrelations between R-curve processes and materials characteristics, in order that we may on the one hand be able to establish reliable design criteria and, on the other, tailor new, superior ceramics with maximum resistance to damage accumulation and degradation. At NIST we have been engaged on a program during FY 87-89 to investigate these interrelations. A key aspect of our approach has been to establish strong links between properties and processing, fracture mechanics experimentation and modelling, materials design and characterization. The results of these studies are described in the appended publications.

The early work in the program was instrumental in identifying a principal mechanism of this R-curve behavior in elementary ceramics (e.g. aluminas), viz. grain-localized bridging behind the advancing crack [1-3,8]. Hitherto, bridging had not been considered seriously as a mechanism of toughening in ceramics. Our studies using in situ techniques showed clearly that grains exert significant tractions on the crack walls behind the advancing crack front by a frictional pullout mechanism.

With this mechanism identified, fracture mechanics models were developed [2,3,5,11]. These models incorporated the essential elements of the

microstructure in the underlying constitutive stress-separation function for the grain pullout. The most recent version [11] takes special account of the microstructural scaling (grain size) and internal residual stresses in this constitutive law, and thereby opens the way to optimal processing design of ceramics microstructures.

A primary feature of the R-curve is that it leads to a marked insensitivity of the strength to initial crack size, i.e. "flaw tolerance". This has a strong appeal to the structural engineer, because components may be designed to a specific stress without great concern for variable flaw distributions, either prior to or during service. Special studies have been made to demonstrate the benefits of this forgiving property in relation to processing flaws, such as pores [10]. Proper attention to development of a strong R-curve eases the demands on flaw elimination in processing.

To this end, NIST has developed an in-house processing capability (in addition to forming a formal collaborative link with the Ceramics Processing group under Professors M.P. Harmer and H.M. Chan at Lehigh University). Our aim is to begin with simple monophase materials, systematically investigating such simple microstructural variables as grain size and shape. We ultimately intend to extend our studies to complex composites. This part of the work is well under way, and we have begun testing our own alumina ceramic materials with controlled grain sizes and shapes [9,11,14,15].

Another important aspect of our work has been to extend the mechanical properties evaluation from toughness and strength to fatigue and wear. It might be argued that the underlying source of the grain-pullout frictional stresses responsible for the R-curve characteristic, i.e. internal residual stresses, could have counter-beneficial effects in repeated loading

conditions: e.g. in cyclic fatigue and wear. With regard to the latter, we have given attention to the nature of localized contact damage [6,7], and carried out actual machining [4] and wear [14] tests on various aluminas. We do indeed find that aluminas with stronger R-curves show reduced wear resistance. These results suggest that specific materials may have to be designed for specific applications.

Work on fatigue properties has also begun. We have extended the R-curve modelling to include slow crack growth effects, so as to predict static and dynamic fatigue behavior [12]. Data on aluminas substantiate the modelling. With this theory established, we can then extend the predictions to cyclic loading. Preliminary tests on the same aluminas using indentation flaws [13] indicate, somewhat surprisingly, that for short cracks no deleterious effects over and above those of slow crack growth occur.

The work described above is scheduled to continue under AFOSR sponsorship through FY 90-92.

1. "Crack-Interface Grain Bridging as a Fracture Resistance Mechanism in Ceramics: I. Experimental Study on Alumina"

    P.L. Swanson, C.J. Fairbanks, B.R. Lawn, Y-W Mai and B.J. Hockey

    J. Am Ceram. Soc. 70 279 (1987).

Crack-Interface Grain Bridging as a Fracture Resistance Mechanism in Ceramics: I, Experimental Study on Alumina

PETER L. SWANSON,* CAROLYN J. FAIRBANKS, BRIAN R. LAWN,* YIU-WING MAI,*
and BERNARD J. HOCKEY

Ceramics Division, National Bureau of Standards, Gaithersburg, Maryland 20899

Direct microscopic evidence is presented in support of an explanation of *R*-curve behavior in monophase ceramics by grain-localized bridging across the newly formed crack interface. In situ observations are made of crack growth in tapered cantilever beam and indented flexure specimens of a coarse-grained alumina. The fractures are observed to be highly stable, typical of a material with a strongly increasing resistance characteristic, but are discontinuous at the microstructural level. Associated with this discontinuity is the appearance of overlapping segments in the surface fracture trace around bridging grains; the mean spacing of such "activity sites" along the trace is about 2 to 5 grain diameters. These segments link up with the primary crack beneath the specimen surface, and continue to evolve toward rupture of the bridge as fracture proceeds. The bridges remain active at large distances, of order 100 grain diameters or more, behind the crack tip. Scanning electron microscopy of some of the bridging sites demonstrates that secondary (interface-adjacent) microfracture and frictional tractions are important elements in the bridge separation process. Evidence is sought, but none found, for some of the more popular alternative models of toughening, notably frontal-zone microcracking and crack-tip/internal-stress interaction. It is suggested that the crack-interface bridging mechanism may be a general phenomenon in nontransforming ceramics.

I. Introduction

THERE is a growing realization that the crack resistance properties of ceramics have an intrinsic size dependence.[1] At crack sizes small in relation to the microstructure the toughness has values characteristic of bulk cleavage (transgranular) or grain boundary (intergranular) energies. At large crack sizes the toughness tends to somewhat higher, limiting values characteristic of the polycrystalline aggregate. The toughness function connecting these two extremes in crack size is the so-called "*R*-curve" function, after the rising crack resistance curves originally found for metals.[2] Such *R*-curve behavior is of great interest in the case of engineering ceramics, for both the structural designer, who needs to know the toughness characteristic in specifiable flaw size ranges, and the materials processor, who seeks a basis for tailoring new and superior materials.

Despite this increasing awareness of the importance of microstructurally related size effects, there have been remarkably few attempts at definitive identification of underlying crack resistance mechanisms. A notable exception is in the zirconia-based ceramics, where transformation toughening is now unequivocally

established as a principal factor.[3-5] The transformation events are generally taken to be confined within a "process zone" about the advancing crack tip, in analogy to the plastic zone responsible for the *R*-curve behavior of metals. However, important as it is as a mode of crack impedance, transformation toughening is currently restricted to a select few ceramics and does not operate in "simple" monophase materials like aluminas. Crack size effects in these latter materials have been attributed to several alternative causes, with virtually no direct experimental substantiation. Perhaps the most widely quoted of these is the proposal of a frontal *microcrack* cloud, in which discrete microfractures act as effective energy sinks in the field of the primary crack.[6,7] Another proposal is that an advancing crack tip is progressively impeded via direct interactions with locked-in internal stresses (e.g., thermal expansion mismatch stresses).[8] Other possibilities that have been considered include crack restraint by pinning and bowing[9] and by deflection and twisting,[10] although these are noncumulative mechanisms; they do not have provision to account for the remarkably long crack size range over which the *R* curve rises in many materials.[1]

Which of the above mechanisms, if any, predominates in the *R*-curve behavior of aluminas and other nontransforming ceramics? The current literature relating to this question is based almost exclusively on the capacity of theoretical models to match measured fracture mechanics (e.g., applied load vs crack size) data. The question of whether or not the proposed mechanisms actually operate in the assumed fashion is not directly addressed in this literature; support is provided only by circumstantial evidence from limited postfailure examinations of fracture specimens. However, there is one set of observations, by Knehans and Steinbrech,[11] which allows us to narrow down the possibilities. They grew cracks through several millimeters in alumina test specimens, and found strong rising *R* curves. Then they removed material adjacent to the walls *behind* the crack tip by sawcutting, taking care to leave intact the immediate region *at* the tip. On restarting the crack, the resistance reverted immediately to the base of the *R* curve. The unmistakable implication was that the toughening processes must operate in the wake of the advancing tip. Of the mechanisms considered thus far, it is that of distributed microcracking which is most compatible with this notion of a wake effect; indeed, the Knehans and Steinbrech experiment has been cited as evidence for the microcracking model.[7]

However, Knehans and Steinbrech raised another possibility, that the source of the rising resistance may lie in some physically restraining force across the newly formed crack interface. This alternative proposal had received only passing mention in the preceding ceramics literature.[12,13] Knehans and Steinbrech have since taken their case further, arguing specifically in favor of a grain interlocking mechanism.[14,15] The idea of an interfacial restraint is not the exclusive domain of the ceramics community; it has been developed even more strongly in concrete[16,17] and rock mechanics,[18,19] although the detailed micromechanics of the actual separation processes are hardly better understood. Thus it would seem that the key to improving the toughness of nontransforming ceramics could depend primarily on events which occur behind rather than at or ahead of the advancing crack. Clearly there are important implications here in the microstructural design of ceramic materials.

The present work is directed to the development of a crack resistance model incorporating the essential elements of the inter-
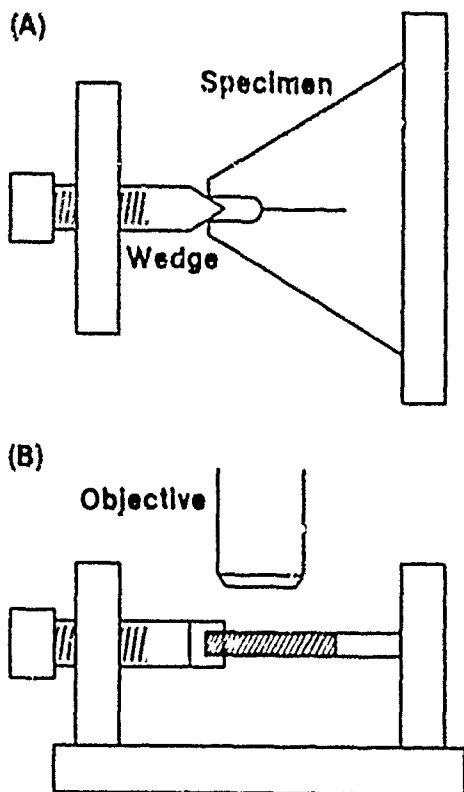
(A)

(B)

Fig. 1. Schematic of tapered double cantilever beam test specimen used to observe crack growth during loading: (A) top view; (B) side view. Specimen cut from triangular slab, 12-mm edge length and 2-mm thickness, to produce crack 7 mm long. Starter notch length 300 μm, radius 100 μm. Wedge angle 60°.

(A)

(B)

Fig. 2. Schematic of indentation flaw test used to observe radial crack evolution to failure: (A) plan view, showing Vickers flaw on tensile surface; (B) side view, showing flexure system. Specimen dimensions 25-mm diameter by 2-mm thickness. Biaxial loading, 2-mm-radius punch on 10-mm-radius (3-point) support.

facial restraint concept. It is in two parts. Part I describes experimental observations of controlled crack growth in a coarse-grained alumina with strong R-curve behavior. A critical feature of these experiments is the facility to follow the crack response along its entire length while the driving force is being applied. We confirm the presence of grain-localized "bridges" across the crack interface, over large distances (several millimeters) behind the tip. Part II deals with quantitative aspects of the R-curve behavior, by a formulation of the bridging concept in terms of theoretical fracture mechanics. In this endeavor we borrow from analogous treatments in the fiber-reinforced composite and concrete literature. Our analysis does not aspire to a complete understanding of the physical ligamentary rupture process, but nevertheless establishes a sound mechanical framework for characterizing the crack resistance properties.

Before proceeding, it is well that we should draw attention to a recent study on the strength properties of ceramic specimens containing indentation flaws.[20-22] Indeed, some of the issues raised in that study provided a strong motivation for the present work. There, the idea was to investigate the fracture size range between the extremes of the microscopic flaw and the macroscopic crack by systematically varying the indentation load from specimen to specimen. It was found that on reducing the indentation flaw size the corresponding strength did not increase indefinitely, as required by ideal indentation fracture theory (i.e., theory based on the notion of an invariant toughness), but tended instead to level off at a strength characteristic of the intrinsic microstructural flaws. This response was attributed to the influence of R-curve behavior. Im-
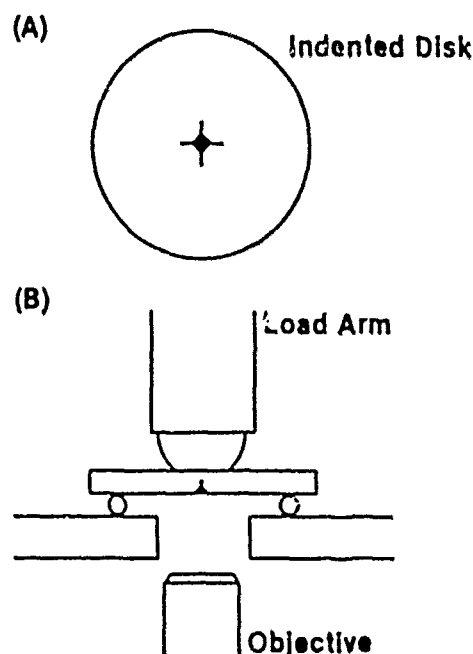
portantly, the strength plateau at small flaw sizes was seen in three groups of ceramics, aluminas, glass-ceramics, and barium titanates, indicating a certain generality in the R-curve phenomenon. Also, the magnitude of the effect was in some cases considerable, amounting to an effective increase in toughness of more than a factor of 3 over a crack size range of some tens of grain sizes or more. In that earlier study[20] the microstructural element was introduced into the fracture mechanics in a somewhat phenomenological manner; here we seek to place the fracture mechanics on a firmer footing by relating this element more closely to identifiable crack restraint mechanisms. Accordingly, a detailed analysis of indentation fracture data in terms of the bridging concept may be foreshadowed as a future goal of our work.[23]

II. Experimental Procedure

It was decided in this work to focus on one material, a nominally pure, coarse-grained alumina.[*] We have already made allusion to the implied generality of the R-curve phenomenon 'Section I); our choice is intended to meet the requirement of a ..presentative" material, but at the same time one which exhibits the R curve to particularly strong effect. (For quantitative measures of the pertinent R curve the reader is directed to the VI-labeled curves in Figs. 4 and 10 in Ref. 20, Figs. 6 and 7 in Ref. 1, and Figs. 1 and 3 in Ref. 22.) The relatively large microstructure of our material (mean grain diameter 20 μm) also lends itself to in situ experimentation using ordinary means of microscopic observation. In certain instances where it was deemed useful to run comparative tests on specimens without the influence of microstructure, sapphire was used as a control material.

As indicated, a major feature of our experimental procedure is the facility to monitor the evolution of fracture during the application of stress. Accordingly, direct observations were made of the crack growth by optical microscopy, using the two loading configurations shown in Figs. 1 and 2. The specimens were surface-relief polished with 0.3-μm Al_2O_3 powder to delineate the coarser grain boundary structure. In some cases a thermal etch pretreatment at (1050°C for 2 h) was used to enhance fine details in

this structure. An important element of our experimental philosophy here is that, by virtue of the enhanced stabilization in crack growth which attends strong R-curve behavior,[1] we may hope to observe critical events which in conventional postfailure analysis (or even in interrupted tests) might pass unnoticed.

The first of the test configurations, Fig. 1, is a modification of the familiar double cantilever beam specimen. Generally, the regular rectangular beam geometry is retained for *quantitative* evaluation of the R-curve behavior (Part II). Here, however, a tapered geometry was used, width increasing in the direction of ultimate crack propagation. The main crack was started at a sawcut notch by inserting a metal wedge. Subsequent crack extension could be controlled via a micrometer drive system, to which the wedge was fixed. The whole system was attached to the stage of an optical microscope to allow for continuous monitoring of the crack evolution. Pertinent dimensions of the test geometry are included in the caption to Fig. 1.

The second configuration, Fig. 2, simulates the controlled flaw test used previously to infer R-curve behavior from strength data (Section I). A Vickers diamond was used to introduce an indentation flaw at the center of a disk flexure specimen. The disk was then loaded axially in a circular-flat on three-ball-support fixture,[24] with the indentation on the tension side. Again, the entire fixture was attached to a microscope stage for in situ viewing of the crack evolution. A video recording unit was particularly useful in interpreting some of the more subtle features observed with this configuration. Reference is made to Fig. 2 for relevant test geometry dimensions.

Some additional, static observations were made on the above specimens to add weight to our ensuing case. For example, in the event of toughening associated with a frontal microcrack cloud, one might anticipate some detectable surface distortion either ahead or in the wake of the primary crack tip. Accordingly, surface profilometry scans were taken perpendicular to the crack traces on some of the cantilever specimens. The cantilever configuration was more convenient in this regard because the entire wedge-loading fixture could be transferred onto the profilometer stage, thereby allowing the crack to be examined without unloading. Also, anticipating that we might need to look more closely at events at the level of the grain size *or below*, some of the unloaded disk specimens were examined by scanning electron microscopy.

III. Results

(1) General Observations

Our initial examinations of the fracture patterns produced in the alumina test specimens revealed some interesting general features. The clearest and most immediate indication that we were dealing with a crack-interface effect was that, after "failure" (as marked by a sudden propagation of the cracks to the edges of the specimen), the fractured segments tended to remain intact. An additional force was required to separate the pieces completely. This was our first clue that the walls behind an advancing tip must indeed be restrained by some remnant forces acting across the interface.

Closer surface inspections along the crack traces at various stages of propagation soon helped to reinforce this last conviction. The fracture in our material was predominantly intergranular, as previously reported.[20,21] There were signs of some "secondary activity" adjacent to the walls of the otherwise primary crack interface, but never further distant than one or two grain diameters from this interface. It will be our aim in the following sections to confirm that this interface-related activity is a manifestation of a grain-localized ligamentary rupture process, and not of some relaxation effect associated with the wake of an advancing microcrack cloud.

(2) Cantilever Beam Experiments

The in situ observations of fracture in the tapered cantilever beam specimens (Fig. 1) were carried out while carefully and slowly driving in the mouth-opening wedge. These observations were all made in air, so that some rate effects were apparent in the crack growth (although the velocities were usually much less than 10^{-3} m·s^{-1}). There was a tendency for the first stage of fracture to occur suddenly over a distance of several grain diameters from the starter notch tip. "Pop-in" behavior of this kind is not uncommon in notched specimens, of course; in such cases the initial fracture response can be influenced strongly by the local notch configuration. However, discontinuous crack growth was also commonly observed in the subsequent loading, over distances as small as one or two grains. There is the suggestion here of an element of discreteness in the mechanics which ultimately underlies the R-curve behavior.

Appropriately, attention was focused on regions of identifiable "activity sites" behind the advancing crack tip during monotonic loading to "failure." An example of the kind of observation made is shown in Fig. 3, a low-magnification reflected-light mosaic of a particular specimen at six successive stages of fracture. The field of view along the crack length covers the first 2 mm from the starter notch at left (not included in the figure). At final loading, stage VI in Fig. 3, the crack extends clearly across the full 7-mm length of the specimen, although again without separating into two parts. The areas labeled (A), (B), and (C) illustrate particularly clear examples of progressive crack-flank damage evolution through the loading sequence. These areas are magnified in Figs. 4 to 6 for closer scrutiny of the microstructural detail.

In zone A, Fig. 4, we can follow the formation and rupture of a single ligamentary bridge through all six stages. In stage I the surface fracture trace appears to be segmented about a large grain, as though the primary crack may have stopped and then reinitiated on a secondary front. However, on switching to transmitted light (e.g., see Fig. 7(B)) and focusing into the subsurface regions of the transparent material, the apparently isolated segments were found to connect together into a common crack interface. Hence the bridge is grain-localized in the projected fracture plane. On proceeding to stage II we note that the crack segments about the bridging grain have increased their overlap but have not yet linked up, although the detectable main tip is now some 0.75 mm distant. There is an indication of enhanced reflectivity beneath this same grain, indicating that the crack-segment overlap extends *beneath* as well as *along* the surface. By the time the primary tip has advanced more than 1.2 mm beyond the bridge, stage III, the upper crack segment appears to have linked up completely with the main fracture trace. This does not signify the final state of rupture, however, for there are signs of continued local crack activity around the grain of interest, notably at left, through stages IV and V. We point out that the primary crack tip is at least 2 mm, i.e., approaching 100 grain diameters, ahead of the bridge site. Finally, at stage VI, the lower crack associated with the original bridge appears to have closed up somewhat, perhaps reflecting the release of some interfacial frictional tractions.[1]

Zone B, in Fig. 5, evolves in much the same way, but with certain of the above-mentioned features delineated more strongly. The initial crack segmentation, stage III, and subsequent linkup, stage IV, differ little in essence from that observed in zone A. However, the trace of the crack segment which runs *below* the bridging grain (and which, incidentally, would appear in stage III to be the more likely to lead to the ultimate rupture of the ligament) closes up much more abruptly and completely than its counterpart in zone A. Interfacial tractions persist on loading to stage V, as evidenced by the appearance of additional small-scale fissures about the separating grain. Examination in transmitted light during this stage revealed substantial subsurface activity. Even more dramatic indications of unrelieved tractions are evident from the postmortem configuration at stage VI. Final separation has occurred through virgin material, seemingly "avoiding" the incipient fracture paths apparent in the previous micrographs, a measure of the disruption caused by this final rupture is given by the extensive debris, visible as the region of highly diffuse reflection, lodged

---

Interfacial tractions and bridging by as-yet unruptured grains may *independently* provide traction across the nascent fracture surface. Distinction between these two potential sources of traction is not a principal concern here, owing to the experimental difficulties in resolving finer details in the subsurface damage processes.[1,2]

Fig. 3. Reflected light micrograph mosaic of crack evolution in tapered DCB specimen of alumina, shown at six stages of loading. Wedge remains inserted in notch (just out of field at left) in all stages.
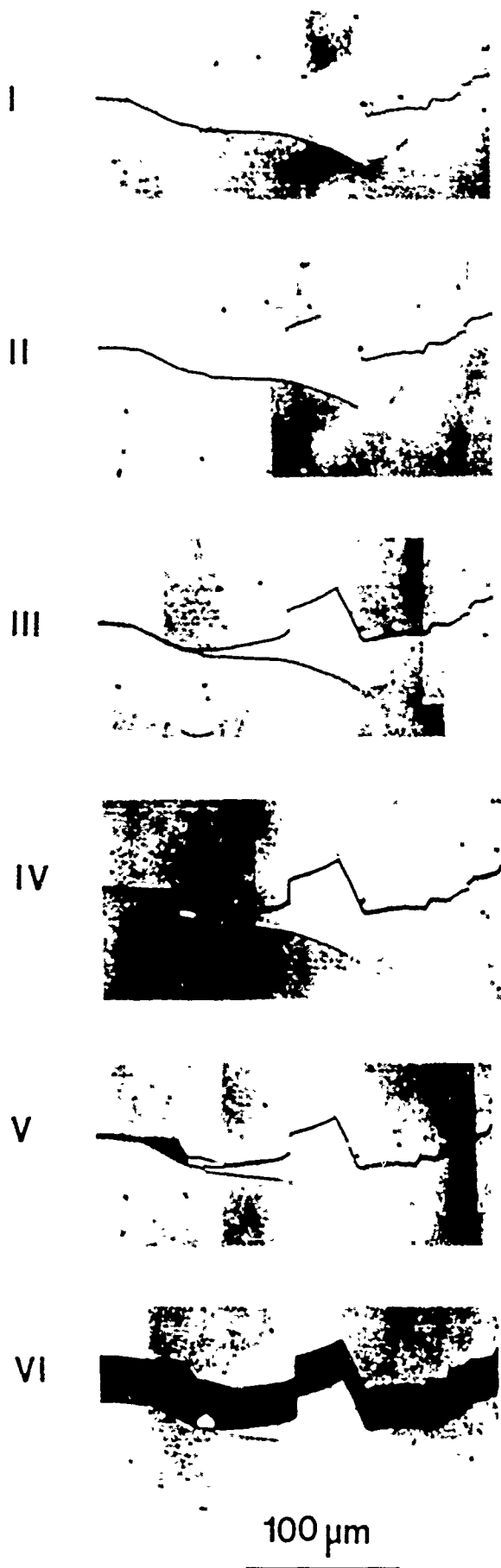
100 μm

100μm

Fig. 4.   Enlargement of zone A in Fig 3, showing evolution of a grain bridging site from inception to failure. Persistence of interface-related secondary cracking is apparent through stage V.
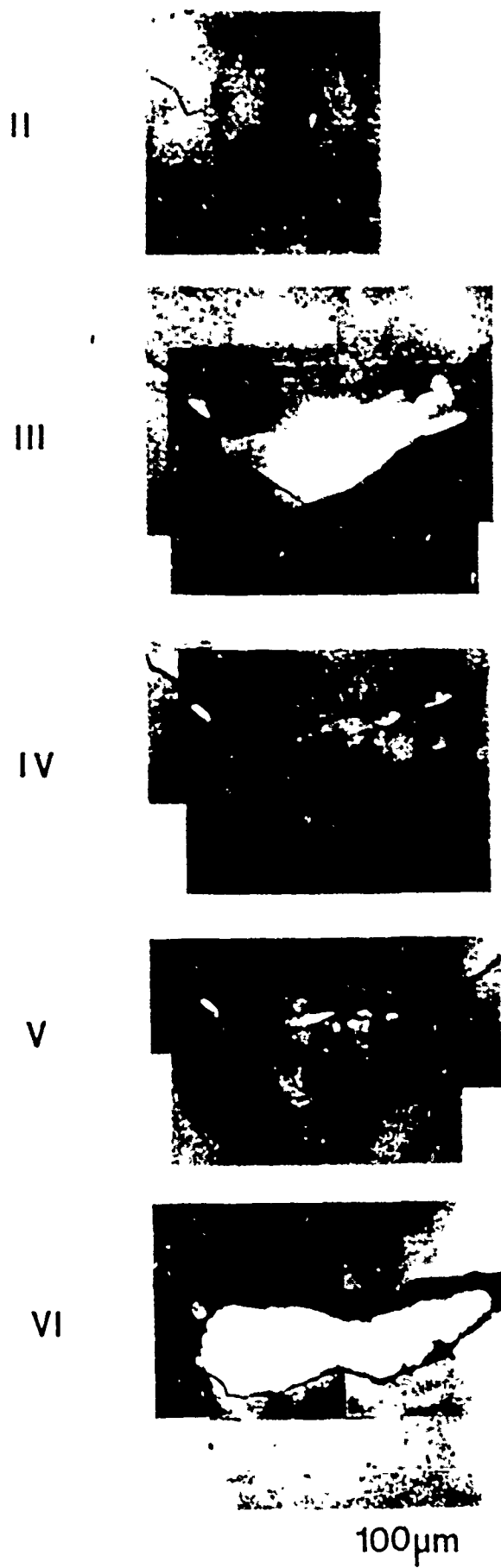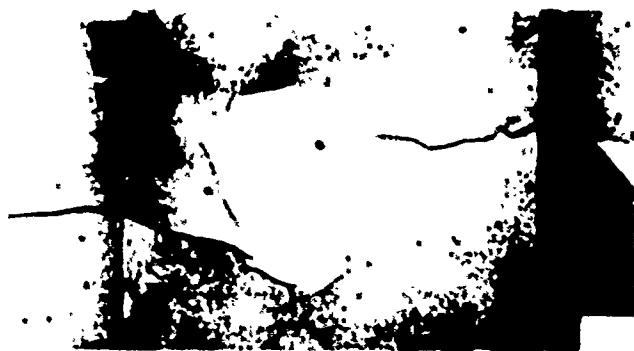
Fig. 5.   Enlargement of zone B in Fig 3. Note continually changing course of the local fracture path through the loading to failure.

Fig. 6. Enlargement of zone C in Fig. 3. Substantial transgranular fracture accompanies the bridge rupture.

between the crack walls at the original bridge site.

Consider now the third area in Fig. 6, zone C. In the initial stage, IV, substantial microcrack overlap occurs, predominantly along grain boundaries, followed by transgranular microrupture *within* the initial span of bridging material, stage V. Again, the final rupture path largely ignores the previously formed, localized crack segments.

We note that at each bridge-rupture site (zones A, B, C) the cumulative amount of surface-exposed crack length is approximately *3 times* the shortest straight-line path through the bridging sites. Moreover, the total fracture surface area incorporates a significant amount of transgranular fracturing. The bridges clearly represent an intrinsically high-energy source of fracture resistance.

In choosing our examples above we have, for obvious reasons, focused on the most conspicuous sites, i.e., the sites involving the largest bridging grains. Higher magnification examinations of loaded crack systems such as that in Figs. 3 to 6 revealed a high density of smaller, but no less active, sites, particularly toward the fracture terminus. These were again evident as surface offset traces in reflection or subsurface scattering centers in transmission. It was thereby estimated that the mean separation between grain ligaments could be as low as 2 to 5 grain diameters.

With the realization that our microscopic observations were capable of detecting grain-scale microfractures while load was maintained, particularly in illumination by transmitted light, attention was turned to the region *ahead* of the primary crack terminus.

Figure 7 shows typical micrographs of this region. In particular, evidence was sought which might point to the existence of a cloud of distributed microcracks about the terminus. In keeping with the popular notion of discrete microfracture initiation at or above some critical tensile stress level within the near crack field, we might expect to observe diffuse scattering within an extensive frontal microcrack zone.[6,7] No such extended diffuse scattering was ever detected in our experiments. Sometimes apparently unconnected surface traces were observed in the terminus region (e.g., as in Fig. 7(B)) but, like their segmented counterparts *behind* the tip, these invariably connected up at a depth of a grain diameter or so beneath the surface.

Further null evidence for an extended transverse microcracking zone was provided by the surface profilometer traces. These were taken perpendicular to the loaded crack configuration seen in stage IV, Fig. 3. The results of several scans, both ahead and behind the crack tip, are shown in Fig. 8. Minute surface detail associated with the relief polishing is apparent in the scans, but in no case is there any indication of a general dilation-induced uprising of material adjacent to the crack interface.

(3) Indentation-Strength Experiments

Direct observations were made of crack growth from Vickers indentation flaws during loading to failure (Fig. 2). An example of the final fracture pattern produced in this configuration is given in Fig. 9. We see that once the initial radial cracks traverse the central

(A)

100 μm

(B)

Fig. 7. Reflection (A) and transmission (B) micrographs of loaded DCB specimen (equivalent in growth to about stage IV in Fig. 3).

Height Scale   1 μm

Crack

1 mm

1 mm

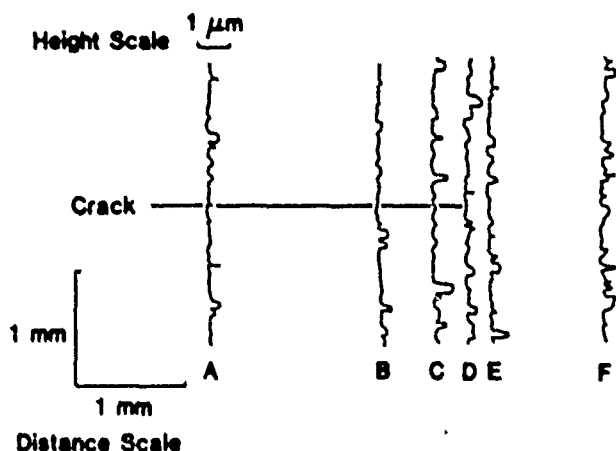A   B C D E   F

Distance Scale

Fig. 8. Surface profilometer traces transverse to crack plane in loaded alumina DCB specimen. Detectable crack tip lies on trace D. Height scale on scan greatly magnified relative to distance scale. No surface uplift adjacent to crack walls is evident (diamond stylus radius ≈1 μm; horizontal position uncertainty ≈100 μm, vertical uncertainty <10 nm for long wavelength, i.e., ≥10 μm, topography variations).

Fig. 9. Reflected light micrograph of a Vickers indentation site in a "fractured" alumina disk. Initial radial cracks from low-load (5 N) indentation arrest at first encounter with grain boundary, and grow discontinuously along boundaries as flexural stress is applied. Specimen thermally etched to reveal grain structure.

grains which encompass the indentation impression, the fracture proceeds primarily in the familiar intergranular mode. Once more, this fracture runs to the specimen extremities without causing complete separation.

One of our acknowledged goals here was to look in fine detail at the crack response *prior to* failure. Accordingly, the tests were run at slow stressing rates, in air, for greatest ease of observation. Typically, the time to failure was several minutes. At high indentation loads (≥100 N), such that the scale of the starting radial cracks substantially exceeded that of the microstructure, the fracture showed an even stronger tendency to discontinuous evolution, over distances of a few grains or so, than noted in the cantilever

beam experiments. Notwithstanding these discontinuities, the cracks were characterized by strong prefailure stability, sometimes extending to the edges of the 12.5-mm-radius disks without any sign of catastrophic growth. There is no doubt that local residual contact stresses contribute to this stability,[9] but only in part: comparative runs on sapphire (microstructure-free) specimens under identical test conditions show much smaller, i.e., <1 mm, precursor stable growth prior to failure. It seems reasonable to conclude that the enhanced stabilization in the polycrystalline alumina is a direct manifestation of a rising R curve.[1]

At low indentation loads (1 to 10 N) the evidence for discontinuity in the stabilized crack growth was even more emphatic
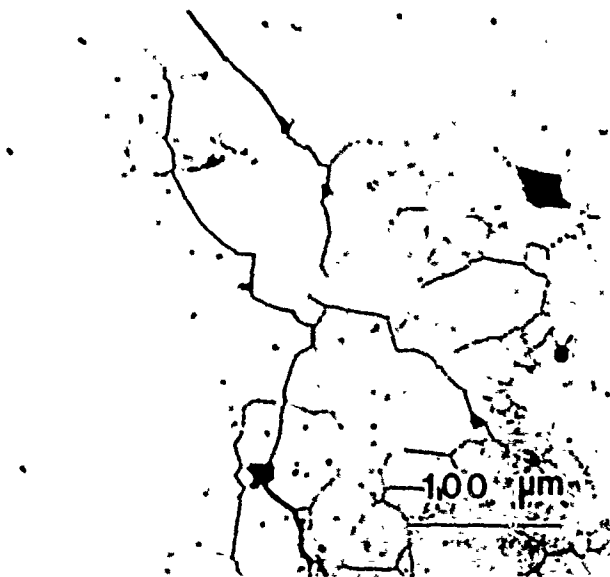
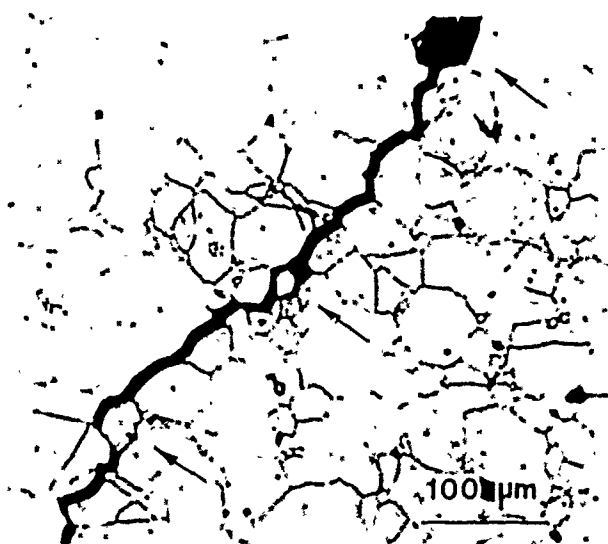Fig. 10. Reflected light micrograph of a segmented radial crack in a partially fractured alumina disk.

Fig. 11. Reflected light micrograph of portion of a radial crack in a fractured-but-intact alumina disk. Disturbance of some interface-adjacent grains is evident (arrows).

This is the region of the load-insensitive plateau in the strength data[20] referred to in Section I. The radial cracks seemed to remain "trapped" at the encompassing grain boundaries (see Fig. 9) during the flexural loading up to some critical level, at which point a sudden burst of growth ensued. This initial growth pattern was highly variable from specimen to specimen. In many cases the growth distance was small, of the order of grain dimensions, before arresting. Also, individual radial cracks tended to propagate independently, at different levels in the loading. We may liken this initial phase of the fracture evolution to the pop-in observed in the beam configuration (Section II(2)); however, now we can be certain that we are indeed observing an intrinsic property of the small-scale flaw and not some artifact due to the fracture (e.g., notch) geometry. On increasing the applied loading further these radial cracks continued to extend intermittently, but at an increasing jump frequency with respect to stress increment. Thus the "smoothness" in the approach to ultimate failure depended on the number of jumps activated during the loading. In some extreme cases the initial burst of crack propagation was so "energetic" as to take the stressed system spontaneously to failure.

It was also observed that the same kind of discontinuous crack growth and arrest occurred at prominent *natural* flaws in the alumina specimens. These flaws included grain pullout sites on imperfectly polished surfaces and internal fabrication pores. Occasionally such flaws provided the ultimate center of failure, most notably at the low end of the indentation load scale. There seemed little tendency for these competing sites to interact with each other, although inevitably neighbors would occasionally combine to produce an enlarged, yet still stable, composite crack.

Our observations of strong discontinuity and enhanced stabilization in the indentation-strength specimens turns our attention, as in the cantilever beam experiments, to events behind the growing crack tip. Essentially, our in situ examinations of the radial crack evolution to failure revealed the same kind of general grain-bridging features as described earlier in Figs. 4 to 6. Figure 10 shows an example of a particularly large bridging site behind the tip of an extended radial crack. Sites of this kind located as far back as the indentation impression corners remained active throughout the growth to failure, even in those specimens with millimeter-scale stable extensions, confirming that interface restraints act over distances on the order of 100 grains or more. The self-consistency of the grain separation patterns in the two specimen types examined here serves to allay any concern that we might be observing some test-geometry-specific artifact (although geometry effects can still

be an important factor in the R-curve behavior; see Part III).

Some of the broken specimens remained intact to a degree which left much of the grain bridging debris trapped between the crack walls. An example is shown in Fig. 11. There are clear indications of loosening and dislodging of interface-adjacent grains along the crack trace. It appears from the way some of these disturbed grains are rotated about their centers that there are intense local tractions at work. In extreme cases the intensity of these tractions is sufficient to detach the grain completely, and with some energy to spare: in some of the in situ video recording sequences individual grains occasionally disappeared along the crack trace in a single frame interval (e.g., upper left of trace in Fig. 9). Such "pop-out" events invariably occurred as the applied loading was being increased, so the tractions cannot be attributed to spurious closure forces.

For more detailed investigation of the crack-interface events, specimens of the kind shown in Fig. 11 were examined by scanning electron microscopy. Figures 12 to 14 are appropriate micrographs. Figure 12 shows clear examples of the physical contact restraints that can persist at an otherwise widely opened crack interface. Figure 13 presents a slightly more complex picture. Here the grains in the centers of the fields of view have developed secondary microfractures in the base region of attachment to one of the crack walls. There is a strong element of transgranular failure associated with this microfracture process, particularly evident in Fig. 13(A). Lastly, Fig. 14 illustrates a case in which a bridging grain has broken away from both walls and is presumably on the verge of detachment from the interface. Indeed, some minor fragments of material have already been thrown off as fracture debris, notably at lower left of the micrograph.

As with the cantilever beam specimens, evidence was sought that might reveal the presence of an extended frontal microcracking zone about the tips of arrested primary cracks in the strength specimens. Again, no such evidence was found in the SEM observations.

IV. Discussion

We have looked closely, at the microstructural level, into the processes of crack restraint in a coarse-grained alumina. This material, although ostensibly a simple, nontransforming ceramic, shows strong R-curve characteristics. Our observations provide clear evidence for grain-localized bridges at the newly formed crack interface behind the tip. These observations tie in with the sawcutting experiments of Knehans and Steinbrech[11] (Section I).
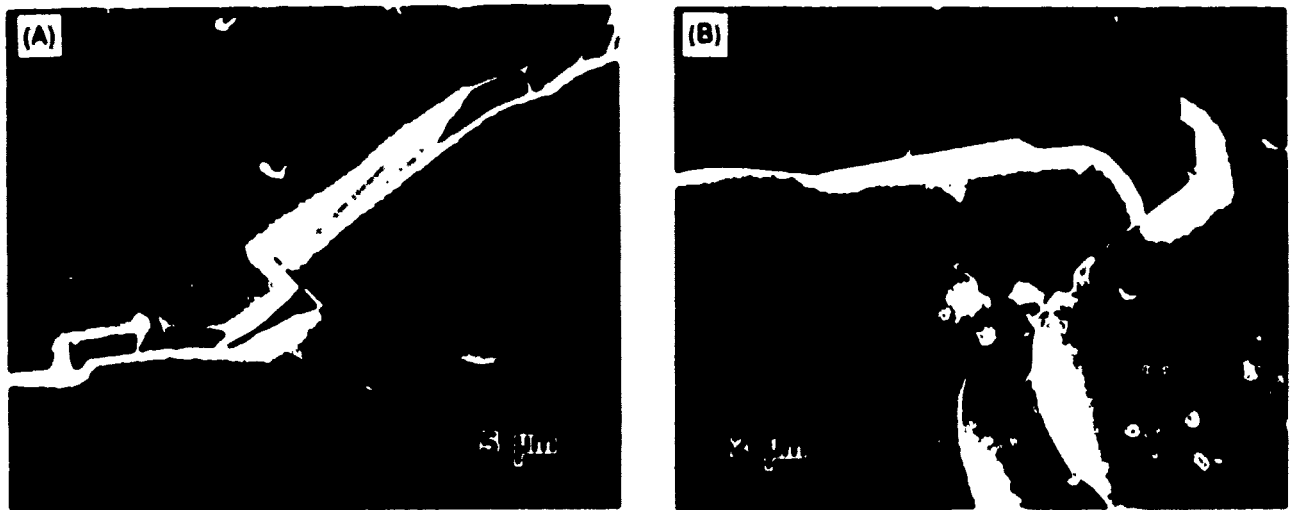
Fig. 12.   Scanning electron micrographs of fractured-but-intact alumina disk, showing examples of apparent frictional interlocking at grain bridging sites
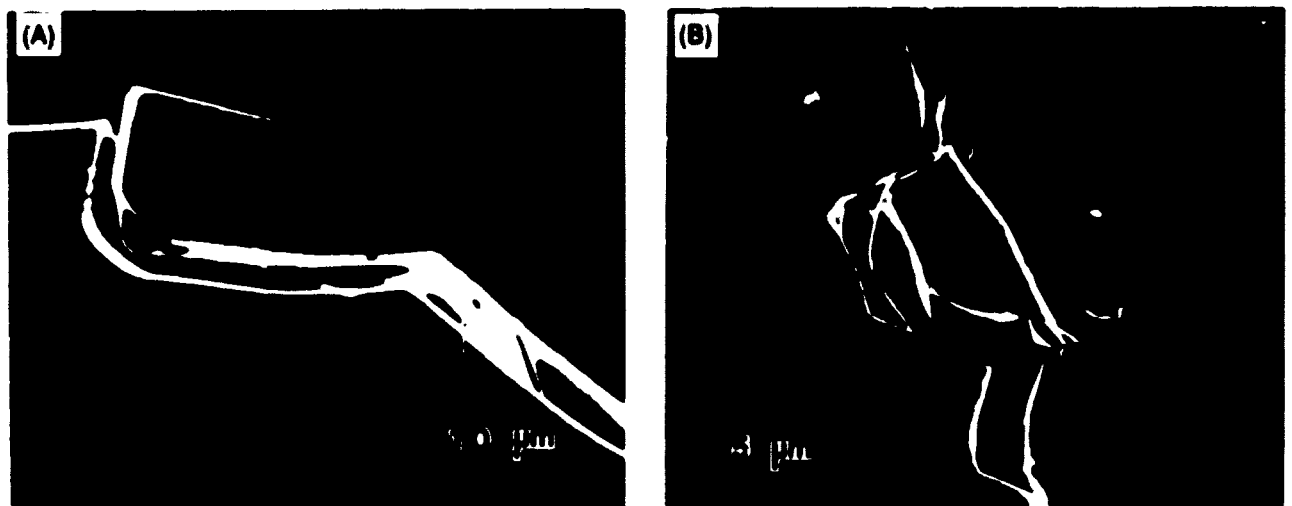

Fig. 13.   Scanning electron micrographs, showing secondary microfracture about bridging grains, indicating the intensity of interface traction forces

in which the crack wake was identified as the crucial source region for the R-curve behavior. Here, in situ experiments have proved most informative, revealing features in the crack response that are not at all apparent from the usual post-mortem (or even interrupted) tests. Not only is the growth highly stable, typical of a rapidly rising toughness characteristic, but it is discontinuous on the microscale. Associated with this discontinuity is the appearance of segmented fracture traces at the specimen surfaces. However, these segments connect beneath the surface into a common, primary crack interface. We picture these discrete, incipient grain bridging sites as uniformly distributed in the projected fracture plane. As the fracture front advances the grain bridging sites are left behind and provide a restraining force which must ultimately be overcome for failure to occur.

It is well to reemphasize at this point that the notion of a physically restrained crack interface is not exactly revolutionary. Many years ago Hoagland et al. in a metallographic sectioning study, presented much the same picture for the brittle fracture of rocks. Again, Hillerborg et al. and others in the concrete literature have been considering the prospect of bridging mechanisms for a decade or so. More recently, one of us has identified analogous mechanisms (using in situ video recording units, acoustic emission location techniques, etc.) in geological rock specimens. There is

Fig. 14   Scanning electron micrograph showing detached end of a bridging grain from fracture interface

therefore plenty of evidence to suggest that this is a general phenomenon. As far as the present study goes, our focus on alumina does not allow us to extend this generalization to other ceramics. However, some preliminary observations on other ceramic systems in these laboratories, e.g., glass-ceramics, along with the implied universality in the *R*-curve phenomenology from the earlier, broader-based indentation-strength study[50,51] (see Section I), indicate that the interface-bridging mode may be far more widespread than hitherto suspected.

Although there appears to be little doubt about the *location* of the toughening agents in our material, the *nature* of the actual separation process remains somewhat obscure. We have presented compelling evidence for the continual development of secondary fractures, accompanied by frictional tractions, around bridging grains, confirming in large part a mechanism foreshadowed by Knehans and Steinbrech and co-workers.[14,15] However, what we have *not* been able to determine is the specific form of the discrete force-separation function that defines the micromechanics of the bridge rupture event. About all that we might say about this function is that it probably has a pronounced tail, bearing in mind the persistent activity at the bridging sites in Figs. 4 to 6 (in some cases long after one or the other of the overlapping crack segments appears to have linked up with the primary fracture surface).

The present study, in addition to identifying a most likely source of toughening in nontransforming ceramics, calls into question the validity of practically all alternative models. Recall our earlier assertion (Section I) that the evidence cited in favor of these alternative models in the literature is almost invariably circumstantial, based at best on post-mortem fractography. The popular notion of a profuse frontal microcracking zone is a prime case in point. We are unaware of any direct observation of such a zone about a growing crack in any nontransforming ceramic material (although there are some recent indications that microcracking may have a role to play in *transforming, multiphase* ceramics[24]). Our own observations gave no indication of dispersed microcracking (other than the bridging grain secondary fractures immediately adjacent to the crack walls). Yet according to the frontal-zone models[7] we would expect events in the alumina to be observable as far distant as several millimeters from the crack interface (Appendix). Moreover, one would expect to find these events manifested cumulatively as a general uprising of material adjacent to the crack trace on the free surface of the fracture specimens, since it is via a predicted dilatancy that the microcracking makes its predominant contribution to the toughening.[7] Striking examples of this kind of uprising have in fact been reported in studies on zirconia,[29,30] where the dissipation-zone description is beyond dispute. Again, the ceramics profilometry examinations revealed nothing (at least within the resolution limit of the profilometer) to support the dilatancy argument in the alumina studied here.

Reference was made in Section I to another possible model, based on crack-tip/internal-stress interactions, for explaining the *R*-curve behavior. At first sight this model does appear to be able to account for most important features of the *R* curve, especially the long range in crack sizes (relative to the grain structure) over which the toughness rises; it is argued that the microscale cracks are most likely to experience the full effect of local tensile forces but that, as extension proceeds, the cracks should gradually average out over alternative tensile and compressive grain elements.[8] However, if this were to be the whole story, the toughness of our polycrystalline alumina should saturate out at the grain boundary energy, so that, since the grain boundary is weaker than the matrix single crystal (for otherwise the fracture would be transgranular), the saturated toughness could never exceed that of sapphire. This is inconsistent with the previous indentation-strength study, where the strength load[20] (or equivalently, toughness-load[23]) curves for polycrystalline alumina and single-crystal sapphire cross each other. Moreover, the internal stress model cannot explain the observation of *R*-curve behavior in specimens with large starter notches; the stress-averaging effect is necessarily already complete in such large crack configurations. Of course, the possibility remains that these same internal stresses could play a secondary role, by acting in concert with some other toughening mechanism,

again, the absence of any abrupt increases in the crack resistance curve (i.e., on the scale of the microstructure itself) excludes certain mechanisms, e.g., deflection, pinning and bowing, as potential partners. Whether internal stresses have anything to do with the bridging mechanism advocated here, e.g., by establishing suitable conditions for creating the ligamentary elements in the first place, is a possibility that might well be explored.

In summary, our observations provide strong, direct evidence for grain-localized bridging elements as a principal source of *R*-curve behavior in nontransforming ceramics. The actual physical separation process involves secondary cracking and frictional interlocking, but the detailed micromechanics remain obscure. We have nevertheless managed to obtain some feeling for the critical dimensions involved in this process for the alumina used here. In particular, we gauge the mean bridge spacing, as reflected by the scale of discontinuous crack growth, to be ≈2 to 3 grain diameters, and the interfacial traction-zone length behind the crack tip to be ≳100 grain diameters. These dimensions will serve as a basis for our fracture mechanics modeling in Part II.

APPENDIX

Evans and Faber[7] provide a formulation of the frontal microcrack zone model from which we can estimate the spatial extent of any microcracking. Assuming that the primary-crack/microcrack interaction arises principally from an averaged dilatancy within the frontal zone, yet (to a first approximation) without perturbing the stress field outside the zone, these authors take the zone width (measured perpendicular to the crack plane) as

$$h = [3^{1/2}(1 + \nu^2)^2/12\pi](K^\infty/\sigma_c)^2$$

where ν is Poisson's ratio, K^∞ is the stress intensity factor associated with the applied field, and σ_c is the critical local stress for microcrack initiation. Inserting $\nu = 0.22$, $K^\infty = 6.5$ MPa·m$^{1/2}$ (saturation toughness, see Part II), and $\sigma_c = 20$ MPa (estimate from Evans and Faber), we obtain $h \approx 5$ mm for our alumina.

References

[1] Y.-W. Mai and B.R. Lawn, "Crack Stability and Toughness Characteristics in Brittle Materials," *Ann. Rev. Mater. Sci.*, 16, 415–39 (1986)
[2] D. Broek, Chs. 5 and 8 in Elementary Fracture Mechanics. Martinus-Nijhoff, Boston, 1982.
[3] R.C. Garvie, R.H. Hannink, and R.T. Pascoe, "Ceramic Steel," *Nature (London)*, 258 [5537] 703–704 (1975).
[4] Advances in Ceramics, Vol. 3, Science and Technology of Zirconia. Edited by A.H Heuer and L.W. Hobbs. American Ceramic Society, Columbus, OH, 1981
[5] R.A. McMeeking and A.G. Evans, "Mechanics of Transformation Toughening in Brittle Materials," *J Am. Ceram. Soc*, 65 [2] 242–46 (1982)
[6] R.G. Hoagland and J.D. Embury, "A Treatment of Inelastic Deformation Around a Crack Tip Due to Microcracking," *J Am. Ceram. Soc.*, 63 [7–8] 404–10 (1980)
[7] A.G. Evans and K.T. Faber, "Crack Growth Resistance of Microcracking Brittle Materials," *J Am. Ceram. Soc.*, 67 [4] 255–60 (1984)
[8] R.W. Rice, R.C. Pohanka, and W.J McDonough, "Effect of Stresses from Thermal Expansion Anisotropy, Phase Transformations, and Second Phases on the Strength of Ceramics," *J Am. Ceram. Soc*, 63 [11–12] 703–10 (1980)
[9] F.F Lange, "The Interaction of a Crack Front with a Second-Phase Dispersion," *Philos. Mag.*, 22, 983–92 (1970)
[10] K.T. Faber and A.G. Evans, "Crack Deflection Processes I Theory, II Experiment," *Acta Metall*, 31 [4] 565–76, 577–84 (1983)
[11] R Knehans and R Steinbrech, "Memory Effect of Crack Resistance During Slow Crack Growth in Notched Al$_2$O$_3$ Specimens," *J Mater Sci Lett*, 1 [8] 327–29 (1982)
[12] A.G Evans, A.H Heuer, and D.L Porter, pp. 529–56 in Fracture 1977, Vol. 1 Edited by D.M R Taplin. University of Waterloo Press, Ontario, Canada, 1977
[13] H Hubner and W Jillek, "Subcritical Crack Extension and Crack Resistance in Polycrystalline Alumina," *J Mater Sci*, 12 [1] 117–25 (1977)
[14] R Knehans and R Steinbrech, "Effect of Grain Size on the Crack Resistance Curves of Al$_2$O$_3$ Bend Specimens," *Sci Ceram*, 12, 613–19 (1983)
[15] F Deuerler, R Knehans, and R Steinbrech, "Testing Methods and Crack Resistance Behavior of Al$_2$O$_3$," to be published in *Sci Ceram* Vol 13
[16] A Hillerborg, M Madeer, and P E Peterson "Analysis of Crack Formation and Crack Growth in Concrete by Means of Fracture Mechanics and Finite Elements," *Cem Concr Res*, 6 [6] 773–82 (1976)
[17] M Wentharatana and S P Shah Prediction of Nonlinear Fracture Process Zone in Concrete," *J Eng Fract Mech* 109 [5] 1231 46 (1983)
[18] P L Swanson, "Subcritical Fracture Propagation in Rocks An Examination Using the Methods of Fracture Mechanics and Non-Destructive Testing Ph D

Thesis. University of Colorado, Boulder, CO, 1984.

[20] P. L. Swanson, pp. 299–317 in Fracture Mechanics of Ceramics, Vol. 8. Edited by R. C. Bradt, A. G. Evans, D. P. H. Hasselman, and F. F. Lange. Plenum, New York, 1986.

[21] R. F. Cook, B. R. Lawn, and C. J. Fairbanks, "Microstructure-Strength Properties in Ceramics: I, Effect of Crack Size on Toughness," J. Am. Ceram. Soc., 68 [11] 604–15 (1985).

[22] R. F. Cook, B. R. Lawn, and C. J. Fairbanks, "Microstructure-Strength Properties in Ceramics: II, Fatigue Relations," J. Am. Ceram. Soc., 68 [11] 616–23 (1985).

[23] C. J. Fairbanks, B. R. Lawn, R. F. Cook, and Y.-W. Mai, pp. 23–37 in Fracture Mechanics of Ceramics, Vol. 8. Edited by R. C. Bradt, A. G. Evans, D. P. H. Hasselman, and F. F. Lange. Plenum, New York, 1986.

[24] R. F. Cook, C. J. Fairbanks, B. R. Lawn, and Y.-W. Mai, to be published in J. Mater. Res.

[25] D. B. Marshall, "An Improved Biaxial Flexure Test for Ceramics," Am. Ceram.

Soc. Bull., 59 [5] 551–53 (1980).

[26] P. L. Swanson, "Tensile-Fracture Resistance Mechanisms in Brittle Polycrystals: An Ultrasonics and In-Situ Microscopy Investigation," unpublished work.

[27] D. B. Marshall, B. R. Lawn, and P. Chantikul, "Residual Stress Effects in Sharp-Contact Cracking: II, Strength Degradation," J. Mater. Sci., 14 [9] 2225–35 (1979).

[28] R. G. Hoagland, A. R. Rosenfield, and G. T. Hahn, "Mechanisms of Fast Fracture and Arrest in Steels," Metall. Trans., 3 [1] 123–35 (1972).

[29] M. Rühle, N. Claussen, and A. H. Heuer, "Transformation and Microcrack Toughening as Complementary Processes in ZrO₂-Toughened Al₂O₃," J. Am. Ceram. Soc., 69 [3] 195–97 (1986).

[30] M. V. Swain and R. H. J. Hannink, pp. 225–39 in Advances in Ceramics, Vol. 12, Science and Technology of Zirconia II. Edited by N. Claussen, M. Rühle, and A. H. Heuer. American Ceramic Society, Columbus, OH, 1985.

[31] D. B. Marshall, "Strength Characteristics of Transformation-Toughened Zirconia," J. Am. Ceram. Soc., 69 [3] 173–80 (1986).

2. "Crack-Interface Grain Bridging as a Fracture Resistance Mechanism in
    Ceramics: II. Theoretical Fracture Mechanics Model"
    Y-W Mai and B.R. Lawn
    J. Am. Ceram. Soc. $\underline{70}$ 289 (1987).

Crack-Interface Grain Bridging as a Fracture Resistance Mechanism in Ceramics: II, Theoretical Fracture Mechanics Model

YIU-WING MAI[*] and BRIAN R. LAWN[*]

Ceramics Division, National Bureau of Standards, Gaithersburg, Maryland   20899

A fracture mechanics model is developed for nontransforming ceramics that show an increasing toughness with crack extension (*R*-curve, or *T*-curve, behavior). The model derives from the observations in Part I, treating the increased crack resistance as the cumulative effect of grain bridging restraints operating behind the advancing tip. An element of discreteness is incorporated into the formal distribution function for the crack-plane restraining stresses, to account for the primary discontinuities in the observed crack growth. A trial force-separation function for the local bridge microrupture process is adopted, such that an expression for the microstructure-associated crack driving (or rather, crack closing) force may be obtained in analytical form. The description can be made to fit the main trends in the measured toughness curve for a coarse-grained alumina. Parametric evaluations from such fits conveniently quantify the degree and spatial extent of the toughening due to the bridging. These parameters could be useful in materials characterization and design. It is suggested that the mechanics formulation should be especially applicable to configurations with short cracks or flaws, as required in strength analysis.

I. Introduction

WE HAVE presented direct experimental evidence in Part I for a mode of crack restraint by grain-localized interfacial bridging behind the advancing tip.[1] The suggestion was made that this mode of restraint is probably a dominant mechanism of *R*-curve behavior in ceramics, at least in nontransforming ceramics. Consequently, there is a need to develop a suitable fracture mechanics model, to establish a sound basis for materials design.

This need constitutes the primary driving force for Part II of our study. We shall derive a formulation for the crack resistance as an increasing function of crack size, bounded in the lower limit by some intrinsic toughness (determined by bulk cleavage or grain boundary energies) and in the upper limit by the macroscopic toughness (representative of the microstructural composite). Following Part I, we shall again take coarse-grained alumina as our representative material, using the measured scaling dimensions for the interfacial bridging process as a basis for quantitative analysis of the observed *R* curve (or, as we shall come to call it, the *T* curve). In setting up our model we will be particularly mindful of the discontinuous (yet highly stable) nature of the crack growth during the loading to failure, most notably in the strength configurations.[1] Speaking of strength configurations, the present analysis supersedes that described in an earlier study using controlled flaws,[2,3] where the microstructural contribution to the fracture mechanics was introduced empirically without reference to any specific toughening mechanism.

An important feature of our modeling will be the capacity for separating out the fracture mechanics from the material characteristics. Essentially, our formalism requires us to specify a local force-separation relation for the restraining interfacial ligaments

Our observations in Part I provide little clue as to what fundamental material quantities should appear in this relation, but they contain some indications as to the *form* (i.e., pronounced tail) and *spatial extent* (i.e., as determined by the critical bridging dimensions referred to above) of the functional dependence. It is thus inevitable that our treatment, while structured on a well-confirmed physical separation model, will retain an element of empiricism. We shall make use of precedents set elsewhere in deciding on an appropriate function for our alumina. This approach will preclude us from making a priori predictions of R-curve behavior in *other* materials. Accordingly, questions as to why R-curve behavior is so variable from material to material (even for materials of the same nominal composition, differing only in the grain boundary structures), are posed as important topic areas for future researchers. Conversely, our formulation will enable us to describe the complete crack resistance behavior for a given material without explicit knowledge of the fundamental underlying separation relations.

Once again, let us foreshadow one of the ultimate goals of our study, to account for the anomalous strength characteristics shown by materials with strong R-curve behavior.[23] In this paper we shall confine ourselves to *qualitative* explanations of some of the more distinctive features of the crack response from indentation flaws, namely, the relative insensitivity of failure stress to flaw size at low loads and the associated growth discontinuities. A detailed quantitative treatment of the problem, in which the indentation-strength data are inverted to obtain the R curve, will be given elsewhere.[4]

II. Interfacial Crack Restraint Model

In this section we develop a fracture mechanics model for a crack restrained at its newly formed interface by distributed closure forces. These closure forces are identified with unruptured bridges whose specific nature is determined by the ceramic microstructure. As such, the restraint is analogous to that considered in the fiber-reinforced ceramic composite models,[5-7] although the underlying microstructural rupture mechanisms in the monophase materials of primary interest here may be of an entirely different kind. We shall begin with a general statement of the crack resistance problem and progressively introduce factors specific to the processes described in Part I.

(1) General Statement of Crack Resistance Problem

Our analysis here is based on equilibrium fracture mechanics, i.e., on the Griffith notion that a crack is on the verge of extension when the net mechanical driving force on the system is just equal to the intrinsic resistance (toughness) of the material.[8] The equilibrium can be stable or unstable, depending on the crack-size variation of the opposing force terms. The terminology "R curve" derives from energy release rate (G) considerations, where $R = R(c)$ is the crack-size-dependent fracture surface energy of the material. Here we shall work instead with stress intensity factors (K) because of their simple linear superposability, replacing R with an analogous toughness parameter $T = T(c)$: hence our preference for the term "T curve".[9]

Our starting point is a general expression for the net stress intensity factor for an equilibrium crack:[9]

$$K = K_a + \sum_i K_i = T_0 \qquad (1)$$

$K_a = K_a(c)$ is the familiar contribution from the applied loading. The terms $K_i = K_i(c)$ represent contributions from any "internal" forces that might act on the crack, such as the microstructure-associated forces that we seek to include here. T_0 is taken to be the intrinsic material toughness (i.e., the effective K_{Ic} for bulk cleavage or grain boundary fracture), strictly *independent of crack size*. Of the individual K terms in Eq. (1) it is only K_a which is monitored directly, via the external loading system, in a conventional fracture test. Consequently, it has become common practice to regard the K_i terms implicitly as part of the toughness characteristic. This philosophy is formalized by rewriting Eq. (1) in the form[9]

$$K_a = T = T_0 - \sum_i K_i. \qquad (2)$$

The quantity $T = T(c)$ defines the effective toughness function, or T curve. To obtain a rising T curve, the $K_i(c)$ functional dependencies must be either positive decreasing or negative increasing.

The existence of a rising T curve introduces a stabilizing influence on the crack growth. We have alluded to such stabilization repeatedly in Part I. From Eq. (1), the condition for the equilibrium to remain stable is that $dK/dc \le 0$ (recalling that $dT_0/dc = 0$). Conversely, the condition for instability is that $dK/dc > 0$ (although satisfaction of this condition does not always guarantee failure; see Section IV). In terms of Eq. (2) the corresponding stability/instability conditions are expressible as $dK_a/dc \le dT/dc$. This latter forms the basis for the conventional T-curve (R-curve) construction.

(2) Microstructure-Associated Stress Intensity Factor

Now let us consider the way in which the microstructural crack restraining forces may be folded into the fracture mechanics description. Specifically, we seek to introduce the effect of restraining bridges behind the growing crack tip as an internal stress intensity factor $K_i = K_\mu$. We shall focus specifically on line cracks in this paper, although this should not be seen as restricting the general applicability of the approach.

The configuration on which our model is to be based is shown in Fig. 1. The interfacial bridging ligaments are represented by the array of force centers (circles) projected onto the crack plane. (This array is depicted here as regular but in reality of course there will be a degree of variability in the distribution of centers.) Here c is the distance from the mouth to the front of the crack and d is the mean separation between closure force centers. Note that at very small crack sizes, $c < d_0$, where d_0 is the distance to the *first* bridge (not *necessarily* identical with d; see Section III), the front encounters no impedance. As the front expands, bridges are activated in the region $d_0 \le x \le c$. These bridges remain active until, at some critical crack dimension c^* ($>d$), ligamentary rupture occurs at those sites most remote from the front. Thereafter a steady-state activity zone of length $c^* - d_0$ simply translates with the growing crack.

This configuration would appear to have all the necessary ingredients to account for the most important features in the crack response observed in Part I. The enhanced stability arises from the increasing interfacial restraint as more and more bridging sites are activated by the expanding crack. The discontinuous nature of the growth follows from the discreteness in the spatial distribution of closure forces at the crack plane. Thus the initial crack may become trapped at first encounter with the bridge energy barriers. If these barriers were to be sufficiently large the entire crack front could be retarded to the extent that, at an increased level of applied stress, the next increment of advance would occur unstably to the second set of trapping sites (pop-in). With further increase in applied stress the process could repeat itself over successive barriers, the jump frequency increasing as the expanding crack encompasses more sites within its front. There is accordingly a smoothing out of the discreteness in the interfacial restraints as the crack grows larger until ultimately, at very large crack sizes, the distribution may be taken as continuous.

In principle, we should be able to write down an appropriate stress intensity factor for any given distribution of discrete restraining forces of the kind depicted in Fig. 1. Unfortunately, the formulation rapidly becomes intractable as the number of active restraining elements becomes larger. To overcome this difficulty we resort to an approximation, represented in Fig. 2, in which the summation over discrete forces $F(x)$ is replaced by an integration over continuously distributed stresses $p(x) = F(x)/d^2$. These stresses have zero value in the region $x < d_0$, reflecting the necessary absence of restraint prior to intersection of the first bridging sites. They have nonzero value in the region $d_0 < x < c$ up to the crack size at which ligamentary rupture occurs ($d_0 \le c \le c^*$), and thereafter in the region $d_0 + c - c^* < x < c$ where a steady-state configuration obtains ($c > c^*$). This approximation is tantamount to ignoring all but the first of the discontinuous jumps in the
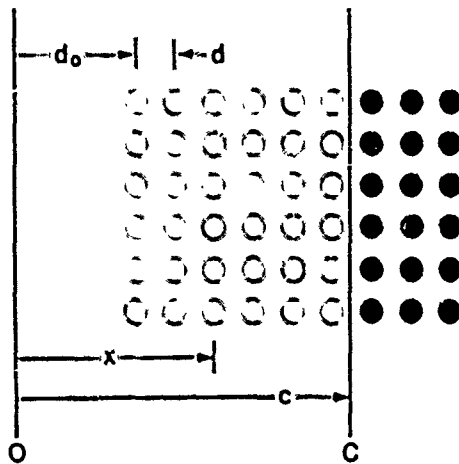
Fig. 1. Schematic of bridging model. O denotes origin. C front, of crack. Circles indicate bridges; open circles denote active sites, closed circle potential sites.

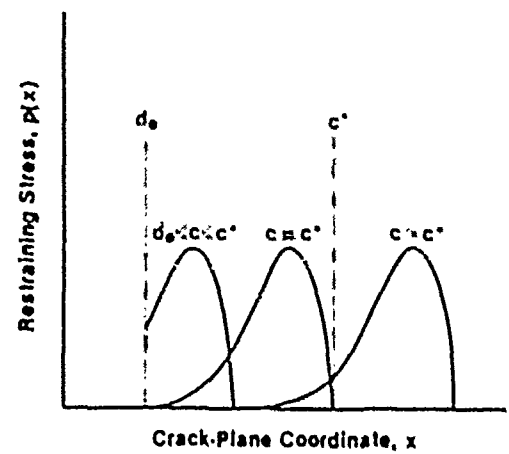Fig. 2. Representation of bridging restraint over crack plane by continuous closure stress distribution. Distributions shown for three crack lengths c relative to d_o and c^* (see Fig. 1).

observed crack evolution. We might consider such sacrifice of part of the physical reality to be justifiable in those cases where the critical crack configuration encompasses many bridging sites, as perhaps in a typical strength test.[4]

The problem may now be formalized by writing down a microstructure-associated stress intensity factor in terms of the familiar Greens function solution for line cracks:[9,10,11]

$$K'_\mu = 0 \qquad (d_o > c) \qquad (3a)$$

$$K'_\mu = -(2\psi/\pi)c^{1/2}\int_{d_a}^{c} p(x)\,d(x)/(c^2 - x^2)^{1/2}$$

$$(d_o \leq c \leq c^*) \qquad (3b)$$

$$K'_\mu = -(2\psi/\pi)c^{1/2}\int_{d-x_o-x^*}^{c} p(x)\,d(x)/(c^2 - x^2)^{1/2}$$

$$(c > c^*) \qquad (3c)$$

where ψ is a numerical crack geometry term ($\approx \pi^{1/2}$). At this point another major difficulty becomes apparent. We have no basis, either theoretical or experimental, for specifying *a priori* what form the closure stress function $p(x)$ must take. On the other hand, we do have some feeling from Part I, albeit limited, as to the functional form $p(u)$, where u is (one half) the crack opening displacement. Moreover, it is $p(u)$ rather than $p(x)$ which should in principle (if not readily in practice) be amenable to *independent* experimental or theoretical determination. Thus, given knowledge of the crack profile, we should be able to replace x by u as the integration variable in Eq. (3), and thereby proceed one step closer to a solution.

However, even this step involves some uncertainty, since the crack profile itself is bound to be strongly influenced by the distribution of surface tractions; i.e., $u(x)$ strictly depends on $p(x)$ (as well as on the applied loading configuration), which we have just acknowledged as an unknown. A proper treatment of the fracture mechanics in such cases leads to a nonlinear integral equation,[5] for which no analytical solutions are available. With this in mind we introduce a simplification by neglecting any effect that the tractions might have on the *shape* of the profile, yet at the same time taking due account of these tractions, via the way they modify the *net* driving force K in Eq. (1), in determining the *magnitude* of the crack opening displacements. Accordingly, we choose the familiar near-field solution for a slitlike crack in equilibrium, i.e., at $K = T_u$:[10,11]

$$u(x,c) = (\sqrt{8}\psi T_u/\pi E)(c - x)^{1/2} \qquad (4)$$

where E is Young's modulus. Substitution of Eq. (4) into Eq. (3)

then gives, in the approximation $d_o \to c$ (e.g., specimens with large notches; see Section III)

$$K'_\mu = 0 \qquad (d_o > c) \qquad (5a)$$

$$K'_\mu = -(E/T_o)\int_a^{u_{d,u}} p(u)\,du \qquad (d_a \leq c \leq c^*) \qquad (5b)$$

$$K'_\mu = -(E/T_o)\int_a^{u^*} p(u)\,du \qquad (c > c^*) \qquad (5c)$$

We point out that $u^* = u(d_o, c^*)$ is independent of c, so K'_μ cuts off at $c \geq c^*$.

Thus by sacrificing self-consistency in our solutions, we have obtained simple working equations for evaluating the microstructure-associated stress intensity factor. We have only to specify the stress-separation function, $p(u)$.

(3) Stress-Separation Function for Interfacial Bridges

The function $p(u)$ is determined completely by the micromechanics of the ligamentary rupture process. We have indicated that we have limited information on what form this function should take. Generally, $p(u)$ must rise from zero at $u = 0$ to some maximum, and then tail off to zero again at the characteristic rupture separation u^*. There are instances in the literature where the rising portion of the curve is the all-dominant feature, e.g., as in brittle-fiber-reinforced composites where abrupt failure of the ligaments cuts off an otherwise monotonically increasing frictional restraining force.[5,6] On the other hand, there are cases where the tail dominates, as in concretes where the separation process is much more stable. Our observations on the alumina in Part I would suggest that it is the latter examples which relate more closely to the polycrystalline materials of interest here. Moreover, specific modeling of *one* of the potential separation factors alluded to in Part I, frictional pullout of interlocking grains, does indeed result in a monotonically (linearly) decreasing $p(u)$ function.[12]

Thus we are led to look for a trial stress separation function which is tail-dominated. The function we choose is

$$p(u) = p^*(1 - u/u^*)^m \qquad (0 \leq u \leq u^*) \qquad (6)$$

where p^* and u^* are limiting values of the stress and separation, respectively, and m is an exponent. This equation is illustrated by the solid curves in Fig. 3 for three values of m: $m = 0$ is the simplistic case of a uniformly distributed stress over the bridging activity zone; $m = 1$ corresponds to the frictional pullout mechanism just mentioned;[12] $m = 2$ is the value adopted empirically for fiber concretes.[11] As we shall see, m reflects most strongly in the way that the ultimate T curve cuts off in the large crack size limit
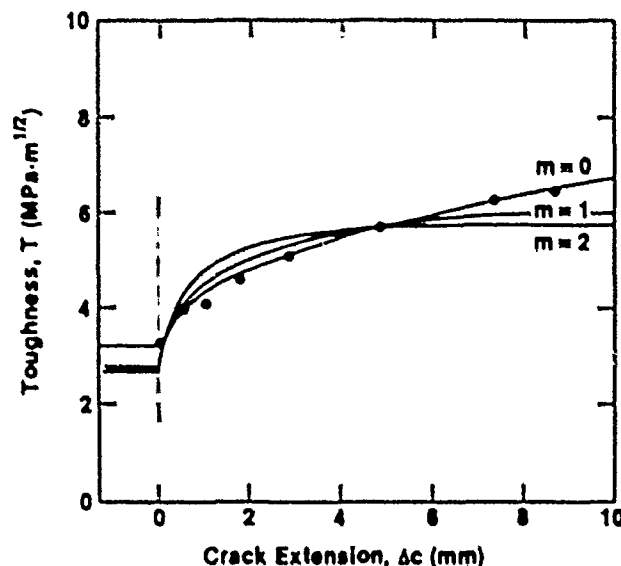
Fig. 3. Trial stress-separation function $p(u)$ for three values of exponent m in Eq. (6). Broken curve is more "realistic" function.

Note that the representation is extreme in the sense that it *totally* ignores the rising portion of $p(u)$ (cf. the broken curve in Fig. 3).

Equation (6) may now be substituted into Eq. (5) and the integration carried out to give

$$K_\mu = 0 \qquad (d_u > c) \tag{7a}$$

$$K_\mu = -(T_\infty - T_u)\{1 - [1 - ((c - d_0)/(c^* - d_0))^{1/2}]^{m+1}\}$$

$$(d_a \leq c \leq c^*) \tag{7b}$$

$$K_\mu = -(T_\infty - T_u) \qquad (c > c^*) \tag{7c}$$

where we have made use of Eq. (4) to eliminate $u^* = u(d_u, c^*)$ in favor of c^*, i.e.

$$c^* = d_u + (\pi E u^*/2\sqrt{2}\,\psi T_u)^2 \tag{8}$$

and where we have defined

$$T_\infty = T_u + Ep^*u^*/(m + 1)T_u \tag{9}$$

to eliminate p^*.

III. Crack Resistance Curve

We are now in a position to generate the effective toughness function from Eq. (2), i.e.

$$T(c) = T_u - K_\mu(c) \tag{10}$$

once the parameters T_u, T_∞, c^*, d_u, and m are known for any given material. Here we shall focus on the derivation of these parameters for coarse-grained alumina, leaving consideration of the crack stability (including the grain-scale discontinuities in growth referred to in Part I) to the Discussion (Section IV).

Usually, crack resistance data are obtained from test configurations which employ a starter notch, as introduced, for example, by sawcutting. The use of such a notch, in addition to providing a favorable geometry for running the crack, conveniently establishes the origin of extension at the base of the T curve. We now need to transform our coordinates, as defined in Fig. 4; we have $c = c_u + \Delta c$, $d_u = c_u + d$, where c_u is the notch length. Combining Eqs. (7) and (10) then gives

$$T(\Delta c) = T_0 \qquad (d > \Delta c) \tag{11a}$$

$$T(\Delta c) = T_\infty - (T_\infty - T_0)$$
$$\times \{1 - [(\Delta c - d)/(\Delta c^* - d)]^{1/2}\}^{m+1}$$

$$(d \leq \Delta c \leq \Delta c^*) \tag{11b}$$

Fig. 4. Coordinates for crack system with starter notch. Effect of notch is to remove all "memory" of bridging restraints over OO', equivalent to redefining the crack origin at O'. Circles indicate bridging sites as in Fig. 1.

$$T(\Delta c) = T_\infty \qquad (\Delta c > \Delta c^*) \tag{11c}$$

Thus within the limits of the approximations used here (most notably the "small-scale zone" approximation used to derive Eq. (5)), we obtain a T curve which is geometry insensitive, i.e., independent of c_0. Note also that the steady-state bridging zone length from Eq. (8)

$$\Delta c^* = d + (\pi E u^*/2\sqrt{2}\,\psi T_0)^2 \tag{12}$$

is likewise geometry insensitive. We shall have more to say about this in Section IV. At this stage the rationale for our parameter definitions becomes apparent: T_0 and T_∞ define the lower and upper bounds, and Δc^* the spatial extent, of the T curve.

To illustrate the applicability of the formulation we examine the degree of fit of Eq. (11) to some experimental data, provided to us by M. V. Swain on a coarse-grained alumina. The material tested by Swain was of closely similar microstructure to that of the alumina used by us in Part I, i.e., reasonably large grain size (16 μm; cf. 20 μm in Part I) and nominally pure composition. He used rectangular double cantilever beam (DCB) specimens, dimensions 50 by 8 by 5 mm, notch length 11 mm, to obtain his crack data. These particular data were chosen over others in the literature because of the special precautions taken to minimize specimen end effects (see Section IV). Swain's results are plotted as the data points in Fig. 5. The theoretical fits, shown as the solid curves for fixed exponents $m = 0$, 1, and 2, were computed for trial values of $d = 50 \mu$m (≈ 3 grain diameters) and $\Delta c^* = 10$ mm (≈ 600 grain diameters) in accordance with the estimates from Part I, with T_0 and T_∞ as regression adjustables.

A word of caution is in order here. Any "goodness of fit" that we might consider evident in Fig. 5 may properly be taken as lending credence to our model. However, it should not be seen as constituting *proof* of our model. In essence, our equations contain five parameters whose values are, to a greater or lesser extent, unknown a priori. Thus, for instance, the accuracy of the fit is not sensitive to the trial value of d, but it *is* sensitive to Δc^* (reflecting the fact that the DCB data are weighted toward the region $\Delta c \gg d$). Such sensitivity to the choice of any *one* parameter inevitably contributes to the uncertainty in the *other* parameters. Consequently, despite all outward appearances in Fig. 5, we would be reluctant to assert that $m = 0$ is the "true" value of the toughness exponent.

Notwithstanding these uncertainties in the parameter determinations, we may usefully estimate the force-separation parameters p^* and u^* in Eq. (6). Thus, substituting $E = 400$ GPa, $\psi = \pi^{1/2}$ (ideal line cracks), along with the best-fit values of T_u, into Eq. (12) gives $u^* \approx 1 \mu$m (independent of m). This is of the order of the crack opening displacements evident in the micrographs in Part I. Further substitution together with the regressed T_∞ values into Eq. (9) gives $p^* \approx 25$ MPa ($m = 0$), 40 MPa

Fig. 5. Fit of Eq. (11) to double cantilever beam (DCB) toughness data on coarse-grained alumina. Fits are for $d = 50\ \mu m$, $\Delta c^\circ = 10$ mm, and $m = 0$, 1, and 2, with T_0 and T_* as adjustables. (Data courtesy M. V. Swain.)

($m = 1$), and 55 MPa ($m = 2$). If these stress levels seem low, we may note that the composite quantity $p^\circ u^\circ/(m + 1)$, which represents the work per unit area to separate the bridges across the fracture plane (see integral in Eq. 5(c)), is of order 20 J·m^{-2}, i.e., comparable with typical fracture surface energies.

Finally in this section, let us note that we have yet to address the issue of crack instabilities in the T-curve characteristic. Recall that our analysis smoothes out all but the very first bridge discontinuity, i.e., at $c = d_0$; the data in Fig. 5 are insufficiently detailed in this region to allow any quantitative resolution of this question. We need to go to short-crack configurations. An account of the T-curve construction for such configurations is deferred to Section IV.

IV. Discussion

We have derived a T-curve (R-curve) model based on bridging tractions at the crack interface behind the advancing tip. The model contains several adjustable parameters, but parameters to which we may nonetheless attach physical meaning. Thus the spatial parameters c° (Δc°) and d, respectively, define the *range* of the T curve and the *characteristic separation* between bridging elements. The toughness parameters T_0 and T_* respectively define the *base crack resistance* in the absence of microstructural restraints (lower limit to T curve) and the *macroscopic crack resistance* (upper limit). Then we have the parameters m, p°, and u°, which determine the empirical force-separation "law" for the bridging process. These parameters, once evaluated for a given material, could be useful in structural design.

It is instructive to consider how the present treatment of the microstructural contribution to crack resistance characteristics differs from that proposed in an earlier study of indentation-strength systems.[2,3] In that study the microstructure-associated stress intensity factor K_m (cf. K_μ used in this work) was introduced in terms of an empirical grain-localized driving force at the radial crack center, in direct analogy to the (well-documented) residual-contact force field.[14,15] There, K_m was defined as a *positive* term *decreasing* with respect to crack size, with T_* as the reference toughness level (i.e., the level at which $K_m = 0$). Here, K_μ is defined as a *negative* (closure) term *increasing* with respect to crack size, with T_0 to the reference toughness level ($K_\mu = 0$). Conventional fracture mechanics measurements, i.e., measurements of crack size as a function of applied load, cannot in themselves distinguish between these two alternative K descriptions. It is in this context

that the direct observations in Part I may be seen as critical. Moreover, the new model has its roots in a positively identifiable toughening mechanism, so taking us one step closer to a fundamental base for a priori predictions.

However, it needs to be reemphasized that the element of empiricism has not been entirely eliminated in the present treatment. There is the issue of the force-separation relation $p(u)$, which we have represented by the tail-dominated function in Eq. (6). Ideally, we would like to be able to determine $p(u)$ from first principles, but this would require a more detailed understanding of the grain bridging micromechanisms than is available at present. Only then may we hope to specify what intrinsic material properties, other than E and T_0 (see Eq. (5)), govern the toughness behavior. At that stage we may be in a position to answer some of the more pressing questions that arise in connection with observed T-curve trends. Thus, what is the explicit dependence of toughness on grain size, and (perhaps more intriguingly) what is it about the incorporation of a glassy grain boundary phase which so dramatically washes out the T-curve effect?[2,3] What role do internal microstresses play? It is with such issues that our ultimate ability to tailor superior structural ceramics must surely rest.

There are other limitations of our analysis which warrant further comment, particularly in relation to geometric effects. In our quest for an analytical solution to the fracture mechanics equations we have resorted to a questionable approximation of the crack-wall displacement profile, Eq. (4). Quite apart from the fact that this approximation is strictly justifiable only for traction-free walls, i.e., in clear violation of the very boundary conditions that we seek to incorporate into our analysis, it requires that we should not attempt to extend the description beyond the confines of the near field. Yet the results of our experimental observations in Part I show bridging activity zones of order millimeters, which is by no means an insignificant length in comparison to typical test specimen dimensions. Thus, contrary to the predictions of Eq. (11), we should not be surprised to find a strong geometry dependence in the measured T-curve response. Such a dependence has been observed in practice, particularly in single-edge-notched beam specimens of alumina with different starter notch lengths.[16-19] There are in fact reported instances, in fiber-reinforced cements,[20] where specimen size effects can *dominate* the intrinsic component in the T-curve characteristic. This is an added concern for the design engineer, whose faith in the T-curve construction is heavily reliant on our ability to prescribe $T(c)$ as a true material property.

Notwithstanding the above reservations, let us return to the question of crack growth discontinuities raised toward the end of Section III. It was pointed out that we need to consider short cracks, i.e., cracks smaller in length than the distance to the first bridging sites, and indeed preferably smaller than the mean bridge spacing itself. This is, of course, the domain of natural flaws. The indentation method is one way of introducing cracks of this scale, with a high degree of control, and will be the subject of a detailed quantitative analysis elsewhere.[4] For the present, we simply consider such a crack, but without residual contact stresses, subjected to a uniformly applied tensile stress, σ_a. Figure 6 is a schematic T-curve construction for this system, showing how the initial crack at $c_i < d$ evolves as the applied stress is increased to failure. The plot is in normalized logarithmic coordinates, to highlight the response at small c. This same plotting scheme allows for a convenient representation of the applied stress intensity factor, $K_a = \psi \sigma_a c^{1/2}$, as a family of parallel lines of slope $\frac{1}{2}$ at different stress levels. The sequence of events is then as follows: (i) at loading stage 1, $K_a = K_a(\sigma_a)_1$, the crack remains stationary; (ii) at stage 2, the crack attains equilibrium at $K_a = T(c)$, and extends from an unstable state at I ($dK_a/dc > dT/dc$) to a stable state at J ($dK_a/dc < dT/dc$); (iii) on increasing the load to stage 3, the crack propagates stably through J to L up the T curve; (iv) at stage 4, a tangency condition is achieved at M, whence failure occurs. Thus our model has the capacity to account for the first crack jump discontinuity (pop-in), as well as the enhanced stability, we have come to associate with this class of material.

As a corollary of the construction in Fig. 6, note that the critical loading condition at M is not affected in any way by the initial
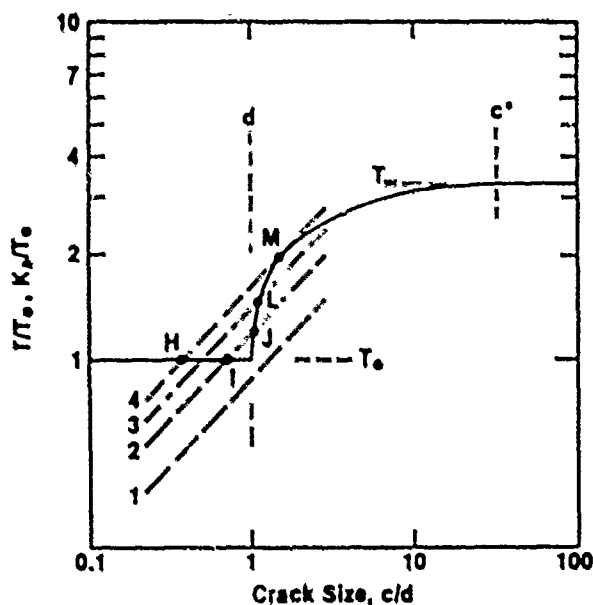
Fig. 6. *T*-curve construction for short crack c_i ($c_N \le c \le c_N$). Solid curve is $T(c)$ function. Inclined dashed lines 1 → 4 represent K_a loading lines for successively increasing values of applied stress σ_a. Crack "pops in" along IJ at stage 2 in the stressing, then progresses through JLK along curve to failure at stage 4. Note failure stress is determined exclusively by tangency condition at M, independent of initial crack size.

present treatment further, especially in regard to the bridging force-separation function. Further, the formulation should be extended to include nonequilibrium states, where the T curve is expected to manifest itself in intriguing ways, e.g., in fatigue limits and non-unique crack velocity $v(K_a)$ functions. Our model is just the first step to a proper understanding of the toughness behavior of materials in terms of microstructural variables, which we must ultimately control if the goal of the property-tailored ceramic is ever to be realized.

crack size c_i, provided this initial size falls within the range $c_N \le c_i \le c_N$. This explains why the strengths of specimens containing controlled flaws tend to level off at diminishing crack size (indentation load).[3] Thus we have a region of "flaw tolerance," a desirable quality from the standpoint of engineering design.

Finally, we are led to believe that the notion of crack interface bridging may have a far greater generality in the accounting of T-curve behavior in ceramics than previously suspected. We have singled out coarse-grained alumina for special study, but the earlier indentation-strength studies on a wide range of materials suggests a certain commonality in the underlying mechanisms of toughening.[11] At the same time, the validity of popular alternative models, particularly those founded on the hypothesis of a dispersed microcracking zone, is in serious doubt. These strong conclusions derive primarily from the direct observations described in Part I. The use of such observations as a means of identifying the responsible toughening mechanisms has been conspicuously absent in the ceramics literature. There is a clear need to develop the

References

[1]P. L. Swanson, C. J. Fairbanks, B. R. Lawn, Y. W. Mai, and B. J. Hockey, "Crack-Interface Grain Bridging as a Fracture Resistance Mechanism in Ceramics: I. Experimental Study on Alumina", this issue, preceding article

[2]R. F. Cook, B. R. Lawn, and C. J. Fairbanks, "Microstructure-Strength Properties in Ceramics: I. Effect of Crack Size on Toughness," *J. Am. Ceram. Soc.*, 68 [11] 604–15 (1985)

[3]R. F. Cook, B. R. Lawn, and C. J. Fairbanks, "Microstructure-Strength Properties in Ceramics: II. Fatigue Relations," *J. Am. Ceram. Soc.*, 68 [11] 616–23 (1985)

[4]R. F. Cook, C. J. Fairbanks, B. R. Lawn, and Y. W. Mai; to be published in *J. Mater. Res.*

[5]D. B. Marshall and A. G. Evans; pp. 557–68 in Proceedings of the 5th International Conference on Composite Materials. Edited by W. C. Harrigan, J. Strife, and A. K. Dhingra. Metallurgical Society of A.I.M.E., Warrendale, PA, 1985

[6]D. D. Marshall, B. N. Cox, and A. G. Evans, "The Mechanics of Matrix Cracking in Brittle-Matrix Fiber Composites," *Acta Metall.*, 33 [11] 2013–21 (1985)

[7]D. B. Marshall and A. G. Evans; pp. 1–15 in Fracture Mechanics of Ceramics, Vol. 7. Edited by R. C. Bradt, A. G. Evans, D. P. H. Hasselman, and F. F. Lange. Plenum, New York, 1986.

[8]B. R. Lawn and T. R. Wilshaw; Ch. 3 in Fracture of Brittle Solids. Cambridge University Press, London, 1975.

[9]Y. W. Mai and B. R. Lawn, "Crack Stability and Toughness Characteristics in Brittle Materials," *Annu. Rev. Mater. Sci.*, 16, 415–39 (1986).

[10]G. I. Barenblatt, "The Mathematical Theory of Equilibrium Cracks in Brittle Fracture," *Adv. Appl. Mech.*, 7, 55–129 (1962).

[11]H. Tada, P. C. Paris, and G. R. Irwin; Part III in The Stress Analysis of Cracks Handbook. Paris Productions, St. Louis, MO, 1985.

[12]A. G. Evans, A. H. Heuer, and D. L. Porter; pp. 529–56 in Fracture 1977, Vol. 1. Edited by D. M. R. Taplin. University of Waterloo Press, Ontario, Canada, 1977

[13]R. Ballarini, S. P. Shah, and L. M. Keer, "Crack Growth in Cement-Based Composites," *Eng. Fract. Mech.*, 20 [3] 433–45 (1984).

[14]D. B. Marshall and B. R. Lawn, "Residual Stress Effects in Sharp-Contact Cracking: I. Indentation Fracture Mechanics," *J. Mater. Sci.*, 14 [9] 2001–12 (1979)

[15]B. R. Lawn, A. G. Evans, and D. B. Marshall, "Elastic/Plastic Indentation Damage in Ceramics: The Median/Radial Crack System," *J. Am. Ceram. Soc.*, 63 [9–10] 574–81 (1980).

[16]R. Knehans and R. Steinbrech, "Memory Effects of Crack Resistance During Slow Crack Growth in Notched Al₂O₃ Specimens," *J. Mater. Sci. Lett.*, 1 [8] 327–29 (1982)

[17]F. Deuler, R. Knehans, and R. Steinbrech, "Testing Methods and Crack Resistance Behavior of Al₂O₃", to be published in *Sci. Ceram.*, Vol. 13.

[18]H. Hubner and W. Jillek, "Subcritical Crack Extension and Crack Resistance in Polycrystalline Alumina," *J. Mater. Sci.*, 12 [1] 117–25 (1977).

[19]H. Wieninger, K. Kromp, and R. F. Pabst, "Crack Resistance Curves of Alumina and Zirconia at Room Temperature," *J. Mater. Sci.*, 21 [2] 411–18 (1986).

[20]R. M. L. Foote, B. Cotterell, and Y. W. Mai; pp. 135–44 in Advances in Cement-Matrix Composites. Edited by D. M. Roy. Materials Research Society, Pennsylvania, 1980.

3. "Crack Resistance by Interfacial Bridging: Its Role in Determining
    Strength Characteristics"
    R.F. Cook, C.J. Fairbanks, B.R. Lawn and Y-W. Mai
    J. Mater. Research 2 345 (1987).

Crack resistance by interfacial bridging: Its role in determining strength characteristics

Robert F. Cook
IBM, Thomas J. Watson Research Center, Yorktown Heights, New York 10598

Carolyn J. Fairbanks, Brian R. Lawn, and Yiu-Wing Mai[a]
Ceramics Division, National Bureau of Standards, Gaithersburg, Maryland 20899

An indentation-strength formulation is presented for nontransforming ceramic materials that show an increasing toughness with crack length (T curve, or R curve) due to the restraining action of interfacial bridges behind the crack tip. By assuming a stress-separation function for the bridges a microstructure-associated stress intensity factor is determined for the penny-like indentation cracks. This stress intensity factor opposes that associated with the applied loading, thereby contributing to an *apparent* toughening of the material, i.e., the measured toughness in excess of that associated with the intrinsic cohesion of the grain boundaries (intergranular fracture). The incorporation of this additional factor into conventional indentation fracture mechanics allows the strengths of specimens with Vickers flaws to be calculated as a function of indentation load. The resulting formulation is used to analyze earlier indentation-strength data on a range of alumina, glass–ceramic, and barium titanate materials. Numerical deconvolution of these data determines the appropriate T curves. A feature of the analysis is that materials with pronounced T curves have the qualities of flaw tolerance and enhanced crack stability. It is suggested that the indentation-strength methodology, in combination with the bridging model, can be a powerful tool for the development and characterization of structural ceramics, particularly with regard to grain boundary structure.

I. INTRODUCTION

Recent studies have shown that many polycrystalline, non-phase-transforming ceramics exhibit an increasing resistance to crack propagation with crack length.[1-8] At small flaw sizes, comparable to the scale of the microstructure, the toughness T is an intrinsic quantity representative of the weakest fracture path. At large flaw sizes the toughness tends to a higher, steady-state value representative of the cumulative crack/microstructure interactions in the polycrystal. The progressive transition from the low-to-high toughness limits during crack extension is described as the T curve. [The concepts of T curve and R curve are equivalent.[9] In the former the equilibrium condition is obtained by equating the net stress intensity factor K, characterizing the net applied load on the crack, to the toughness T (alternatively designated K_{IC} in some of the earlier literature) characterizing critical crack resistance forces. In the latter, the mechanical energy release rate G, derived from the work done by the applied loading during crack extension, is equated to the energy necessary to create the fracture surfaces R.]

Perhaps the most comprehensive studies of this T-curve behavior have been made using a controlled flaw technique,[1-4] in which the strengths of specimens containing indentations are measured as a function of indentation load. It was found that, for large flaws, the strengths tend to an "ideal" $-\frac{1}{3}$ power law dependence of strength on indentation load, indicative of a nonvarying toughness. At small flaw sizes, however, the strengths decrease markedly from this ideal behavior, tending instead to a load-independent plateau. Significantly, in a group of polycrystalline alumina materials it was found that the strengths at large flaw sizes were all greater than those of single-crystal sapphire, whereas the reverse tended to be true at small flaw sizes.[1] Taken with the observation that the fracture in these aluminas is intergranular, these results suggest that the grain boundaries are paths of weakness but that there is some mechanism operating that more than compensates for this intrinsic weakness as the flaw size increases. Moreover, the strength-load responses of the polycrystalline materials themselves, even those with similar grain sizes, tended to cross each other.[1] It would appear that the nature of the grain boundary, as well as the grain size, influences the fracture behavior.

Two other sets of experiments provide vital clues as to the mechanism of crack/microstructure interaction

---

[a] On leave from the Department of Mechanical Engineering, University of Sydney, New South Wales 2006, Australia.

underlying the T-curve behavior. In the first set, Knehans and Steinbrech[6] propagated large cracks in alumina using the single-edge-notched beam geometry. They observed strongly rising T-curves as cracks propagated from the tip of the notch. However, when interfacial material was removed from behind the crack tip by careful sawing, the toughness did not continue up the T curve but reverted to its original level, implying that the critical mechanism must be operating in the "wake" of the crack tip. In the second set of experiments, Swanson *et al.*[8] observed crack propagation in alumina using both indented-disk and tapered-cantilever beam specimens. Active grain-localized "bridges" were observed at the primary crack interface, over a "zone length" of millimeter scale. The implication here is that interfacial bridging ligaments *behind* the tip are providing a restraining influence on crack extension. The reversion to the base of the T curve in the experiments of Knehans and Steinbrech may be interpreted in terms of the removal of these restraining ligaments.

Mai and Lawn[10] developed a fracture mechanics model for the propagation of ligamentary bridged cracks, incorporating parameters characterizing the interbridge spacing, the intrinsic intergranular toughness, and the force-extension "law" for the bridges. They applied the model to the propagation of full-scale cracks propagating under double cantilever loading and thereby demonstrated consistency with the measured T-curve response in a polycrystalline alumina.

Here we shall apply the Mai–Lawn bridging model to the mechanics of the indentation-strength test. It is appropriate to do this for two reasons. First, indentation cracks are strongly representative of the small "natural" flaws that control the strengths of ceramic materials in service.[1] Second, and most important, the indentation methodology will be seen to be ideally suited to quantitative analysis of the T-curve function. For this purpose, recourse will be made to several earlier sources of indentation-strength data, covering a broad spectrum of ceramic materials.[1,3,4,11] The consequent manner in which the indentation-strength test highlights one of the most important manifestations of T-curve behavior, namely flaw tolerance, will emerge as a uniquely appealing feature of the approach. The potential for using the attendant parametric evaluations in the T-curve analysis as a tool for investigating the role of chemical composition and processing variables as determinants of toughness properties is indicated.

II. INTERFACIAL CRACK RESTRAINT MODEL

An earlier fracture mechanics model[10] for straight-fronted cracks restrained by interfacial bridging ligaments is reproduced here in modified form, appropriate to penny-like indentation cracks.

A. Equilibrium crack propagation

A fracture system is in equilibrium when the forces driving the crack extension are equal to the forces resisting this extension. Equilibria may be stable or unstable, depending on the crack-length dependence of these forces.[9] Here we shall characterize the driving forces by stress intensity factors $K(c)$ and the fracture resistance by toughness $T(c)$, where c is the crack size. We may consider separately the stress intensity factor arising from the applied loading K_a, which is directly monitored, from that associated with any internal forces intrinsic to the microstructure K_i, such as the ligamentary bridging forces we seek to include here. We may then conveniently regard the fracture resistance of the material as the sum of an intrinsic interfacial toughness of the material T_0 and the internal K_i terms.[9] Hence our condition for equilibrium may be written

$$K_a(c) = T(c) = T_0 - \sum_i K_i(c), \qquad (1)$$

where we have summed over all internal contributions. We emphasize that T_0 is strictly independent of crack length. The quantity $T(c)$ is the effective toughness function, or T curve, for the material. To obtain a rising T curve, i.e., an increase in toughness with crack length, the sum over the $K_i(c)$ terms must be either positive decreasing or negative increasing. In terms of Eq. (1) the condition for stability is that $dK_a/dc < dT/dc$ and for instability $dK_a/dc > dT/dc$.[9] We see then that a rising T curve, where $dT/dc > 0$, will lead to increased stabilization of the crack system.

B. Microstructure-associated stress intensity factor

We seek now to incorporate the effect of restraining ligaments behind the growing crack tip into a microstructure-associated stress intensity factor, $K_\mu = \Sigma_i K_i$. In the context of indentation flaws we shall develop the analysis for cracks of half-penny geometry.

A schematic model of the proposed system is shown in Fig. 1. The interfacial bridging ligaments are represented as an array of force centers, $F(r)$, projected onto the crack plane. Here c is the radius of the crack front and d is the characteristic separation of the centers. At very small cracks sizes, $c < d$, the front encounters no impedance. As the front expands, bridges are activated in the region $d < r < c$. These bridges remain active until, at some critical crack size c^* ($> d$), ligamentary rupture occurs at those sites most distant behind the front. Thereafter a steady-state annular zone of width $c^* - d$ simply expands outward with the growing crack.

The qualitative features of the crack response observed by Swanson *et al.*[8] would appear to be well described by the above configuration. Enhanced crack sta-
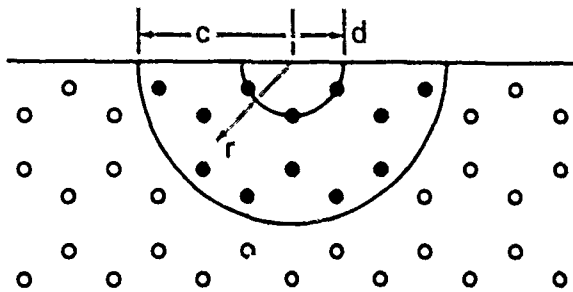
FIG. 1. Schematic diagram of a half-penny, surface crack propagating through a material with bridging ligaments impeding the crack motion. Here d is the mean ligament spacing, c is the crack radius, and r is the radial coordinate from the penny origin; ● denotes the active ligament sits and ○ denotes potential ligament sites.

CRACK-PLANE COORDINATE, r

FIG. 2. Stress distribution applied by the restraining ligaments over the crack plane as a function of radial distance from the center of the crack. Note that the stress is zero for $r < d$ and reaches a steady-state distribution for $c > c^*$.

bility arises from the increasing interfacial restraint as more and more bridging sites are activated by the expanding crack front (the number of active bridges will increase approximately quadratically with the crack radius). The discontinuous nature of the crack growth follows from the discreteness in the spatial distribution of the closure forces in the crack plane. Thus we imagine the crack to become trapped at first encounter with the barriers. If these barriers were to be sufficiently large the crack front could be "trapped" such that, at an increased level of applied stress, the next increment of advance would occur unstably to the second set of trapping sites. Further increases in applied stress would lead to repetitions of this trapping process over successive barriers, the jump frequency increasing as the expanding crack front encompasses more sites. There must accordingly be a smoothing out of the discreteness in the distribution of interfacial restraints as the crack grows until, at very large crack sizes, the distribution may be taken as continuous. With regard to the steady-state zone width ($c^* - d$) referred to above, our own observations and those of Swanson et al.[8,12] indicate that, for a given material, there is a characteristic distance behind the crack tip that contains apparently intact bridges.

In principle, we should be able to write down an appropriate stress intensity factor for any given distribution of discrete restraining forces of the kind depicted in Fig. 1. However, an exact summation becomes intractable as the number of active restraining elements becomes large. To overcome this difficulty we approximate the summation over the discrete force elements $F(r)$ by an integration over continuously distributed stresses $\sigma(r) = F(r)/d^2$. We plot these stresses for three crack configurations in Fig. 2. These stresses have zero value in the region $r < d$, reflecting the necessary absence of restraint prior to the intersection of the crack front with the first bridging sites. They have nonzero

value in the region $d < r < c$ up to the crack size at which ligamentary rupture occurs ($d < c < c^*$) and thereafter in the region $d + c - c^* < r < c$, where a stready-state configuration is obtained ($c > c^*$). This approximation is tantamount to ignoring all but the first of the discontinuous jumps in the observed crack evolution. We might consider such a sacrifice of part of the physical reality to be justifiable in those cases where the critical crack configuration encompasses many bridging sites, as perhaps in a typical strength test.

The problem may now be formalized by writing down a microstructure-associated stress intensity factor in terms of the familiar Green's function solution for penny-like cracks[13]:

$$K_\mu = 0 \quad (c < d), \tag{2a}$$

$$K_\mu = -\left(\frac{\psi}{c^{1/2}}\right) \int_d^c \sigma(r) \, r \frac{dr}{(c^2 - r^2)^{1/2}} \quad (d < c < c^*), \tag{2b}$$

$$K_\mu = -\left(\frac{\psi}{c^{1/2}}\right) \int_{d + c - c^*}^c \sigma(r) r \frac{dr}{(c^2 - r^2)^{1/2}} \quad (c > c^*), \tag{2c}$$

where ψ is numerical crack geometry term. At this point another major difficulty becomes apparent. We have no basis, either theoretical or experimental, for specifying a priori what form the closure stress function $\sigma(r)$ must take. On the other hand, we do have some feeling from the observations of Swanson et al., albeit limited, as to the functional form $\sigma(u)$, where u is the crack opening displacement. Further, it is $\sigma(u)$ rather than $\sigma(r)$ that

is the more fundamental bridging quantity and that is more amenable to independent specification. Thus, given a knowledge of the crack profile, we should be able to replace r by u as the integration variable in Eq. (2) and thereby proceed one step closer to a solution.

However, even this step involves some uncertainty, as the crack profile itself is bound to be strongly influenced by the distribution of surface tractions, i.e., $u(r)$ strictly depends on $\sigma(r)$ (as well as on the applied loading configuration), which we have just acknowledged as an unknown. A rigorous treatment of this problem involves the solution of two coupled nonlinear integral equations, for which no analytical solutions are available.[14] We thus introduce a simplification by neglecting any effect the tractions might have on the *shape* of the crack profile, while taking account of these tractions through their influence on the net driving force $K = K_a + K_\mu$ from Eq. (1), in determining the *magnitude* of the crack opening displacements. Accordingly, we choose Sneddon's solution[15] for the near-field displacements of an equilibrium crack, i.e., $K = T_0$,

$$u(r,c) = (\psi T_0/Ec^{1/2})(c^2 - r^2)^{1/2}, \qquad (3)$$

where E is the Young's modulus. Substitution of Eq. (3) into Eq. (2) then gives

$$K_\mu = 0 \quad (c < d), \qquad (4a)$$

$$K_\mu = -\left(\frac{E}{T_0}\right)\int_0^{u(d,c)} \sigma(u)du \quad (d < c < c^*), \qquad (4b)$$

$$K_\mu = -\left(\frac{E}{T_0}\right)\int_0^{u^*} \sigma(u)du \quad (c > c^*). \qquad (4c)$$

We note that $u^* = u(d,c^*)$ is independent of c so K_μ cuts off at $c > c^*$.

Let us note here that our choice of the Sneddon profile, Eq. (3), leads us to an especially simple solution for K_μ in Eq. (4). In particular, we note that this term is conveniently expressible as an integral of the surface closure stress as a function of the crack opening displacement, i.e., a work of separation term. This simple solution obtains *only* with the Sneddon profile. It might be argued that a Dugdale-type profile[16] is more appropriate, but it can be shown that the fracture mechanics are not too sensitive to the actual profile chosen.[17] Our main objective here is to emphasize the physical variables involved. Thus by sacrificing self-consistency in our solutions, we have obtained simple working equations for evaluating the microstructure-associated stress intensity factor. We have only to specify the stress-separation function $\sigma(u)$.

C. Stress-separation function for interfacial bridges

The function $\sigma(u)$ is determined completely by the micromechanics of the ligamentary rupture process. We have indicated that we have limited information on

what form this function should take. Generally, $\sigma(u)$ must rise from zero at $u = 0$ to some maximum and then decrease to zero again at some characteristic rupture separation u^*. The observations of crack propagation in alumina by Swanson *et al.* suggest that it is the decreasing part of this stress-separation response that is the most dominant in the polycrystalline ceramics of interest here.[8] The stable crack propagation observed by those authors has much in common with the interface separation processes in concrete materials that are often described by tail-dominated stress-separation functions.

The stress-separation function chosen is[10]

$$\sigma(u) = \sigma^*(1 - u/u^*)^m \quad (0 < u < u^*), \qquad (5)$$

where σ^* and u^* are limiting values of the stress and separation, respectively, and m is an exponent. We consider three values of m: $m = 0$ is the simplest case of a uniformly distributed stress acting over the annular activity zone; $m = 1$ corresponds to simple, constant-friction pullout of the interlocking ligamentary grains; $m = 2$ is the value adopted by the concrete community (equivalent to a decreasing frictional resistance with increasing pullout). As we shall see, the choice of m will not be too critical in our ability to describe observed strength data. Note that the representation of the stress-separation function by Eq. (5) is an infinite modulus approximation in that it totally neglects the rising part of the $\sigma(u)$ response.

Equation (5) may now be substituted into Eq. (4) to yield, after integration,

$$K_\mu = 0 \quad (c < d), \qquad (6a)$$

$$K_\mu = -(T_\infty - T_0)\{1 - \{1 - [c^*(c^2 - d^2)/ c(c^{*2} - d^2)]^{1/2}\}^{m+1}\} \quad (d < c < c^*), \qquad (6b)$$

$$K_\mu = -(T_\infty - T_0) \quad (c > c^*), \qquad (6c)$$

where we have eliminated the stress-separation parameters σ^* and u^* in favor of those characterizing steady-state crack propagation, c^* and T_∞:

$$c^* = 2(Eu^*/\psi T_0)^2\{1 + [1 + 4(\psi T_0 d^{1/2}/Eu^*)^4]^{1/2}\} \qquad (7)$$

and

$$T_\infty = T_0 + E\sigma^*u^*/(m + 1)T_0. \qquad (8)$$

These latter parameters are more easily incorporated into the strength analysis to follow.

A useful quantity is the work necessary to rupture an individual ligament. This work is a composite measure of the maximum sustainable stress and maximum range of the stress-extension function of Eq. (5) and is given by the area under the stress-separation curve $\sigma(u)$. We may express this area as

$$\Gamma_i = \int_0^{u^*} \sigma(u)du = \frac{\sigma^*u^*}{(m + 1)}. \qquad (9a)$$

It is useful to compare this quantity with the intrinsic interfacial energy[9]

$$\Gamma_0 = T_0^2/2E. \tag{9b}$$

The Γ terms in Eq. (9) are related, through Eq. (8), by the ratio

$$\Gamma_I/\Gamma_0 = 2(T_\infty - T_0)/T_0 \tag{10}$$

which may conveniently be regarded as a toughening index.

D. Strength-indentation load relations

We are now in the position to consider the mechanics of a test specimen containing an indentation crack produced at load P and subsequently subjected to an applied stress σ_a. To obtain the "inert strength" σ_m, we need to determine the equilibrium instability configuration at which the crack grows without limit.

In indentation crack systems the stress intensity factor associated with the residual contact stresses K_r, augments the stress intensity factor associated with the applied loading K_a, effectively giving rise to a *net* applied stress intensity factor K'_a.[18,19] Equation (1) becomes

$$K'_a = K_a + K_r = T(c)$$

$$= \psi \sigma_a c^{1/2} + \chi P/c^{3/2} = T_0 - K_\mu(c), \tag{11}$$

where χ measures the intensity of the residual field. We note that K_r is inverse in crack size and hence will further stabilize the fracture evolution.[19] The indentation load determines the initial crack size at $\sigma_a = 0$, but *because* of the stabilization in the growth we should not necessarily expect this initial size to be an important factor in the fracture mechanics. Our problem then is to combine Eqs. (6) and (11) and invoke the instability condition $dK'_a/dc > dT/dc$ to determine the strength as a function of indentation load.

Unfortunately, it is not possible to obtain closed form solutions to this problem. Limiting solutions *can* be obtained analytically, however, and we consider these first.

(i) Small cracks (low P). In the region $c \ll d$ we revert to the ideal case of zero microstructural interaction, such that Eq. (6a) applies. In this region it can be readily shown that the equilibrium function $\sigma_a(c)$ obtained by rearranging Eq. (11) passes through a maximum, up to which point the crack undergoes stable growth.[19] This maximum therefore defines the instability point $d\sigma_a/dc = 0$ (equivalent to the condition $dK'_a/dc = dT/dc = 0$ here):

$$\sigma_m^0 = 3T_0^{4/3}/4^{4/3}\psi(\chi P)^{1/3}. \tag{12}$$

The region of validity of this solution is indicated as region I in Fig. 3.

(ii) Large cracks (high P). In the region $c > c^*$, Eq. (6c) applies P we have maximum microstructural in-

teraction. The procedure to a solution is entirely the same as in the previous case, except that now T_∞ replaces T_0 in Eq. (12). Thus

$$\sigma_m^\infty = 3T_\infty^{4/3}/4^{4/3}\psi(\chi P)^{1/3}. \tag{13}$$

This solution applies in region III in Fig. 3.

It is for intermediate cracks, region II in Fig. 3, that analytical solutions are difficult to obtain. Here numerical procedures will be required, but the route is nevertheless the same as before; determine $\sigma_a(c)$ from Eq. (11) in conjuction with Eq. (6b) and apply the instability condition, taking account of the increased stabilization arising from the K_μ term. To proceed this way we must first determine the values of the parameters in Eqs. (6) and (11). We address this problem in the next section.

III. DERIVATION OF T CURVE FROM INDENTATION STRENGTH DATA

A. Crack geometry and elastic/plastic contact parameters

Our first step towards a complete parametric evaluation of the $\sigma_m(P)$ data is to seek *a priori* specifications of the dimensionless quantities ψ and χ in Eq. (11). The parameter ψ is taken to be material independent, since it is strictly a crack geometry term. The parameter χ does depend on material properties, however, relating as it does competing elastic and plastic processes in the indentation contact.[13] We note that these parameters do not appear in the microstructural term K_μ in Eq. (6), so ideally we can "calibrate" them from
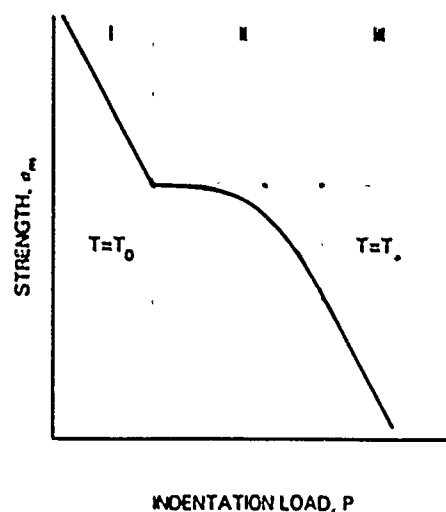
FIG. 3. Schematic strength versus indentation load plot incorporating the influence of bridging ligaments into the crack propagation response (logarithmic coordinates). The solid line represents the general solution [Eqs. (6) and (11)]. The dashed lines represent asymptotic solutions obtained analytically for small cracks [region I, Eq (12)] and large cracks [region III, Eq. (13)]

tests on materials that do *not* exhibit T-curve behavior. The details of such calibrations are given in the Appendix. The values we use are $\psi = 1.24$ and $\chi = 0.0040 \, (E/H)^{1/2}$, where H is the hardness.

B. Bounding parameters for the regression procedure

We have indicated that solutions for region II of the strength-load response of Fig. 3 must be obtained numerically. Here we shall outline the regression procedure used to deconvolute the T curve for a given set of $\sigma_m (P)$ data.

To establish reasonable first approximations for a search/regression procedure, we note two experimental observations. The first is from the indentation/strength data of Cook *et al.*[1] In a number of materials the $\sigma_m (P)$ data tended strongly to the asymptotic limit of region III at large indentation loads (Fig. 3), reflecting the upper, steady-state toughness T_∞ [see Eq. (13)]. No analogous transition corresponding to T_0 -controlled strengths in region I was observed: at low indentation loads the strength data were truncated by failures from natural flaws. Notwithstanding this latter restriction, we may use Eqs. (12) and (13) (with calibrated values of ψ and χ from Sec. III A) to set upper bounds to T_0 and lower bounds to T_∞ from strength data at the extremes of the indentation load range. We expect from the observations of Cook *et al.* that the lower bound estimate of T_∞ probably lies closer to the true value than the upper bound estimate to T_0.

The second experimental observation is from the crack propagation work of Swanson *et al.*,[a] who estimated the average distance between bridging sites at 2–5 grain diameters. We accordingly take the lower bound estimate for the interligament spacing d at 1 grain diameter. Similar bounding estimates for c^* are more difficult, although the condition $c^* > d$ must be satisfied.

There is one further parameter we have to specify, and that is the exponent of the ligament stress-extension function m. We have alluded to the fact that the observations of Swanson *et al.* indicate that a stabilizing, tail-dominated stress-separation function should be appropriate, with $m > 1$ in Eq. (5).

C. Regression procedure

With the first approximations thus determined we search for the set of parameters for each set of $\sigma_m (P)$ data. The scheme adopted to do this is as follows.

(1) The T curve is set from Eqs. (1) and (6) and the equilibrium $\sigma_a (c)$ response is calculated from Eq. (11) at each indentation load for which there are *measured* strength data.

(2) The *predicted* strength at each indentation load is determined numerically from the instability require-

ment $d\sigma_a / dc = 0$ (with the proviso that if more than one maximum in the $\sigma_a (c)$ function exists, it is the greater that determines the strength—see Sec. IV).

(3) The predicted strengths are compared with the corresponding measured strengths and the mean variance thereby calculated for a given set of T-curve parameters.

(4) The T-curve parameters are incremented and the calculation of the variance repeated, using a matrix search routine. The increments in the search variables were 0.05 MPa m$^{1/2}$ for the toughness parameters T_0 and T_∞ and 5 μm for the dimension parameters d and c^*.

(5) The set of T-curve parameters yielding the minimum residual variance is selected.

IV. RESULTS

The materials analyzed in this study are listed in Table I, along with their Young's modulus, hardness, grain size, and minor phase percentage. Previously published[1,3,4,11] indentation-strength data for these materials was used for the T-curve deconvolutions. [Some data were removed from the original $\sigma_m (P)$ data sets at large indentation loads, where the influence of secondary lateral cracking was suspected to have significantly decreased the magnitude of the residual stress intensity factor.[30]] The resultant parameter evaluations are given in Table II.

Our first exercise was to select a fixed value of the exponent m for the T-curve evaluations. Accordingly a preliminary analysis of the $\sigma_m (P)$ data for two materials displaying particularly strong T-curve influences in their strength responses, namely the VI1 and VI2 aluminas, was carried out. Figure 4 shows the minimum resid-
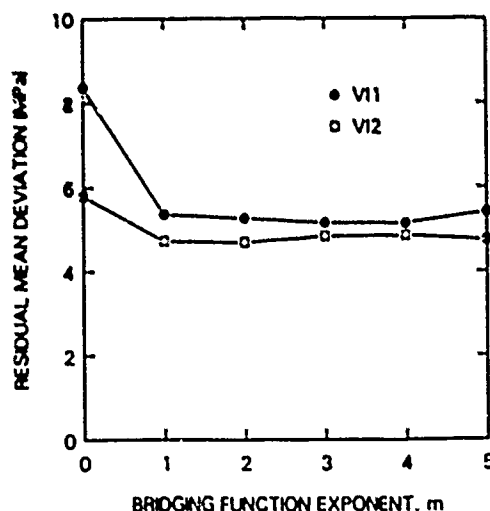
FIG. 4. The residual mean deviation between fitted and measured indentation-strength functions versus bridging function exponent m for the VI aluminas. Note the relative insensitivity for $m > 1$.

ual mean deviation as a function of m for these materials. The deviation for both materials is greatest at $m = 0$ but thereafter at $m \gtrsim 1$ is insensitive to the choice of exponent. The value somewhat arbitrarily chosen for this study was $m = 2$ in accord with that adopted in the concrete literature.[10]

To illustrate the procedure and at the same time to gain valuable insight into the crack evolution to failure let us focus now on just two of the listed alumina materials in Table I, VI2 and AD96. Figure 5 shows the strength versus indentation load data for these materials.[1] The data points in this figure represent means and standard deviations of approximately ten strength tests at each indentation load. The solid lines are the best fits [Eqs. (1), (6), and (11)] to the data. The dashed lines represent T_0- and T_∞-controlled limits [Eqs. (12) and (13)]. As can be seen, the fitted curves smoothly intersect the T_∞-controlled limit at large indentation loads, this tendency being greater for the AD96 material. This smooth connection is a reflection of our choice of m above; for $m < 2$ the $\sigma_m (P)$ curve intersects the T_∞ limit with a discontinuity in slope. At intermediate indentation loads the strengths tend to a plateau level, more strongly for the VI2 material. In line with our contention that this plateau is associated with a strong microstructural influence we might thus expect the VI2 material to exhibit a more pronounced T curve. The larger separation of the T_0- and T_∞-controlled limits for the VI2 material in Fig. 6 supports this contention. Finally, at small indentation loads the strengths cut off abruptly at the T_0-controlled limit, corresponding to the case
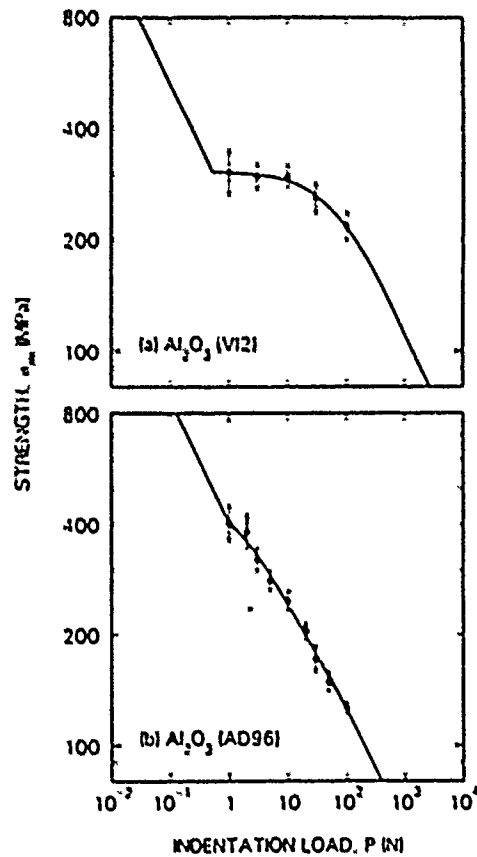
FIG. 5. Indentation-strength data fits for the VI2 and AD96 aluminas. Note the relatively pronounced plateau for the VI2 material, indicative of a strong T-curve influence. Oblique dashed lines are T_0- and T_∞-controlled limiting solutions.

TABLE I. Materials analyzed in this study.

Material		Young's modulus $E/$GPa	Hardness $H/$GPa	Grain size μm	Minor phase %	Ref.
Alumina	VI1	393	19.1	20	0.1	1
	VI2	393	19.0	41	0.1	1
	AD999	386	20.1	3	0.1	1
	AD96	303	14.1	11	4	...
	AD90	276	13.0	4	10	1
	F99	400	16.1	11	1	1
	HW	206	11.7	28	0.3	1
	Sapphire	425	21.8	...	...	1
Glass-ceramics	SL1	87.9	4.4	1.2	33	1,3
	SL2	87.9	4.3	1.9	22	1,3
	SL3	87.9	4.8	2.3	20	1,3
	Macor	64.1	2.0	17	50	4
	Pyroceram	108	8.4	1	...	4
Barium titanate	CH(cub.)	123	5.9	7	1	11
	CH(tet.)	123	5.9	7	1	11

where the crack intersects no bridges prior to unlimited instability.

Figures 6 and 7 show the corresponding equilibrium σ_a (c) and $T(c)$ functions that underlie the curve fits in Fig. 5. The σ_a (c) responses are plotted for several indentation loads, embracing the data range covered in the indentation-strength experiments (e.g., Fig. 5). The most distinctive feature of these curves is that at low indentation loads, where the initial crack size is somewhat smaller than the first barrier distance d, there are two maxima, most notably in the VI2 material. The first maximum, at $c < d$, is a pure manifestation of the crack stabilization due to the residual contact stress term [Eq. (11)].[19] The second maximum, at $c > d$, results from the additional, abrupt stabilization associated with the microstructural closure forces. Of the two maxima, it is the greater that determines the strength. Thus at very low P (corresponding to region I in Fig. 3) the first maximum wins, and the instability takes the crack system to failure without limit (e.g., the $P = 0.1$ N curves for both the VI2 material in Fig. 6 and the AD96 material in Fig. 7). At intermediate P (region II in Fig. 3) the second maximum becomes dominant, in which case the

FIG. 7. (a) Applied stress versus equilibrium crack length and (b) corresponding T curve, for AD96 alumina.

crack arrests before failure can ensue (e.g., the $P = 1$ N curves in Figs. 6 and 7). Note that the second maximum for the VI2 alumina occurs at $\simeq 100\mu$m, consistent with abrupt initial jumps of 2–5 grain diameters reported by Swanson *et al.* At large P (region III in Fig. 3) the curves tend more and more to a single pronounced maximum, as we once more enter a region of invariant toughness. In all cases, however, we note that the stabilizing influences of the residual and microstructural stress intensity factors render the strength insensitive to the intial crack length.

It is in the transition region, region II, where the form of the T curve most strongly influences the crack stability and strength properties. The T curve for the VI2 alumina rises more steeply than that for the AD96 alumina. The difference in responses for the two materials may be seen most clearly in the σ_a (c) curves for $P = 10$ N, Figs. 6 and 7. In VI2 alumina the restraint exerted on the crack by the interfacial bridges is apparently much stronger than in AD96. We note that the indentation-strength curves in Fig. 5 may be seen as "rotated" versions of the T curves in Figs. 6 and 7.

A word is in order here concerning the "sensitivity" of the parameter evaluation to the range of data. Figure

FIG. 6. (a) Applied stress versus equilibrium crack length at different indentation loads and (b) corresponding T curve, for VI2 alumina, as derived from the indentation-strength data in Fig. 5.

8 shows the deconvoluted T curves for the VI2 material with individual data points at either end of the indentation load range deliberately omitted from the base data in Fig. 5(a). When data are "lost" from the large *P* end, the high *T(c)* part of the curve is most affected; similarly, for data omissions at the small *P* end, the low *T(c)* part of the curve is most affected. We may regard the curve shifts in Fig. 8 as characterizing the *systematic* uncertainty in our parameter evaluations, just as the mean residual deviation in the regression procedure characterizes the *random* uncertainty. We note that it is those parameters that control the upper and lower bounds of the T curve that are subject to the greatest uncertainty, since it is in these extreme regions (especially in the T_0-controlled region) where indentation-strength data are most lacking. The central portions of the T curves in Fig. 8 are not altered substantially by the deletion of strength data.

Subject to the above considerations, we may now usefully summarize the relative T-curve behavior for the remainder of the materials listed in Table II. The T curves are shown in Figs. 9–11 for each of the material types, aluminas, glass–ceramics, and barium titanates. Special attention may be drawn to the fact that the curves for the microstructurally variant materials in each of these composite plots tend to cross each other. We note in particular that the curves for the polycrystalline aluminas in Fig. 9 cross below that for sapphire at small crack sizes, consistent with earlier conclusions that the intrinsic polycrystal toughness (T_0) is governed by grain boundary properties.[1]

FIG. 9. Composite plot of the deconvoluted T curves for the alumina materials.

V. DISCUSSION

We have considered a fracture toughness model based on an independently verified interface restraint mechanism[8,9] for explaining the microstructural effects previously reported in indentation/strength data.[1-4] A key feature of our modeling is the strong stabilizing effect of grain-scale ligamentary bridges on the stability conditions for failure. (In this sense our explanation differs somewhat from that originally offered by us in

FIG. 8. Deconvoluted T-curve plots for the VI2 alumina using full indentation-strength data set from Fig. 5(a) (solid line) and same data truncated (dashed lines) by removal of extreme data points at (a) low *P* and (b) high *P*.
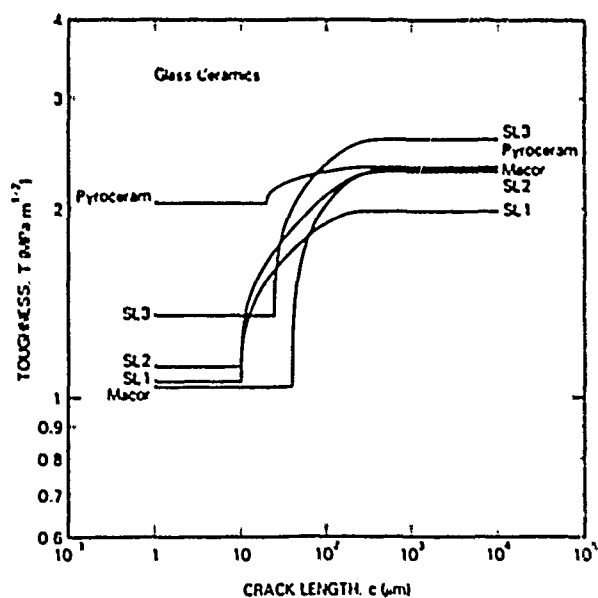
FIG. 10. Composite plot of the deconvoluted T curves for the glass-ceramic materials.
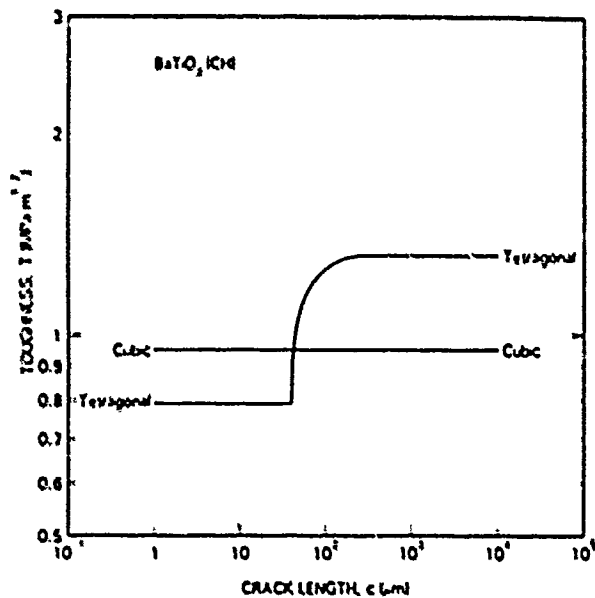
FIG. 11. Composite plot of the deconvoluted T curves for the barium titanate material.

Ref. 1, where it was tacitly suggested that the microstructural influence might be represented as a *positive decreasing* function of crack size. The distinction between negative increasing and positive decreasing K_μ functions is not easily made from strength data alone.) Although the earlier experimental observations used to establish the model[1x] were based almost exclusively on one particular alumina ceramic,[1] our own detailed crack observations, and those of others, strongly suggest that the model is generally applicable to other nontransforming ceramics; the discontinuous primary crack traces

characteristic of the bridging process have since been observed in other aluminas,[12-21] glass-ceramics,[12,21,22] SiC ceramics,[23] and polymer cements.[24] The fact that the resultant strength equations from the model can be fitted equally well to all the materials examined in the present study serves to enhance this conviction.

A characteristic feature of the failure properties of the materials with pronounced T curves (e.g., VI2 alumina) is the relative insensitivity of the strength to initial flaw size. This is a vital point in relation to structural design. Materials with strong T-curve responses have the quality of flaw tolerance. Ideally, it would seem that one should seek to optimize this quality. Associated with this tolerance is an enhanced crack stability. This offers the potential detection of failures. On the other hand, there is the indication that such benefits may only be wrought by sacrificing high strengths at small flaw sizes. This tendency is clearly observed in the way the strength curves cross each other in Figs. 7–9 in Ref. 1 (corresponding to crossovers seen here in the T curves, Figs. 9–11). In other words, the designer may have to practice the gentle art of compromise.

We reemphasize that the T-curve parameters derived from the strength data (Table II) are elements of curve fitting and are subject to systematic as well as to the usual random uncertainties. Since any four of these parameters are independent, our numerical procedure, regardless of "goodness of fit," cannot be construed as "proof" of our model. Nevertheless, we may attach strong physical significance to these parameters. For example, the relatively large values of Γ_f and c^* for the VI materials relative to the corresponding parameters for the F99 alumina is a clear measure of a greater T-curve effect in the former. More generally, the aluminas with

TABLE II. T-curve parameters derived from strength data for m = 2 (from Refs. 1, 3, 4, 11).

Material	T_0 (MPa m$^{1/2}$)	T_∞ (MPa m$^{1/2}$)	Γ_u (J m^{-3})	Γ_f (J m^{-3})	d (μm)	c^* (μm)	σ^* (MPa)	u^* (μm)
VI1	1.73	4.08	3.8	10.4	40	420	280	0.11
VI2	1.49	4.63	2.8	11.8	60	540	328	0.11
AD999	2.22	4.30	6.4	12.0	15	715	188	0.19
AD96	2.16	2.87	8.5	5.6	15	460	80	0.19
AD90	2.76	3.21	13.8	4.6	15	210	75	0.18
F99	2.70	3.50	9.1	5.4	15	30	405	0.04
HW	2.64	4.31	16.9	21.4	95	710	153	0.42
Sapphire	3.10	3.10	11.3	0	...	...	...	...
SL1	1.06	1.98	6.4	11.2	10	335	122	0.27
SL2	1.12	2.29	7.1	15.0	10	485	129	0.35
SL3	1.35	2.58	10.4	19.0	25	505	133	0.43
Macor	1.04	2.30	5.4	20.4	40	535	132	0.46
Pyroceram	2.04	2.33	19.3	5.4	20	415	35	0.48
CH(cub.)	0.95	0.95	3.7	0	...	...	...	...
CH(tet.)	0.79	1.35	2.5	3.6	40	330	70	0.14

glassy phases at their grain boundaries,[24] or with smaller grain size (Tables I and II) have relatively low toughness indices, Γ_I/Γ_0, indicating that there is some kind of trade-off between macroscopic and microscopic toughness levels, and that this trade-off is controlled by the microstructure. We note also that the maximum stress-separation range parameters u^* for the materials are in the range 0.1–0.4 μm, consistent with crack opening displacement observations at the bridging sites.[4,12,21–23] We thus suggest that such parameters could serve as useful guides to materials processors, for tailoring materials with desirable, predetermined properties, especially with regard to grain boundary structure.

Mention was made in Sec. IV of the sensitivity of the parameter evaluations to the available data range. This has implications concerning conventional, large-crack toughness measurements. To investigate this point further we plot in Fig. 12 the T_∞ values determined here against those measured independently by macroscopic techniques. The degree of correlation in this plot would appear to lend some confidence to our fitting procedure (and to our *a priori* choices for the parameters ψ and χ). Since most of our strength data tend to come from regions toward the top of the T curve we should perhaps not be too surprised at this correlation.

Finally, we may briefly address the issue of test specimen geometry in connection with the accuracy of the parameter evaluations. It has been argued elsewhere[9] that test specimen geometry can be a crucial factor in the T-curve determination. It might be argued, for instance, that "superior" parameter evaluations could be obtained from larger crack geometries, particularly the c^*, T_∞ parameters. However, the indentation methodology takes us closer to the strengths of specimens with natural flaws, in particular to the T_0-controlled regions (notwithstanding our qualifying statements earlier concerning this parameter), so that the present evaluations may be more appropriate for designers.

VI. CONCLUSIONS

(1) An independently confirmed ligament bridging model is used as the basis for analyzing observed indentation-strength data for a wide range of polycrystalline ceramic materials.

(2) Those materials with pronounced T curves show the qualities of "flaw tolerance" and enhanced crack stability.

(3) A fracture mechanics treatment of the indentation fracture system with microstructure-associated factors incorporated allows for the (numerical) deconvolution of toughness/crack-length (T-curve) functions from these data.

(4) Comparisons within a range of aluminas suggest that those materials with "glassy" grain boundaries and smaller grain size have less pronounced T curves than those with "clean" boundaries.

(5) The indentation-strength technique and the toughness parameters deriving from it should serve as useful tools for the development of ceramic materials with predetermined properties, especially with respect to grain boundary structure and chemistry.

APPENDIX: EVALUATION OF ψ AND χ

Here we derive numerical values for the dimensionless parameters ψ and χ characterizing the crack geometry and the intensity of the residual contact stress, respectively. The choices for these should yield agreement between measured strength and toughness properties of homogeneous materials with no measurable T-curve behavior (i.e., $K_\mu = 0$, $T = T_0 = T_\infty$).

We begin with the geometrical ψ term, which is assumed to be material independent. From the applied stress (strength) σ_m and crack length c_m at the instability point of an indentation, we can show that[25]

$$\psi = 3T/4(\sigma_m c_m^{1/2}). \tag{A1}$$

Measurements of $\sigma_m c_m^{1/2}$ for several homogeneous mate-
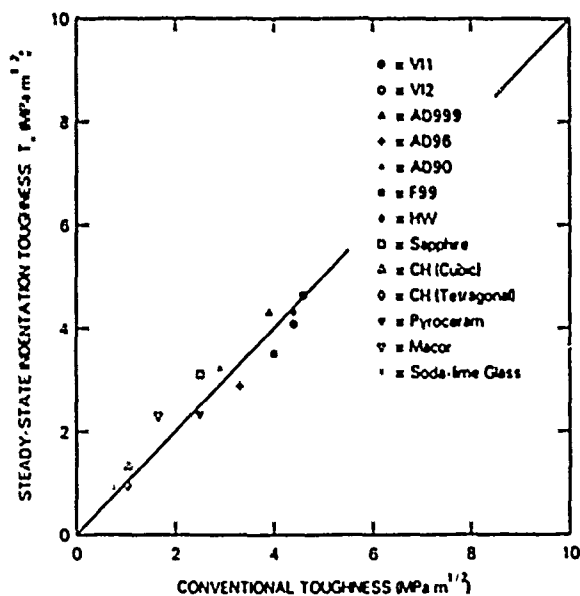
FIG. 12. Plot of T_∞ (Table II) as a function of independently measured toughness using conventional macroscopic specimens.

rials confirm that Eq. (A1) describes the toughness/instability properties[25,26] for $\psi = 1.24$. We note that this is very close to the value of 1.27 calculated by finite element analyses of semicircular cracks in surfaces of bend specimens.[27]

For the γ term we turn to Ref. 13, where it is shown that

$$\gamma = \xi(E/H)^{1/2}, \tag{A2}$$

where ξ is a material-independent constant. With this result Eq. (12) may be rewritten as[24]

$$T_0 = \eta(E/H)^{1/8}(\sigma_m^0 P^{1/3})^{3/4}, \tag{A3}$$

where

$$\eta = (256\psi^{1/2}\xi/27)^{1/4} \tag{A4}$$

is another material-independent constant. From measurements of $\sigma_m^0 P^{1/3}$ for a similar range of homogeneous material we obtain $\eta = 0.52$.[26] Hence eliminating ξ from Eqs. (A2) and (A4) yields

$$\gamma = 27\eta^4(E/H)^{1/2}/256\psi^3, \tag{A5}$$

which gives $\gamma = 0.0040(E/H)^{1/2}$.

REFERENCES

[1] R. F. Cook, B. R. Lawn, and C. J. Fairbanks, J. Am. Ceram. Soc. **68**, 604 (1985).

[2] R. F. Cook, B. R. Lawn, and C. J. Fairbanks, J. Am. Ceram. Soc. **68**, 616 (1985).

[3] R. F. Cook, S. W. Freiman, and T. L. Baker, Mater. Sci. Eng. **77**, 199 (1986).

[4] C. J. Fairbanks, B. R. Lawn, R. F. Cook, and Y.-W. Mai, in *Fracture Mechanics of Ceramics*, edited by R. C. Bradt, A. G. Evans, D. P. H. Hasselman, and F. F. Lange (Plenum, New York, 1986), Vol. 8, pp 23–37.

[5] H. Hubner and W. Jillek, J. Mater. Sci. **12**, 117 (1977).

[6] R. Knehans and R. Steinbrech, J. Mater. Sci. Lett. **1**, 327 (1982)

[7] R. Steinbrech, R. Knehans, and W. Schaawachter, J. Mater. Sci. **18**, 265 (1983).

[8] P. L. Swanson, C. J. Fairbanks, B. R. Lawn, Y.-W. Mai, and B. R. Hockey, J. Am. Ceram. Soc. **70**, 279 (1987).

[9] Y.-W. Mai and B. R. Lawn, Annu. Rev. Mater. Sci. **16**, 415 (1986)

[10] Y.-W. Mai and B. R. Lawn, J. Am. Ceram. Soc. **70**, 289 (1987).

[11] R. F. Cook, S. W. Freiman, B. R. Lawn, and R. C. Pohanka, Ferroelectrics **50**, 267 (1983).

[12] P. L. Swanson, in *Advances in Ceramics* (in press).

[13] B. R. Lawn, A. G. Evans, and D. B. Marshall, J. Am. Ceram. Soc. **63**, 574 (1980).

[14] D. R. Clarke, B. R. Lawn, and D. H. Roach, in Ref. 4, pp. 341–350.

[15] I. N. Sneddon, Proc. R. Soc. London Ser. A **187**, 229 (1946).

[16] B. R. Lawn and T. R. Wilshaw, *Fracture of Brittle Solids* (Cambridge U. P., Cambridge, 1975).

[17] D. B. Marshall, B. N. Cox, and A. G. Evans, Acta Metall. **33**, 2013 (1985).

[18] D. B. Marshall and B. R. Lawn, J. Mater. Sci. **14**, 2001 (1979).

[19] D. B. Marshall, B. R. Lawn, and P. Chantikul, J. Mater. Sci. **14**, 2225 (1979).

[20] R. F. Cook and D. H. Roach, J. Mater. Res. **1**, 589 (1986).

[21] R. F. Cook (unpublished work).

[22] K. T. Faber and A. G. Evans, Acta Metall. **31**, 577 (1983).

[23] K. T. Faber and A. G. Evans, J. Am. Ceram. Soc. **66**, C-94 (1983).

[24] S. L. Fortner (unpublished work).

[25] R. F. Cook and B. R. Lawn, J. Am. Ceram. Soc. **66**, C-200 (1983).

[26] R. F. Cook, Ph.D. thesis, University of New South Wales, Australia, 1985.

[27] J. C. Newman and I. S. Raju, Eng. Fract. Mech. **15**, 185 (1981).

[28] P. Chantikul, G. Anstis, B. R. Lawn, and D. B. Marshall, J. Am. Ceram. Soc. **64**, 539 (1981).

4. "Microstructural Effects on Grinding of Alumina and Glass-Ceramics"

    D.B. Marshall, B.R. Lawn and R.F. Cook

    J. Am. Ceram. Soc. 70 C-139 (1987).

Microstructural Effects on Grinding of Alumina and Glass-Ceramics

DAVID B. MARSHALL[*]

Rockwell International Science Center, Thousand Oaks, California 91360

BRIAN R. LAWN[*]

Ceramics Division, National Bureau of Standards, Gaithersburg, Maryland 20899

ROBERT F. COOK[*]

I.B.M., Thomas J. Watson Research Center, Yorktown Heights, New York 10598

Grinding forces were measured in aluminas and glass-ceramics with various microstructures. The microstructures were found to exert a profound influence on the machinability. In particular, the controlling toughness variable is that which pertains to small cracks, not that conventionally measured in a large-scale fracture specimen.

IT IS well documented that the principal material variable in microfracture-controlled properties of brittle ceramics, such as erosion, wear, and machining, is the "toughness."[1] This is in accord with intuition: the greater the resistance to fracture, the harder it should be to remove material in localized, cumulative, surface contact processes. Implicit in existing material removal theories is the presumption that toughness is a single-valued quantity for a given material. Recent studies of the fracture properties of a wide range of ceramics call this presumption into serious question; toughness is generally *not* a material constant, but rather some increasing function of crack size (R curve, or T curve).[2] In certain aluminas, for example, the toughness can increase by a factor of 3 or so, depending on the microstructure.[3,4] The T-curve effect is seen most strongly in aluminas with larger grain sizes and lower contents of grain-boundary glassy phase. Most notably, the T curves for different aluminas tend to cross each other,[4] so that the toughness rankings at large and small crack sizes appear to be reversed. Clearly, if we wish to retain toughness as an indicator of wear resistance, we need to qualify the scale on which this parameter is determined. Indeed, such a need was foreshadowed in an earlier experimental study on the erosion resistance of ceramic materials by Wiederhorn and Hockey.[5]

Accordingly, surface grinding tests were made on selected ceramic materials for which well-characterized T-curve data are available. The primary materials were aluminas from a previous study,[4] where the resistance characteristics were determined from the strengths of specimens containing indentation flaws.[6] In addition, two commercial glass ceramics were tested. A subsequent quantitative analysis of the indentation-strength data has provided upper (large crack size) and lower (small crack size) bounds, T_∞ and T_0, to the T curves for these materials.[6] Table I lists these parameters for comparison with the grinding results.

The grinding forces were measured using a dynamometer on the table of a surface grinding machine. Runs were made at fixed depths of cut, 5, 10, 15, and 20 μm, using a 240-grit diamond wheel (width 10 mm), rotating at 3300 rpm with a horizontal feed rate of 16 mm·s^{-1} and with water-soluble oil lubrication. The conditions of our experiments were such that the scale of individual damage events was always much smaller than the depths of cut. The specimens were first cut into bars 5 mm wide and then mounted in a row on the dynamometer so that force measurements could be made on all materials in a single pass. The results are plotted in

Fig. 1. Note from the relative positions of the curves that the aluminas and glass-ceramics have been ranked in order of diminishing grinding resistance in Table I.

It is immediately apparent from Fig. 1 that different aluminas and different glass-ceramics can vary widely in their grinding resistance. Thus the alumina with the highest resistance in Table I (i.e., AD90) is that with the greatest glass content. This result may come as no surprise to those who prepare ceramic powders by ball milling; alumina spheres with high glass content are found to be far more durable than similar high-purity spheres.[7] Note also from Table I that for aluminas of comparable purity those with higher grinding resistance have finer grain sizes (cf. A999 and Vistal). Most interesting, however, is the quantitative correlation between grinding resistance and toughness parameters. The macroscopic toughness T_∞ (i.e., the toughness K_{IC} we measure in conventional large-scale fracture tests) actually shows an *inverse* correlation with the grinding resistance. On the other hand, the microscopic toughness T_0 does appear to scale in the right direction. The implication here, of course, is that the grinding damage process is determined at the scale of the microstructure. The data for the two glass-ceramics in Table I serve to reinforce the point; on the basis of the T_∞ values we would be unable to choose between the two materials, whereas the relative values of T_0 confirm Macor (specified as a machinable glass-ceramic by its manufacturer) as the material of lower grinding resistance.

We conclude, therefore, that the time-honored conception of "toughness" as a universal indicator of superior mechanical properties, at least on the microscale, needs to be carefully qualified. The use of conventional fracture toughness evaluations to predict resistance to wear, erosion, and machining may lead to imprudent choices of materials for structural applications. On the positive side, a more complete understanding of the micromechanics that determine the complete crack resistance curve may ultimately help us optimize microstructural elements (glass content, grain size, etc.) for minimum surface degradation.

Table I. Comparison of Toughness and Grinding Resistance Parameters[*]

Material		Additive (%)	Grain size (μm)	T_0 (MPa·m$^{1/2}$)	T_∞ (MPa·m$^{1/2}$)
Alumina	AD90[†]	10	4	3.2	2.8
	Sapphire[‡]			3.1	3.1
	AD96[†]	4	11	2.9	2.2
	AD999[†]	0.1	3	4.3	2.2
	Vistal I[§]	0.1	20	4.1	1.7
	Vistal II[§]	0.1	40	4.6	1.5
Glass-ceramic	Pyroceram[¶]		1.5	2.3	2.0
	Macor[¶]		13	2.3	1.0

[*]T_∞ and T_0 evaluated from indentation-strength data (Ref. 5). Material rankings in order of decreasing resistance (from Fig. 1). [†]Coors Porcelain Co., Golden, CO. [‡]Adolf Meller Co., Providence, RI. [§]Corning Glass Co. Corning, NY.
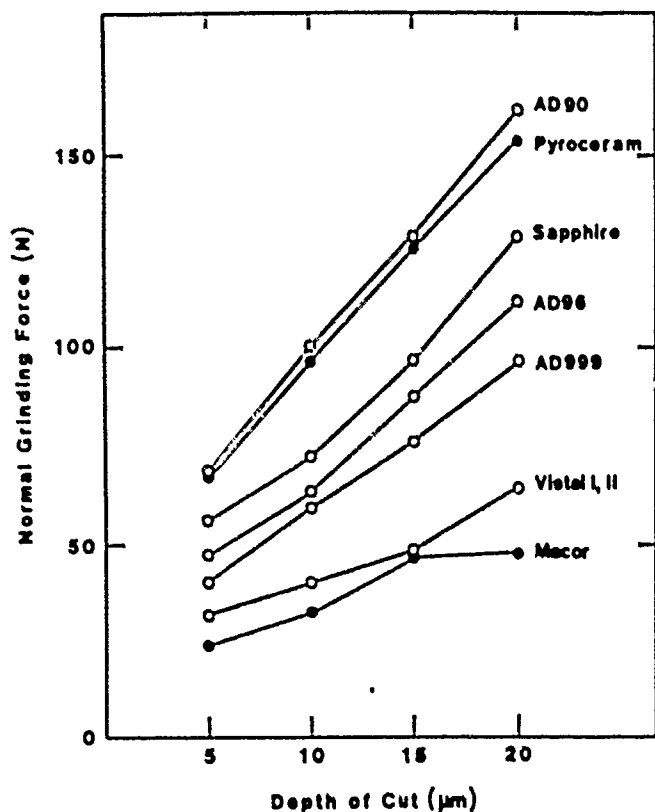
Fig. 1. Vertical grinding forces as function of depth of cut. Open symbols represent aluminas; closed symbols represent glass ceramics.

REFERENCES

[1]A. W. Reed and S. M. Wiederhorn, Ch. 2 in Treatise on Materials Science and Technology, Vol. 16. Edited by C. M. Preece. Academic, New York, 1979.

[2]Y.-W. Mai and B. R. Lawn, "Crack Stability and Toughness Characteristics in Brittle Materials," Ann. Rev. Mater. Sci., 16, 415–39 (1986).

[3]R. Knehans and R. Steinbrech, "Memory Effects of Crack Resistance During Slow Crack Growth in Notched Alumina Specimens," J. Mater. Sci. Lett., 1 [8] 327–29 (1982).

[4]R. F. Cook, B. R. Lawn, and C. J. Fairbanks, "Microstructure-Strength Properties in Ceramics: I, Effect of Crack Size on Toughness," J. Am. Ceram. Soc., 68 [11] 604–15 (1985).

[5]S. M. Wiederhorn and B. J. Hockey, "Effect of Material Parameters on the Erosion Resistance of Brittle Materials," J. Mater. Sci., 18 [3] 766–80 (1983).

[6]R. F. Cook, C. J. Fairbanks, B. R. Lawn, and Y.-W. Mai, to be published in J. Mater. Res.

[7]F. F. Lange, private communication.

5. "Toughness and Flaw Response in Non-Transforming Ceramics: Implications for NDE"

   B.R. Lawn and C.J. Fairbanks

   Review of Progress in Quantitative NDE, D.O. Thompson and D.E. Chimenti, eds., Plenum, New York, Vol. 6B, p. 1023, 1987.

TOUGHNESS AND FLAW RESPONSES IN NONTRANSFORMING CERAMICS:

IMPLICATIONS FOR NDE

Brian R. Lawn and Carolyn J. Fairbanks

Ceramics Division
National Bureau of Standards
Gaithersburg, MD 20899

INTRODUCTION

Recent developments in the characterization of the strength of ceramics have made it necessary to re-examine several "tradition", long-standing definitions and assumptions that form the modern-day fracture mechanics basis of NDE. Ceramics are very brittle materials. They are highly susceptible to failure from small scale (1-100 μm) "flaws". These flaws may be in the form of machining damage, grain boundary fissures, processing defects (pores or inclusions), etc. Theoretically, flaws have been represented as scaled-down versions of large cracks, so that the macroscopic "laws" of fracture might be assumed to apply at the micro-sale. This philosophy is embodied in the Griffith strength formalism,

$$\sigma_m = T_0/Yc^{1/2} \qquad (1)$$

where c is the flaw size, T_0 is the toughness (K_{IC} in metallurgical terminology) and Y is a geometrical constant. Implicit in Eq. 1 are two major conclusions which dictate the entire approach to NDE in ceramics:

(i) Failure occurs spontaneously at the critical stress (σ_m);

(ii) Toughness (T_0) is single-valued.

It is from these two conclusions that the concept of a critical flaw size for failure derives.

In the ceramics literature, the validity of these conclusions and of the extrapolation of large-crack data to the region of microstructure-scale flaws has been questioned by many, but few experimental attempts have been made to answer these questions. Here we shall present some recent data obtained at NBS that seriously questions the entire basis of present-day NDE philosophies for brittle materials. In particular, we shall point out shortcomings in the critical flaw concept due to so-called "crack resistance" (R-curve or T-curve) behavior where toughness becomes a function of crack size [1]. Some potentially beneficial aspects of this behavior will be emphasized.

STRENGTH CHARACTERISTICS OF SPECIMENS WITH CONTROLLED FLAWS

In setting out to test the validity of Eq. 1 we sought an experimental method which could be used to study systematically a wide range of flaw sizes, from macroscopic crack dimensions down to the scale of the microstructure. The indentation technique [2] was chosen because of its well documented capacity for controlling the scale of the starting flaw. Further, the crack evolution could be directly observed during strength testing in subsequent four-point bend or biaxial flexure (Fig. 1). A detailed fracture mechanics analysis of this test configuration [2,3] allows for the elimination of crack size in favor of indentation load, P, from Eq. 1, retaining the assumption of a single-valued toughness, T_0:

Hence by observing the $\sigma_m(P)$ response, we can test the basis for macroscopic to microscopic extrapolations; if T_0 is indeed a single-valued constant, σ_m should plot as a straight line with slope -1/3 in logarithmic coordinates.

Alumina was chosen as the "model" ceramic for the experimental study because of its availability in a wide range of microstructures. We show results here for single crystal sapphire and two polycrystalline materials, one nominally pure and the other containing a glassy grain boundary phase.

The results are shown in Fig. 2. Each data point represents the mean of about 10 specimens at a given load; error bars are omitted, but standard deviations are typically 10%. The curves through the data are best fits [4,5]. The linear fits for sapphire and the glassy polycrystalline material are in accord with Eq. 2, suggesting that the macroscopic toughness can indeed be extrapolated back to the flaw scale. However, the fit for "pure" alumina deviates dramatically from the ideal linear behavior at smaller flaw sizes. Thus, for this, third material predictions based on extrapolations from the macroscale greatly overestimate the actual strengths. It is as though the toughness, T, is systematically diminished as the flaw size gets smaller, i.e., consistent with R-curve (T-curve) behavior. On the other hand, we have the desirable feature of a region of "flaw tolerance" where the strength is constant over a range of flaw sizes.

a   b

$$c = c(T_0, P)$$ $$\sigma_m = \sigma_m(T_0, P)$$
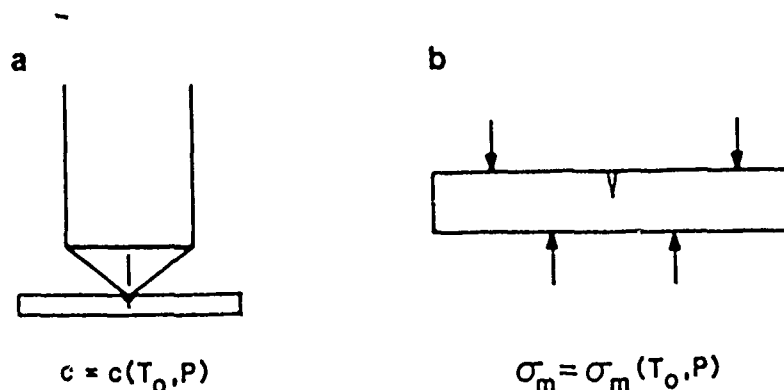
Figure 1.   Schematic of indentation flaw test used to observe crack evolution to failure: (a) indentation, to introduce controlled flaw; (b) bend test, to measure strength of specimen with flaw.
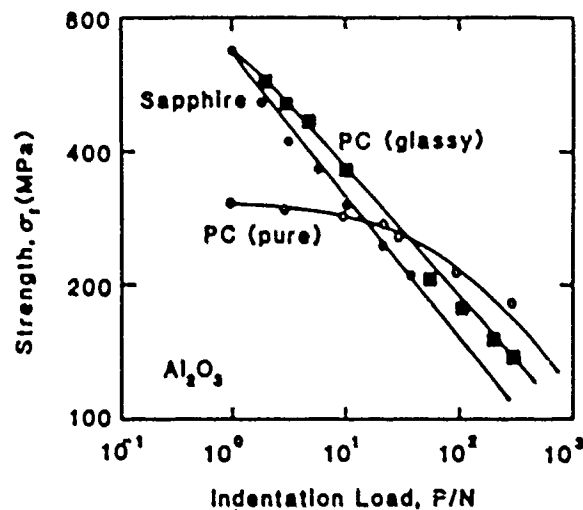
Figure 2. Inert strength vs indentation load of three aluminas, single crystal (sapphire) and polycrystalline with and without glassy grain boundary phase (PC-glassy and PC-pure, respectively).

From these results, we conclude:

(i) Extrapolation of macroscopic fracture data unconditionally into small-flaw regions can be dangerous;

(ii) Toughness is not generally single valued, but can be a function of crack size, $T(c)$;

(iii) The toughness function (T-curve) is microstructure sensitive, and the grain boundary structure appears to hold the key to this sensitivity.

MECHANISMS OF T-CURVE BEHAVIOR

There are several possible mechanisms which have been put forward to explain T-curve behavior. The most popular of these are the "frontal zone" mechanisms. Martensitic phase transformation is probably the most powerful of all the toughening mechanisms but, to date, has been observed exclusively in zirconias [6]. The concept of microcracking has also received much attention [7] in nontransforming ceramics. In both these mechanisms, there is a frontal zone which travels with the extending crack tip and thereby dissipates energy from the loading system. Somewhat remarkably, very little attempt has been made to verify these (or indeed any other) mechanisms by direct observation (except in the transforming zirconias).
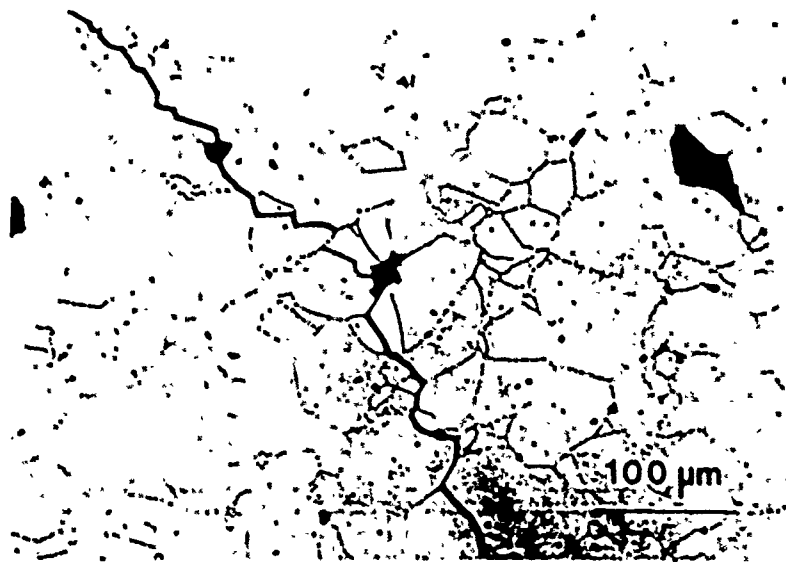
Figure 3. Vickers indentation (P = 5N) site of "fractured" alumina disc.
Specimen thermally etched to reveal grain structure.

IN SITU OBSERVATIONS OF CRACK EVOLUTION IN ALUMINA

By using the arrangement in Fig. 1 and focussing a microscope onto the indentation site during stressing, the crack evolution to failure could be observed directly [8]. These observations led to some surprises. Whereas in sapphire failure was spontaneous, in the "pure" polycrystalline alumina it certainly was not. The cracks in the latter material were stabilized. At "failure" these specimens seemed to be fully fractured (the crack ran from edge to edge and through the thickness of the sample) yet remained intact.

The center region of a broken specimen of the latter material is shown in Fig. 3. At initial loading the indentation remained stationary, confined at surrounding grain boundaries until at a critical point the cracks suddenly "popped in". With subsequent load increments, grain-dimension "jumps" occurred in a stable but erratic manner for several millimeters before failure. Despite intensive searching, no evidence could be found for any frontal zone mechanism, microcracking or otherwise. On the other hand, inspection of the crack interface behind the tip revealed a high density of "active" regions where grains remained attached to both walls. The crack tip was clearly held up by these partially attached grains. Two specific examples of active grain sites are shown in Fig. 4. In both cases in Fig. 4, secondary grain fracture is evident, suggesting that the interfacial restraining forces must be high.

To summarize the experimental observations:

(i) Crack growth in the "pure" alumina was discontinuous over small groups of grains, yet stable over 10-100 grains (cf. relatively spontaneous fracture in the other aluminas in Fig. 2);

(ii) Grain attachment sites were active behind the crack tip, over many millimeters in the "pure" alumina;

(iii) No evidence was found for a frontal microcrack zone.

1026
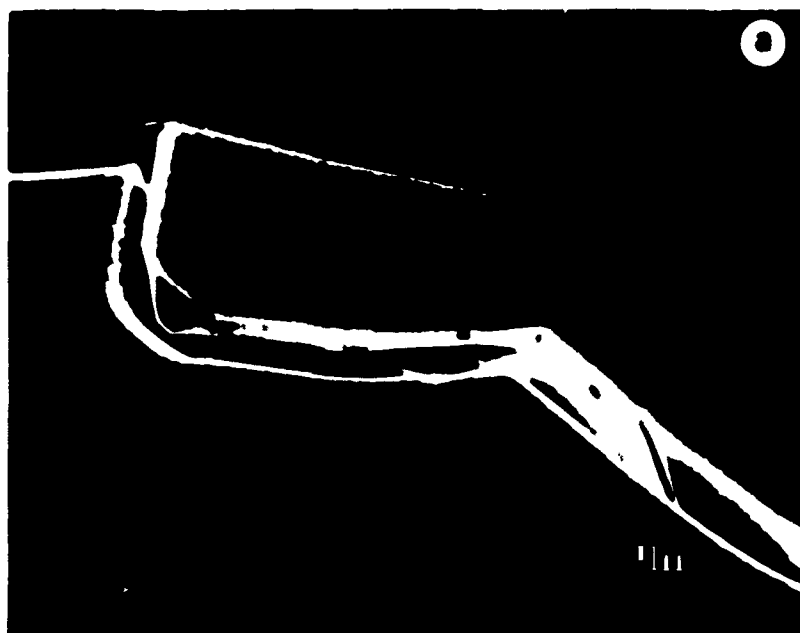
Figure 4. Scanning electron micrographs showing two examples of secondary microfracture about bridging grains.

Thus the macroscopic evidence implies that the T-curve behavior in our "pure" alumina is due primarily to bridging forces at the crack interface. More recent work by Swanson on other materials [9] suggests that this observation may generally be true of other ceramic types as well.
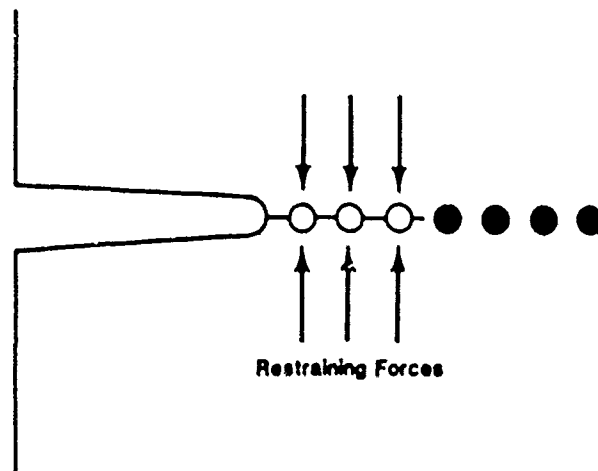
Figure 5. Schematic of bridging model (shown here for crack growth from notch).

MODEL

A fracture mechanics model of the bridging mechanism has been developed [10] (see Fig. 5). Circles denote bridging sites; open and closed circles distinguish active sites behind the tip and future sites ahead of the tip. The sequence of calculations involved is as follows:

(i) The T-curve is taken to be expressible as the sum of the intrinsic (grain boundary) toughness, T_0, and an "internal" restraining term, K_i, i.e.

$$T(c) = T_0 - K_i(c) \qquad (3)$$

For restraining forces, K_i is negative;

(ii) The internal closure force, $K_i(c)$, is determined by integrating the closure forces over the bridging zone, assuming a specific force-separation law. Since more bridges are intersected as the crack grows, K_i is an arithmetically increasing function of c;

(iii) The critical condition for crack instability, $K_a(c) = Y \sigma_a c^{1/2} = T(c)$, $dK_a/dc = dT/dc$, [11] is computed to determine the strength vs load function, $\sigma_m(P)$;

(iv) From the $\sigma_m(P)$ data in Fig. 2, the T(c) function is (numerically) deconvoluted.

Figure 6 is a composite plot of the results for those aluminas in Fig. 2 using this approach (with several approximations in the analysis). Some of the more important features to note are:

(i) The crack size scale of the T-curve can be large, of order millimeters, consistent with the scale of the observed bridging zones;

(ii) The T-curves are microstructure sensitive: the only difference between the aluminas represented in Fig. 6 are the grain sizes and grain boundary phases;
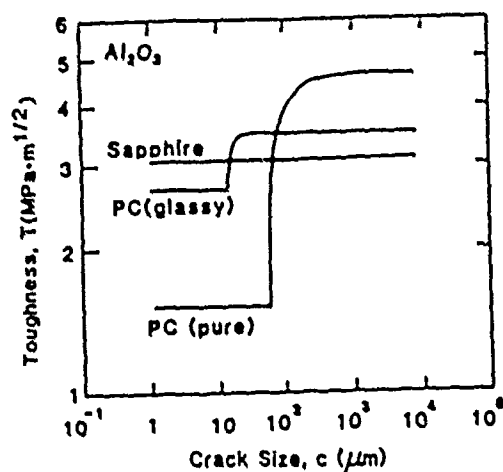
Figure 6. Toughness as a function of crack length deconvoluted for aluminas from Fig. 2.
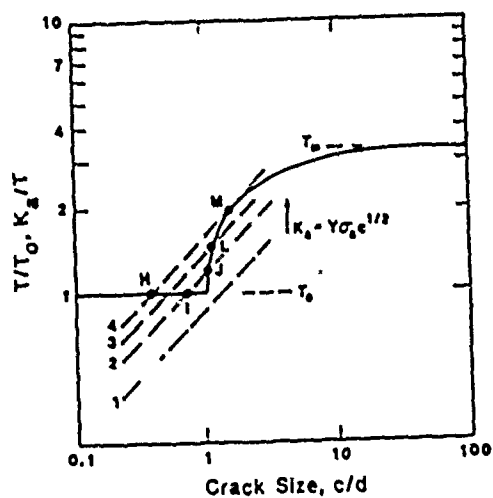
Figure 7. T-curve construction.

(iii) There appears to be an inverse relationship between T_0 and T_∞ (lower and upper plateau levels): thus large-scale toughness can be a poor indicator of small-scale toughness.

Consider now how the results in Fig. 6 explain the observed crack evolution for materials with strong T-curve behavior (e.g., the poly-crystalline "pure" material in Fig. 6). A construction for such a material is reproduced in schematic form in Fig. 7. The solid curve represents the $T_{(c)}$ function and lines 1 through 4 represent $K_a = Y \sigma_a c^{1/2}$ "loading lines" for successively increasing values of applied stress, σ_a. Suppose our flaw has initial size corresponding to point I. Then the crack remains stationary until stage 2 is reached in loading, at which point abrupt pop-in occurs, along IJ. With further loading the crack subsequently progresses stably through JLM along the curve, until at stage 4, failure ensues. Actually, a more exact numerical deconvolution than we have attempted in our data analysis would yield several secondary plateaus along the rising T-curves in Fig. 6, consistent with the observation that crack growth occurs in discrete jumps throughout its evolution. Thus the failure stress is determined uniquely by the tangency condition at M, independent of the initial crack size.

IMPLICATIONS

What are the implications of our results concerning NDE in ceramics? First, we have shown that materials which exhibit strong T-curve behavior can be extremely "flaw tolerant". The failure stress for these materials is independent of the initial flaw size. For the engineer, this is an extremely attractive prospect, for not only is the concept of a well-defined design stress feasible, but the material is now much less susceptible to strength degradation in service. However, at the same time this raises the question as to whether we can retain the notion of critical flaw size as a basis for screening. Secondly, there can be strongly enhanced crack stability in these materials; the cracks can grow large distances (tens or hundreds of grains) over the rising portion of the T-curve, prior to failure. Importantly, this growth can occur discontinuously. Thus, the precursor growth stage may be usefully employed as an "early warning" of impending failure. The possibilities of turning this to advantage are clear.

REFERENCES

1. Y. W. Mai and B. R. Lawn, Ann. Rev. Mat. sci. 16; 415 (1986).
2. D. B. Marshall and B. R. Lawn, J. Am. Ceram. Soc. 14; 2001, 225 (1979).
3. P. Chantikul, G. R. Anstis, B. R. Lawn, and D. B. Marshall, J. Am. Ceram. Soc. 64; 539 (1981).
4. R. F. Cook, B. R. Lawn, and C. J. Fairbanks, J. Am. Ceram. Soc. 68; 604 (1985).
5. C. J. Fairbanks, B. R. Lawn, R. F. Cook, and Y. W. Mai, p. 24, in: "Fracture Mechanics of Ceramics," R. C. Bradt, A. G. Evans, D. P. H. Hasselman, and F. F. Lange, eds., (Plenum Press, New York, 1986).
6. A. H. Heuer, L. W. Hobbs, eds. Science and Technology of Zirconia: Advances in Ceramics, 3, Am. Ceram. Soc., (Columbus, Ohio, 1981).
7. A. G. Evans and K. Faber, J. Am. Ceram. Soc. 67; 225 (1984).
8. P. L. Swanson, C. J. Fairbanks, B. R. Lawn, Y. W. Mai, and B. J. Hockey, J. Am. Ceram. Soc., in press.
9. P. L. Swanson, Advances in Ceramics, in: "Proc. of Conf. on Fractography of Glasses and Ceramics," to be published.
10. Y. W. Mai and B. R. Lawn, J. Am. Ceram. Soc., in press.

DISCUSSION

Ron Streit, Laurence Livermore: The concern I had with some of the things you were presenting is fracture mechanics and the KIC concept of continuum mechanic's principles. You are applying it to stuff the size of 1 grain, 2 grains, 3 grains. And when you present your indentation data, the strength falloff point on your curve was suspiciously similar in size to 1 grain size. Are we not pushing fracture mechanics beyond where it should be?

Mr. Lawn: I don't believe we are. In most of the cases that I'm dealing with here, the cracks do tend to be intergranular. So, provided that we can regard the crack growth in the intergranular phase to be characterized by an intergranular toughness--that's the T term-- I believe the fracture mechanics applies in principle, although one must ask exactly what the stress intensity factor means when you are going through a very narrow interphase.
   Again, it raises some very subtle questions, but I believe that the basic principles remain valid. But it's a point well-raised, and I think you have to be very cautious.

Mr. John Ross (General Electric): I'm not sure I understand.. Are you saying that the crack progresses and meets a grain, loses part of its energy; the radius of the crack tip increases until other grains or other cracks decline around the grain?

Mr. Lawn: What I'm saying is this: our model shows a crack growing from a notch, but it might be a crack that's growing right from scratch.
   So, the initial indentation crack goes along the weak grain boundary and meets virtually no resistance, and if that was the whole story, this whole material would have no toughness at all. But then it comes across an obstacle and it has to run around that grain, we believe, leaving the grain attached to both walls. So as the crack grows, it's meeting some strength behind the crack tip. Then as it goes on further and further and encompasses more of these grains and they still remain active behind the grain, it's building up more and more restraint behind the crack. Hence, the toughness seems to be going up.

Mr. Ross: So the closing portions that are the restraining forces control the toughness.

Mr. Lawn: Exactly how these grains impose those forces is still a little bit obscure. When you do the fracture mechanics, you have to bring that in an empirical way. The actual physics of it is still a little bit obscure, but the observation of it is very definite. You can see the crack going around the grain and have the microscope trained on that grain. You can see the thing developing and the reflected light flashing subsurface even though the main crack is miles away.

Mr. Ross: Like lateral stability.

Mr. Lawn: I guess there's an analogy there.

Mr. Gordon Kino, Stanford: Is there something we can do, as NDE people, to measure for what's going on? For instance, when you are doing these measurements which you do along the surface, you don't really look at the depth of the crack. When you have taken the whole thing apart, is the crack growing in a similar way?

And secondly, is the system uniform? In other words, if you
do the same experiment on the same ceramic on another part of it,
would everything be about the same? In other words, would you
measure, say, the elastic properties of the grains? Would that
provide some information that you need?

Mr. Lawn: Well, the second question is--again, you are getting into
the actual details of the mechanism, and that is something we are
still working on. But maybe NDE can help out there, too, to
understand a little bit as to how these grains actually pull
apart.

Optical microscopy will tell you something, but in most of these
materials that we looked at, they are, at best, translucent, and
so there's a lot of questions as to what goes on underneath the
surface of these materials, and that's where I think things like
acoustic emission could be extremely useful.

One of my co-authors was Peter Swanson, who came from the rock
mechanics area. He has done similar experiments where he runs huge
cracks through big rocks, and he used acoustic triangulation
techniques to locate the sources of these active sites behind the
crack tip. Maybe that's something we can also do with NDE, because
in many of these materials, we are talking about the zone lengths
at the fracture interface of several millimeters, up to 10 milli-
meters, in some cases. So it's not beyond the realms of possibility.
We can do that.

John McClelland (Center for NDE): I was wondering, from what you are
saying, is there any reason to guess that most of the failures are
due to the flaws that are connected to the surface rather than imbedded
in the material?

Some NDE methods are better at looking at surface-related flaws
than deep flaws, and if you have this bridging mechanism working,
does that work more effectively on internal flaws and therefore
minimize their role in causing failure, or is there no reason to
speculate that way?

Mr. Lawn: Well, it depends on the material. When we started doing our
first experiments, we polished down our surfaces and we polished
them very badly. This led to some grain pull-outs on the surface,
and when we did our test, we observed the cracks starting from the
indentations. Also, they started from some of these other pull-
outs on the surface, and after a while, some of them ran into each
other. Then we started to polish much better, but we still got
breaks from internal flaws in some cases, particularly with small
indentations.

So, I think it depends very much on the actual material, although
in most of the cases we have looked at, it seems that we are not
looking at just the surface effect, but this is something charac-
teristic of the microstructure itself, something intrinsic to it,
and it occurs under the surface. So I have a suspicion that you
are not going to get away with just looking at surfaces. It has
to be in the interior as well.

6. "Indentation Deformation and Fracture of Sapphire"

   H.M. Chan and B.R. Lawn

   J. Am. Ceram. Soc. 71 29 (1988).

Indentation Deformation and Fracture of Sapphire

HELEN M. CHAN* and BRIAN R. LAWN*

Ceramics Division, Institute for Materials Science and Engineering, National Bureau of Standards, Gaithersburg, Maryland 20899

Relatively little is known about the fundamental deformation processes in intrinsically hard, brittle materials, and even less about how these processes lead to the initiation of cracks. In this paper, transmission electron microscopy is used to study the deformation structure within Vickers indentation zones of single-crystal sapphire with (11$\bar{2}$0) surface orientation. The relative misorientation of regions within these zones, as mapped by convergent-beam kikuchi patterns, is found to be severe, indicative of shear processes operating close to the cohesive limit. Two principal types of deformation are identified, basal twinning and pyramidal slip. Incipient microcracks are observed at both the twin interfaces and the slip planes. These incipient "flaws" act as nucleation sites for the ensuing radial and lateral cracks.

I. Introduction

IN RECENT years, indentation analysis[1-3] has emerged as a powerful tool for evaluating and characterizing the deformation and fracture properties of ceramic materials, particularly as quantified by hardness and toughness.[4-6] The basic concept behind indentation testing is attractive in its simplicity. A standard "sharp" indenter (e.g., Vickers) is loaded onto the surface of the test material. The intense stress concentration beneath the indenter contact causes the material to undergo both reversible and irreversible deformation. The most obvious manifestation of the latter component is, of course, the residual hardness impression. The irreversible component is also responsible for any attendant crack *initiation*.[7-10] Furthermore, residual stresses can continue to exert a strong influence on crack *propagation* well beyond the near-contact zone.[2,3,11,12] A fundamental understanding of contact-induced deformation processes would therefore appear to be an essential prerequisite to any complete description of flaw micromechanics in highly brittle ceramics.

A notable restriction implicit in present-day indentation fracture mechanics is the assumption of homogeneity and isotropy of material structure. This restriction is apparent in experimental as well as theoretical work, particularly in the strong tendency to adopt silicate glasses as model test materials. Studies into the mechanisms of indentation-induced crack initiation have been carried out *almost exclusively* on glasses.[7-10] Such studies reveal the sources of initiation in the amorphous structures as "shear faults" punched in irreversibly by the penetrating indenter. Characteristic of these faults is that they form on curved surfaces, governed by trajectories of maximum shear, at stress levels close to the theoretical cohesive limit. Such characteristics would appear to represent a substantial departure from our traditional notions of slip deformation in *crystalline* materials by low-stress dislocation processes. Yet there are general features of the indentation deformation/fracture pattern in brittle materials, not least the clear tendency for the radial cracks to initiate near the impression corners, that suggest some commonality in underlying mechanisms. The implication here is that the classical picture of crystal plasticity by dislocation glide may require some qualification when applied to ceramics, especially to the tougher, harder ceramics with intrinsically strong covalent-ionic bonding.

Accordingly, the purpose of this study was to characterize the indentation deformation-fracture pattern in a selected single-crystal system, namely sapphire, using a transmission electron microscopy (TEM) procedure developed by Hockey.[13] The choice of sapphire was based principally on the requirement that the structure[14,15] and mechanical properties[16] should be reasonably well documented. (Another, longer-term motive was that the study should ultimately be extendable to practical ceramics, in this case to polycrystalline alumina, so that the influence of such microstructural variables as grain-boundary structure might be systematically evaluated.) Our principal goal was to identify the basic deformation elements associated with crack nucleation in sapphire, with the hope that this might allow us to make some statements about crystalline solids in general. Because crack nucleation is a critical first step in flaw development, we may anticipate our findings to be of relevance to important practical issues concerning the degradation of mechanical strength[2] (e.g., in small particle impact), wear and erosion, etc.

II. Experimental Procedure

The method of specimen preparation for TEM examination was similar to that previously described by Hockey.[13] Disks (3-mm diameter) were cut using an ultrasonic drill from a thin slice of sapphire of (11$\bar{2}$0) orientation.* This particular orientation was chosen because [11$\bar{2}$0] is the zone axis for a large number of planes that are susceptible to shear deformation (Section III). The disks were ground and polished to a thickness of 100 to 150 μm. The final polishing step was carried out using 0.3-μm Al$_2$O$_3$ powder to remove any remnant grinding damage which might be confused with the indentation structure. The samples were indented with a Vickers indenter at loads from 0.1 to 2.0 N, although for the majority of indentations a load of 0.25 N was used. The disks were then thinned by ion-beam milling from the back only, i.e. the side away from the indentation surface. Following carbon coating, the samples were examined in the TEM[†] at 150 keV. Some of the indented specimens were also examined by scanning electron microscopy (SEM) to reveal surface topographical features.

III. Results

(1) General Features

The indentation sites were readily identified in the TEM as localized regions of intense diffraction contrast. Figure 1, which shows sites for two different Vickers orientations relative to the specimen surface, is a typical example. The characteristic spreading of radial crack arms outward from the impression corners is clearly evident in these micrographs. The intense contrast within the indentation zone, together with the ubiquitous appearance of bend contours about the peripheries, is strongly indicative of a high-strain deformation process. Closer inspection of the indentation zones reveals crystalline shear elements which we identify as mechanical twins and slip faults. Microcracking associated with these shear elements is also identified. Details of such identifications are given in the following subsections.

(2) Shear Deformation Elements

(A) *Twins—Morphology:* Selected-area-diffraction TEM was used to identify some of the shear elements as basal twins. Examples are indicated in Figs. 1 to 4. For the (11$\bar{2}$0) foil orientation, the twin planes are perpendicular to the plane of the foil and have surface traces perpendicular to the [0001]. No rhombohedral twins were detected. The same surface traces were visible in the
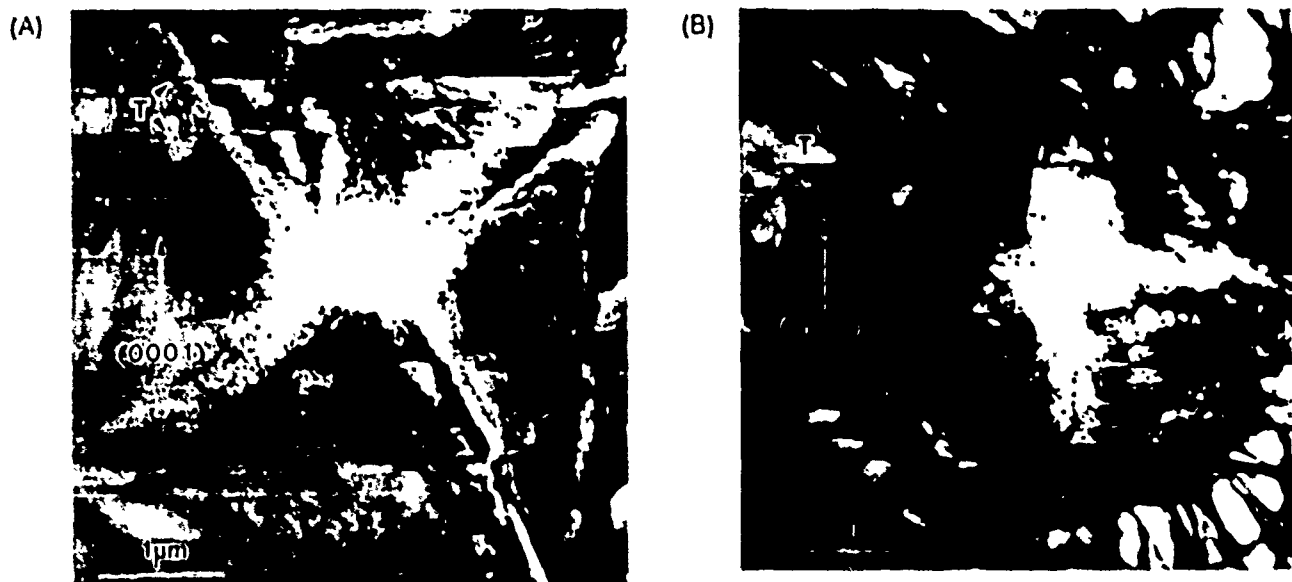
(A)

(B)

Fig. 1. TEM micrographs of 0.25 N Vickers indentations in sapphire. A. Orientation A (indent diagonals at 45° to [0001]). Basal twin (T) density lower for the two quadrants where the impression edge is parallel to [0001]. B. Orientation B (indent diagonals parallel and perpendicular to [0001]). Basal twin density uniform in all four quadrants

Fig. 2. micrograph of 2-N Vickers indentation in sapphire, showing twin slip traces at the surface. Radial cracks initiate from near impression corners

SEM by topographical contrast (Fig. 2), indicating that the shear direction has a component normal to the foil (e.g., [1̄010] or [011̄0] relative to the (112̄0) surface orientation). The morphological evidence is therefore consistent with a twinning plane $(K_1 = (0001))$ and twinning direction $(\sigma_1 = (101̄0))$. By viewing the shear planes edge-on, e.g., as in Fig. 3(A), the width of the twins was determined to be 10 to 50 nm.

The density of twins within the four quadrants of the indentation zone was found to depend on the orientation of the indenter. It can be seen that for orientation A in Fig. 1(A) the twins are located almost exclusively in the two quadrants whose impression edges lie perpendicular to [0001]. For orientation B in Fig. 1(B), on the other hand, the twin density is more or less equal in all four quadrants. This absence of twins in the left and right quadrants for orientation A may be rationalized in terms of the stress trajectory field beneath the indenter;[1,2] the basal planes in these two quadrants lie *normal* to the surfaces that experience the greatest punch-type shear stresses (see Fig. 9, later). In all other quadrants there is some component of resolved shear stress along the twinning direction. Herein lies our first strong manifestation of crystallographic constraint. It will be appreciated that the extreme anisotropy in twinning density means that there *must* exist other, perhaps more potent, shear deformation modes; for, otherwise, how might we possibly account for the residual impression in

(A)

(B)
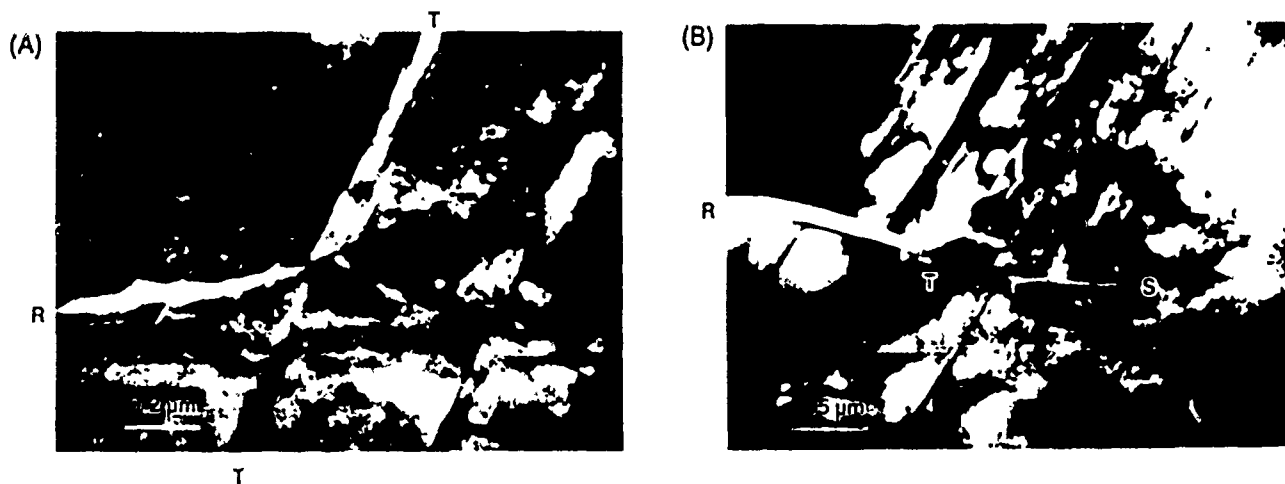
Fig. 3. Microcracks in indentation zone in sapphire (for orientation A, Fig. 1(A)). at basal twin interfaces near impression edge, showing nucleation along twin (T). (B) at intersections between twins (T) and slip faults (S), at impression corner. Note how microcracks extend into radial arms at left

twin-free quadrants such as those in Fig. 1."

These observations of the twin patterns were typical of all the indentation sites examined in this study, the only noteworthy departure from complete similarity was an apparent, slight tendency for the average thickness and the density of the twins to increase with load.

(B) Slip Faults—Morphology and Misorientation   Attempts were made to resolve the slip elements responsible for the bulk of the residual deformation in the central indentation zone. This proved difficult owing to the extremely high strain density. Nevertheless, by systematically tilting the foils in the TEM it was possible to image fault planes of localized high dislocation density, e.g., as seen in Figs. 3(B) and 4. These faults generally appeared to be much narrower than their twin counterparts and were interpreted as planes of concentrated slip. Selected-area diffraction in such regions showed no spurious reflections, confirming that the defects were *not* microtwins. From the TEM evidence, along with corresponding observations of fault traces in the SEM (e.g., Fig. 2), the slip plane for the faults was determined to be {1123}, i.e., of the pyramidal type. Because of the extreme intensity of contrast, attempts at Burgers vector determinations of the dislocations were unsuccessful.

Accordingly, another means was sought by which more quantitative information on the associated deformation might be obtained. Convergent-beam kikuchi patterns were used for this purpose. Thus the relative change in orientation in moving from the center to the edge of the indentation zone, in the manner shown schematically in Fig. 5(A), was mapped from the corresponding series of
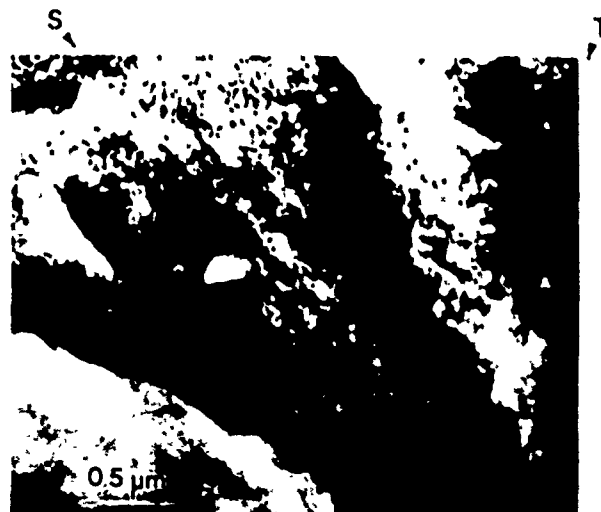
Fig. 4. TEM micrograph of 0.25-N Vickers indentation near impression corner in sapphire. Slip faults *SS* represent planes of concentrated slip lying parallel to {1123}. Twins *TT* also visible.
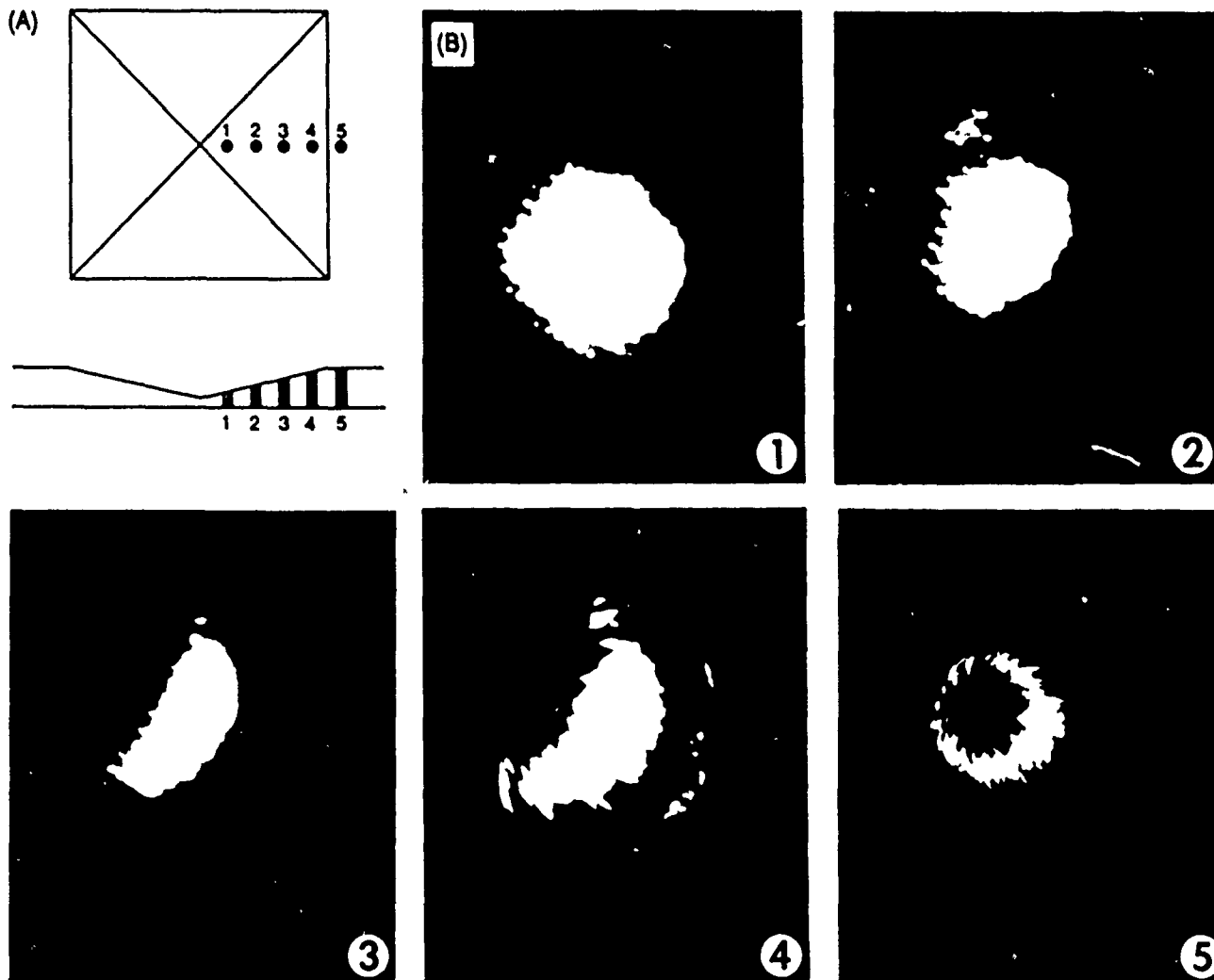
Fig. 5. Use of convergent-beam kikuchi patterns to measure misorientation within indentation zone. (A) Schematic showing spot traverse for mapping out lattice rotations across each quadrant of indentation: upper diagram, plan view; lower diagram, profile view. (B) The corresponding kikuchi patterns.
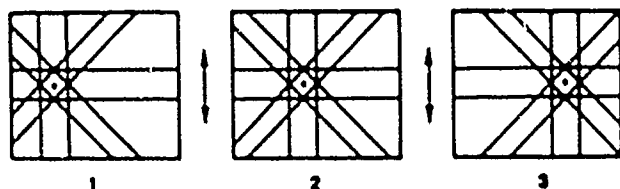
Fig. 6. Schematic diagram indicating invariant tilt axis (parallel to arrows) where the shift *1* → *2* → *3* in kikuchi patterns is collinear.

Fig. 7. Diagram showing trace of {11$\bar{2}$3} planes (shown as dashed lines) with respect to the indenter for orientations *A* and *B*. In orientation *A* the two sets of {11$\bar{2}$3} planes are symmetrically oriented with respect to the indenter. In orientation *B* preferred slip occurs on set of {11$\bar{2}$3} planes *SS*. Hence unique tilt axis in latter case.

kikuchi patterns, Fig. 5(*B*). The electron probe size was ~0.1 μm, and typically five patterns were obtained per quadrant (including at least one outside the indentation area, to give a "zero misorientation" calibration). Because the position of the kikuchi pattern relative to the transmitted spot is highly sensitive to minute changes in orientation, the shift between successive patterns provides us with an accurate measure of the misorientation. More specifically, the *magnitude* of the shift determines the *angle* of misorientation, γ, and the *direction* of the shift determines the *axis* of misorientation (Fig. 6). The values of γ in the near-center regions of the indentation (i.e., positions *1* to *4* in Fig. 5(*A*)) ranged from 2° to 10°; this range appeared to be independent of load. These values are too high to be simply due to foil bending. Indeed, γ = 6° corresponds to a shear strain tan γ = 0.1, which is of the order of the theoretical cohesive limit.[17] This result is not surprising when one considers the ratio of hardness to shear modulus for sapphire, *H/G* = 20 GPa/150 GPa = 0.13 (recalling that, by definition, hardness is a measure of the "average" stress beneath the indenter). It is clear that we are dealing with a high-stress shear process here.

The slip configurations were sensitive to the indent orientation. For orientation *B* the direction of the kikuchi pattern shifts tended to be collinear, indicating that material rotation was taking place about an invariant tilt axis. This tilt axis was consistent with slip on a single crystallographic system (specifically, on {11$\bar{2}$3}⟨$\bar{1}$100⟩). For orientation *A*, however, although the magnitudes of the misorientations were similar, there was no such invariant tilt axis.

The difference in behavior between the two orientations can be explained by reference to Fig. 7. In this figure surface traces of the active {11$\bar{2}$3} planes (imaged in the TEM as planes of concentrated slip) are sketched in as dashed lines.[1] Only two of the three possible surface traces are shown, as no evidence for slip was obtained for the third set. For orientation *B* one set of {11$\bar{2}$3} planes, that with its trace more closely parallel to the impression edge, is clearly more disposed to slip than the other. For orientation *A* symmetry prevails, so the two sets are equally well disposed to slip. Hence the lack of a well-defined tilt axis in the latter orientation.

As mentioned above, each trace actually represents a pair of planes; it is assumed, however, that only the plane which experiences the greater component of the shear stress[7] will be active. It is believed that although the third set of {11$\bar{2}$3} planes (surface trace perpendicular to the [0001]) would appear to be favorably oriented for slip in orientation *A*, basal twinning occurs preferentially.

(3) Microcracks

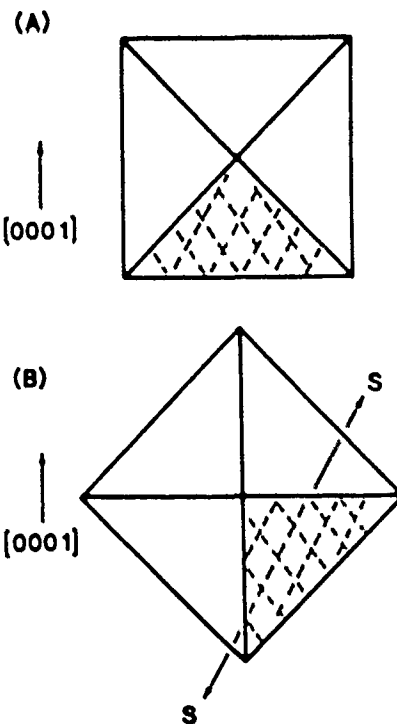Particular attention was given to the presence of fine micro-

cracks within the indentation zone, with the express intent of determining the source of nucleation centers for large-scale radial fracture. Examples are shown in Figs. 3, 4, and 8. No such microcracks were ever detected in the undisturbed crystal regions, eliminating the possibility that we might simply be observing a preexistent flaw population. Further, the incidence of microcracks appeared to be as great in the thicker regions of the foil as in the thinner, suggesting that the results are no mere artifacts of the foil preparation.[8]

By tilting the foil until the cracks were seen edge-on, it could be determined that nucleation occurred preferentially at either the {11$\bar{2}$3} slip planes or the (0001) twin interfaces. Figures 3 and 8 show examples. In Fig. 3(*A*) we see twin-induced microfissures along *TT* degenerating into a larger-scale radial crack *R* at lower left. (Close inspection reveals that the radial crack actually extends back a little way to the right, into the indentation zone.) It is noted that (0001) is *not* a favored cleavage plane in sapphire, so it is difficult to envisage how these fissures might ever be interpreted as anything other than the result of nucleation events. In Fig. 8 analogous, slip-plane fissures are evident, again degenerating into a radial crack configuration. We note the segmented appearance of this particular crack system near the impression corner, strikingly reminiscent of the radial patterns observed in glass (e.g., Fig. 7 in Ref. 9).

IV. Discussion

Using electron microscopy, we have been able to identify basal twinning and pyramidal slip as the principal shear deformation elements for Vickers indentations in (11$\bar{2}$0) sapphire. In addition, we have observed microcracking associated with the shear elements. These processes all operate at stress levels close to the

[1]It should be noted that altogether there are six variants of the {1123} plane. These can be regarded as consisting of three pairs of variants, where within each pair the two planes intersect the (1120) plane along the same direction, but are inclined at equal and opposite angles to the specimen surface.

[8]Note that even if foil relaxations *were* to be a factor, our conviction that we are witnessing intrinsic nucleation processes would hardly be diminished; such spurious relaxations might then be viewed as causing essentially the same (but *premature*) opening of the microcracks as would ultimately occur in any subsequent external loading.

Fig. 8. TEM of 0.25-N Vickers indentation in sapphire, showing how slip faults intersect at impression corner to nucleate microcracks and thence to initiate the larger-scale radial cracks. Note crack "segments" parallel to impression diagonal in corner region. This suggests that, on sensing the tensile stress field that exists outside the hardness zone, the newly created microcracks make several unsuccessful attempts to "pop in" to the radial configuration, only to be arrested by an adjacent fault further removed from the center.

Fig. 9. Schematic illustration of how (A) twinning and (B) slip act to accommodate the punch-type shear stresses induced by the indenter

theoretical cohesive limit. In this respect the nature of the contact damage in sapphire appears to differ little from that in glassy materials. However, the anisotropy in deformation patterns for different indenter orientations (Fig. 1) indicates that crystallography imposes severe constraints on the capacity of the contact stress fields to activate slip. It is in this context that we discuss in some detail, with reference to Fig. 9, the manner in which the sapphire deforms to accommodate the penetrating indenter and thereby generates microcracks.

(1) Deformation Mechanisms

Basal twinning has been observed in sapphire by several other workers.[18-20] What is perhaps surprising is that no evidence of *rhombohedral* twinning[19,20] was detected here. We have already alluded (Section III) to a strong crystallographic constraint factor in sapphire, it is therefore possible that the rhombohedral type could be activated in other foil and indenter orientations. It can thus be argued that we are dealing with highly competitive deformation processes in this material and that, for our {1120} surface orientation, it is the basal plane, by virtue of its favorable disposition relative to the direct ons of principal shear, that is strongly favored.

Although basal twinning can accommodate *some* of the permanent deformation induced by the indenter, it cannot account for all of it. To see this, consider the twinning geometry in Fig. 9(A). It is readily shown that the semiangle of the hardness impression is given by

$$\tan \phi = [d/(d + D)] \tan \alpha \qquad (1)$$

where D is the mean spacing between twins, d is the twin thickness, and α is the twin shear angle. Inserting appropriate values, $D = 500$ nm and $d = 50$ nm from the electron microscopy evidence, and $\alpha = 35°$ from geometrical considerations, we calculate $\phi = 4°$ for the impression angle. This is substantially less than the corresponding angle 16° between the faces of the Vickers pyramid and the specimen surface. It is clear that other deformation mech-

anisms must act in concert with the twinning.
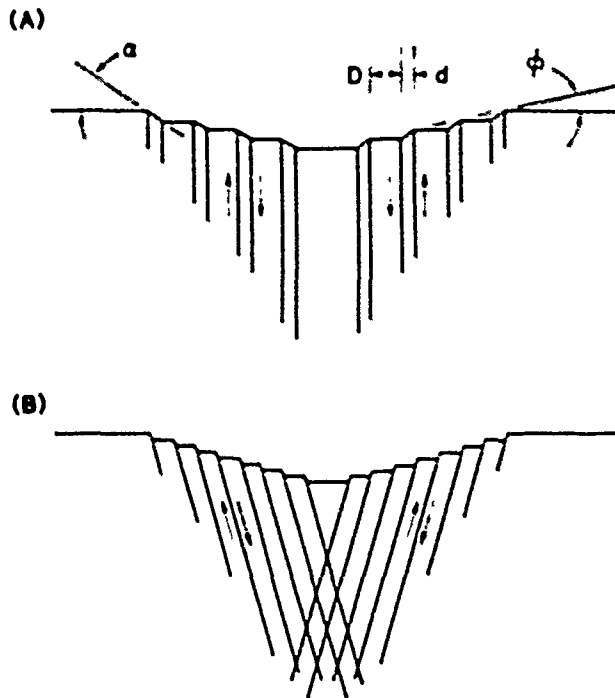
Our results indicate that pyramidal slip, Fig. 9B, is predominant among these other deformation modes. This is in accord with previous sharp particle impact work by Hockey[19] on {1123} surfaces; for that particular contact configuration it was possible to resolve individual dislocation arrays at the periphery of the deformation zone, and thence to confirm the {1123}⟨1100⟩ primary system. However, the detailed nature of the slip process remains somewhat obscure, particularly in the regions of highest stress concentration (i.e., at the impression center and diagonals). We have mentioned the difficulties in carrying out Burgers vector determinations in the regions of intense diffraction contrast. Given the strong inhomogeneity of the typical indentation stress field,[1] together with the constraints imposed by the indenter shape (especially at the contact diagonals), it is not unreasonable to expect that some multiple slip-plane activity must occur.

The fact that the slip processes operate close to the cohesive limit means that there are high Peierls energy barriers to dislocation motion. High Peierls barriers are, of course, characteristic of all ceramics with a large component of covalent bonding.[19] The question arises as to how valid it is to retain the picture of plasticity by (activated) glide dislocation motion in such cases. Hill and Rowcliffe,[22] in analyzing analogous indentation-induced dislocation structures in silicon, suggested a catastrophic shear mechanism, for which they coined the term "block slip." In their interpretation the observed dislocations simply represent the end result of lattice mismatch between opposing, slipped surfaces, somewhat akin to the configuration one would expect for a healed shear crack. It might be argued that such distinctions amount to no more than an exercise in semantics; after all, the final dislocation array is the same. On the other hand, the concept of block slip, unlike that of simple dislocation motion, does extend naturally to noncrystalline materials, thus the shear faulting observed in glass[4-7] may well be described in these terms.

(2) Crack Nucleation

Regardless of the detailed nature of the shearing process in sapphire, it is apparent that the slip planes, as well as the twin

interfaces, can be viewed as high-energy planar defects. As such, they represent favored sites for microcrack nucleation, consistent with the experimental results in Section III. We are unaware of any study of crack nucleation in sapphire in the literature (apart from inferences drawn from incidental observations, e.g., postfailure fractography of strength specimens[23]), so we shall explore the possible mechanism in greater detail below.

First, it may be reiterated that we are dealing with true nucleation events here, and not simply with the propagation (if stable) of preexisting flaws. Experimental studies on double-cantilever beam fracture specimens[24] demonstrate that (0001) is the *least* favored of all crystallographic planes for cleavage (a result that is readily rationalized in terms of the high cost in energy to separate surfaces of oppositely charged ions). Yet one of the sets of microcracks in our indentation experiments was observed at the basal twin interfaces. Such energetically unfavorable fracture configurations are to be expected only under conditions of extraordinary constraint, as indeed occur beneath a Vickers indenter. There the local stress concentrations are presumably so intense, with a strongly suppressed tensile component, as to override the usual dominating influence of surface energy.[†]

Accordingly, by analogy with the shear-fault modeling in earlier studies on glass,[7,8] it is proposed that crack nucleation in sapphire occurs preferentially on the twin and slip interfaces. Exactly where along these interfaces the nucleation begins is open to speculation, but there are certain sites that appear more favored than others. Among these are points of intersection between twin and slip planes in adjacent quadrants, especially in the vicinity of the impression diagonals.[9] There are strong parallels here with the time-honored dislocation pileup models of crack initiation of the Zener-Stroh-Cottrell type[17-19] for metals. An important difference in the covalent-ionic material of interest here is that the "pileup" planes themselves, because of their state of high energy, are likely to become an integral part of the crack embryos once the process has begun. It follows that for "subthreshold" indentations in which nucleation has not yet been effected, these planes will remain as potential sources of weakness in any subsequent, external stressing and/or environmental attack, as is indeed found to be the case in optical glass fibers.[20]

The issues raised above have important implications concerning the mechanical properties of intrinsically hard, brittle ceramics. It is generally accepted that the chief cause of strength degradation in ceramic materials with initially pristine surfaces is the presence of small "flaws," and yet scant attention has been paid to the fundamental, precursor defects from which these flaws generate. Instead, there is a deeply rooted tendency for those involved in strength analysis to disregard such potential "complications," and to treat flaws as scaled-down versions of large-scale cracks subject exclusively to externally applied stresses. The results of our study indicate that this picture can be highly oversimplistic. Not only may the response of these flaws in external fields be dominated by the residual nucleation stresses and local crystallographic constraints, but the flaws themselves may exist in a "subthreshold" state. In such cases the mechanics of failure differ dramatically from those that derive from the traditional "Griffith microcrack" theories.[31] We may envisage a similar impact on the micromechanics of other, practically important, contact-related processes, such as erosion by particle impact, and wear by machining, grinding, and polishing, etc. The additional complications that will inevitably occur in *polycrystalline* aluminas and other engineering ceramics remain a subject for future investigation.

V. Conclusions

For the indentation of (1120) sapphire, the deformation processes which occur have been shown to be sensitive to the orientation of the indenter with respect to the crystallography. The principal modes of deformation were identified as basal twinning, and pyramidal slip. The basal twin interfaces and pyramidal slip planes were observed to act as nucleation sites for incipient microcracks. Since these interfaces represent planes of weakness in the structure, one can consider flaws as existing along these boundaries in a subthreshold state. The findings of our studies on crack nucleation processes suggest that the concept of a "Griffith microcrack," which is subject (in its mechanical response) only to external stress fields, may be overly simplistic.

References

[1] B. R. Lawn and T. R. Wilshaw, "Indentation Fracture: Principles and Applications," *J. Mater. Sci.*, 10 [6] 1049-81 (1975).
[2] B. R. Lawn; pp. 1-25 in Fracture Mechanics of Ceramics, Vol. 5. Edited by R. C. Bradt, D. P. H. Hasselman, and F. F. Lange. Plenum Press, New York, 1983.
[3] B. R. Lawn; pp. 67-86 in Strength of Glass. Edited by C. R. Kurkjian. Plenum Press, New York, 1985.
[4] A. G. Evans and E. A. Charles, "Fracture Toughness Determinations by Indentation," *J. Am. Ceram. Soc.*, 59 [7-8] 371-72 (1976).
[5] G. R. Anstis, P. Chantikul, D. B. Marshall, and B. R. Lawn, "A Critical Evaluation of Indentation Techniques for Measuring Fracture Toughness. I. Direct Crack Measurements," *J. Am. Ceram. Soc.*, 64 [9] 533-39 (1981).
[6] P. Chantikul, G. R. Anstis, E. R. Lawn, and D. B. Marshall, "A Critical Evaluation of Indentation Techniques for Measuring Fracture Toughness. II. Strength Method," *J. Am. Ceram. Soc.*, 64 [9] 539-43 (1981).
[7] J. T. Hagan and M. V. Swain, "The Origin of Median and Lateral Cracks at Plastic Indents in Brittle Materials," *J. Phys. D*, 11 [15] 2091-102 (1978).
[8] J. T. Hagan, "Shear Deformation Under Pyramidal Indenters in Soda-Lime Glass," *J. Mater. Sci.*, 15 [6] 1417-24 (1980).
[9] B. R. Lawn, T. P. Dabbs, and C. J. Fairbanks, "Kinetics of Shear-Activated Indentation Crack Initiation in Soda-Lime Glass," *J. Mater. Sci.*, 18 [9] 2785-97 (1983).
[10] H. Multhopp, B. R. Lawn, and T. P. Dabbs; pp. 681-93 in Deformation of Ceramic Materials, II. Edited by R. C. Bradt and R. E. Tressler. Plenum Press, New York, 1984.
[11] D. B. Marshall and B. R. Lawn, "Residual Stress Effects in Sharp-Contact Cracking. I," *J. Mater. Sci.*, 14 [8] 2001-12 (1979).
[12] D. B. Marshall, B. R. Lawn, and P. Chantikul, *J. Mater. Sci.*, 14 [9] 2225-35 (1979).
[13] B. J. Hockey, "Plastic Deformation of Aluminum Oxide by Indentation and Abrasion," *J. Am. Ceram. Soc.*, 54 [5] 223-31 (1971).
[14] M. L. Kronberg, "Plastic Deformation of Single Crystals of Sapphire," *J. Am. Ceram. Soc.*, 5 [9] 507-24 (1957).
[15] A. H. Heuer and J. Castaing; pp. 238-57 in Advances in Ceramics, Vol. 10. Edited by W. D. Kingery. American Ceramic Society, Columbus, OH, 1984.
[16] R. M. Cannon; pp. 818-38 in Advances in Ceramics, Vol. 10. Edited by W. D. Kingery. American Ceramic Society, Columbus, OH, 1984.
[17] A. Kelly, Strong Solids, pp. 1-35. Clarendon Press, Oxford, 1966.
[18] B. J. Hockey, "Pyramidal Slip and Basal Twinning in Aluminum Oxide"; pp. 167-79 in Deformation of Ceramic Materials, I. Edited by R. C. Bradt and R. E. Tressler. Plenum Press, New York, 1975.
[19] A. H. Heuer, "Deformation Twinning in Corundum," *Philos. Mag. A*, 13 [122] 379-93 (1966).
[20] E. Stofel and H. Conrad, "Fracture and Twinning in Sapphire (α-Al₂O₃) Crystals," *Trans. Metall. Soc. AIME*, 227 [5] 1053-60 (1963).
[21] W. D. Scott; pp. 235-49 in Deformation of Ceramic Materials, II. Edited by R. C. Bradt and R. E. Tressler. Plenum Press, New York, 1984.
[22] M. J. Hill and D. J. Rowcliffe, "Deformation of Silicon at Low Temperatures," *J. Mater. Sci.*, 9 [10] 1569-76 (1974).
[23] P. F. Becher, "Fracture-Strength Anisotropy of Sapphire," *J. Am. Ceram. Soc.*, 59 [1-2] 59-61 (1976).
[24] S. M. Wiederhorn, "Fracture of Sapphire," *J. Am. Ceram. Soc.*, 52 [9] 485-91 (1969).

[†] It is interesting to note that sapphire is not the only material in which indentation-induced cracking on other than primary cleavage planes is observed. In both LiF and MgO, radial crack arms can be made to extend relatively large distances along {110} planes, even though it is {001} which constitute the easy fracture planes;[25] there, because of the relative softness of the material, the critical slip events responsible for the generation of the noncleavage cracks are much more readily apparent.

[28]B. R. Lawn and D. B. Marshall, "Indentation Fractography — A Measure of Brittleness," *J. Res. Natl. Bur. Stand.(U.S.)*, 89 [6] 435-41 (1984).

[29]J. T. Hagan, "Micromechanics of Crack Nucleation During Indentation," *J. Mater. Sci.*, 14 [12] 2975-80 (1979).

[30]C. Zener, pp. 3-31 in Fracturing of Metals. American Society of Metals, Cleveland, OH, 1948.

[31]A. S. Singh, "The Formation of Cracks as a Result of Plastic Flow," *Proc. R. Soc. London, Ser. A*, A223, 404-14 (1954).

[32]A. H. Cottrell, "Theory of Brittle Fracture in Steels and Similar Metals," *Trans. Metall. Soc. AIME*, 212 [2] 192-203 (1958).

[33]T. P. Dabbs and B. R. Lawn, "Strength and Fatigue Properties of Optical Glass Fibers Containing Microindentation Flaws," *J. Am. Ceram. Soc.*, 68 [11] 563-69 (1985).

[34]C. R. Fuller, B. R. Lawn, and R. F. Cook, "Theory of Fatigue for Brittle Flaws Originating from Residual Stress Concentrations," *J. Am. Ceram. Soc.*, 66 [5] 314-21 (1983).

7. "Temperature Dependence of Hardness of Alumina-Based Ceramics"

    C.J. Alpert, H.M. Chan, S.J. Bennison and B.R. Lawn

    J. Am. Ceram. Soc. 71 C-371 (1988).

Temperature Dependence of Hardness of Alumina-Based Ceramics

CHARLES P. ALPERT,* HELEN M. CHAN,*' STEPHEN J. BENNISON,*' AND
BRIAN R. LAWN*

Ceramics Division, National Bureau of Standards, Gaithersburg, Maryland   20899

Hardness was measured as a function of temperature (20° to 1000°C) for several
Al_2O_3 ceramics, including single-crystal sapphire and polycrystalline aluminas
containing different amounts of second phase. Hardness decreased steadily with
increasing temperature for all materials tested, in accordance with a semi-
empirical relation of the form $H = H_0 (1 - T/T_0)$. This behavior conformed with a
thermally activated slip process, limited by Peierls stresses. At lower tempera-
tures, the hardness values for debased aluminas were less (smaller H_0) than for
the pure materials, consistent with a reduction in shear modulus resulting from
the "soft" phase. However, at higher temperatures the hardness values for all
the aluminas converged (identical T_0, i.e., material-invariant activation energy).
The latter behavior indicated that the temperature dependence of the indentation
deformation was controlled predominantly by the Al_2O_3 component.

IN VIEW of the potential use of ceramics as high-temperature materials, it is perhaps remarkable that so little is known about their "hot hardness" properties. Studies by Westbrook,[1] Atkins and Tabor,[2] and Naylor and Page[3] stand out as important, but isolated, contributions. Particularly surprising is the lack of attention in this respect paid to Al_2O_3, one of the most widely used of all ceramics. The data that do exist on this material[1,4,5] show a general tendency for the hardness to decrease strongly with temperature, suggesting some activated process. However, there apparently has been no attempt to compare data for pure and debased aluminas, or even for single-crystal and polycrystal aluminas, to determine the influence of micro-structure. Thus, the role of such factors as grain-boundary phase, so critical to creep properties, remains largely undetermined.

The present work investigates the temperature dependence of several Al_2O_3 ceramics, with the aim of examining the role of microstructural variables.

Experimental Procedure

The materials tested included single-crystal sapphire and nominally pure and debased polycrystalline aluminas. Table I lists these materials, along with some of their essential properties. The second phase in the debased materials was determined by scanning and transmission electron microscopy to be a partially crystallized aluminosilicate glass, concentrated primarily in pockets between the grains (Fig. 1).

Before hardness testing, each sample was mechanically polished to a 1-μm surface finish. Hot-hardness tests[1] were made at 10-N loads using a Vickers indenter at a constant penetration rate (300 μm s) and fixed dwell time (15 s) at maximum load. Measurements were taken at 200°C intervals to 1000°C (homologous temperature $T/T_m \approx 0.55$) under 1 mPa (10⁻⁸ torr). Indentation half-diagonals were measured from optical and scanning electron micrographs and converted to hardness values using $H = P/2a^2$, with P the load and a the indentation half-diagonal. Mean and standard deviations were evaluated from five indentations per temperature setting per material.

Results

Figure 2 plots hardness as a function of temperature for the different aluminas. The typical standard deviation for the points in this plot is ±5%, but error bars are omitted to avoid data overlap. The hardness for all materials decreases nearly linearly with temperature. For sapphire[1] and the nominally pure polycrystalline aluminas,[6,7,8] the data are practically indistinguishable. This indicates that, for the range of temperatures studied, grain boundaries play no significant role in determining hardness. On the other hand, the data for the debased aluminas fall below those for the pure aluminas. This is not inconsistent with the expected role of a soft phase. However, the greatest differences in values occur at the lower tem-

Table I. Properties of Materials Used in This Study

Material	Second phase (vol%)	Grain size (μm)	μ (GPa)	H_0 (GPa)
Sapphire*			174	23.2
Vistal'	0.2	20	161	23.2
AD999'	0.2	3	158	23.2
AD96'	7	11	125	17.6
AD90'	18	4	113	15.8

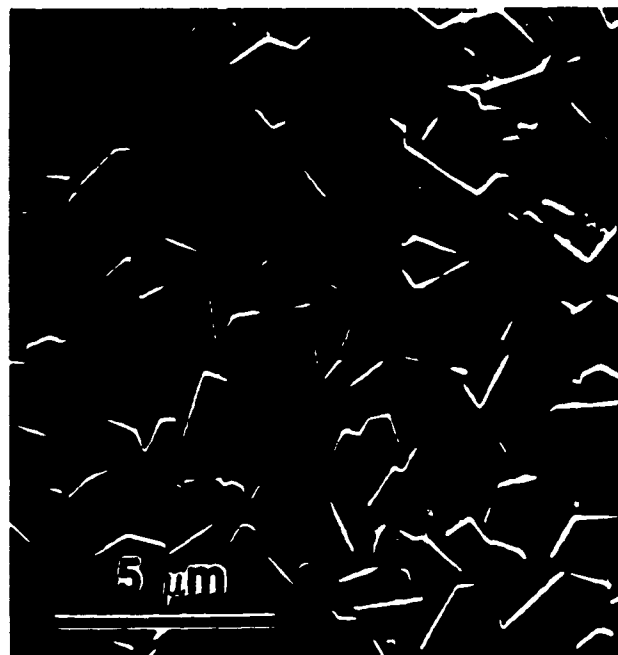*Adolph Mellor Co., Providence, RI, surface orientation (2110). 'Coors Porcelain Co., Golden, CO

Fig. 1   SEM of polished section of debased (AD90) alumina, showing pockets of aluminosilicate glass phase between the Al_2O_3 grains. Note that the latter grains make close contact with adjacent neighbors, i.e., the Al O structure is "connected."
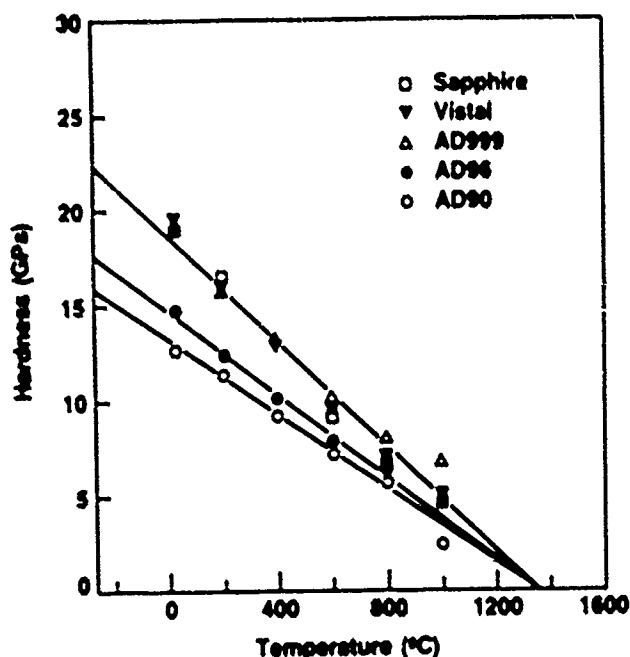
Fig. 2. Plot of hardness versus temperature for the alumina materials listed in Table I. Solid lines are linear fits to Eq. (2).

peratures: indeed, the data for all materials converge strongly at the upper end of the temperature scale.

The general implication of these qualitative observations is that the activation process for the deformation is controlled by the same, primary component in all the materials, i.e., the Al_2O_3. Microscopic examination of the surface regions around the indentation sites revealed the extent and density of slip lines to be comparable in the sapphire and the relatively coarse-grained polycrystalline alumina[4] at elevated temperatures (albeit confined within the grains in the latter material), suggesting that the availability of suitably oriented slip systems is no limiting factor in the deformation process.

HARDNESS AS A THERMALLY ACTIVATED SLIP PROCESS

With these features in mind, an attempt was made to reconcile the results with theoretical relations for dislocation-controlled strain rates. An earlier paper[6] argued that dislocation slip processes account for the greater part of the hardness deformation in sapphire, even at room temperature (although the indentation shear stresses were close to the theoretical cohesive limit for the Al_2O_3 structure, and twinning was also active). More quantitative studies[7,8] of the deformation processes in sapphire confirmed the activity of well-defined dislocation slip systems; moreover, the flow stresses for these systems follow the same precipitous decreases with

temperature that appear in Fig. 2. Accordingly, a semiempirical relation for dislocation velocities for activation over energy barriers[9] yields

$$v = \beta b v \exp\left[-(\Delta F_0/kT)(1-\tau/Y)\right] \quad (1)$$

where β is a dimensionless constant, b is the Burgers vector, v is a lattice vibration frequency, ΔF_0 is a zero-stress ($\tau=0$) activation energy for the dislocation motion, τ is the resolved shear stress on the relevant slip plane, Y is the theoretical shear strength of the crystal ($\times\mu$, with μ the shear modulus), k is Boltzmann's constant, and T is absolute temperature. The barriers in Eq. (1) could be associated with either the intrinsic lattice resistance or extrinsic obstacles. The main feature of this equation is the appearance of a strong stress term in the activation exponent.

Consider the conditions under which the hardness tests were made. Recall that the indenter in the present experiments was loaded at a constant penetration rate, followed by a fixed dwell time. In the approximation that the bulk of the deformation occurred during the initial penetration stage (i.e., neglecting any additional deformation that might have occurred in the dwell time after achieving maximum load), the average steady-state shear-strain rate in the near-contact field was the same for all indentations, regardless of material or temperature. But for dislocation-controlled deformation, the steady-state shear rate is simply $b\rho v$, where ρ is the dislocation density. Surely, ρ will depend on the resolved shear stress, τ (notably at the higher temperatures), but such a dependence will appear only as a preexponential factor (usually power law[v]) in the shear-strain rate, and to a first approxima-

tion may be neglected compared to the exponential dependence in Eq. (1). With this qualification, v is constant. Finally, the hardness, H, will scale directly with the resolved shear stress, τ. Then Eq. (1) may be rearranged to give

$$H = H_0(1-T/T_0) \quad (2)$$

where $H_0 \times Y \times \mu$ is the hardness at 0 K and $T_0 \times \Delta F_0$ is the "softening" temperature at which the hardness goes to zero.

The solid lines in Fig. 2 are fits of Eq. (2) to the data. In this fitting, no attempt is made to distinguish between the single-crystal and pure polycrystal forms of Al_2O_3. However, separate lines are drawn through the data for two debased aluminas. All the data can be fitted to a common value of $T_0 \approx 1350$ K. The values of H_0, however, differ for each curve. These values are included in Table I.

DISCUSSION

Can one attach any physical significance to the parameters obtained from the data fits? First, it should be emphasized that the "goodness" of fit obtained in Fig. 2 establishes consistency with, but not proof of, a flow process controlled by dislocation motion over lattice barriers. There are several variants of Eq. (1),[9] along with the usual (empirical) Arrhenius function, and most of these fit equally well to the data.

The modeling indicates that the deformation is stress activated. Moreover, the apparent constancy in T_0 ($\times\Delta F_0$) suggests that the activation energy is the same for all alumina materials, which in turn suggests that it may be slip in the hard, primary Al_2O_3 component that controls the activation process. This possibility differs somewhat from that advanced by Czernuszka and Page[5] in an earlier hardness–temperature study of two debased aluminas, that suggested that the sharp falloff in hardness with increasing temperature might result in part from a softening of the second phase. However, those workers made no attempt to compare their results with controls containing no second phases. Also, the estimated softening temperature of the glass in the alumina materials used here,[9,11] $\approx 900°C$ (from viscosity data for aluminosilicate glass[10]), suggests that the second phases may retain much of their load-bearing capacity at intermediate temperatures. Furthermore, it appears from Fig. 1 that, despite the presence of the glassy pockets, the Al_2O_3 grains in the debased structures maintain close contact with their neighbors; i.e., the alumina structure remains effectively "connected." In this latter context, the indentation field contains a large hydrostatic-stress component that would help to enhance such intergranular contact.

This picture of a connected alumina structure is also consistent with the "athermal" element of the hardness behavior. The shear modulus for such a

structure would be expected to diminish systematically with increasing glass content, in accordance with some law of mixtures. The reduction in H_a ($\times \mu$) with increasing glass content (Table I) might thus be interpreted as a reduction in capacity for the structure to withstand shear loading: H_a indeed appears to scale approximately with the measured shear modulus listed in Table I.

From these observations, soft phases (at least at the levels considered in the present work) may not always be unduly deleterious to the load-sustaining capacity of ceramics at moderate temperatures (to 1000°C), particularly if the loading has a large compressive component (e.g., as in the contact events responsible for erosion and wear). This insensitivity to composi-

tion directly contrasts to creep properties at higher temperatures.

ACKNOWLEDGMENT

REFERENCES

[1] J. H. Westbrook, "The Temperature Dependence of Hardness of Some Common Oxides," *Rev. Hautes Temp. Refract.*, 3 [1] 47–57 (1966).

[2] A. G. Atkins and D. Tabor, "Hardness and Deformation Properties of Solids at Very High Temperatures," *Proc. R. Soc. London A*, 292, 441–58 (1966).

[3] M. G. S. Naylor and T. F. Page, "Microstructural Studies of the Temperature Dependence of Deformation Structures around Hardness Indentations in Ceramics," *J. Microsc. (London)*, 130 [6] 345–60 (1982).

[4] T. N. Loladze, G. V. Bokuchava, and G. E.

Davidova, pp. 251–57 in Science of Hardness Testing and Its Applications. Edited by J. H. Westbrook and H. Conrad. American Society for Metals, Metals Park, OH, 1973.

[5] T. T. Cremovicka and T. F. Page, "A Problem in Assessing the Wear Behavior of Ceramics: Load, Temperature, and Environmental Sensitivity of Indentation Hardness," *Proc. Br. Ceram. Soc.*, 34, 51, 145–56 (1984).

[6] H. M. Chan and B. R. Lawn, "Indentation Deformation and Fracture of Sapphire," *J. Am. Ceram. Soc.*, 71 [1] 29–35 (1988).

[7] A. H. Heuer, N. J. Tighe, and R. M. Cannon, "Plastic Deformation of Fine-Grained Alumina (Al_2O_3): II. Basal Slip and Nonaccommodated Grain-Boundary Sliding," *J. Am. Ceram. Soc.*, 63 [1–2] 53–58 (1980).

[8] R. M. Cannon, "Mechanical Properties of MgO and Al_2O_3," pp. 818–38 in Advances in Ceramics, Vol. 10, Structure and Properties of MgO and Al_2O_3 Ceramics. Edited by W. D. Kingery. American Ceramic Society, Columbus, OH, 1984.

[9] H. J. Frost and M. F. Ashby, Deformation Mechanism Maps: Ch. 2. Pergamon Press, Oxford, 1982.

[10] E. B. Shand; p. 247 in Engineering Glass, Modern Materials, Vol. 6. Academic Press, New York, 1968.

8.   "Crack-Interface Traction: A Fracture Resistance Mechanism in Brittle

Polycrystals"

P.L. Swanson

Advances in Ceramics, American Ceramic Society, Vol. 22, p. 135, 1988.

Crack-Interface Traction: A Fracture-Resistance Mechanism in Brittle Polycrystals

Peter L. Swanson*

Institute for Materials Science and Engineering
National Bureau of Standards
Gaithersburg, MD   20899

Crack-interface tractions have been identified as a source of increasing resistance to fracture with crack extension, or rising R-curve behavior, in previous studies on coarse-grained alumina. Real time, in situ, microscopy observations are used in the present study to investigate the generality of crack-interface tractions as a crack-resistance mechanism in three alumina and three glass-ceramics with varying R-curve characteristics. Interface tractions are found to operate to varying degrees in each material. Observed sources of interface traction include: (1) frictional or geometrical interlocking of microstructurally rough fracture surfaces and (2) ligamentary bridging by intact islands of material left behind the advancing fracture front. Ligamentary-bridge formation is compared with the development of twist hackle, inclusion/wake hackle and cleavage hackle in simple material systems. Both sources of interface traction remain active as far as 100 particle dimensions behind the primary crack tip and, with sufficient crack-opening displacement, are eventually overcome by interface-localized microfracturing. Simple analytical fracture mechanics concepts are used to assess the influence of interface tractions on macroscopic fracture behavior. Because of the observed crack-history dependence of the interface-traction crack-tip shielding, it is suggested that neither R-curve behavior nor applied-K_I/subcritical crack velocity relationships are unique properties of these and similar materials.

Our understanding of fracture micromechanisms in brittle polycrystals has recently been advanced through elementary studies of the fracture-extension process using real time in situ microscopy techniques.[1-3] These studies have demonstrated that, although our understanding of the basic phenomenology of fracture in these materials is still in its infancy, there is great potential for effective engineering design of fracture properties through elucidation of the various roles that a material's microstructure plays in providing resistance to fracture. An important characteristic of macroscopic fracture serving to focus attention on fracture micromechanisms is the crack-length-dependent toughness observed in certain polycrystalline ceramics. Of greatest interest are materials exhibiting *increasing* resistance to fracture with crack extension or rising R-curve behavior.[4-6]

*Now with U.S. Bureau of Mines, Denver Federal Center, Denver, CO 80225.
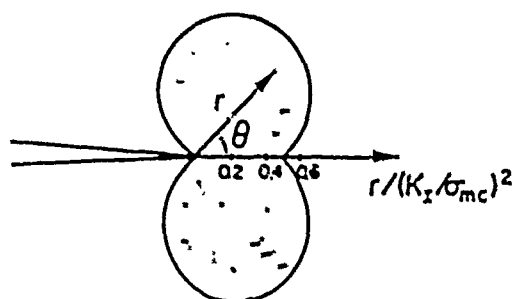
Fig. 1. Diffuse microcrack zone predicted by microcrack-toughening models incorporating a critical-principal-tensile microcracking stress, σ_{mc}.

Rising R-curves imply that a material has an increased tolerance of cracks and flaws. As critical flaws in ceramics are generally very small and very difficult to detect using nondestructive testing techniques, the benefits of sustaining larger flaws before reaching critical failure conditions are obvious. Thus, a fundamental understanding of the mechanisms by which a material resists fracture is crucial to the development of strong flaw-tolerant ceramics.

Numerous mechanisms have been suggested to be responsible for R-curve behavior in single-phase, nontransforming ceramics, particularly frontal-zone microcracking (Fig. 1). This commonly cited toughening mechanism was specifically tested for its applicability to alumina ceramics in a recent microscopy study.[3] No distributed microcracking ahead of the primary fracture tip was observed with either optical reflection/transmission microscopy or diamond-stylus surface profilometry.[3]

While failure to find experimental evidence for distributed microcracking cannot be used as direct evidence of its nonexistence, these studies have demonstrated that another mechanism is active which provides a reasonable explanation for a variety of macroscopic fracture phenomena, including R-curve behavior. It is a mechanism of restraining forces acting across the nascent fracture interface which shields the primary crack tip from high levels of stress. The effect is similar to the action of fibers in fiber-reinforced composites; as a crack extends through the matrix of the composite, the increasing restraining effect of the fibers must be overcome for continued propagation. Figure 2 schematically illustrates two sources of restraining force, or crack-interface traction, observed in polycrystalline alumina[3] and multi-phase crystalline rocks.[7] They are: (1) geometrical or frictional interlocking of topographically-rough fracture surfaces and (2) ligamentary bridging by intact "islands" of material left behind the advancing fracture front.

Secondary microcracking was, in fact, observed in the microscopy experiments.[3,7] It is important to note, however, that it did not occur by the critical-principal-tensile-stress mechanism (Fig. 1). Instead, microcracking occurred behind the visibly-defined primary crack tip at positions where tractions were transmitted across the fracture interface. Interface-localized microcracking, including both friction-induced microcracking and localized microcrack rupture of

136

(I) FRICTIONAL INTERLOCKING
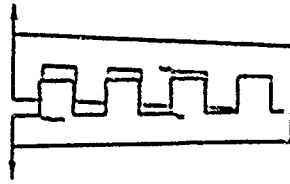
(II) GRAIN BRIDGING

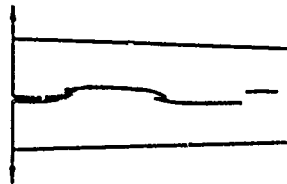(INTACT-MATERIAL "ISLANDS" LEFT
BEHIND ADVANCING FRACTURE FRONT)

Fig. 2. Sources of crack-interface traction observed in coarse-grained alumina (3) and multi-phase crystalline rocks (7).

the intact ligamentary bridges, served as a mechanism for overcoming the crack-plane tractions.

The energetic importance of the interface-traction shielding "activity" was first demonstrated directly in R-curve experiments on alumina by Knehans and Steinbrech.[8] They measured as much as a four-fold increase in the energy required for crack extension after propagation distances of only a few hundred micrometers. By removing the traction-supporting interface with careful sawcutting, they showed that the rising R-curve is reduced to original (short-crack) levels of fracture energy. Contributions to the fracture energy from a frontal microcrack cloud were not needed to explain the increasing resistance to fracture with crack extension. In the final energy-budget analysis, the increased resistance to fracture can largely be traced to the increase in secondary microcrack surface area. The multiple, interface-related microcracks often occur along transgranular fracture paths thus providing an intrinsically high-energy source of fracture-surface energy.[3] Additional fracture energy may be consumed through other friction-related dissipative mechanisms.

In the present paper, photo-documentation of real time in situ microscopic observations of tensile-fracture propagation in several different alumina and glass-ceramics is presented. The generality of the interface-traction crack-resistance mechanism in these materials is explored, suggestions as to the conditions which lead to interface-traction formation are offered, and the consequences of their action on macroscopic fracture behavior through a generic interface-traction fracture model are considered.
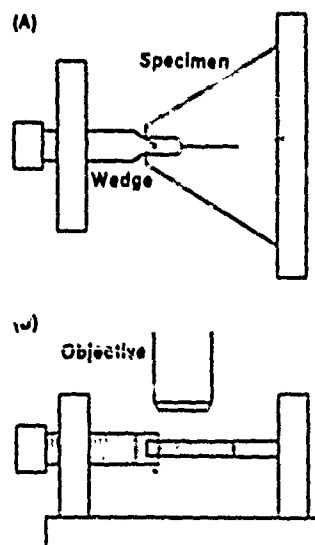
137

Fig. 3. Wedge-loaded double-cantilever beam (WLDCB) geometry used in real-time observations of fracture; (a) plan view, (b) side view.

Experimental Technique

Mode-I fractures were propagated in small wedge-loaded double cantilever beam (WLDCB) specimens of polycrystalline alumina (nominal grain size 3 μm (AD999[*]), 6 μm (FF[†]), and 80 μm (VI[*])) and glass ceramics (5-μm cordierite laths (PC[‡]), 8-μm mica platelets (MA[§]), and 15 to 30 μm lithium-alumino-silicate platelets (SL3[¶]) dispersed in glass matrices). Both tapered WLDCB specimens (2-mm thick, 12-mm per side equilateral triangles (Fig. 3)) and rectangular WLDCB specimens (1.5 by 5 by 12 mm) were employed.[**]

Crack velocities ranged between approximately 10^{-5} and 10^{-9} m/s in both air and vacuum (10^{-7} torr) environments. Observations were made through an optical microscope (Fig. 3) equipped with Nomarski interference contrast capability and a scanning electron microscope. Specimens were polished with successively finer diamond grit sizes down to 1 μm, followed by 0.3 μm alumina powder. The SEM specimens were given a light coating of gold. The optical microscope specimens were left uncoated to preserve optical transmissibility.

Precracks were initiated from 130-μm-wide starter notches by direct wedge loading in air. Load was supplied via a 60° screw-driven, carbide-tipped, tool-steel wedge. Crack-guide grooves were not employed.

After each load increment, subcritical crack extension was monitored through

the microscope until the crack velocity dropped below approximately 10^{-8} m/s. A mosaic of micrographs was obtained while the sample remained under load and then the sequence was repeated. Samples were not unloaded at any time during the tests. Crack propagation direction was from left to right in each micrograph.

Results

General Observations

As is commonly observed in many brittle polycrystalline systems, fractures display a general tendency to deflect along appropriately-oriented low-fracture-energy particle boundaries. Extension along these boundaries (as well as transgranular segments) occurs in discrete jumps, with the extension-increment length closely related to the size of the constituent particles. The increments are quantized not only in the direction of macrocrack propagation but also laterally along the length of the crack front. Consumption of fracture energy is not, therefore, necessarily accompanied by visible crack extension on the surface.

While the overall macrocrack velocity was in the range of 10^{-5} to 10^{-9} m/s, the speed with which the individual increments advanced varied. In the large-grained alumina, the discrete-increment speed was usually much faster than the eye could follow ($\gtrsim 10^{-3}$ m/s at 200×). It thus appeared as if the macrocrack growth rate was limited, not by propagation over individual increments, but by initiation of the increments. Exceptions to this were observed at very low velocities where the increment speed occasionally approached the average velocity.

Crack extension also was discontinuous in the glass-ceramics; however, compared to the aluminas, the discrete-increment velocity more closely approximated the overall average velocity.

No evidence of a diffuse frontal-zone microcrack cloud surrounding the primary fracture tip was observed in any of the crack growth experiments. Crack-interface tractions, however, were observed to some degree in all of the materials investigated. Due to the difficulty in viewing three-dimensional fracture structure from a two-dimensional surface perspective, separation of the interface-traction sources into the two categories shown in Fig. 2 was not always possible. Since many of the materials studied range from transparent to partially translucent, it was possible to resolve some three-dimensional crack structure in transmitted light. However, both the limited depth-of-field available at high magnification and scattering from both rough fracture surfaces and related interface microcracking make positive differentiation between the two sources difficult. It is relatively simple, though, to detect interface "activity" without specifying the exact nature of the traction source.

Interface Tractions

Figure 4 illustrates a relatively clear example of how geometrical interlocking leads to interface-localized microcracking in the coarse-grained (VI) alumina. Frictional resistance to the shearing components of local crack-opening displacement (modes -II and -III) provides the tensile (or mixed-mode) driving force for the reverse-propagating secondary microcrack. Friction-driven extension of the microcrack in Fig. 4 persists even though the macrofracture has traversed the entire specimen length (boundary of specimen is 1 mm to the right of the secondary-crack site). Continued loading of the "failed" sample resulted in

139

Fig. 4. Interface-localized microcrack produced in coarse-grained alumina (VI) by frictional resistance to separation of interlocking fracture surfaces.

complete detachment of the contacting asperity to produce a loose particle of specimen debris. In general, the amount of debris along the fracture interface of cracked specimens decreases as the crack tip is approached.

The evolutionary process of bridge formation and rupture in the coarse-grained alumina is shown in Fig. 5. This sequence of photos shows the same field of view at three different stages of loading. The distances between the primary crack tip and bridge site in Fig. 5(a) through (c) are approximately 0.4, 0.7, and 4.7 mm, respectively. (Interface tractions were observed to remain active for several millimeters behind the crack tip in this particular material.) In general, bridging segments encompass a single grain or small groups of grains (exceptions are later noted). In the example of Fig. 5, predominantly grain-boundary crack segments initially overlap around several grains to form the intact "island" or ligamentary bridge of material. Subsurface viewing shows that the apparently isolated surface-crack traces actually connect at depth. With further loading (Fig. 5(b)), both the amount of crack overlap and the amount of secondary microcracking within the span of bridging material increase. Eventually, the final fracture surface (Fig. 5(c)) takes a completely different, often transgranular, rupture path through the bridging segment. Ruptured bridges sometimes produce complex interlocking fracture surfaces which subsequently undergo additional microcrack damage and specimen-debris production by frictional-interlocking tractions (e.g., Fig. 4).

As Figs. 4 and 5 illustrate, standard optical reflection microscopy techniques are sufficient to study the structural evolution of fractures in medium-to-large-grained materials. In the finer-grained aluminas (Fig. 6), resolving crack structure is difficult. Even simple determination of the crack-tip location in reflected light (upper photo) is difficult. However, by illuminating the translucent sample with a spot source of light placed adjacent to the fracture trace and viewing with crossed polars, the light scattered from the fracture interface throughout the near-subsurface region provides an estimate of both the crack-tip location and traction-zone length. In the two fine-grained alumina materials (AD999 and FF),
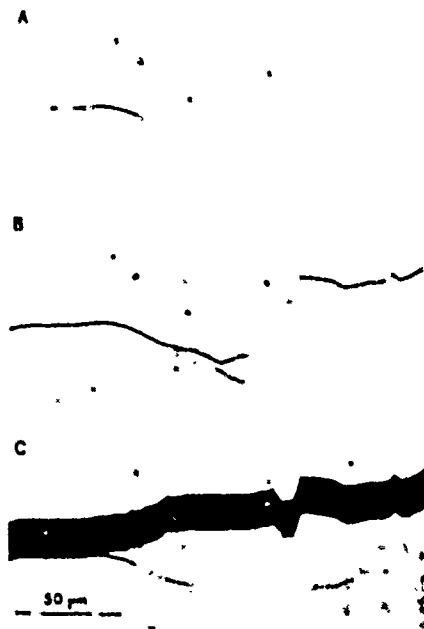
140

Fig. 5. Ligamentary-bridge formation and rupture in alumina (VI). This single bridge site is 0.4 (a), 0.7 (b) and 4.7 mm (c) behind the advancing crack tip.

a gradual transition in the light transmission/reflection characteristics was observed as the illumination source was translated parallel to the fracture trace. When positioned well ahead of the crack tip, there was maximum light transmission. When the light source was placed adjacent to well formed segments of the fracture, there was maximum reflection. The transition between these extremes extended over 100 to 150 μm for both fine-grained aluminas (3 and 5 μm grain size). Similar side-scan illumination measurements on glass show an abrupt transition between maximum reflection and maximum transmission. The transition zones in the polycrystals therefore are interpreted as representing a measure of the interface-traction-zone length. Since both traction sources (Fig. 2) allow partial transmission of light, it was not possible to distinguish between the two using this technique.

Greater detail of fracture-trace features is available in in situ SEM experiments. Unfortunately, two significant advantages are lost. First, subsurface observations in optically translucent materials are no long·r possible. Secondly, the applied stress-intensity range over which moisture-enhanced slow crack growth takes place is reduced in the SEM vacuum. This makes controlled crack growth experiments more difficult to perform. One unanticipated advantage of the SEM technique is related to the need to provide a conductive coating on poor electrical conductors. When the crack breaks through the gold surface coating, the poorly conducting ceramic interior is partly exposed to the electron beam causing charging. Intact-material bridges, on the other hand, remain coated and relatively
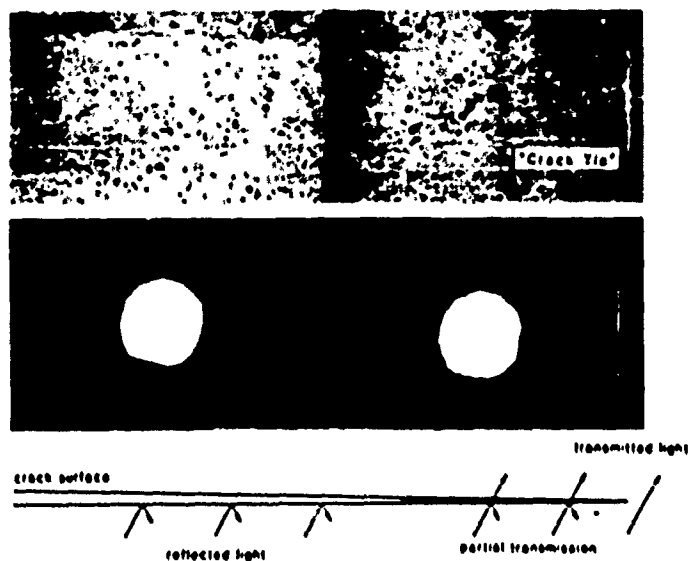
Fig. 6. Reflected light (top photo) and side-scan illumination (bottom photo) of fracture in fine-grained alumina (FF). Gradual transition (100–150 μm) from maximum to minimum light transmission gives indication of interface-traction zone lengths.
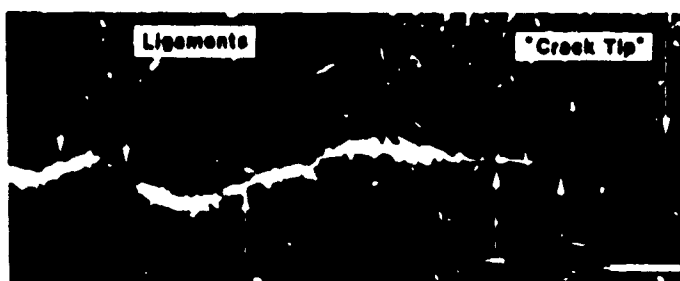

Fig. 7. SEM micrograph of intact interfacial ligaments left behind advancing fracture front in cordierite glass-ceramic (PC).

dark, and therefore readily recognizable. Several examples of ligamentary bridges observed in an experiment on the cordierite glass-ceramic are shown in Fig. 7. Similar interface traction activity, including friction-induced microcrack damage and particle-debris production, also was observed to varying degrees in the other glass ceramics. Ligamentary bridges encompassing many particles (Fig. 8) occasionally persisted for up to a millimeter behind the advancing crack tip in these materials.
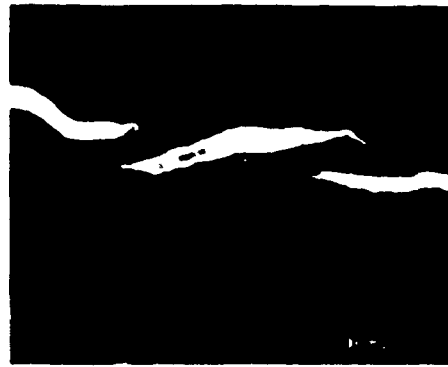
Fig. 8. Large ligamentary bridges left 1 mm behind crack tip during fracture of glass-ceramic (PC) in the SEM.

Interface-Traction Formation

Contained within the morphology of a fracture surface is the convolution of the spatial variation in resistance to fracture and the stress state present during the fracturing process. This fundamental tenet of fractography holds whether one is investigating fracture on the scale of single crystals, planetary bodies, or centimeter-size structural-ceramic components. In consideration of the sequence of events leading to interface-traction formation, our scale of interest lies within the scale of the microstructure. At this scale, the resistance to fracture and the stress field are not simply describable in continuum terms; both quantities vary considerably as a function of position resulting in significant deflection of the crack tip on this microstructural scale. Although geometrical shielding by crack deflection is considered a source of toughening by itself,[9] it does not account for the long range nature of rising R-curves observed in large crack-fracture mechanics tests.[3] We emphasize instead, in the following discussion and presentation of additional supportive observations, the role that local crack-tip deflection plays in developing conditions leading to both fracture-surface interlocking and grain-scale ligamentary bridging.

Geometrical Interlocking

Substantial crack deflection, as idealized to an extreme in Fig. 2(a), is essential for developing interlocking fracture surfaces. Note how the degree of interlocking, for constant fracture surface roughness, depends sensitively on the long wavelength curvature of the crack-opening profile. Simple translation of these rough mating surfaces in the direction of the crack-plane normal (Fig. 2(a)) does not lead to mechanical interference as does rotation about the crack tip or crack opening accompanied by finite curvature. This observation suggests a sensitivity of this crack-resistance mechanism to fracture-test geometry (discussed more fully in the next section).

Several other factors which may act to impede fracture surface separation include: (1) the locally heterogeneous nature of elastic strain on the grain scale: (2) inhomogeneous shape and volume changes associated with localized release of residual thermoelastic/elastic strain: (3) inelastic deformation: and (4) the block-
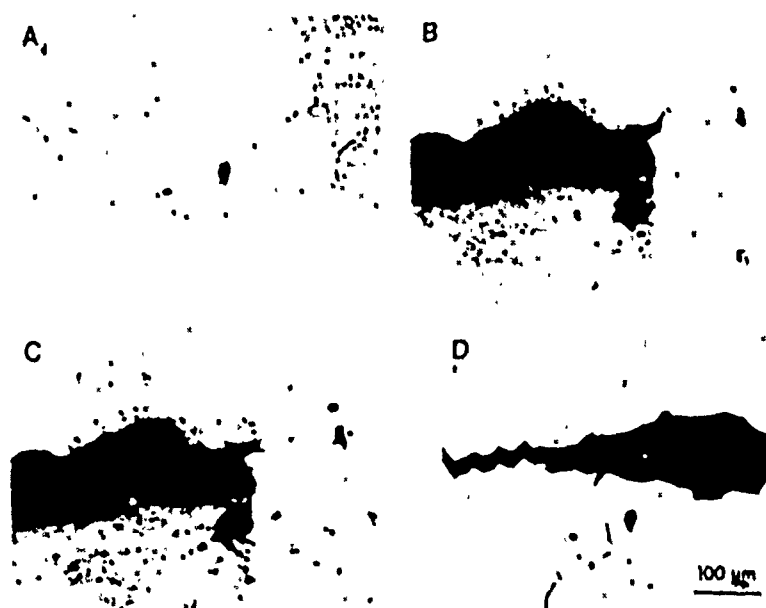
Fig. 9. Interaction between fracture and large pore in alumina (VI) leads
to strong crack deflection and subsequent interface damage: (a)
reflected-light micrograph of crack trace and tip of pore on surface, (b)
transmitted-light view of (a), (c) transmitted-light view 40 μm below
surface, (d) interface damage and debris production produced after one
additional mm of propagation (reflected light).

age, by trapped specimen debris, of local fracture-interface segments undergoing
shear displacement.

Crack-tip deflection is not restricted to the scale of individual particles. If the
macrofracture "feels" the influence of microstructural features of larger scale
(e.g., clustering of ceramic particles in the glass-ceramics) or distributed features
of low volume-fraction (e.g., dispersions of second-phase inclusions or processing
defects), crack deflection may occur on a larger scale. An example of crack/
microstructure interaction and deflection on a scale larger than individual particles
is shown in Fig. 9. The upper reflection micrograph (a) shows a fracture surface
trace in the coarse-grained alumina. This particular alumina contains a low-volume-
density dispersion of large pore-like processing defects up to 100 μm. The tip of
one of the preexisting volume defects intersects the sample surface approximately
80 μm away from the trace of the arrested fracture tip (Fig. 9(a)). Figure 9(b)
shows the same field of view in transmitted light. By focussing 40 μm below the
sample surface (Fig. 9(c)), one sees an abrupt localized deflection of the crack into
the main body of the approximately 50-μm wide defect. Upon intersecting the
massless pore, the effective fracture-tip deflection has instantly increased to a
150-μm-wide lateral excursion, leading to a signficant perturbation in the fracture
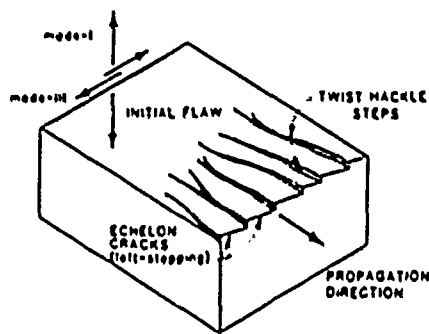surface topography. Figure 9(d) illustrates the ultimate result of this fracture-path

Fig. 10. Development of twist-hackle fracture markings by addition of mode-III load to initial tensile fracture (after 10–12).

deviation in a reflection micrograph of the surface after several additional primary-crack extension increments. The extensive interface damage occurred when the fracture tip was located 1 mm to the right of the local deflection site.
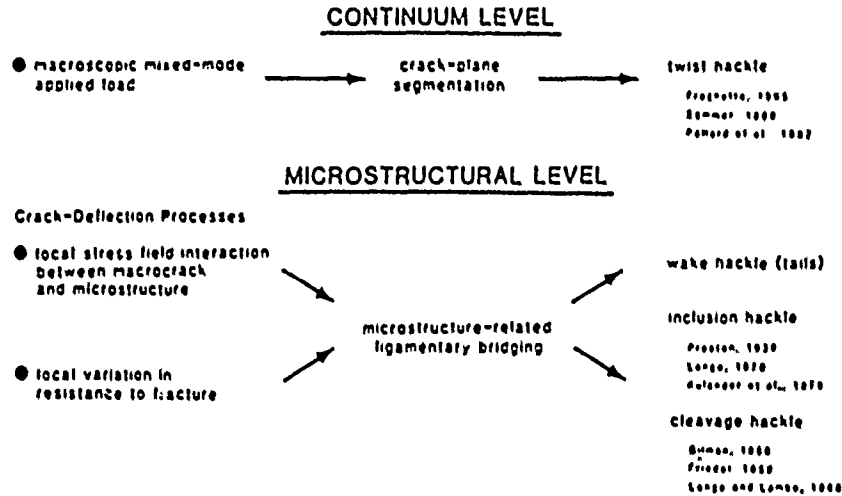
By all outward appearances, the interface damage was associated with geometrical interlocking and subsequent friction-induced debris production. However, as mentioned earlier, it was not always possible to differentiate between the two traction sources with complete certainty. Nevertheless, it is quite apparent that localized deflection associated with crack/microstructure-interaction can lead to significant interface damage and additional consumption of fracture energy over and above simple geometrical-deflection (apparent) toughening.

Ligamentary Bridge Formation

The brittle-materials fractography literature contains few references to morphological features associated with frictional interlocking. There are, however, many references to the concept of ligamentary bridging. In the following, we contrast examples of ligamentary bridge formation found in simple materials, such as glass, with examples found in the relatively complex materials of the present work. Using these comparisons, we argue that no new mechanisms are needed to explain ligamentary bridge formation in the polycrystals. The mechanisms previously identified in postmortem studies of simple material systems are still active in the polycrystals; they are only more difficult to recognize because of the complexity of the fracture morphology.

Table I lists several fracture-surface markings (hackle) associated with ligamentary-bridge formation and rupture in simple material systems. (We exclude from consideration hackle markings defined by the special dynamic-fracture sequence of mirror, mist, and hackle.) The best known fracture marking characteristic of applied-stress-induced ligamentary-bridge formation is "twist hackle."[10-12] This distinctive fracture morphology (Fig. 10) is produced when an initially tensile fracture is split into parallel, offset, finger-like cracks upon encountering a component of macroscopic antiplane (mode-III) shear stress. The echelon array of segmented cracks is held together by adjoining intact ligaments which trail behind the advancing fracture front and provide an increase in the

145

TABLE 1: LIGAMENTARY-BRIDGE FORMATION

CONTINUUM LEVEL

● macroscopic mixed-mode applied load ⟶ crack-plane segmentation ⟶ twist hackle

MICROSTRUCTURAL LEVEL

Crack-Deflection Processes

● local stress field interaction between macrocrack and microstructure

● local variation in resistance to fracture

microstructure-related ligamentary bridging

wake hackle (tails)

inclusion hackle

cleavage hackle

resistance to fracture. Upon complete separation .the resultant fracture surface markings, or traces of twist-hackle steps, are parallel to the direction of crack propagation. The markings are so named because the fracture, upon encountering the macroscopic mixed-mode stress field (generally a combination of modes -I, -II, and -III). "twists" into an orientation perpendicular to the new principal tensile stress direction.

Examples of twist-hackle markings are found on a variety of scales, from the surfaces of secondary (and lesser) twist-hackle-step markings on ruptured ligamentary bridges in laboratory samples of glass[10] to kilometer-scale fractures in rock formations of Earth's crust.[12] As a corresponding example in the present investigation, Fig. 11 illustrates macroscopic crack-plane segmentation in a WLDCB specimen of fine-grained alumina initially subjected to a complex mixed-mode stress field. The exact combination of mixed-mode loads in this predominantly-tensile fracture experiment is not known; the nonuniformity resulted from loading with a damaged wedge surface. Note the consistent left-stepping of the crack traces in this example (crack tip is 5 mm to the right of bridging site). The consistency indicates that the source volume of the mixed-mode loading was at least as large as the volume encompassing the segmented-crack array; i.e., it indicates the remotely applied nature of the mixed-mode field in the example of Fig. 11.

With uniform applied load, both left-stepping and right-stepping individual ligamentary bridges were observed (Figs. 5–7). The size of the ligaments ranged from the subgrain to the multigrain scale. Bridges of microstructural particle groups, because of their large size, often survive greater crack-opening displacement than smaller bridging sites and hence remain intact for greater distances behind the advancing crack tip. This makes them easier to detect than their smaller, more numerous, counterparts closer to the crack tip.

After observing several multigrain ligamentary bridges (comprising tens of grains) form and rupture in one of the fine-grained alumina (FF) specimens using
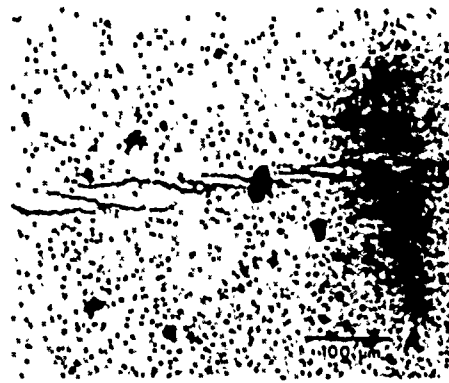
146

Fig. 11. Crack-plane segmentation in fine-grained alumina (FF) subjected to unintentional, but repeatable, macroscopic mixed-mode loading. Consistent left-stepping crack traces interpreted as twist-hackle fingers locally propagating normal to sample surface.

optical microscopy, the fractured surfaces were examined by SEM. The large bridging sites left either a strong localized depression or a protrusion in the fracture surface topography and were often associated with loosened specimen debris (Fig. 12). In addition, anomalously large fractured grains of alumina and/or spinel were found near most of the large bridging sites, but these did not, in the examples of Fig. 12, actually serve as the ligaments themselves. A systematic relationship between anomalous-particle position and ligament geometry has not yet been established. At this time only their close spatial proximity and similar size are noted. The preliminary interpretation of these observations is that the bridging ligaments formed as a result of local mixed-mode interaction (in particular, modes-I and -III) between the stress field of the advancing fracture and the nearby anomalous heterogeneity in the microstructure. For bridging to occur in this fashion, the mixed-mode field must maintain continuity over a volume at least as large as the (initial) ligamentary bridge.

Another example of mixed-mode—stress-induced disruption of the crack plane leading to interface traction was twice observed when a fracture in the coarse-grained alumina propagated between two large, closely spaced processing defects without actually intersecting them (Fig. 11 in Ref. 13). As these events were observed in the interior of the specimen, the 3-dimensional details of the disruption which led to the interface traction activity are not clear. What is apparent from these observations is the close association of the initial stress-field interaction between the primary crack tip and a microstructural element exhibiting an unusual stress boundary condition (large pore or anomalous grain) and subsequent crack-interface traction activity.

Bridging ligaments in the glass-ceramics also were occasionally observed to span a volume considerably in excess of a single microstructural particle (Fig. 8). Anomalously large crystalline particles were not evident in the microstructure as
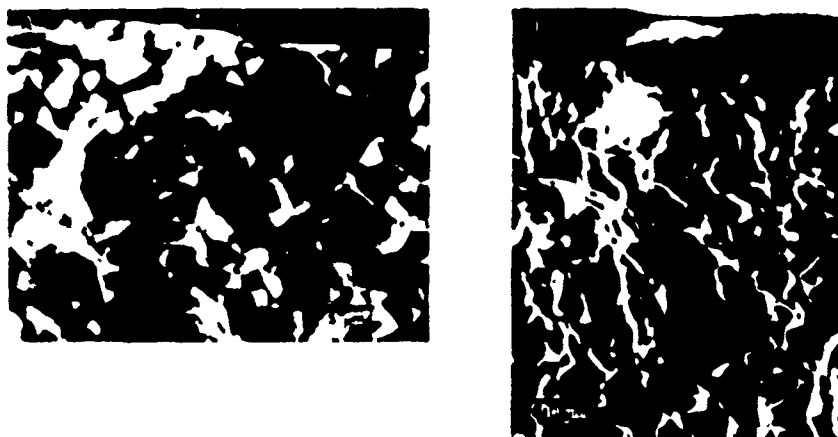
147

Fig. 12. SEM micrographs of alumina fracture surface (FF) in vicinity of large individual bridging sites (polished surfaces at top of figures). Initial ligamentary bridge in (a) is marked by debris fragment consisting of approximately ten grains. Partial ligamentary bridge (b) left as debris fragment in local depression. Note anomalously large fractured grains (alumina/spinel) near bridging sites.

observed in the alumina. It is conceivable, though, that local inhomogeneous mixing of the crystalline particles provides a larger-scale structure that plays some role in developing large bridges.

Other large-to-intermediate ligaments in the glass-ceramics were observed to form during, or immediately after, the incrementing of the load, usually following long periods (hours to days) of sustained subcritical crack growth (also observed to a lesser extent on the grain scale in the aluminas). Although possibly attributable to subtle differences in the *applied* stress field experienced by a crack propagating under fixed-grip (fixed-displacement) vs increasing-load conditions, the consistency of crack stepping expected with such load adjustment was not observed. Of potential importance in explaining this observation is the shear stress contributed to the crack tip field by the nearby interface tractions. Although macroscopically the net mode-II and -III fields average to zero, the traction sources *close* to the crack tip provide strong contributions to all three fundamental displacement modes (-I, -II, and -III). By opening the crack after propagating under fixed-grip conditions, the various components of local crack-interface traction are abruptly modified, giving rise to relatively sudden change in the local mixed-mode field. Local segmentation may then occur in regions experiencing appropriate components of mode-I and -III stress.

Grain-scale bridging (Figs. 5 and 7) appears to contain the same elements that lead to "wake hackle" or "inclusion hackle" formation in simple material systems. These fracture markings form as follows:[10,14-16] Upon encountering a heterogeneity (second-phase inclusion, anomalous grain, etc.) in an otherwise uniform material (glass, single crystals, very-fine-grained ceramic, etc.), a macroscopic tensile fracture is locally deflected due to the perturbation of the local stress field and/or the variation in the local resistance to fracture. Localized deflection around the particle boundary often results in propagation along separate
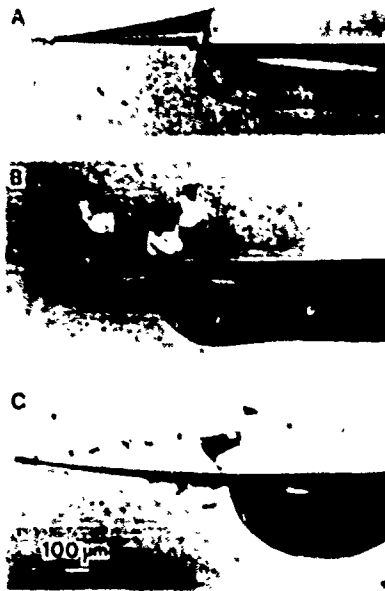
Fig. 13. Fracture lances (a-c). Remnants of trailing ligaments produced in glass after fracture interacted with heterogeneous structure (local propagation to left). Delicate, 3-dimensional lance structure (a) is subject to interface-localized microcrack damage (b, c) by frictional tractions.

noncoplanar segments. Merging of the split fracture front does not immediately follow circumvention of the particle. Instead, the segments of the fracture propagate in an offset, nearly parallel, fashion for a short distance, leaving a trailing intact ligament (tail) adjacent to the heterogeneity.

The heterogeneity may or may not serve as a restraining ligament. For example, the trailing ligament structure shown in Fig. 13(a) (known more appropriately in the postmortem state as a hackle step or, in this particular case, a fracture lance)[11] was produced when a macroscopic mode-1 crack in glass encountered a scratch placed on the sample surface with a diamond scribe. Interaction with this heterogeneous structure, i.e., scribe-induced damage and attendant residual stress, led to propagation along nearly parallel overlapping crack segments (local propagation is to left in photo). Formation of a ligamentary tail is accomplished without the pinning effect of a "tough" inclusion. We also note that the topographically-rough hackle-step features (lances) are susceptible to further damage by geometrical interlocking and friction-induced microcracking (Fig. 13(b) and (c)), particularly during slow crack growth or cyclic fatigue conditions.[13]

It thus appears that the grain-scale ligamentary bridges observed are examples of the polycrystalline form of the inclusion/wake-hackle phenomenon. Appropriately situated grains, or combination of grains and other microstructural features, provide the initial mixed-mode deflection conditions conducive to propagation on locally noncoplanar segments. If fracture is predominantly intergranular, the offset and occasionally overlapping segments are separated by individual grains which

149

constitute the initial bridge. Subsequent tail formation is restricted (or enhanced) by the adjacent microstructural-scale fracture properties and stress conditions. This type of grain-scale ligament formation and rupture has been suggested to be responsible for plumose structures found on large-scale fracture surfaces of a wide variety of polycrystalline rocks.[16] The widespread occurrence of these fracture surface markings, especially well recognized in the field of structural geology, implies that this grain-scale source of crack-interface traction is commonplace in these polycrystalline materials.

Crack-plane segmentation on the subgrain scale (Table 1) is associated with transgranular fracture in single crystals which readily split along cleavage planes. When a cleavage-plane crack is subjected to applied mode-I loading, it usually propagates on multiple offset planar segments as a result of intersecting screw dislocations.[17-18] Cleavage-plane segmentation also occurs under applied mode-I/mode-III conditions, and when transgranular fractures in polycrystals encounter grains of different orientation.[19] The restraining effect of the cleavage-related ligaments in single crystals has long been appreciated.[17-20]

Influence of Interface Tractions on Macroscopic Fracture

To demonstrate how interface tractions influence the macroscopic response of fractures, we model the traction sources as point or line restraining forces acting symmetrically across the fracture surfaces. In a fashion similar to the classical "thin-zone" models of Dugdale and Barenblatt,[19] we start with a sharp, two-dimensional, mathematically-flat, traction-free crack and then add to the surfaces the counteracting net normal forces supplied by the tractions. Although the crack-plane forces oppose the action of the applied loads, we do not require them to cancel the singular field. The stress intensification experienced by the primary crack tip is then expressed as

$$K_I(\text{tip}) = K_I(\text{appl}) + K_I(\text{trac}) \tag{1}$$

The $K_I(\text{appl})$ is the conventional applied stress-intensity factor, $\sigma_o\sqrt{\pi a}$, where σ_o is the remotely applied tensile stress and a is the primary-crack half-length. In this particular application, $K_I(\text{trac})$ is negative, or resistive, and is determined by integrating the restraining forces over the traction-zone length, x_t, through the use of an appropriate Green's function $G(a,x)$.[21] Note that x_t increases from zero, for a traction-free crack, to the steady-state value characteristic of an equilibrium traction-zone length. For convenience, we consider the restraining forces to be continuously distributed and representable as stresses $\sigma_{yy}^t(x,0)$, acting at a position $(x,0)$. The $K_I(\text{trac})$ becomes

$$K_I(\text{trac}) = -\int_{-a}^{a} G(a,x)\sigma_{yy}^t(x,0)dx \tag{2}$$

From the perspective of the experimentalist who measures an R-curve ($\sigma_o\sqrt{\pi a}$ vs Δa) we obtain

$$K_R(\text{appl}) = K_{IC}(\text{tip}) + \int_a^a G(a,x)\sigma_{yy}^t(x,0)dx \tag{3}$$

where K_R(appl) is the value of K_I(appl) needed to extend the crack and K_{IC}(tip) is an averaged grain-boundary/single-crystal toughness, considered here to be an inherent property of the material.

In describing an R-curve with Eq. (3), an increasing resistance to fracture with crack extension can be associated with an increase in K_I(trac) without an a priori need to invoke changes in the fundamental bond rupture processes (described by K_{IC}(tip)) acting at the advancing fracture front. The R-curve measurements show that K_I(trac) can be as great as four to five times K_{IC}(tip) in certain alumina ceramics.[22] The magnitude of K_I(trac), of course, is dictated by the magnitude of σ'_{yy} and $\sigma'_{yy}(x,0)$ is, in turn, governed by the density of traction sites and the specific restraining-force/crack-opening displacement relation developed at each traction site. The force-separation relation ³ akin to cohesive-force "laws" in atomic-scale fracture models.[19]

From the examples of bridging and interlocking shown in previous sections, it is apparent that there is no single force-separation law at work on the microstructural scale in any one material. For example, large ligamentary bridges maintain restraining forces over larger crack-opening displacements than grain-scale or subgrain-scale bridges. However, for purposes of discussion, we consider there to be a single "effective" or averaged force-separation law specific to each material, which accounts for all sources of traction. This allows us to describe the average local restraining force according to the average local displacement ($\sigma'_{yy} = \sigma'_{yy}(v(x))$). Since the local crack-opening displacement is dependent upon both the applied K_I and the integrated effect of the interface tractions, the traction-zone length and force-displacement law are not independent. This leads to a nonlinear singular integral equation for K_I(trac), solvable only by numerical techniques.[23] A quantitative solution is not pursued here. Some recent literature describes similar cohesive-zone approaches to modelling fracture in rocks,[24] concrete,[25] composites,[26] and ceramics.[27] We use this approach not as a pragmatic way of determining engineering toughness parameters, but as a simple analytical tool for incorporating the effects of microstructure into the mechanics analysis—even if only qualitatively—and assessing the response of macroscopic fractures.

In separating the mechanics into crack-tip and crack-flank terms (Eq. (3)), the question of characterization uniqueness immediately comes to mind. By admitting the existence of R-curve behavior, we have already given up the standard one-parameter (K_{IC}(appl)) description of fracture. "Is there a unique K_R versus Δa relation?" To answer this, we must first appreciate the conditions under which the single parameter K_I is adequate for describing fracture at any crack length. Conventional engineering fracture mechanics philosophy dictates that fracture toughness measurements be obtained from tests in which the influence of specimen size and/or geometry is removed from the fracturing process,[28] so that the toughness measurements are "valid" or material specific. Satisfaction of the small-scale inelastic deformation requirement, or confinement of the material-breakdown zone to a region which is small in comparison to pertinent specimen dimensions (e.g., $x/a < 2\%$), is necessary for this condition.[28] As long as $x/a < 2\%$, the applied K_I is taken to represent the intensity of the elastic field surrounding the entire material-breakdown zone and the resulting toughness measurements, for a given crack length, are independent of sample geometry.

In the present experiments, we have found several instances of gross violation of the small-scale breakdown assumption (i.e., x/a approaching 100%). Under these conditions, the magnitude of K_I(trac) becomes a strong function of the

crack-opening profile produced by the particular specimen geometry. This influence can be accounted for if the crack-opening profile, the force-separation law and the appropriate $G(x,c)$ are known. The measured R-curve, however, is still inherently dependent upon specimen geometry.

Under small-scale breakdown conditions, where specimen-geometry effects are absent, there is still another complication which makes the K_R vs Δa curve nonunique. This is the effect of crack-opening displacement history. Because the act of surmounting interface tractions irreversibly consumes fracture energy, there is no one-to-one relationship between crack-opening displacement and interface-traction magnitude (i.e., σ'_{xx} is hysteretic). Consequently, even if the force-separation law is known exactly, it is still necessary to know details of the crack-opening history to determine K_I(trac) and hence the driving force experienced by the primary crack tip. This strongly suggests that the R-curve is *not* an inherent property of these materials; in general, it is nonunique, depending upon the extrinsic variables of crack length, crack-opening displacement and crack-opening displacement history.

Without a quantitative measure of the force-separation relationship, the form of the R-curve cannot be predicted quantitatively, even under monotonic loading conditions. Nevertheless, it is instructive to formulate qualitative predictions of macroscopic behavior based upon assumed forms of the force-separation law or the resultant $\sigma'_{xx}(x,0)$. In this fashion, we can reconcile the observation that each of the materials investigated exhibited crack-interface traction activity, but each did not exhibit R-curve behavior. The exercise also emphasizes the importance of determining force-separation relationships quantitatively for different individual traction sources and/or for material samples as a whole to establish "effective" force-separation laws.

Two equilibrium crack-interface traction distributions are shown schematically in Fig. 14. The tractions are in equilibrium in the sense that the magnitude of K_I(trac) remains constant with crack extension. Other pertinent material properties such as the intrinsic grain-scale toughness (K_{IC}(tip)) and the density of individual traction sites are taken to be identical, the only difference being the functional form of the force-separation law associated with the unspecified traction source. The traction-zone lengths, x_t, are identical, but the shielding provided by material B is significantly greater than that provided by material A. Consequently, material B exhibits a higher steady-state crack-growth resistance at the top of the R-curve. Obviously, mere detection of long lengths of crack-interface traction activity (Fig. 14) by itself does not imply significantly increased resistance to fracture; there must be significant *energy* consumption. Two illustrative examples from the microscopy experiments can be cited here.

The fine-grained aluminas exhibited traction activity persisting for roughly equal distances (100–150 μm) behind the crack tip. According to Cook et al.,[29] one alumina (AD999) exhibits significantly greater R-curve behavior than the other (FF). From the simple interface-traction fracture model (and assuming everything else equal), we would associate the AD999 and FF with traction distributions B and A, respectively. Similarly, the mica and cordierite glass-ceramics exhibited roughly equal traction-zone lengths for long cracks under monotonic loading but one (MA) exhibits R-curve behavior and the other (PC) does not.[30] Thus, the need for direct measurements of the force-displacement relations associated with various traction sources is clear. Simple visual examination, as essential as it is, is not by itself sufficient for this task.

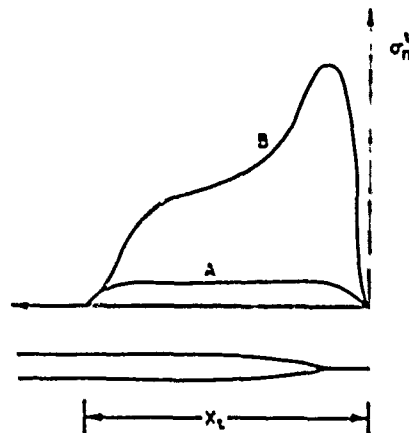The interface-traction concept also provides a rational explanation for some

152

Fig. 14. Two hypothetical interface-traction $(\sigma^t_{yy}(x,0))$ distributions associated with different force-separation "laws." (a) and (b) have identical equilibrium traction-zone lengths, x_t, but (b) exhibits much stronger R-curve behavior than (a).

of the observed inconsistencies in fracture mechanics parameters used to describe subcritical crack growth. It is well known that experimentally-determined "constants" in the empirical relationship between applied stress-intensity factor and crack velocity ($v \approx v_0 K^n_I$) often depend upon specimen geometry and/or technique.[31] Agreement between subcritical crack growth parameters obtained by different methods or sample geometries is found in only a select few, very homogeneous, materials such as certain glasses, glass-ceramics, and some very fine-grained (<10 μm) polycrystalline ceramics.[32] Pletka and Wiederhorn[31] have suggested that this inconsistency is due in part to increasing resistance to fracture with crack extension.

Pletka and Wiederhorn[31] and others also note that when using the double-torsion relaxation technique to determine v-K_I data in many common polycrystalline ceramics, the data often do not define a single v-K_I relationship. Similar observations of nonuniqueness in force-relaxation measurements (relaxation rate assumed proportional to crack extension rate) in polycrystals have been noted by this author.[33] Using nondestructive testing techniques, the force relaxation was shown to be produced not only by extension of the primary crack but also by time-dependent adjustment of the interface tractions.[13] The above observations are consistent with the assumed crack-history and test-geometry dependence of the interface-traction magnitude K_I(trac).

Conclusions

In situ microscopy observations have been made of the stable crack-extension process in six different alumina and glass-ceramics of varying R-curve characteristics. No evidence of a diffuse cloud of microcracking distributed ahead of the primary crack tip, as predicted by critical-principal-tensile-stress-based microcrack models, was found in any of the materials using these techniques. Localized microcracking was observed as far as 100-particle dimensions *behind* the crack tip and was associated with overcoming crack-interface tractions.

Crack-interface tractions were provided by (1) frictional or geometrical interlocking of the rough fracture surfaces and (2) ligamentary bridging by intact islands of material left behind the advancing fracture front. The ligamentary bridging appears to represent the development of the polycrystalline form of twist, inclusion/wake, and cleavage hackle.

Through the use of simple fracture mechanics concepts, the macroscopic fracture response was shown to be related to the restraining-force action of the traction sources and the extrinsic variables of crack length, crack-opening displacement, and crack-opening displacement history. Using this approach, the interface-traction mechanism was shown to provide a rational explanation for both R-curve behavior and the inconsistency in subcritical crack growth data observed for these materials.

Acknowledgments

References

[1]P. L. Swanson, B. Douglas, and H. Spetzler, "Resistance to Mode-I Fracture in Brittle Polycrystalline Materials: A Contribution from Crack-Plane Friction," Eos Trans. Am. Geophys. Union, 65, 1061 (1984).

[2]R. Knehans, U. Wöstmann, and R. Steinbrech, "Nachkerbexperimente an Al_2O_3 Biegeproben zur Untersuchung des R-Kurven-Effekts," in Festigkeit Keramischer Werkstoffe, Deutscher Verband f. Materialprüfung, Berlin, 1984.

[3]P. Swanson, C. J. Fairbanks, B. R. Lawn, Y. -W. Mai, and B. J. Hockey, "Crack-Interface Grain Bridging as a Fracture Resistance Mechanism in Ceramics: I. Experimental Study on Alumina," J. Am. Ceram. Soc., 70, 279-89 (1987).

[4]H. Hübner and W. Jillek, "Sub-Critical Crack Extension and Crack Resistance in Polycrystalline Alumina," J. Mater. Sci., 12, 117-25 (1977).

[5]R. Steinbrech, R. Knehans, and W. Schaarwachter, "Increase of Crack Resistance During Slow Crack Growth in Al_2O_3 Bend Specimens," J. Mater. Sci., 18, 265-70 (1983).

[6]R. F. Cook, B. R. Lawn, and C. J. Fairbanks, "Microstructure-Strength Properties in Ceramics: I. Effect of Crack Size on Toughness," J. Am. Ceram. Soc., 68, 604-15, 1985.

[7]P. Swanson, "Tensile-Fracture Resistance Mechanisms in Brittle Polycrystals: An Ultrasonics and In-Situ Microscopy Investigation," J. Geophys. Res., 92, 8015-36 (1987).

[8]R. Knehans and R. Steinbrech, "Memory Effect of Crack Resistance During Slow Crack Growth in Notched Al_2O_3 Bend Specimens," J. Mater. Sci. Lett., 1, 327-29 (1982).

[9]K. Faber and A. G. Evans, "Crack Deflection Processes: I, Theory; II, Experiment," Acta. Met., 31, 565-84 (1983).

[10]V. D. Frechette, "Characteristics of Fracture-Exposed Surfaces," Proc. Brit. Ceram. Soc., 5, 97-106 (1965).

[11]E. Sommer, "Formation of Fracture 'Lances' in Glass," Eng. Frac. Mech., 1, 539-46 1969.

[12]D. D. Pollard, P. Segall, and P. T. Delaney, "Formation and Interpretation of Dilatant Echelon Cracks," Geol. Soc. Am. Bull., 93, 1291-1303 (1982).

[13]P. L. Swanson, "A Fracture Mechanics and Non-Destructive Evaluation Investigation of the Subcritical-Fracture Process in Rock"; pp. 299-318 in Fracture Mechanics of Ceramics. Edited by R. C. Bradt, A. G. Evans, D. P. H. Hasselmann, and F. F. Lange. Plenum, New York, 1986.

[14]F. F. Lange, "The Interaction of a Crack Front with a Second-Phase Dispersion," Philos. Mag., 22, 983-92 (1970).

[15]J. C. Swearengen, E. K. Beauchamp, and R. J. Eagan, "Fracture Toughness of Reinforced Glasses"; pp. 973-87 in Fracture Mechanics of Ceramics, Vol. 4. Edited by R. C. Bradt, D. P. H. Hasselman, and F. F Lange. Plenum, New York, 1978.

[16]B. R. Kulander, C. C. Barton, and S. L. Dean, "The Application of Fractography to Core and Outcrop Fracture Investigations," U. S. DOE METC SP-79.3, U. S. Dept. of Energy, Morgantown Energy Research, Center, Springfield, VA, 1979.

[17]J. J. Gilman. "The Propagation of Cleavage Cracks in Crystals. *J. Appl. Phys.* 27, 1262–69 (1956).

[18]J Friedel. "Propagation of Cracks and Work Hardening . pp. 498–523 in Fracture Edited by B L. Averbach et al John Wiley. New York 1959

[19]B. R. Lawn and T R. Wilshaw. Fracture of Brittle Solids. Cambridge University Press. 1975

[20]F F. Lange and K A. D. Lambe. "Interaction Between a Crack Front and Cleavage Steps," *Philos. Mag.* 18, 129–36 (1968)

[21]P C. Paris and G. C. Sih. "Stress Analysis of Cracks", pp. 30–83 in Fracture Toughness Testing and Its Applications. ASTM STP 381, 1965.

[22]H. Wieninger. K. Kromp, and R F Pabst. "Crack Resistance Curves of Alumina and Zirconia at Room Temperature." *J. Mater. Sci.*, 21, 411–18 (1986)

[23]H. Anderson and H. Bergkvist, "Analysis of a Non-Linear Crack Model." *J. Mech Phys. Solids*, 18, 1–28 (1970).

[24]J. F. Labuz, S. P. Shah. and C. H Dowding. 'Experimental Analysis of Crack Propagation in Granite," *Inter. J. Rock Mech. Miner. Sci.*, 22, 85–98 (1985).

[25]Fracture Mechanics of Concrete Edited by F. H. Wittman Elsevier. New York, 1983.

[26]Application of Fracture Mechanics to Cementitious Composites. Edited by S. P. Shah. Martinus Nijhoff. Boston, 1985.

[27]Y. -W. Mai and B. R. Lawn, "Crack-Interface Grain Bridging as a Fracture Resistance Mechanism in Ceramics: II, Theoretical Fracture Mechanics Model," *J. Am. Ceram. Soc.* (in review). 1986.

[28]J. F. Knott. Fundamentals of Fracture Mechanics. Butterworth, Boston. 1976.

[29]C. J. Fairbanks, B. R. Lawn, R. F. Cook, and Y. -W. Mai, "Microstructure and Strength of Ceramics." in Fracture Mechanics of Ceramics. Edited by R. C. Bradt, A. G. Evans, D. P H. Hasselmann, and F F. Lange. Plenum, New York, 1986.

[30]S. M. Wiederhorn and J. E. Ritter. Jr., "Application of Fracture Mechanics Concepts to Structural Ceramics', pp. 202–14 in Fracture Mechanics Applied to Brittle Materials, ASTM STP 678, 1979.

[31]B. J. Pletka and S. M. Wiederhorn, "A Comparison of Failure Predictions by Strength and Fracture Mechanics Techniques," *J. Mater. Sci.* 17, 1247–68 (1982).

[32]P. L. Swanson. "Subcritical Crack Growth and Other Time- and Environment-Dependent Behavior in Crustal Rocks," *J. Geophys. Res.*, 89, 4137–52 (1984).

9.	"Effect of Heat Treatment on Crack-Resistance Curves in a Liquid-Phase-Sintered Alumina"

S.J. Bennison, H.M. Chan and B.R. Lawn

J. Am. Ceram. Soc. 72 677 (1989).

Effect of Heat Treatment on Crack-Resistance Curves in a Liquid-Phase-Sintered Alumina

Stephen J. Bennison,* Helen M. Chan,*·' and Brian R. Lawn*

Ceramics Division. National Institute of Standards and Technology. Gaithersburg. Maryland 20899

The effects of heat treatment on the R-curve (crack-resistance) behavior of a commercial liquid-phase-sintered (LPS) alumina have been studied using the indentation–strength test. An enhancement of the R-curve characteristic of this LPS alumina is obtained by a treatment that increases the scale of the microstructure. The enhanced R-curve characteristic leads to the desirable property of flaw tolerance, albeit at the expense of a diminished strength at small crack sizes. The implications of these findings are discussed with reference to processing and design strategy. [Key words: alumina, sintering, cracks, mechanical properties, strength.]

SEVERAL workers have reported that the toughness of liquid-phase-sintered (LPS) aluminas can be improved by suitable heat treatments.[1-4] Those workers attributed the changes to modification of residual thermal expansion mismatch stresses or to crystallization of the amorphous intergranular phase. Such claims deserve detailed attention because they open up the prospect of tailoring mechanical properties via simple heat treatments.

Implicit in these previous studies, however, is an assumption which is now known to be restrictive; i.e., that the "toughness" is a single-valued material quantity. Recently it has been shown, using indentation–strength[5-7] and double-cantilever-beam[8-10] techniques, that the toughness of alumina (and other) ceramics is not generally single-valued, but tends to increase with increasing crack size (R-curve behavior). The extent of the increase is found to depend critically on the microstructure, with the grain size and the nature of the intergranular phase the apparent controlling parameters.

The form of the R curve has significant implications for structural applications.[11] In particular, flaw tolerance becomes an important design factor. One

interesting feature of the alumina data collected by Cook *et al.*[5-7] is the tendency for the R curves to cross each other, corresponding to an inverse relationship between large-scale and small-scale toughness values (a result of special consequence to wear resistance[12]). Hence, in evaluating the significance of toughness "improvements," it is important to specify the crack size range over which measurements are made. In this context, we note that the previous studies[1-4] of the effect of heat treatment on toughness were generally made at "large" crack sizes; i.e., large with respect to the scale of the microstructure. A complete assessment of the changes in mechanical properties requires a determination of the entire R curve.

Accordingly, the aim of the present study was to investigate the effects of microstructural changes resulting from simple heat treatments on the R-curve behavior of a LPS alumina. We use the indentation–strength technique because of its special usefulness in the investigation of R-curve characteristics at small as well as large crack sizes.[5]

Experimental Procedure

A commercial LPS alumina† containing ≈10 wt% (≈18 vol%) intergranular second phase was chosen for the study. The samples were provided as disks, 25 mm in diameter and 2 mm thick, suitable for biaxial flexure testing.

Heat treatments (HT) of the as-received material were conducted in air using a MoSi₂ resistance furnace according to the schedules in Table I. The aims of the heat treatments were to (1) vitrify the second phase without changing the grain size (HT-1), (2) recrystallize the intergranular phase without changing the grain size (HT-2), and (3) increase the grain size with a controlled (vitrified) in-

tergranular phase (HT-3). A heating and cooling rate of 250°C/h was used for all firings.

The following specimen characteristics were determined: (1) the degree of crystallinity and composition of the intergranular phase, using transmission electron microscopy (TEM) and energy-dispersive X-ray microanalysis (X-ray EDS); (2) grain size, using scanning electron microscopy (SEM) with a lineal intercept method;[13] and (3) density, using the Archimedes method. The specimen characteristics resulting from the heat treatments are included in Table I.

The prospective tensile face of each specimen was diamond polished to a 1-μm finish prior to mechanical testing. Most of the disks were indented at the face centers with a Vickers diamond pyramid at contact loads of 2 to 300 N. Indentations were made through a piece of carbon paper to mark the contact sites. Some specimens were left unindented as controls. All indentations were made in air and the samples allowed to stand for 10 min. The biaxial strength tests were made using a flat circular punch, 4 mm in diameter, on three-point support, 20 mm in diameter.[14] A small drop of silicone oil was placed on the indentations prior to testing, and failure times were kept below 20 ms to minimize effects from static fatigue. Strength values were calculated from the breaking loads and specimen dimensions using thin-plate and beam formulas.[14,15] Care was taken to examine all specimens after they fractured to verify the contact site as the origin of failure. Unsuccessful breaks were incorporated into the data pool for unindented controls.

Results

Figure 1 plots the results of the mechanical tests of the various heat-treated

Table I. Heat Treatments Used for Liquid-Phase-Sintered Alumina and the Resulting Material Characteristics

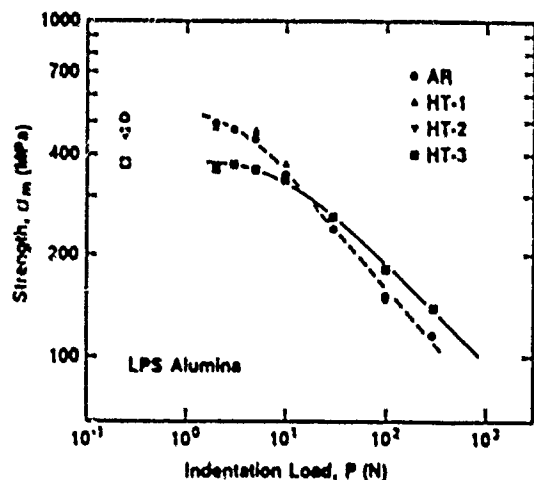| Material	Anneal temp. (°C)	Time (h)	Grain size (μm)	Density (Mg·m⁻³)	Second phase*
As-received			4.2	3.61	A/C
HT-1	1600	8	4.8	3.63	A
HT-2	1600	8	4.8	3.64	C
	1200	48			
HT-3	1600	196	24.2	3.60	A

*A is amorphous and C is crystalline

Fig. 1. Results of the indentation–strength tests for alumina specimens subjected to the heat treatments in Table I. Open symbols at left represent strength values for specimens that broke from natural flaws. Curves through data are fits to as-received (dashed line) and HT-3 (solid line) materials; note data for HT-1 and HT-2 materials are indistinguishable from those of the as-received.

aluminas, inert strength, σ_m, versus indentation load, P. Each point on the plot represents the mean of at least 10 specimens per load. The standard deviation for each point is ≈11%. (Error bars are omitted from the plot for clarity.) From the fracture-mechanics analyses based on a crack-interface bridging model,[16-18] the flattening of the response may be interpreted as an enhancement of the R-curve characteristic. The curves through the data in the figure are best fits to the as-received (dashed line) and HT-3 (solid line) materials, respectively, from such analyses. The results in Fig. 1, in conjunction with

the microstructural characteristics illustrated in the SEM photograph in Fig. 2, enable us to deduce the effect of the heat treatments on the mechanical behavior.

The as-received material has a grain size of ≈4 μm, as shown in Fig. 2(A). The individual grains are surrounded by a continuous second phase, which is partially crystalline in form. All the classical features of a LPS material, such as wetting of grains, pockets of amorphous phase, and facetted grain structures, are evident. Microanalysis indicates that the intergranular phase consists primarily of silicates of calcia, magnesia, and alumina.

Note from the dashed line in Fig. 1 that the $\sigma_m(P)$ response of this control material deviates only slightly from the $P^{-1/3}$ dependence appropriate to a single-valued toughness; i.e., the R-curve characteristic for this particular material is not pronounced.

Examine now the effects of changing only the degree of crystallinity of the intergranular phase on the mechanical behavior by referring to the data for the HT-1 and HT-2 materials. Analysis by TEM shows that the intergranular phases in these two materials are, respectively, completely amorphous and predominantly crystalline. However, the $\sigma_m(P)$ data points for HT-1 and HT-2 in Fig. 1 are virtually indistinguishable from the dashed-line fit for the as-received material. Thus, in these two cases, the effect of heat treatment on the R curve is insignificant.

The effect of increased grain size, on the other hand, is significant, as seen from the solid line fit for the HT-3 material in Fig. 1. The scale-up in grain size, from ≈4 to ≈24 μm, is readily apparent from a comparison of the morphology for this material in Fig. 2(B) with the corresponding morphology for the as-received material in Fig. 2(A). The HT-3 material shows reduced strength at small indentation loads, with a distinctive plateau in the $\sigma_m(P)$ response in this region, and a countervailing increase in strength at large indentation loads. This third heat treatment has led to a noticeably stronger R-curve behavior.

DISCUSSION

The above results lead us to an important conclusion: *the toughness properties of ceramic materials can be modified by simple heat treatments.* For the alumina material studied here, the most significant modifications were achieved by a treatment that coarsened the microstructure (although the possiblility of a contributing effect resulting from some subtle change in the grain-boundary toughness cannot be entirely discounted). More generally, this means that one may be able to adjust properties of as-received ceramic components before placement in service. In the present case, the desirable feature of flaw tolerance is obtained at the expense of a decreased strength in the region of small crack sizes (balanced somewhat by an increased strength at large crack sizes). An enhanced R-curve characteristic may not, however, always be beneficial, e.g., in applications in which maximum resistance to microfracture-controlled wear and erosion is a premium requirement.[12] We need also be aware that the toughness properties of ceramic components exposed to thermal cycles may change, for better or for worse (again, depending on the application), during service.

It is interesting to consider the findings here in the context of the previous studies,[1-4] where no attempt was made to
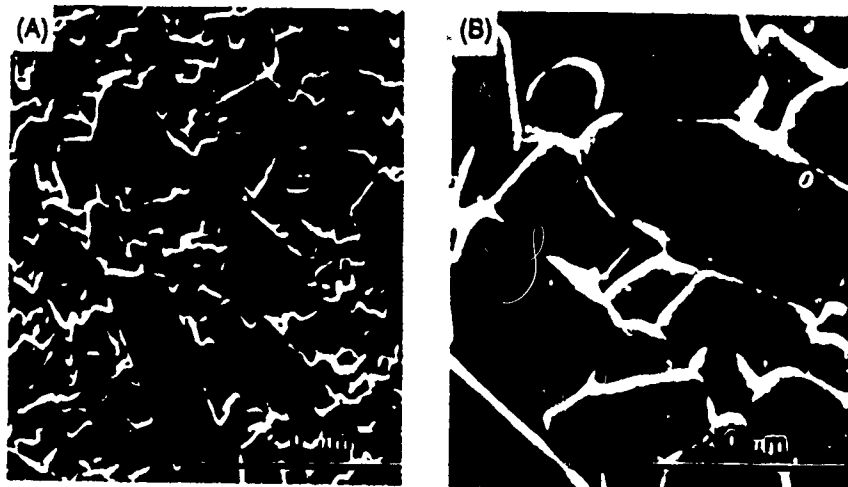

Fig. 2. S.E.M. photographs of a liquid-phase-sintered alumina for (A) as-received material and (B) following heat treatment HT-3 designed to increase the grain size. These specimens were first polished, then thermally etched at 1500°C for 1 h in air to reveal grain structure. (Pockets of intergranular phase were removed by this preparation.) Note the sixfold increase in grain size in the latter material. Faceting of alumina grains is apparent in both micrographs.

define the operative region of crack size. Note that if our materials were to have been tested at a single, intermediate crack size, corresponding to an indentation load of ≈10 N, the change in R curve for HT-3 would have passed unnoticed. Alternatively, tests by two sets of experimenters operating at extremes of large and small crack sizes would have lead to totally opposite conclusions. The danger of toughness evaluations at a single crack size is that any such perceived improvement (or, indeed, degradation) may all too easily be misconstrued as universal.

This still leaves unanswered the question of the role of the heat treatment in relation to the underlying mechanism of the R curve. We alluded in the previous section to toughening by bridging.[16-18] In this interpretation the increased crack resistance arising from the scale up of grain size may be attributed to an enhancement of frictional tractions associated with pullout of grains bridging the interfacial walls in the wake of the crack tip. Residual stresses arising from thermal expansion mismatch[1-4] could play an important role in augmenting these frictional tractions by "clamping" the bridging grains into the alumina "matrix". A detailed description of this residual stress-induced friction process will be presented elsewhere.[19] It

seems that, contrary to earlier suggestions,[11] the degree of crystallinity is not necessarily the principal factor in determining the influence of such residual stresses on the R curve, at least in the type of LPS aluminas studied here.

ACKNOWLEDGMENTS

REFERENCES

[1]N. A. Travitzky, D. G. Brandon, and E. Y. Gutmanas, "Toughening of Commercial 85 wt% Al₂O₃ Controlled Heat Treatments," *Mater. Sci. Eng.*, 71, 65–70 (1985).

[2]Y. Yeshurun, Z. Rosenburg, D. G. Brandon, and N. A. Travitzki, "Effect of Heat Treatment on the Dynamic Response of Commercial 85 wt% Al₂O₃," *Mater. Sci. Eng.*, 71, 71–75 (1985).

[3]N. A. Travitzky, D. G. Brandon, and E. Y. Gutmanas, "Effect of Rapid Cooling on the Microstructure and Mechanical Properties of Commercial 85 wt% Al₂O₃," *Mater. Sci. Eng.*, 71, 77–86 (1985).

[4]W. A. Zdaniewski and H. P. Kirchner, "Toughening of a Sintered Alumina by Crystallization of the Grain-Boundary Phase," *Adv. Ceram. Mater.*, 1 [1] 99–103 (1986).

[5]R. F. Cook, B. R. Lawn, and C. J. Fairbanks, "Microstructure-Strength Properties in Ceramics: I. Effect of Crack Size on Toughness," *J. Am. Ceram. Soc.*, 68 [11] 604–15 (1985).

[6]R. F. Cook, B. R. Lawn, and C. J. Fairbanks, "Microstructure-Strength Properties in Ceramics: II. Fatigue Relations," *J. Am. Ceram. Soc.*, 68 [11] 616–23 (1985).

[7]R. F. Cook, "Strength Characteristics of Ceramics Using Controlled Indentation Flaws"; Ph.D. Dissertation. Department of Applied Physics, University of New South Wales, Australia, 1985.

[8]R. Knehans and R. Steinbrech, "Memory Effect of Crack Resistance During Slow Crack Growth in Notched Al₂O₃ Bend Specimens," *J. Mater. Sci. Lett.*, 1 [8] 327–29 (1982).

[9]R. Steinbrech, R. Knehans, and W. Schaarwächter, "Increase of Crack Resistance During Slow Crack Growth in Al₂O₃ Bend Specimens," *J. Mater. Sci.*, 18 [10] 265–70 (1983).

[10]M. V. Swain, "R-Curve Behavior in a Polycrystalline Alumina Material," *J. Mater. Sci. Lett.*, 5 [12] 1313–15 (1986).

[11]R. F. Cook and D. R. Clarke, "Fracture Stability, R-Curves and Strength Variability," *Acta Metall.*, 36 [3] 555–62 (1988).

[12]D. B. Marshall, B. R. Lawn, and R. F. Cook, "Microstructural Effects on Grinding of Alumina and Glass-Ceramics," *J. Am. Ceram. Soc.*, 70 [6] C-139–C-140 (1987).

[13]J. C. Wurst and J. A. Nelson, "Lineal Intercept Technique for Measuring Grain Size in Two-Phase Polycrystalline Ceramics," *J. Am. Ceram. Soc.*, 55 [2] 109 (1972).

[14]D. B. Marshall, "An Improved Biaxial Flexure Test for Ceramics," *Am. Ceram. Soc. Bull.*, 59 [5] 551–53 (1980).

[15]R. J. Roark, Formulas for Stress and Strain, 4th ed.; Ch. 7. McGraw-Hill, New York, 1965.

[16]Y. W. Mai and B. R. Lawn, "Crack-Interface Grain Bridging as a Fracture Resistance Mechanism in Ceramics: II. Theoretical Fracture Mechanics Model," *J. Am. Ceram. Soc.*, 70 [4] 289–94 (1987).

[17]R. F. Cook, C. J. Fairbanks, B. R. Lawn, and Y. W. Mai, "Crack Resistance by Interfacial Bridging: Its Role in Determining Strength Characteristics," *J. Mater. Res.*, 2 [3] 345–56 (1987).

[18]P. L. Swanson, C. J. Fairbanks, B. R. Lawn, Y. W. Mai, and B. J. Hockey, "Crack-Interface Grain Bridging as a Fracture Resistance Mechanism in Ceramics: I. Experimental Study on Alumina," *J. Am. Ceram. Soc.*, 70 [4] 279–89 (1987).

[19]B. R. Lawn and S. J. Bennison; unpublished work.   □

10. "Flaw Tolerance in Ceramics With Rising Crack-Resistance Characteristics"

    S.J. Bennison and B.R. Lawn

    J. Mater. Sci. $\underline{24}$ 3169 (1989).

Flaw tolerance in ceramics with rising crack resistance characteristics

STEPHEN J. BENNISON*, BRIAN R. LAWN
Ceramics Division, National Institute of Standards and Technology, Gaithersburg, Maryland 20899, USA

The stabilizing influence of increasing toughness with crack size associated with a cumulative closure-stress process (R-curve, or T-curve) on the strength properties of brittle ceramic materials is analysed. Three strength-controlling flaw types are examined in quantitative detail: microcracks with closure-stress history through both the initial formation and the extension in subsequent strength testing; microcracks with closure stresses active only during the subsequent extension; spherical pores. Using a polycrystalline alumina with pronounced T-curve behaviour as a case study, it is demonstrated that the strength is insensitive to a greater or lesser extent on the initial size of the flaw, i.e. the material exhibits the quality of "flaw tolerance". This insensitivity is particularly striking for the flaws with full closure-stress history, with virtually total independence on initial size up to some 100 μm; for the flaws with only post-evolutionary exposure to the closure elements the effect is less dramatic, but the strength characteristics are nevertheless significantly more insensitive to initial flaw size than their counterparts for materials with single-value toughnesses. The implications of these results to engineering design methodologies, as expressed in conventional R-curve constructions, and to processing strategies for tailoring materials with optimal crack resistance properties, are discussed.

1. Introduction

The mechanical characterization of ceramics continues to be based in large part on the traditional notion of a single-valued crack resistance R, (or toughness, T)'. An explicit prediction of any theory of strength based on invariant R is that failure should occur spontaneously from some pre-existent ("Griffith") flaw when a critical applied stress is reached, such that the strength varies inversely with the flaw size. This prediction is the cornerstone of nearly all non-destructive evaluation of structural ceramics. It has resulted in a strong movement toward a processing philosophy of flaw elimination [1–5], in which systematic efforts are made to remove all potentially severe flaws. It is, therefore, not difficult to understand why "flaw sensitivity" has remained the most pervasive concept in the entire theory of the strength of ceramics.

The recent realization that many ceramics display an increasing resistance with continued crack extension [6], so-called R-curve (or T-curve) behaviour, requires that this philosophy be re-examined. Materials with significant R-curves do not fail spontaneously: rather, the critical flaw first grows stably, often over a considerable distance, before failure ensues [6–12]. This enhanced stability imparts a certain "flaw tolerance" to the material, because it is the final, not the initial, size that determines the instability. Such tolerance is of great benefit to the structural designer, because of a tendency to increased reliability (increased Weibull modulus [13, 14]) coupled with a reduced sensitivity to subsequent damage in service [7]. It also offers the attractive prospect of early detection by non-destructive evaluation [11]. Most importantly, perhaps, it reduces the onus on the ceramics processor to fabricate full-density and defect-free materials.

One of the most useful methodologies for examining the influence of R-curve behaviour in the context of flaw instability is that of indentation-strength testing, where the strength, q_m, is determined as a function of indentation load, P [7, 11, 12]. The R-curve is manifest as a deviation of σ_m from the classical $P^{-1/3}$ dependency for materials with fixed toughness to a distinctive plateau at low indentation loads. By deconvoluting the $\sigma_m(P)$ data set, the R-curve can be extracted [12]. For materials with strong R-curve characteristics the low-load plateau often appears to correspond to the strength for failure from processing defects [7]. Despite this demonstrated correspondence there is a widespread perception in the ceramics fracture mechanics community that indentation flaws, by virtue of their

"artificial" origin, cannot be representative of the natural flaw population; and, therefore, that the latter are not subject to the stabilizing influence of the R-curve.

In this paper we examine the effect of R-curve characteristics on the strength response for some well-defined natural flaw types: sharp microcracks of some grain-facet dimensions with a full R-curve history; the same but without any R-curve history prior to extension; relatively large-scale processing pores. We use indentation-strength data on a specific coarse-grained alumina to establish the toughness characteristics, and invoke a basic R-curve instability condition to determine the variation of strength with initial flaw size for the various flaw types in this same material. The R-curve mechanism in our selected material is identifiable as grain-localized bridging behind the crack tip [9-12, 15]; however, our statements concerning the mechanics of flaw response will be of a general nature. It will be shown that the natural flaw types do indeed exhibit the same kind of tolerance as their artificial indentation counterparts. In arriving at this conclusion we shall dwell on some of the pitfalls that can arise from widely used R-curve constructions that represent the flaw size as a negative intercept of the applied loading function on the crack-size coordinate.

2. Fracture mechanics for flaws in materials with T-curve characteristics

2.1. General conditions for crack equilibrium and stability

We begin by defining a general net stress intensity factor, K, for a uniformly stressed equilibrium crack in a material with R-curve characteristics [6]. We write it as the sum of two terms, an external uniform applied stress term, K_a, and an internal microstructure-associated closure stress term, K_μ

$$K(c) = K_a(c) + K_\mu(c) = T_0 \qquad (1a)$$

where T_0 is an intrinsic toughness, and c is the crack length. Or, alternatively,

$$K_a(c) = T_0 + T_\mu(c) = T(c) \qquad (1b)$$

where $T_\mu = -K_\mu$ may be regarded as a positive contribution to the toughness. With this definition of a net toughness, T (the stress intensity equivalent, $K_c = T$, of the resistance term associated with the mechanical energy release rate, $G_r = R$), we adopt the term "T-curve" to describe the size-dependent resistance characteristic.

Consider now the condition for instability [6]. For $T_0 =$ constant we require the condition

$$dK/dc \geq 0 \qquad (2a)$$

to be satisfied in Equation 1a, or, equivalently,

$$dK_a/dc \geq dT/dc \qquad (2b)$$

in Equation 1b. This latter is the tangency condition in the familiar R-curve construction.

We now consider the micromechanics of failure for three different flaw types in a material with T-curve due to grain-localized bridging at the crack interface,
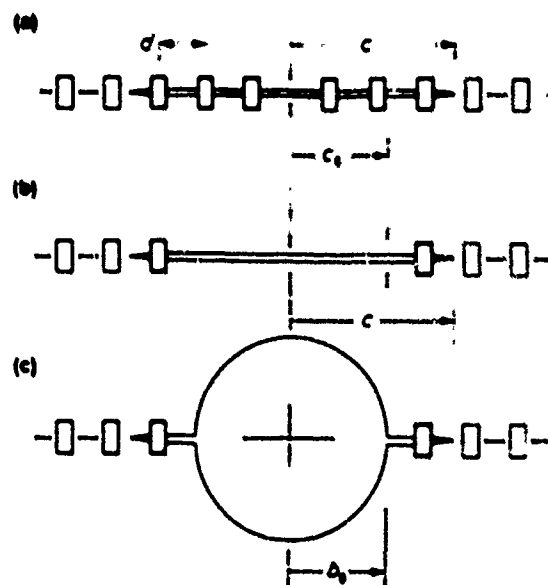
Figure 1 Schematic drawing of flaw types considered in this study: (a) microcracks with full T-curve history, i.e. subject to bridging in initial evolution to $c = c_0$ as well as in subsequent extension at $c > c_0$; (b) microcracks without any T-curve history in evolution to $c = c_0$ prior to extension, but subject to T-curve in subsequent extension $c > c_0$; (c) pores subject to T-curve in extension $c > b$. Squares represent bridging grains, mean separation d; shaded squares are activated bridges; open squares are potential bridges.

a mechanism identified as pertinent to a wide range of non-transforming ceramics [9, 15].

2.2. Microcracks with full T-curve history

Consider first a sharp-crack flaw whose inception and subsequent evolution takes place entirely in the interfacial closure-stress field responsible for the T-curve, Fig. 1a. This might be expected to be a most common state for microcracks with histories unfavourable to the relaxation or destruction of the attendant bridging elements: e.g. flaws developed during the final stages of, or even after, processing. We seek to characterize the response of this flaw type in a subsequent strength test, and thence to determine the dependence of the strength on the "initial" (pre-test) microcrack size, c_0.

Start with the applied stress term, K_a. For a flaw normal to the applied tensile stress this term has the familiar dependence on the crack size, c [6]

$$K_a(c) = \psi \sigma_a c^{1/2} \qquad (c \geq c_0) \qquad (3)$$

where ψ is a geometrical constant ($= 2 \cdot \pi^{1/2}$ for penny cracks).

The K_μ term is derived from the mechanics of crack-interface bridging for penny-shaped cracks [12]. As the crack begins to extend from the initial flaw, bridging elements are activated over the entire area of the crack beyond intersection with the first bridge at $c = d$, i.e. over most of the initial, as well as all of the subsequent area regardless of the value of c_0. The attendant restraint stabilizes the crack growth. The build-up of interfacial surface traction prevails until, at a crack size $c = c_a$, the bridges furthermost behind the advancing tip begin to rupture, at which the bridge configuration translates with the tip in steady state. Derivation of the K_μ term thereby involves integration of the underlying (continuum approximation)

stress-separation function for the bridging elements within $d \leqslant c \leqslant c_{\bullet}$ [10]. Because this bridging term is negative, we adopt the T_{μ} notation of Equation 1b, thus [12]

$$T_{\mu}(c) = 0, \quad (c < d) \qquad (4a)$$

$$T_{\mu}(c) = (T_{\prime} - T_{0})$$
$$\times \{1 - \{1 - [c_{\bullet}(c^{2} - d^{2})/c(c_{\bullet}^{2} - d^{2})]^{1/2}\}^{3}\},$$
$$(d < c < c_{\bullet}) \qquad (4b)$$

$$T_{\mu}(c) = T_{\prime} - T_{0}, \quad (c > c_{\bullet}) \qquad (4c)$$

with $T_{\prime}$ the steady-state value of T.

Let us emphasize that the derivation of this particular relation, or even the identification of bridging as the particular T-curve mechanism, are not issues here; we use Equation 4 only as a formula for representing the experimentally determined results for our chosen alumina test material. Any other analytical expression that fits the T-curve data would serve equally well to demonstrate the tolerance factor in the strength characteristics.

2.3. Microcracks without full T-curve history

Now consider our second microcrack-type flaw, of the same initial size, c_0, but without any (pre-test) history of interfacial bridging, Fig. 1b. Such could be the case if bridges were never to be given the chance to form in the first place (e.g. flaws associated with incomplete densification at an early stage of sintering, grain-boundary triple points), or if any post-fabrication mechanical, thermal or chemical interaction were to destroy existing (i.e. post-evolutionary) bridges.

The applied stress term, $K_{a}(c)$, is identical to that of Equation 3. However, the microstructure-associated $T_{\mu}(c)$ term differs slightly from Equation 4, by virtue of the fact that the bridging stresses are operative only over the area of the extended (not the initial) crack. In this case the T-curve is displaced along the c-axis, corresponding to integration of the stress-separation function for the bridging elements between $c_0 + d \leqslant c \leqslant c_0 + c_{\bullet}$ [10]. The expressions for T_{μ} may thus be obtained by replacing d in Equation 4 with $c_0 + d$ and $c_{\bullet}$ by $c_0 + c_{\bullet}$

$$T_{\mu}(c) = 0, \quad (c < c_0 + d) \qquad (5a)$$

$$T_{\mu}(c) = (T_{\prime} - T_{0})\{1 - (1 - \{[(c_0 + c_{\bullet})$$
$$\times [c^{2} - (c_0 + d)^{2}]\}/c[(c_0 + c_{\bullet})^{2} - (c_0 + d)^{2}]^{1/2})^{3}\},$$
$$(c_0 + d < c < c_0 + c_{\bullet}) \qquad (5b)$$

$$T_{\mu}(c) = T_{\prime} - T_{0}, \quad (c > c_0 + c_{\bullet}) \qquad (5c)$$

which now explicitly involves flaw size, c_0. We emphasize here that this T-curve displacement is not equivalent to a simple shift in origin along the c-axis; i.e. the function $T_{\mu}(\Delta c)$, where $\Delta c = c - c_0$, is not invariant.

2.4. Crack extension from pores

For our third flaw type, consider a spherical pore of radius h_0, from which annular microcracks extend on a diametral plane normal to the subsequently applied tensile field, Fig. 1c. The terminology h_0 is adopted here to distinguish this kind of defect from a sharp

crack (designation unchecked by some). Pores are the most common flaw type known of processing in which full density is not realised.

The applied stress term for the pore is no longer of the simple form given in Equation 3. Note that the true crack size in this case is not c but $c - h_0$. The consequent reduction in effectiveness of the pore as a strength-degrading flaw is negated somewhat by a stress-concentrating capacity. Accordingly, $K_{a}(c)$ is modified as follows

$$K_{a}(c) = \psi \sigma_{a}(c - h_0)^{1/2}/f(h_0, c) \quad (c \geqslant h_0) \quad (6)$$

where the modifying function $f(h_0, c)$ is [16] (neglecting free surface effects at $c = h_0$)

$$f(h_0, c) = (1 + h_0/c)^{1/2}\{1 + (1.2)(h_0/c)^{2}$$
$$+ [3/(7 - 5v)](h_0/c)^{3}\}.$$
$$(c \geqslant h_0) \qquad (7)$$

with v Poisson's ratio. Note that at $c \gg h_0$, $f \to 1$, as required for Equation 7 to restore to Equation 3. As c decreases toward h_0, on the other hand, f becomes increasingly greater than unity, indicative of the stress-concentration effect. Again, there are more sophisticated expressions for $f(c/h_0)$, but the numerical accuracy of Equation 7 is not central to our argument.

For the microstructure-associated $K_{a}(c)$ term we may retain Equation 5 above as for microcracks without T-curve history, but with h_0 replacing c_0 (again in the approximation of negligible free surface effects at $c = h_0$)

$$T_{\mu}(c) = 0, \quad (c < h_0 + d) \qquad (8a)$$

$$T_{\mu}(c) = (T_{\prime} - T_{0})\{1 - (1 - \{[(h_0 + c_{\bullet})$$
$$\times [c^{2} - (h_0 + d)^{2}]\}/c[(h_0 + c_{\bullet})^{2} - (h_0 + d)^{2}]^{1/2})^{3}\}.$$
$$(h_0 + d < c < h_0 + c_{\bullet}) \qquad (8b)$$

$$T_{\mu}(c) = T_{x} - T_{0}, \quad (c > h_0 + c_{\bullet}) \qquad (8c)$$

so that initial flaw size is again a factor. Again, we note that the function $T_{\mu}(\Delta c)$, where $\Delta c = c - h_0$, is not invariant.

3. Calculation of strength – flaw-size relations: case study on a polycrystalline alumina

3.1. A model alumina material

Let us now investigate the above formulations for an alumina with relatively pronounced T-curve (R-curve) characteristics associated with the bridging mechanism. The appropriate parameters needed in order to specify T_{μ} in Equation 3 for this material have been evaluated from the indentation-strength, $\sigma_{m}(P)$, data shown in Fig. 2 [12]. We note the distinct plateau in these data, indicative of the strong T-curve influence referred to earlier. This plateau corresponds closely to the strength level for breaks from natural flaws (including unindented specimens, and indented specimens whose failures did not originate at the contact site). The material is polycrystalline with an average grain size 20 μm (Vistal grade, grain size 20 μm, <0.1% impurity, Coors Ceramics Co., Colorado). It has a strong tendency to intergranular
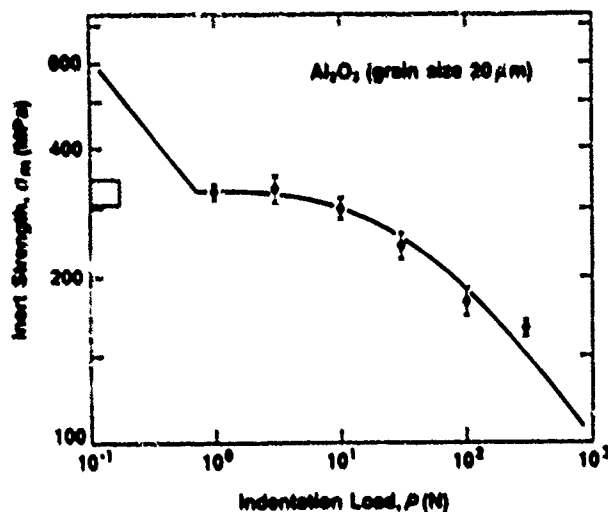
Figure 2 Indentation-strength data for polycrystalline alumina (from [7]). Data points are means and standard deviations fo breaks at indentation flaws formed at different loads. Hatched are at left is strength for breaks from natural flaws. Curve through data is fit used to deconvolute T-curve.

fracture [7], so that the intrinsic toughness, T_0, identifies with the grain-boundary fracture resistance. The specimens were broken in their as-fired state, so that extrinsic machining or polishing flaws might be avoided. However, they contain some readily observable processing defects, microcracks up to 50 μm long ($\approx$ 2 to 3 grain facet lengths) and occasional large pores up to 100 μm radius, examples of which are shown in Fig. 3. These defects have been identified as the failure sites for breaks of unindented specimens (or, at low contact loads, of some indented specimens).

Accordingly, we plot the applied stress $K_a(c)$ function and equilibrium $T(c)$ function of Equation 1b for the three flaw types, in Figs 4 to 6. The crack coordinate is plotted as $c^{1/2}$ in these figures so that $K_a(c)$ for the microcrack-type flaws might be represented in the usual way as straight lines with slope proportional to applied stress. The T-curves have the same form for each of the different flaw types, with lateral displacements along the abscissa depending on the effective initial flaw size. The range in c over which the T-curve rises for this alumina may be taken as a measure of the

large zone lengths ($c - d$) over which the stabilizing effect of the restraining forces can be realized in nontransforming ceramics.

3.2. Microcracks: full T-curve history
Consider first the T-curve construction for microcrack-like flaws with full T-curve history, Fig. 4. In this case the $T(c)$ function, Equation 4, is independent of initial flaw size, c_0. The actual critical condition for failure, Equation 2b, corresponding to the tangency condition $\sigma_a = \sigma_m = \sigma_1$ in the diagram, also shows an independence on c_0, but only within the size range $c_0' \leqslant c_0 \leqslant c_0''$. For the particular value of c_0 illustrated the flaw first "pops in" unstably to the intersection point along the "loading line" at $\sigma_a = \sigma_2$ on the rising branch of the T-curve, and thereafter grows stably up the curve until the critical unstable configuration $c = c_m = c_0''$ is reached at $\sigma_a = \sigma_m^p = \sigma_1$ (superscript P denoting plateau value). This may be regarded as an "activated" instability. For $c_0 < c_0'$ the instability condition $\sigma_a = \sigma_m$ occurs at a higher applied stress level, e.g. σ_2; conversely, for $c_0 > c_0''$ at lower σ_a, e.g. σ_2 or (for very large c_0) σ_1. In these latter cases the instability is "spontaneous". With such a construction we can determine (at least numerically) the functional dependence of σ_m on c_0 over as wide a range of flaw size as we please.

3.3. Microcracks: no previous T-curve history
Consider next the construction for the same microcrack-like flaws, but without T-curve history. As indicated above, the influence of initial flaw size c_0 is now manifest as a shift in the $T(c)$ function, Equation 5, along the c-axis, without any effect on the $K_a(c)$ function. We plot $T(c)$ for $c_0 = 0$ (i.e. equivalent to flaw with full T-curve history, Equation 4), 50 μm (corresponding to the approximate microcrack size actually observed, Section 3.1) and 500 μm (an extreme value approaching "macroscopic" crack dimensions) in Fig. 5. We include $K_a(c)$ loading lines only at the tangency configurations. Note now that even within the flaw size range $c_0' \leqslant c_0 \leqslant c_0''$ (a condition always well satisfied for the 50 and 500 μm flaws represented in Fig. 5) this tangency configuration is not independent
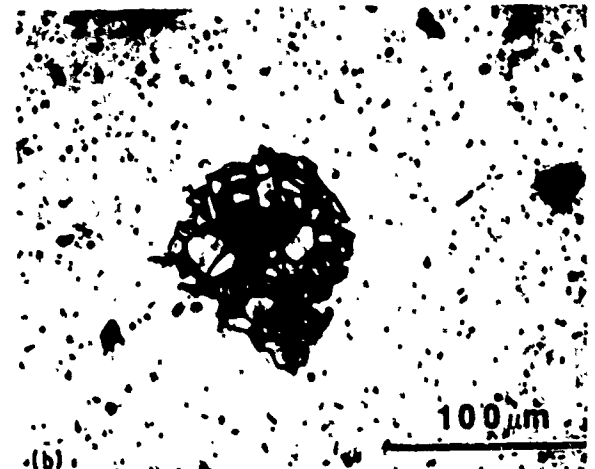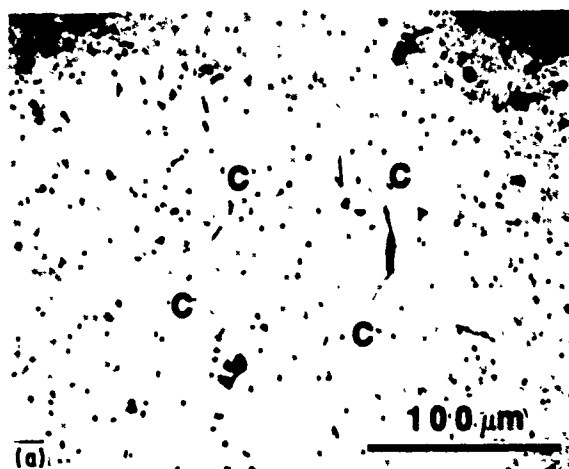

Figure 3 Micrographs of processing flaws in the same alumina as represented in Fig 2 (a) microcracks (C), (b) large pore. Optical transmitted light.
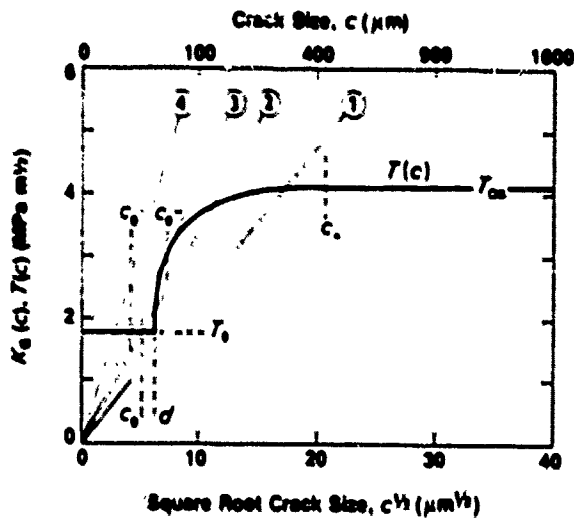
Figure 4 T-curve construction for alumina material in Fig. 2: microcrack flaws with full T-curve history. Lines 1, 2, 3, 4 correspond to increasing a_m in $K_a(c)$ function, Equation 3. $T(c)$ function from Equation 4 using parameters evaluated from Fig. 2 ($T_0 = 1.73$ MPa m$^{1/2}$, $T_\infty = 4.08$ MPa m$^{1/2}$, $d = 40\,\mu$m, $c_m = 420\,\mu$m [12]). Tangency condition at curve 2 defines strength $\sigma_s = c_m = 305$ MPa for flaws with initial size in range $c_0 \leqslant c_a \leqslant c_0''$

of c_a: i.e. the slope of the $K_a(c)$ line, which determines $\sigma_s = \sigma_m$, differs from curve to curve. Nevertheless, not only is the failure still activated, but the stable growth stage prior to final instability is actually enhanced (the tangency point lies further up the T-curve at the two larger values of c_a). Accordingly, the tolerance characteristic imparted by the T-curve will be far from lost, especially where the range of the T-curve greatly exceeds the range of flaw sizes, as is the case for our material in Fig. 5. Again, it is a straightforward matter to determine the functional dependence of σ_m on c_a from this construction.

3.4. Pores

Finally, consider the construction for the pore-like flaws. Now both the $T(c)$ function, Equation 8, and the $K_a(c)$ function, Equations 6 and 7, are dependent on the initial flaw size, h_a. We plot these two functions

for $h_a = 50$ and $500\,\mu$m in Fig. 6 (cf. flaw sizes in Section 3.3); for $K_a(c)$ we include plots for equivalent cracks, $h_a = c_a$ in Equation 3, as the dashed lines. The modifying effect of the effective reduction in crack length (from c to $c - h_a$) associated with the pore is apparent as a pronounced deviation below a linear $K_a(c)$ plot, with cut-off at small crack extensions. However, the stabilizing effect of the T-curve is sufficiently strong that this modification has little noticeable influence on the tangency condition, except at unusually large pore sizes (such as the $500\,\mu$m pore in Fig. 6). Again, the tangency configuration depends on the size of the history-dependent flaw. Note that for this tangency condition to represent the strength configuration it is necessary only that the pore should be circumscribed by a pre-existent annular starter crack, Δc, a few micrometres in dimension (i.e. considerably less than a grain facet length in our material), such that the requirement $c_0' \leqslant h_a + \Delta c \leqslant c_0''$ (cf. Fig. 4) is

Figure 6 As for Fig. 5, but for pores of sizes $h_a = 50$ and $500\,\mu$m. $T(c)$ curves from Equation 8, $K_a(c)$ curves from Equations 6 and 7. Note deviation of $K_a(c)$ below $c^{1/2}$ dependence (dashed lines) at small c, with zero cut-off at $c = h_a$. (Note also that T and K_a crack functions are definable only at $c \geqslant h_a$ for this defect.)
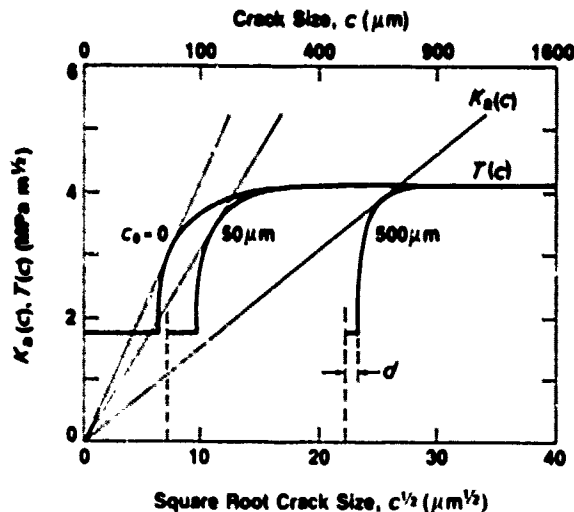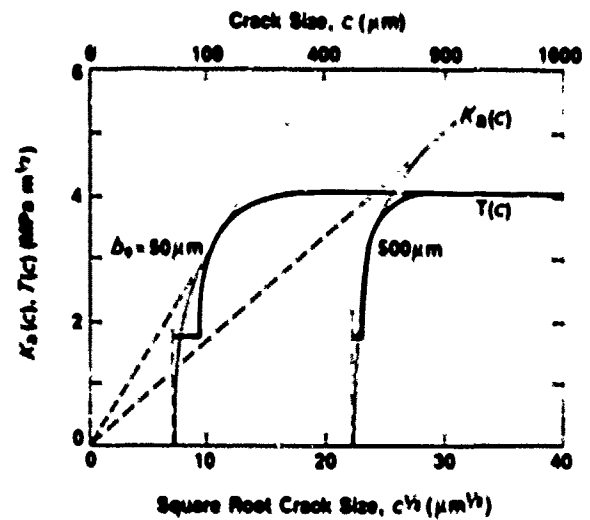

Figure 5 As for Fig. 4, but for microcrack flaws without T-curve history over initial evolution length, c_a. $T(c)$ curves correspond to $c_0 = 0$ reference curve from Fig. 4), 50 and 500 μm in Equation 5. $K_a(c)$ lines are for tangency condition at each T-curve.
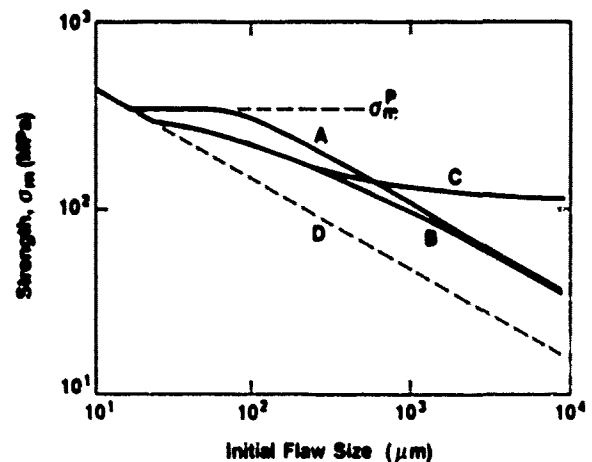

Figure 7 Predicted strength plotted against initial flaw size c_a, for microcracks, h_a, for pores) for alumina material in Fig. 2. A, microcracks with full T-curve history. B, microcracks with T-curve influence only after extension form c. C, pores with T-curve influence after extension from h_a. D, microcracks with no influence of T-curve at any stage of growth. Note well-defined plateau level at σ_m^p is fully achieved only by flaw A.

satisfied. In the interest of conservative design we deal with this "worst case" in Section 3.5 below.

3.5. Strength data

Fig. 7 is the resultant plot of the strength against initial flaw size (c_i, or b_i, whichever is appropriate) for the three flaw types discussed above, indicated as curves A, B and C, respectively. It is evident that the stabilizing influence of the T-curve has produced significant flaw tolerance over the size range 10 to 100 μm (encompassing the range observed in our alumina material, Section 3.1), even if somewhat less pronounced in B and C where bridging is not operative over the initial length. To put these results in perspective, we may compare with the strength characteristics for a hypothetical ceramic with the same material constants as our alumina but without T-curve influence over any of the crack area, extended as well as initial: these characteristics are obtained here by repeating the calculations for sharp microcracks at $T_\mu = 0$ (i.e. with a toughness $T = T_0$) and are plotted as curve D in Fig. 7.

4. Discussion

It has been shown that different flaw types in materials with pronounced T-curve (R-curve) characteristics exhibit the quality of "tolerance" in their associated strength behaviour, to a greater or lesser extent depending on history and geometry. The greatest effect is predicted for those flaws that experience enhanced resistance over their entire area, initial as well as extended. A smaller, but by no means insignificant, effect is predicted for those flaws that experience resistance over only their extended area. This latter point runs counter to traditional thought in the ceramics community where it is presumed that certain flaws, particularly processing defects, are inevitably susceptible to spontaneous failure from their initial configuration. Our results would suggest that in such T-curve materials as the alumina represented in Fig. 7, the improvements in strength gained by eliminating processing flaws much smaller than 100 μm (corresponding to a few bridge spacings) are likely to be minimal.

We have considered just one material (polycrystalline alumina), and just one mechanism (bridging), but the conclusions carry over to any material and any mechanism. It is the form, not the origin, of the T-curve that determines the scale of the effect. (We have recently refined the detailed form of the T-curve for bridging materials given in Equation 4, but these refinements in no way change the substance of our conclusions here.) Note that there are two features of the T-curve that need to be maximized for optimum tolerance, the magnitude $T_\ast - T_\mu$, and the range $c_\ast - d$. For the alumina considered here the magnitude is modest, $T_\ast / T_\mu \approx 2$ to 3, but the range is relatively large, $c_\ast / d \approx 10$ (i.e. some tens of grain diameters). It is interesting to reflect that whereas most theoretical treatments of T-curve behaviour focus almost exclusively on the former, it is the latter that is the key contributing factor to the tolerance in our material, by virtue of its controlling influence on

the scale of the flaw insensitivity range $c_\ast - d$, (Fig. 4). Thus whereas many materials processors seek to optimize only the magnitude $T_\ast - T_\mu$, it is apparent that the range $c_\ast - d$ may be at least as important.

The type of construction depicted in Figs 4 to 6 is just one of several possible ways [6] of representing the T-curve influence on flaw mechanics. One commonly used, alternative construction warrants special mention, because of an unwitting tendency for workers in the ceramics field to regard its scope of application as universal. We refer to the construction in which both T and $K_\ast$ are plotted as a function of crack extension, $\Delta c = c - c_0$ (or, for pores, $\Delta c = c - b_0$), instead of absolute crack size, c [17]. In that scheme a change in flaw size is represented as a shift in the intercept of the $K_\ast(\Delta c)$ load line along the negative Δc coordinate, with an invariant T- or R-curve fixed at some origin along the abscissa. Such a construction might at first sight appear to be equivalent to that shown in Fig. 5 (and 6) for defects without T-curve history over their initial area: there we simply displaced the origin of T instead of $K_\ast$. However, we recall from Sections 2.3 (and 2.4) that the function $T(\Delta c)$ (inserting $c = \Delta c + c_0$ in Equation 5, or $c = \Delta c + b_0$ in Equation 8) is not invariant with c_0 (or b_0): i.e. the shape of the T-curve depends on the initial flaw size. The alternative construction is even more inapplicable to flaws with full T-curve history, such as the microcrack system in Fig. 4, where the relative locations of the T and $K_\ast$ origins are fixed regardless of c_0. For this last flaw type, constructions that shift the relative $K_\ast$ origin will inevitably lead to a significant underestimate of the tolerance level (e.g. will predict a curve closer to B than to A in Fig. 7). It is clear that considerable care needs to be exercised in drawing conclusions regarding strength characteristics from the traditional R-curve representations.

We have seen that the tolerance properties of a material with T-curve behaviour depend strongly on the flaw type. This dependence may be usefully explored in the indentation-strength test, by examining the data set in the low-load region. Thus we note for our alumina material in Fig. 2 that the $\sigma_m(P)$ data tend asymptotically to the strength level for breaks from natural flaws; and, moreover, that this level itself corresponds (within experimental scatter) to the plateau value $\sigma_m^\ast$ in Fig. 7 for microcrack-type flaws with full T-curve history. We conclude that the dominant natural flaws in our alumina must have evolved within the (bridging) T-curve field, and are therefore most likely to be the grain-facet microcracks of the kind shown in Fig. 3a. There is indeed evidence from in situ observations of polished alumina surfaces that such microcracks are the most prevalent source of natural failures [7, 18]. That the $\sigma_m(P)$ plot for the indentation flaws is asymptotic to rather than coincident with the $\sigma_m^\ast$ plateau is attributable to an additional driving force, proportional to P, associated with residual contact stresses [7, 10-12]. For flaws without complete T-curve history, e.g. the pores in Fig. 3b, the attendant reduction in strength values will manifest itself as a cut-off in the $\sigma_m(P)$ plot in the low-load region. This indicates that such defects are not present in a sufficient

number of specimens to lower the mean strengths of our alumina significantly, but there are reported data for several other ceramics without strong T-curve characteristics (including aluminas) that exhibit strong cut-off behaviour [7]. It is these latter defect types that pose the greatest threat to degradation of strength properties.

In conclusion, flaw insensitivity is a natural consequence of T-curve behaviour. The degree of insensitivity depends on such matters as history and geometry. The implications concerning materials design are profound. Nowhere is this more apparent than in ceramics processing strategy. Elimination of all flaws need not be the ultimate objective of materials fabrication. In this view it might not make good sense to pursue unlimited refinement of the microstructural makeup, particularly where the elements of that particular microstructure compensate by enhancing the T-curve. Moreover, the attendant crack stabilization afforded by the rising T-curve could be turned to advantage, to provide early warning of any impending failure [11]. It is clear that future decisions in ceramics design will inevitably require a proper understanding of the underlying mechanics of the T-curve response, along with a complete characterization of the flaw types that are most likely to lead the material system to failure.

Acknowledgements

References

1. F. F. LANGE, *J. Amer. Ceram. Soc.* **66** (1983) 396.
2. F. F. LANGE and M. METCALF, *ibid.* **66** (1983) 398.
3. F. F. LANGE, H. I. DAVIS and I. A. AKSAY, *ibid.* **66** (1983) 407.
4. N. McN. ALFORD, J. D. BIRCHALL and K. KENDALL, *Nature* **330** (1987) 51.
5. K. K. VENKATACHARI and R. RAJ, *J. Amer. Ceram. Soc.* **70** (1987) 514.
6. Y. W. MAI and B. R. LAWN, *Ann. Rev. Mater. Sci.* **16** (1986) 415.
7. R. F. COOK, B. R. LAWN and C. J. FAIRBANKS, *J. Amer. Ceram. Soc.* **68** (1985) 604.
8. R. W. STEINBRECH, R. KNEHANS and W. SCHAARWÄCHTER, *J. Mater. Sci.* **18** (1983) 265.
9. P. L. SWANSON, C. J. FAIRBANKS, B. R. LAWN, Y.-W. MAI and B. J. HOCKEY, *J. Amer. Ceram. Soc.* **70** (1987) 279.
10. Y.-W. MAI and B. R. LAWN, *ibid.* **70** (1987) 289.
11. B. R. LAWN and C. J. FAIRBANKS, in "Review of Progress in Quantitative NDE", Vol. 6B, edited by D. O. Thompson and D. E. Chimenti (Plenum, New York, 1987) p. 1023.
12. R. F. COOK, C. J. FAIRBANKS, B. R. LAWN and Y.-W. MAI, *J. Mater. Res.* **2** (1987) 345.
13. K. KENDALL, N. McN. ALFORD, S. R. TAN and J. D. BIRCHALL, *ibid.* **1** (1986) 120.
14. R. F. COOK and D. R. CLARKE, *Acta Metall.* **36** (1988) 555.
15. P. W. SWANSON, in "Fractography of Glasses and Ceramics", "Advances in Ceramics", Vol. 22 (American Ceramic Society, Columbus, Ohio, 1988) Ch. 23.
16. D. K. SHETTY, A. R. ROSENFIELD and W. H. DUCKWORTH, in "Fracture Mechanics of Ceramics", Vol. 5, edited by R. C. Bradt, A. G. Evans, D. P. H. Hasselman and F. F. Lange (Plenum, New York, 1983) p. 531.
17. D. BROEK, "Elementary Engineering Fracture Mechanics" (Martinus Nijhoff, The Hague, 1983) Ch. 5.
18. R. W. STEINBRECH and O. SCHMENKEL, *J. Amer. Ceram. Soc.* **71** (1988) C-271.

11. "Role of Interfacial Grain-Bridging Sliding Friction in the Crack-Resistance and Strength Properties of Nontransforming Ceramics"

    S.J. Bennison and B.R. Lawn

    Acta Metall., in press.

Blank Pages 1

ABSTRACT

A grain-bridging model of crack-resistance or toughness (R-curve, or T-curve) properties of nontransforming ceramics is developed. A key new feature of the fracture mechanics treatment is the inclusion of internal residual (thermal expansion mismatch) stresses in the constitutive stress-separation relation for pullout of interlocking grains from an embedding matrix. These internal stresses play a controlling role in the toughness properties by determining the scale of frictional tractions at the sliding grain-matrix interface. By providing a physical account of the underlying micromechanics of the bridging process the analysis allows for predetermination of the material factors in the constitutive relation, thereby reducing parametric adjustments necessary in fitting the theoretical toughness curve to experimental data. The applicability of the model is illustrated in a case study on indentation-strength data for a "reference" polycrystalline alumina with particularly strong T-curve characteristics. From theoretical fits to these data the constitutive relation, and thence the entire T-curve, can be deconvoluted. This "parametric calibration", apart from demonstrating the plausibility of the model, allows for quantitative predictions as to how the toughness and strength characteristics of ceramics depend on such microstructural variables as grain size and shape, grain boundary energy, level of internal stress and sliding friction coefficient. An indication of this predictive capacity is provided by a preliminary calculation of the grain-size dependence of strength, using some existing data for other aluminas as a basis for comparison.

2

1. INTRODUCTION

Much recent attention has been paid to the phenomenon of a systematically increasing fracture resistance with crack extension in ceramics (R-curve, or T-curve). In nontransforming ceramics [1] the magnitude of this increase can be respectable, i.e. in excess of a factor of three, depending on the microstructure [1-12]. The range of extension over which the increase can occur is perhaps even more impressive, amounting in some instances to some hundreds of grain dimensions. The R-curve has a stabilising influence on crack growth, strikingly manifested in strength properties as a tendency to flaw insensitivity [13]: hence "flaw tolerance", a concept with especially strong appeal to those concerned with structural design.

This flaw tolerance is especially well demonstrated in indentation-strength tests [3,4,9], where Vickers indentations are used to introduce controlled starter flaws into the surfaces of strength specimens. At decreasing indentation load the strength deviates away from the (logarithmic -1/3) dependence of strength on indentation load predicted for materials with single-valued toughness, and tends instead toward a well-defined plateau. Such plateaus have been reported in a wide range of ceramic materials [3,9], indicating a certain generality in the R-curve phenomenology. Moreover, these plateaus, where they are pronounced, tend to the strengths for failures from processing defects. Thus the indentation-strength test provides R-curve information in the crack-size domain most pertinent to designers, i.e. the domain of natural flaws.

---

[1] As distinct from transforming ceramics (zirconia). The significant increases in toughening in this latter class of material are relatively well documented and understood.

There is now a weight of direct evidence demonstrating that the principal mechanism of rising crack resistance behaviour in nontransforming ceramics is grain-localised <u>bridging</u> at the crack interface <u>behind</u> the advancing tip [4,5,7,10]. In particular, it is observed that frictional tractions associated with the pullout of interlocking grains can restrain the crack opening for large distances (up to several mm in some aluminas) behind the tip, thereby accounting for the range of the R-curve. A traditional preoccupation of ceramics fracture analysts with post-mortem fractographic observations had long precluded identification of this mechanism: the very act of failure destroys the bridges. It is only recently, as a result of <u>in situ</u> crack extension observations made <u>during</u> the stressing to failure, that the bridging mechanism has become clear. Again, the mechanism appears to be common to a wide range of ceramics, especially noncubic ceramics that fail by intergranular failure.

Theoretical descriptions of the bridging mechanism are in their infancy. Mai & Lawn [13] presented a model based on a distribution of closure tractions across the crack walls. This distribution gives rise to a "microstructural" stress intensity factor, which augments the stress intensity factor associated with the applied loading. Since this microstructural stress intensity factor is negative it can be regarded as part of the toughness/crack-size function, $T(c)$; thence the R-curve (or, more strictly, T-curve). Key to the theoretical development is the specification of a constitutive stress-separation function defining the physical restraint exerted by individual bridges. In this regard the approach of Mai & Lawn was phenomenological; they recognised the need for an extensive functional "tail" to account for the large traction zone behind the crack tip, but adopted an empirical inverse

4

relation to describe it. Their empirical function contains the necessary ingredients for a macroscopic description of the failure mechanics, allowing for, among other things, a deconvolution of indentation-strength data to obtain the T-curve [9]. However, while there is some precedent in the concrete literature for tail-dominated relations [14], the empirical approach precludes a fundamental understanding of the underlying material aspects of the phenomenon. What elements of the microstructure control the restraining tractions, and how might we adjust these elements to optimise the R-curve characteristics?

In this paper we set out to answer such questions by incorporating a stress-separation function based on a specific physical mechanism of grain pullout for noncubic materials. We consider the bridging grains to be "locked" into the "matrix" on either side of the crack interface by internal thermal expansion mismatch stresses. The resistance to pullout then derives primarily from Coulomb friction at the sliding matrix-grain interface. In this sense the mechanism is analogous to that of fibre pullout in ceramic composites. Indeed, we shall borrow from established fracture mechanics descriptions for composites in our own formulations. We are led to consider internal stresses as an important factor for two reasons: first, because of an apparent diminishing of the T-curve behaviour with addition of intergranular phases in alumina ceramics, the second phase presumably acting to relax the stress buildup during the processing [3,4]: second, because the T-curve effect has been observed in noncubic, but not cubic, ferroelectric ceramics (viz. barium titanate below and above the Curie temperature [3]). We emphasise at the outset that these internal stresses enter the T-curve analysis only via their influence on the micromechanics of bridging and not

5

via any direct interaction with the field of the advancing tip; we shall argue that the latter possibility, considered as a potential source of toughness variation in the earlier literature [15], cannot account for the scale of the T-curve observed in the materials to be investigated here.

Our goal is to formulate a theory for quantifying the role of such microstructural parameters as size, shape and spacing of bridging grains, grain boundary energy and intergranular sliding friction coefficient, on the strength properties of ceramics. To illustrate the formalism we fit our toughness equations to some data from previous indentation-strength tests on an alumina with particularly strong T-curve characteristics. With the results of this fit we then make some preliminary predictions of the strength/grain-size dependence. The ultimate hope is that such an approach might be used to establish a theoretical base for a processing strategy that allows for optimisation of strength properties of ceramics for specific applications.

2. MICROMECHANICS OF FORCE-SEPARATION FUNCTION FOR INTERLOCKING GRAINS WITH INTERNAL-STRESS-MODIFIED FRICTIONAL TRACTIONS

2.1 Geometrical Factors and Internal Stresses

An important element of our model is the geometrical configuration of interlocking grains at the crack interface, and the role of local residual internal stresses in determining subsequent frictional restraints as these grains are progressively disengaged from the crack walls. Such stresses were first discussed in the context of grain bridging by Swain [16]. However,

6

Swain confined his attention to estimates of the spatial extent of the T-curve, without any consideration of the shape or height of this curve.

Consider first thermal expansion mismatch stresses normal to the separation plane along which the crack is to propagate. These internal stresses arise from crystallographic anisotropy of individual grains within the material microstructure. They are conservative, in that they may be relaxed and restored in any elastic operation that displaces the opposing half-spaces across the separation plane. They consist of both tensile stresses, σ_R, and compressive stresses, σ_R^-:

$$\sigma_R = + \beta_+ E\Delta\alpha\Delta T \qquad (1a)$$

$$\sigma_R^- = - \beta_- E\Delta\alpha\Delta T \qquad (1b)$$

where E is Young's modulus, $\Delta\alpha$ is the differential thermal expansion coefficient, ΔT is the temperature range through which the material deforms elastically, and the β are coefficients < 1. Those grains subject to compression will tend to remain in contact with both sides of the interface in any such reversible separation process, and thence constitute incipient "bridges"; those remaining grains subject to tension may then be considered as making up the constitutive "matrix".

Now define a characteristic grain size ℓ and characteristic bridge spacing d, as illustrated schematically in Fig. 1a for a periodic rectangular lattice, such that the area fraction of bridges is $\ell^2/2d^2$. Then the requirement for the tensile and compressive stresses to balance over any potential separation plane is that

$$\sigma_R(1 - \ell^2/2d^2) = - \sigma_R^-(\ell^2/2d^2). \qquad (2)$$

For the ideal case of a unimodal, homogeneous grain structure, where we expect equal probability of tensile and compressive stress, i.e. $\beta_+ = \beta_-$, Eq. 2 requires that $d = \ell$. This corresponds to the limiting configuration in which every alternate grain is (on average) a bridge.

How might these internal stresses exert restraining forces on prospective crack walls? When we deal with fracture mechanics later we will need to distinguish certain crack-size domains. For very small cracks in the initial stages of development, $c < d$, the walls will feel the full influence of either the matrix tensile stress σ_R (or, alternatively, the compressive stress σ_R^- in the relatively unlikely event of cracks generating from within the bridges themselves). Thus in this domain the discreteness of the microstructure is crucial. For very large cracks, $c \gg d$, the internal stresses must average out to zero over the potential separation plane. In the intermediate domain within the first few bridge intersections the microstructural discreteness, representable as alternate areas of positively and negatively stressed grain facets, will rapidly wash out (the crack area increasing with $\approx c^2$ for the penny-like geometry). Accordingly, we make the approximation that the net internal elastic stress across any crack area beyond the first bridge is zero.

If this last approximation holds, then the origin of the closure stresses needed to produce toughening must lie in some subsidiary, nonconservative source. Suppose the fracture to be intergranular, and consider the internal stresses transverse to the separation plane at the grain-matrix interfaces (Fig. 1b). Some of the grains (those destined to act as bridges) will be in a state of residual compression. At this stage we make no attempt to distinguish fine details of the stress state, assuming a uniform distribution σ_R^- at the boundaries. We shall propose below that Coulomb sliding friction at

8

the compressive grain-matrix interface provides the dominant closure stress as the surfaces are separated along the grain boundaries. It is possible that not all compressively stressed grains will be ideally oriented to provide effective interlocking, in which case we may generally expect $d > \ell$, even in ostensibly homogeneous microstructures. In this model the internal stresses, although not the direct cause of the closure, are (contrary to what one might at first sight conclude from the preceding paragraph) far from benign, since they determine the magnitude of the frictional tractions.

Accordingly, we need to determine a constitutive relation between closure stress, p, and (half) crack-wall separation, u, for this dissipative friction component. We shall adopt the convention, consistent with our notion that frictional tractions will always act to oppose crack opening, that <u>positive</u> p(u) denotes <u>closure</u>. The function p(u) is derived for different crack-size regions in the following subsections.

2.2 <u>Frictional Debonding at Matrix-Grain Interface</u>

Suppose the crack intersects a grain in residual compression, Fig. 2a. The intersected grain initially exerts an opening force on the crack walls. As separation behind the advancing crack tip proceeds, this opening force diminishes and ultimately becomes negative (closure), leaving the grain embedded in the matrix on both sides of the interface. This is the first stage of bridge formation. The ensuing build-up of differential strain between the grain and matrix results in interfacial debonding, starting at the crack plane and extending stably up the interface. Simultaneous with this debonding is the onset of resistive, frictional tractions, increasing in

intensity until debonding is effectively complete.

Calculations of the debonding process have been carried out in the ceramic composites literature, particularly in the context of fibre-reinforced composites. We resort to one such calculation, by Marshall and Evans [17], deferring details to the Appendix. At the outset we may assert that the debonding is unlikely to make a profound contribution to the energy dissipation; although frictional forces are involved, the distances over which these forces are active is limited to the relatively small elastic displacements within the internally stressed bridges. Balancing the integrated frictional shear lag stress over the debonded interface area against the axial stress in the residually stressed bridging grain, one obtains a square root dependence of closure stress p on u [17] (Appendix),

$$p(u) = \{(2\mu\sigma_R E\lambda/\ell^2)^{1/2}/(2d^2/\ell^2 - 1)\}u^{1/2} - \sigma_R \qquad (3)$$

where λ is the circumferential distance around the debonding grain at the separating interface (e.g. $\lambda = 4\ell$ for the rectangular geometry in Fig. 1) and μ is the friction coefficient. We note the appearance of E in Eq. 3, consistent with an elastic relaxation process. We note also the negative intercept, $p(0) = -\sigma_R$, indicative of the opening stress that pertains at initial wall separation.

2.3 Sliding Friction Grain Pullout

Once debonded, the grain can slide out of the matrix, Fig. 2b. The frictional closure stress on the crack wall is now exerted by individual bridging grains as they are pulled out of the embedding matrix. The force

10

exerted by one grain at any wall-wall separation 2u is given by the product of: $\lambda(2u_* - 2u)$, with $2u_*$ the separation at which the grain disengages (area of grain wall in contact with matrix); μ (sliding friction coefficient); and $-\sigma_R^-$ (normal, clamping stress). Noting that the average area occupied by one bridge is $2d^2$ and recalling Eqs. 1 and 2, we obtain

$$p(u) = (\mu\sigma_R \lambda u_* /d^2)(2d^2/\ell^2 - 1)(1 - u/u_*). \tag{4}$$

This relation has the same characteristic falloff with u as assumed empirically in earlier studies [8,9], except that here it is explicitly linear. Such a linear dependence is contingent on an invariant cross-sectional grain geometry during pullout [18], as implicit in our consideration of a rectangular microstructure in Fig. 2. The representation in Fig. 2 also depicts the frictional forces as distributed uniformly and symmetrically over the entire matrix/bridging-grain remnant "contact" interface. Direct observations of the bridging configurations indicate that the reality is more complex: the bridging configuration is, in general, far from rectangular, and the frictional contact regions tend to be concentrated at points of geometrical irregularity (ledges, re-entrant corners, etc.), often across a single (compressively stressed) facet of the disengaging grain, where the resistance forces can be intense (see, for instance, Fig. 12 of Ref. 7). Ours is a somewhat idealised representation of the closure stress function. Nevertheless, Eq. 4 does contain the essential physics of the proposed separation process, and is well structured for incorporation of critical microstructural parameters.

In deriving Eq. 4 we have not considered the possibility that the bridging grains might rupture transgranularly. If such rupture were to occur,

11

p(u) would cut off prematurely at some critical separation. Such cutoffs are indeed predicted in ceramic composites with continuous fibres [17]. They might be expected in our monophase ceramics if the frictional stresses were allowed to build up sufficiently, e.g. at large grain sizes. For the present we neglect this possibility.

Because sliding friction can occur over a large fraction of the embedded grain dimension, we may anticipate pullout to dominate debonding as a contributory factor in the toughening.

2.4 Composite p(u) function

Now let us combine the results in Sects. 2.3 and 2.4 to obtain a composite closure stress-separation function p(u) for the entire evolution of the bridge, from initial formation to rupture and beyond. It is re-emphasised that we are dealing with an approximation in which a discrete distribution of bridging forces is replaced by a continuous stress function. We recall that this approximation is good only for cracks with area large compared to the area occupied by a single bridge (c >> d). As alluded in Sect. 2.1, we shall extend the formalism down to the intermediate crack-size domain, but not to the small-crack domain (c < d) where the internal stresses dominate.

Notwithstanding these provisos, we reduce the closure stress function as follows:

$$p(u) = p_D (u/u_*)^{1/2} - \sigma_R, \qquad (0 \le u \le u_+) \qquad (5a)$$

$$p(u) = p_M (1 - u/u_*), \qquad (u_+ \le u \le u_*) \qquad (5b)$$

$$p(u) = 0, \qquad (u \ge u_*) \qquad (5c)$$

where the scaling quantities

$$p_D = (2\mu\sigma_R E\lambda u_\ast/\ell^2)^{1/2}/(2d^2/\ell^2 - 1) \qquad (6a)$$

$$p_M = (\mu\sigma_R \lambda u_\ast/d^2)(2d^2/\ell^2 - 1) \qquad (6b)$$

are respectively the shear-lag stress in Eq. 3 evaluated at $u = u_\ast$ in the absence of residual stress σ_R and the sliding friction stress in Eq. 4 evaluated at $u = 0$. Equation 5 is plotted schematically in Fig. 3. Thus we have a function $p(u)$ with negative intercept at $p(0) = -\sigma_R$, square root dependence to the crossover point at $u = u_+$, and linear decline to $p(u_\ast) = 0$. The area under the curve in Fig. 3 represents the energy of separation of the bridged interface.

It is instructive to determine the crossover point where the $p(u)$ functions in Eqs. 5a and 5b are identically equal:

$$u_+/u_\ast = (p_D/2p_M)^2\{[1 + 4p_M(p_M + \sigma_R)/p_D^2]^{1/2} - 1\}^2. \qquad (7)$$

As indicated above, we may generally expect to find $p_D \gg p_M + \sigma_R$, $u_+/u_\ast \approx [(p_M + \sigma_R)/p_D]^2 \ll 1$, in which event the debonding term will be relatively insignificant in the fracture mechanics. We shall find this to be the case for our alumina later (Sect. 4).

3. FRACTURE MECHANICS

3.1 General Equilibrium Requirements

Begin by defining a general stress intensity factor condition for the

13

equilibrium of a crack subject to an applied tensile loading field (K_a), a flaw-localised internal tensile field associated with any residual nucleation forces on the crack (K_r) [19], and a microstructure-associated closure field (K_μ) [8]. These stress intensity fields are linearly superposable. A stationary value obtains when the net K on the crack tip, $K_*(c)$ say, just balances the toughness associated with reversible creation of surfaces, T_0:

$$K_*(c) = K_a(c) + K_r(c) + K_\mu(c)$$
$$= T_0 = (2\gamma_0 E')^{1/2} \tag{8}$$

with $E' = E/(1 - \nu^2)$ for plane strain, ν Poisson's ratio. Here γ_0 is an appropriate surface energy term. For the case of special interest to us, that of intergranular fracture, we have

$$2\gamma_0 = 2\gamma_S - \gamma_s, \tag{9}$$

with γ_S the surface energy of the bulk solid and γ_s the grain boundary formation energy.

It is convenient to restate the above equilibrium requirement in a form appropriate to the R-curve phenomenology. We note that, like K_a, K_r is a truly extrinsic mechanical driving force on the crack system. (We shall identify K_r specifically for indentation cracks below.) The quantity K_μ on the other hand is an intrinsic resistive term, always negative, so is more appropriately regarded as part of the toughness, i.e. $T_\mu = -K_\mu$. Accordingly,

$$K_A(c) = K_a(c) + K_r(c)$$
$$= T_0 + T_\mu(c) = T(c). \tag{10}$$

The composite, crack-size dependent toughness term T is equivalent to the

quantity K_R used by some: we adopt the T notation to avoid potential confusion with the negative sign in K_μ, and to emphasise that we are considering an intrinsic material property rather than an extrinsic mechanical force. We may note the equivalence of the above stress intensity factor relation $K_c = K_A = T$ with the mechanical release rate relation $G_c = R$, via the familiar connection $T = (RE')^{1/2}$ [13]; hence our use of the term "T-curve" instead of the more familiar "R-curve".

The critical condition for the crack equilibrium to be unstable is then given by $dK_*(c)/dc \geq dT_0/dc = 0$ in Eq. 8 or, alternatively, by $dK_A(c)/dc \geq dT(c)/dc$ in Eq. 10 [3]. The latter defines the familiar "tangency" condition for materials with T-curves.

3.2 Microstructural Stress Intensity Factor

Consider the idealised penny crack system in Fig. 4. As discussed in Sect. 2.1 we suppose that the crack originates within the matrix (i.e. in a region between bridges) subject to the (conservative) tensile stress σ_R, and subsequently spreads into the surrounding regions defined by the (nonconservative) closure stress function $p(u)$. We shall designate contributions to the microstructural toughness term T_μ from the σ_R component by single prime notation, and from the $p(u)$ component by double prime, i.e. $T_\mu = T_\mu' + T_\mu''$. It is convenient to separate the problem into three crack-size regions: c smaller than d (corresponding to first bridge intersections at one half the spacing $2d$ in Fig. 1); c larger than d but smaller than the critical size c_* at which the first-intersected bridges just rupture; c larger than c_* (such that the entire bridging zone translates with the advancing tip). As we

15

shall see below (Sect. 3.2.2), a further subdivision of the second of these regions may be made.

3.2.1 Precursor tensile zone, $c \leq d$.

Within this region the crack experiences only the matrix tensile stress σ_R. The negative of the stress intensity factor for this region, $T'_\mu = -K'_\mu$, is of the familiar form for uniform stress fields,

$$T'_\mu(c) = -\psi\sigma_R c^{1/2}, \qquad\qquad (c \leq d). \qquad\qquad (11)$$

where ψ is a geometry-dependent coefficient appropriate to penny-like cracks. In this region the contribution from $p(u)$ is, of course, zero, i.e.

$$T'_\mu{}'(c) = 0, \qquad\qquad (c \leq d). \qquad\qquad (12)$$

3.2.2 Bridging zone, $d \leq c \leq c_*$.

Within the bridging zone the crack experiences two contributions, one due to the persistent tensile stresses σ_R over the radial distance $r \leq d$ and the other to the frictional closure stresses $p(u)$ over $r \geq d$. These microstructural contributions will continue to evolve with crack extension as long as the first-intersected bridge at $r = d$ remains intact.

Start with the first of these contributions, $T'_\mu = -K'_\mu$. We use the Green's function solution for penny-like cracks subject to radially distributed stresses $\sigma(r) = \sigma_R$ over $0 \leq r \leq d$, $\sigma(r) = 0$ over $r \geq d$ ([20];

$$T'_\mu(c) = -(\psi/c^{1/2})\int_0^d r\sigma(r)dr/(c^2 - r^2)^{1/2}$$

$$= -\psi\sigma_R c^{1/2}[1 - (1 - d^2/c^2)^{1/2}], \qquad (d \leq c \leq c_*). \qquad (13)$$

The following limits are of interest: at $c = d$, $T'_\mu = - \psi\sigma_R d^{1/2}$, as required to match Eq. 11; at $c \gg d$, $T'_\mu \to - \psi\sigma_R d^2/2c^{3/2}$, which is the solution for a central point-force opening configuration. It is apparent that the influence of the persistent matrix stress diminishes rapidly once the crack enters this bridging zone.

Now consider the second contribution, $T''_\mu = - K''_\mu$. In its exact form, this contribution is expressible as a nonlinear integral equation, which has no general closed-form solution [21]. To avoid a detailed numerical analysis we compute this term analytically in the approximation of "weak shielding" [9,17], where the influence of the closure stresses is taken into account in the stress intensity factor balance but is ignored in the crack-opening displacement relation. The assumption of weak shielding is appropriate for ceramics with modest toughening characteristics, i.e. ceramics for which $T''_\mu <$ T_0; for our model material this condition is satisfied in the crucial small-crack region (see Sect. 4, Fig. 7). In this approximation we have [9,17]

$$T''_\mu(u) = + (E'/T_0)\int_0^{u_z} p(u)du \qquad (14)$$

where u_z is the crack-opening displacement at the stationary edge of the closure zone, Z in Fig. 5.

The integral in Eq. 14 is most conveniently taken in two parts, according to whether the crack-opening displacement u is less or greater than u_+ in Fig. 3. For the first region we insert $p(u)$ from Eq. 5a:

$$T''_\mu(u) = + (E'/T_0)\int_0^{u_z} [p_D(u/u_*)^{1/2} - \sigma_R]du$$

$$= - (E'/T_0)\sigma_R u_z [1 - (2p_D/3\sigma_R)(u_z/u_*)^{1/2}],$$

$$(0 \le u_z \le u_+). \qquad (15a)$$

17

For the second region we insert p(u) from Eqs. 5a and 5b:

$$T_\mu'(u) = + (E'/T_0)\{\int_0^{u_+} [p_D(u/u_*)^{1/2} - \sigma_R]du + \int_{u_+}^{u_z} [p_H(1 - u/u_a)]du\}$$

$$= (E'/T_0)\{- \sigma_R u_+[1 - (2p_D/3\sigma_R)(u_+/u_*)^{1/2}]$$

$$+ p_H u_*[(u_z - u_+)/u_*][1 - [(u_z + u_+)/2u_*]]\},$$

$$(u_+ \leq u_z \leq u_*). \quad (15b)$$

To transform $T_\mu(u)$ to $T_\mu(c)$ we must determine the zone-edge displacement $u_z = u_z(c)$ from an appropriate relation for the crack profile. In the spirit of the weak-shielding approximation we use Sneddon's solution for the near-field profile $u(r,c)$ of a crack _free_ of microstructural closure terms, but with these same terms _included_ implicitly in the equilibrium requirement ($K_* = T_0$ in Eq. 8) [8,9],

$$u(r,c) = (\psi T_0/E'c^{1/2})(c^2 - r^2)^{1/2}. \quad (16)$$

Then the requisite crack-opening displacement $u = u_z = u(d,c) = u(c)$ at the zone boundary $r = d$ is

$$u_z(c) = (\psi T_0/E'c^{1/2})(c^2 - d^2)^{1/2}, \quad (d \leq c \leq c_*). \quad (17)$$

At the debonding/pullout crossover point $u_z(d,c_+) = u_+(c) = u_+$ and critical pullout point $u_z(d,c_*) \doteq u_*(c) = u_*$, Eq. 17 reduces to

$$u_+ = (\psi T_0/E'c_+^{1/2})(c_+^2 - d^2)^{1/2} \quad (18a)$$

$$u_* \simeq \psi T_0 c_*^{1/2}/E' \quad (c_* \gg d) \quad (18b)$$

respectively, where c_+ and c_* define the corresponding crack sizes.

3.2.3 _Steady-state zone_, $c \geq c_*$. Once the critical first-intersected bridge

at Z (Fig. 5) is ruptured the entire bridging zone translates with the advancing crack tip. In the limit $c_* \gg d$, Eq. 13 becomes

$$T'_\mu = 0. \tag{19}$$

For $u_* \gg u_+$, $c_* \gg c_+$, evaluation of Eq. 15b at $u_z = u_*$ similarly gives

$$T''_\mu \approx + E' p_H u_* / 2T_0, \qquad (u \gtrsim u_*). \tag{20}$$

3.3 T-Curve

We now have all the ingredients for constructing the T-curve. At this stage it is convenient to introduce some coefficients that characterise the geometrical features of the microstructure in relation to the grain size, ℓ (Fig. 1). This introduces the concept of geometrical similitude: for microstructures that change only in scale and not in the essential geometry such coefficients remain invariant. Thus we define the following similitude constants:

$$\alpha_d = d/\ell \tag{21a}$$

$$\alpha_L = L/\ell \tag{21b}$$

$$\alpha_\lambda = \lambda/\ell \tag{21c}$$

$$\epsilon_L = 2u_*/L. \tag{21d}$$

The coefficient α_d relates the bridge spacing to the grain size (unity for equiaxed microstructures, Sect. 2.1), and generally defines the area fraction of bridges $(1/2\alpha_d^2)$; α_L is the aspect ratio of the pullout grains, with L the long (embedded) dimension (again, unity for equiaxed microstructures); α_λ is the cross-sectional perimeter to grain-diameter ratio for the embedded grain

(4 for grains of rectangular cross section); and ϵ_L is the "bridge rupture strain". Then we may substitute into Eqs. 7 and 11-20 to determine $T(c) = T_0 + T'_\mu(c) + T''_\mu(c)$ in the following crack-size regions:

$$T(c) = T_0 - \psi\sigma_R c^{1/2}, \qquad (c \leq \alpha_d \ell) \qquad (22a)$$

$$T(c) = T_0 - \psi\sigma_R c^{1/2}(1 - (2p_D/3\sigma_R)(c/c_*)^{1/4}(1 - \alpha_d^2\ell^2/c^2)^{3/4}),$$
$$(\alpha_d\ell \leq c \leq c_+) \qquad (22b)$$

$$T(c) = T_0 - \psi\sigma_R c^{1/2}(1 - (1 - \alpha_d^2\ell^2/c^2)^{1/2} + (c_+/c)^{1/2}(1$$
$$- \alpha_d^2\ell^2/c_+^2)^{1/2}(1 - (2p_D/3\sigma_R)(c_+/c_*)^{1/4}(1 - \alpha_d^2\ell^2/c_+^2)^{1/4}))$$
$$+ \psi p_M c^{1/2}((1 - \alpha_d^2\ell^2/c^2)^{1/2} - (c_+/c)^{1/2}(1 - \alpha_d^2\ell^2/c_+^2)^{1/2})(1$$
$$- \tfrac{1}{2}[(c/c_*)^{1/2}(1 - \alpha_d^2\ell^2/c^2)^{1/2} + (c_+/c_*)^{1/2}(1 - \alpha_d^2\ell^2/c_+^2)^{1/2}]),$$
$$(c_+ \leq c \leq c_*) \qquad (22c)$$

$$T(c) = T_0 + \tfrac{1}{2}\psi p_M c_*^{1/2} = T_*, \qquad (c \geq c_*) \qquad (22d)$$

with

$$p_D = (\alpha_\lambda \epsilon_L \alpha_L \mu \sigma_R E)^{1/2}/(2\alpha_d^2 - 1) \qquad (23a)$$

$$p_M = \alpha_\lambda \epsilon_L \alpha_L \mu \sigma_R (1 - 1/2\alpha_d^2) \cdot \qquad (23b)$$

$$c_* \propto (\epsilon_L \alpha_L E'\ell/2\psi T_0)^2 \qquad (23c)$$

$$[(c_+^2 - \alpha_d^2\ell^2)/c_+]^{1/2} = (\epsilon_L \alpha_L E'\ell/2\psi T_0)(p_D/2p_M)^2((1$$
$$+ 4p_M(p_M + \sigma_R)/p_D^2]^{1/2} - 1)^2, \qquad (23d)$$

the last (implicit) equation defining c_+. Note it is only the spatial scaling terms c_* and c_+, and not the stress scaling terms p_D and p_M, that depend on ℓ. Evaluation of Eq. 22 indicates that $T(c)$ drops below T_0 in its initial extension within $c \leq d$, but quickly increases above T_0 once the bridging zone is entered and the crack extends beyond c_+, ultimately saturating at its steady state value for $c \geq c_*$. We shall illustrate this general trend for our

model alumina material in Sect. 4 below.

3.4 Strength Characteristics for Indentation Flaws

Consider finally the conditions for Vickers half-penny indentation cracks produced at load P to proceed to unlimited failure under the action of an applied tensile stress σ_a. From those conditions we may compute the _inert strength_ σ_m (i.e. the strength in the absence of any kinetic effects) as a function of P, and thence establish the basis for deconvolution of the T-curve from experimental data.

Begin by writing $K_A(c)$ in Eq. 10 in the familiar form for such cracks:

$$K_A(c) = \psi\sigma_a c^{1/2} + \chi P/c^{3/2} \qquad (24)$$

where χ is a coefficient denoting the intensity of the residual Vickers elastic-plastic contact deformation field [22-24]. At equilibrium, $K_A(c) = T(c)$, we have

$$\sigma_a(c) = (1/\psi c^{1/2})[T(c) - \chi P/c^{3/2}]. \qquad (25)$$

We now seek an instability condition for $\sigma_a(c)$. Recall from Sect. 3.1 that the requirement for instability is $dK_A(c)/dc \geq dT(c)/dc$. In terms of Eq. 25 this condition is equivalent to $d\sigma_a(c)/dc \geq 0$ [13]. In general (as we shall demonstrate in Sect. 4), $\sigma_a(c)$ has two maxima, one on either side of c = d: that at c < d is governed by the shorter-range influence of the residual contact field (K_r); that at c > d is governed by the longer-range influence of the microstructural interaction ($K_\mu = - T_\mu$) [9]. The relative heights of the two barriers is determined by the indentation load. Once the first

21

barrier (at c < d) is surmounted the crack becomes unstable. However, the crack propagates spontaneously to failure only if the second barrier (at c > d) is lower. If the second barrier is higher the crack will arrest on a stable branch of the σ_a(c) curve ("pop in") before an unlimited instability can be achieved. Thus the _strength_ σ_m is determined by the greater of the two maxima.

It remains to demonstrate how one may solve Eq. 25 numerically for the strength characteristic, and thence extract the T(c) curve, for a given material system.

4. CASE STUDY ON AN ALUMINA CERAMIC

We demonstrate the above fracture mechanics formalism by analysing indentation-strength, σ_m(P), data for a particular polycrystalline alumina ceramic. [2] This alumina, apart from exhibiting significant T-curve characteristics, has served as a model material in previous studies of the bridging mechanism [3,4,7]. It is a _nominally_ pure material with grain size ℓ ≈ 20 μm. In actuality, the material contains a small amount of sintering aid (< 0.1% MgO and other oxide additive) and has a noticeably nonuniform, nonequiaxed grain distribution (e.g. see micrographs in Ref. [7]), but we shall regard these as mere "perturbations" of an otherwise regular microstructure.

The analytical procedure involves selecting the parameters in Eqs. 21, 22 and 25 to get an iterative best fit to the σ_m(P) data. It is similar in

---

[2]   Vistal grade Al_2O_3, Coors Ceramics Co., Golden, CO.

principle to the procedure described in an earlier study [9], but with some refinements.

4.1 Fitting Procedure

The first step is to specify initial values for the T-curve parameters:

(i) **Material parameters**. First we specify Young's modulus E and Vickers hardness H for our alumina. The values E = 393 GPa (Poisson's ratio ν = 0.20) and hardness H = 19.1 GPa are taken from earlier data [9]. These values are sufficiently accurate (< ± 1% uncertainty) as to be treated as invariants in the iteration process.

The intrinsic grain boundary toughness T_0 and internal stress σ_R can not be specified to the same degree of accuracy (probably not much better than ± 30%). For T_0 we write $T_0/T_S = (1 - \gamma_B/2\gamma_S)^{1/2}$ from Eqs. 8 and 9, with T_S = 3.1 MPa.m$^{1/2}$ the toughness of single crystal sapphire [9]: using a most recent estimate γ_B/γ_S = 1.05 (median) from dihedral angle measurements of thermal grooves at grain-boundary/free-surface junctions in MgO-doped alumina polycrystals [25], we obtain T_0 = 2.1 MPa.m$^{1/2}$; however, an earlier estimate γ_B/γ_S = 0.54 in bicrystals [26] suggests that the true value of T_0 could be somewhat larger. For σ_R we take a value 100 MPa (mean) from measurements of the broadening of spectroscopic lines [27]. In view of the abovementioned uncertainty level, T_0 and σ_R are regarded as subject to minor adjustment.

(ii) **Bridging parameters**. The bridge rupture strain ϵ_L and the sliding friction coefficient μ are even more difficult to specify a priori. An estimate of ϵ_L may be obtained directly from microscopic measurements of

crack-opening displacements. For our alumina grain size $\ell = 20$ μm, displacements $u_* = 1$-2 μm have been observed at active bridging sites some millimeters behind the crack tip, corresponding to $\epsilon_L \approx 0.05$-0.10 (e.g. from micrographs in Ref. [7]). Reichl & Steinbrech [28], in a more detailed study of several "pure" aluminas in the grain size range 3-17 μm, found $\epsilon_L \approx 0.12$. This parameter probably depends strongly on the detailed grain geometry, so again we regard it as an adjustable, with $\epsilon_L \approx 0.10$ as our starting value.

As with any dissipative quantity, the friction coefficient μ is notoriously difficult to predetermine for any given material system. We have already alluded to the existence of geometrical irregularities that might augment μ in the grain pullout configuration (Sect. 2.3), suggesting that we should not be surprised to find unusually large values. A starting estimate of this parameter is accordingly obtained by trial and error using the algorithm described below (Sect. 4.2) in preliminary data-fit runs.

(iii) **Flaw parameters**. Next, we specify the parameters that characterise the Vickers indentation flaws. We use "calibrated" values from previous indentation studies [9]: the geometrical constant $\psi = 1.24$ (close to value 1.27 for ideal penny cracks), and the residual-contact-intensity coefficient $\chi = 4.0 \times 10^{-3} (E/H)^{1/2}$. These are taken as invariants.

(iv) **Similitude parameters**. Lastly, we specify the α similitude parameters in Eq. 21. We take $\alpha_d = 1 = \alpha_L$ and $\alpha_\lambda = 4$, corresponding to an ideally equiaxed and rectangular microstructure. We regard α_L and α_λ as invariants, noting from Eq. 23 that errors in these terms can be largely accommodated in the adjustments of ϵ_L and μ. The bridge spacing parameter α_d we allow to vary.

We then use the following regression algorithm for best-fitting the $\sigma_m(P)$ data:

(i) After evaluating the scaling stress (p_D, p_H) and spatial (c_*, c_+) terms in Eq. 23 using the starting parameters from Sect. 4.1, compute a trial T-curve from Eq. 22.

(ii) Compute the function $\sigma_a(c)$ in Eq. 25 for each indentation load P for which experimental data are available. Determine the strength σ_m as the maximum in this function at each of these loads (recalling that if two maxima exist it is the greater which determines σ_m).

(iii) Compare computed strengths with measured values, and thence evaluate the residual, $\sum_n [\sigma_m(P)_{calc} - \sigma_m(P)_{meas}]^2/(n - 1)$, over all n loads.

(iv) Increment the adjustables ϵ_L and μ in a "coarse" first-run matrix search routine (in steps 10% of starting values), and cycle (i) through (iii). Invoke a minimum variance condition to determine interim best-fit values.

(v) Increment the adjustables ϵ_L, μ, T_0, σ_R and α_d in a "fine", second-run routine (ultimately, in steps of 1% of starting value), and proceed similarly to determine final best-fit values.

4.2 Results

The results of the data analysis for our model alumina are summarised in Figs. 6-8, corresponding to final best-fit values $\epsilon_L = 0.135$, $\mu = 1.80$, $T_0 = 2.50$ MPa.m$^{1/2}$, $\sigma_R = 155$ MPa and $\alpha_d = 1.50$. We note that ϵ_L corresponds to the Reichl & Steinbrech value quoted above; that μ is substantial, as

foreshadowed in Sect. 2.3; that the values of T_0 and σ_R are not substantially different from the first, trial estimates; and that α_d corresponds to a bridge at every third grain. In Fig. 6 the solid curve represents the fit to the experimental $\sigma_m(P)$ data points (error bars on the data points representing standard deviations) [3]. The theory accounts for the major trends in the data, in particular the tendency to a plateau strength at diminishing indentation loads (shorter initial crack lengths).

Also plotted in Fig. 6, as the two dashed curves at left, are the predicted responses for the same alumina corresponding to the following hypothetical "toughness states": frictional stresses "switched off", i.e. bridges removed ($p_D = 0 = p_M$, $d = \infty$), but matrix internal stresses ever present ($\sigma_R \neq 0$), $T = T_0 - T'_\mu$; frictional and internal stresses switched off ($p_D = 0 = p_M$, $d = \infty$, $\sigma_R = 0$), $T = T_0$. These two curves quantify the degrading effect of the internal stress on the strength at low indentation loads (small flaw sizes); and, conversely, the (over-) compensating effect of the friction at high loads (large flaw sizes), leading ultimately to the macroscopic toughness state $T = T_m$.

The deconvoluted T-curve corresponding to the data fit is shown in Fig. 7. The previously mentioned tendency for $T(c)$ to drop below T_0 prior to intersecting the first bridges at $c = d$ (Sect. 3.3) is apparent in this diagram. This is a facet of T-curve behaviour that escapes detection in traditional, large-scale crack tests, where the initial stages of crack propagation generally occurs from ill-defined, rounded notches. The falloff in $T(c)$ continues in the immediate aftermath of the first bridge intersection as the crack enters the debonding zone $d \leq c \leq c_+$, although in our material this region is so small ($c_+/d \leq 1.01$) as to be undetectable in Fig. 7. Once

26

the crack enters the frictional sliding zone $c_+ \leq c \leq c_-$ the T-curve rise rapidly until, at $c \geq c_-$, it begins its familiar rise toward saturation at $T = T_-$. This plot shows again that the internal stress is an important factor in the toughness characteristic; but that in the frictional contribution it is only the pullout, and not the debonding, that is important.

Figure 8 shows plots of applied stress vs crack size for our alumina at different indentation loads. These plots illustrate the instabilities that occur in the crack evolution to failure. At large P it is the second maximum, i.e. the maximum associated with the bridging, that dominates [9]. Within the plateau strength region of Fig. 6 the initial crack "pops in" before growing stably to failure, consistent with observation [7]. The stabilising effect of the bridging is evident in this region as the relatively insensitivity of the second maximum to P. At very small P it is the first maximum, associated with the residual contact field, that dominates. In principle, indentations in this region should allow us to explore the extreme left-hand branch of the $\sigma_m(P)$ plot in Fig. 6, but the almost invariable presence of natural flaws in the size range $c > d$ generally precludes the possibility of exceeding the plateau strength level [3,9].

5. GRAIN-SIZE DEPENDENCE OF STRENGTH

Let us demonstrate the versatility of the "calibrated" formulation above by considering the grain-size dependence of the T-curve, T(c), and thence the indentation-strength function, $\sigma_m(P)$, for alumina ceramics. There are few systematic experimental studies of such grain-size dependencies in alumina

(or, indeed, in any other polcrystalline ceramic material) in the literature. However, there are some earlier indentation-strength data for two aluminas, nominally pure with grain sizes 3 μm and 25 μm, that we may usefully compare with the results for our reference material in Sect 4 [3].[3] Also, there are some unpublished bend-strength data by Charles & Shaw [29] on as-fired "pure" aluminas with grain sizes in the range 6-150 μm that allow a tentative investigation of the underlying $\sigma_m(\ell)$ relation for "natural" flaws.

Consider first the indentation-strength data [3] for the 3 μm and 25 μm aluminas in Fig. 9. We make our comparison by generating the appropriate $\sigma_m(P)$ functions using precisely the same best-fit parameters as obtained in Sect. 4, but with ℓ appropriately adjusted. These functions are plotted as the solid curves in Fig. 9, along with their counterpart for $\ell = 20$ μm (dashed line) from Fig. 6. The calibrated theory therefore has the capacity to predict at least qualitative trends in strength and toughness characteristics with change in the important microstructural parameters.

The informational value of comparative predictions of the type illustrated in Fig. 9 is manifest in the way the curves cross each other. It becomes clear that there can be no simple, single grain-size dependence of strength for materials with strong T-curves (R-curves). In particular, the familiar $\ell^{-1/2}$ (Hall-Petch) dependence does not appear to be obeyed in any crack-size region. Thus, whereas the plateau σ_m tends to diminish with increasing ℓ at low loads (small c), the dependence on ℓ is somewhat less strong than $\ell^{-1/2}$. At high loads (large c), σ_m actually increases with ℓ.

Now consider how the theory compares with the available $\sigma_m(\ell)$ data [29]

---

[3]   AD999 grade (3 μm), and heat-treated Vistal grade (25 μm). Coors
        Ceramics Co., Golden, CO.

for failures from "natural" flaws, Fig. 10. The solid line appropriately represents the predicted dependence of plateau strength for flaws without any residual nucleation field (i.e. $K_r = 0$), once more using the best-fit parameters from the reference alumina material and treating ℓ as an independent variable. We may note that the slope of this line is close to 1/3; and that a force-fitted line with the classical Hall-Petch slope 1/2 cannot be made to pass through the error bars on the data points.

5. DISCUSSION

Our toughness/crack-size (T-curve, or R-curve) model is based on a physical microstructural constitutive relation for crack interfacial bridging, in which thermal expansion mismatch stresses are a governing factor in determining dissipative Coulombic frictional pullout tractions at interlocking grains. The model accounts for the major features of the T-curve function, notably the magnitude and range, for nontransforming ceramics. We emphasise, however, that our T(c) functions have had to be best-fitted to the experimental (indentation-strength) data, with adjustable parameters. In addition, the formulation embodies several approximations, e.g. weak-shielding, undistorted Sneddon crack profile, negligible transgranular fracture. Furthermore, we have given explicit consideration here to just one ceramic material, alumina. Accordingly, any "goodness of fit" evident in the analysis of Sects. 4 and 5 is not to be construed as proving the general validity of the bridging model. Such proof comes from independent, in situ observation of crack micromechanics on this alumina [7] as well as on a wide range of other nontransforming ceramics [10], not from conventional

29

macroscopic fracture mechanics measurements. However, the fit does confirm that the bridging model can account for most documented characteristics of T-curve (R-curve) behaviour, e.g. the flaw tolerance quality and grain-size dependencies.

Moreover, once the T(c) function has been "calibrated" against a "reference" data set, as in Sect. 3, we have the power to predict how the T-curve and associated $\sigma_m(P)$ functions should vary with changes in the microstructure. We alluded to this power in our brief consideration of the strength/grain-size dependence for alumina ceramics in Sect. 4. A more detailed study of the $\sigma_m(\ell)$ dependence in aluminas is currently under way [30]. Similar dependencies of strength on grain boundary toughness (T_0), internal stress level (σ_R), grain-grain friction coefficient (μ), may be similarly evaluated. These are additional factors that might be systematically adjusted by material processors to improve strength characteristics. Thus we have a physically sound basis for optimising the microstructures of the broad range of structural ceramic materials whose toughness behaviour is governed by the bridging mechanism.

The a priori specification of a constitutive stress-separation law is manifestly the single most important factor that distinguishes the present analysis from previous treatments [8,9]. The inclusion of the internal stress parameter σ_R is an especially unique feature. Its strong influence on the mechanical response is apparent in Figs. 6 and 7: in Fig. 6 as the comparison between solid $\sigma_m(P)$ curve (data fit for fully bridged crack) and central dashed curve (zero internal stress, zero bridging), indicative of a countervailing lowering and raising of the strength at small and large crack sizes respectively; in Fig.7 correspondingly as the initially falling (c < d)

but ultimately rising T(c) curve (c >> d). We see that the influence of σ_R can be deleterious at small c, but that this deleterious influence may be more than compensated, via the dissipative frictional sliding interaction, at large c. The route to flaw tolerance is therefore a delicate one of balancing positive and negative elements of inbuilt stress states at opposite ends of the flaw-size spectrum.

It is useful to pursue the issue of short cracks vs long cracks in the context of traditional fracture mechanics testing. Some recent experimental results reported by Steinbrech & Schmenkel [12] on a nominally pure alumina of grain size $\ell = 13 \mu m$ are especially well suited for this purpose. Those authors measured crack growth from single-edge-notched beam specimens to obtain T(c) data on the macroscopic scale, and from naturally occurring flaws in four-point-bend specimens to obtain comparative data on the microscopic scale. Their results are plotted in Fig. 11, together with the theoretically predicted curve for the appropriate grain size from our "calibrated" Eq. 22. The theoretical curve appears at least to reflect the broader trends of the rising T(c) curve large c, although we can hardly expect any such extrapolation of the indentation-strength-calibrated curve to provide an accurate representation in this long-crack domain. Conversely, it is evident that there are important features of the T(c) function at small c which may not be readily quantified by experimentation with long-crack specimens. In particular, the falloff in T(c) at c < d associated with internal tensile matrix stresses will generally pass unnoticed in such specimens. This is the domain of short cracks, where microstructure-scale instabilities in the initial growth (e.g. the initial "pop-in" referred to in Sect. 4) can occur.

If this last point concerning short-crack instabilities is not readily

31

apparent in conventional crack-growth tests, it certainly is manifest in one well-documented aspect of the fracture behaviour of ceramics. This is the tendency of those ceramics with large internal stresses to exhibit spontaneous microfracture at some critical grain size. Let us note that the shape of the diminishing $T(c)$ curve in Fig. 7 prior to the first bridge intersection at $c = d$ is independent of grain size l (Eq. 22a). The effect of increasing d will thus be to extend this portion of the $T(c)$ curve further downward. If we were to scale up l such that $T(c)$ were to intersect the c-axis before the condition $c = d$ is satisfied, then pre-existing flaws would become amenable to unstable extension without any external load applied. Hence the phenomenon of spontaneous microfracture may be seen as a natural, limiting consequence of our model.

The implications of the bridging mechanics presented here extend beyond the immediate question of inert strength, to fatigue and lifetime analysis [31] and to wear properties of brittle ceramics [32].

APPENDIX: Calculation of Frictional Debonding Stress-Separation Function

In this Appendix we reproduce the essence of a calculation by Marshall &
Evans [17] for frictional debonding. We assume that debonding begins at the
crack plane and works itself up the matrix-grain interface a distance Y as the
crack walls separate through displacement u, Fig. 2. At first, we suppose
only that shear-lag tractions $\tau(y)$ do exist, and only later connect these
tractions with internal stresses.

Consider an elemental area of matrix-grain interface bounded by y and y +
dy. At equilibrium, the frictional traction τ over this area must be balanced
by the axial internal stress $\sigma(y)$ in the embedded grain, i.e. $\ell^2 d\sigma(y) = -\tau\lambda dy$, or,

$$d\sigma/dy = -\tau\lambda/\ell^2. \tag{A1}$$

This equation may be integrated at constant τ (neglecting any elastic stresses
at y > Y), over y = 0 to y = Y. We take as boundary conditions $\sigma(0) =$
$p_0(\ell^2/2d^2)$ (recall from Eq. 2 that $\ell^2/2d^2$ is area fraction of bridges) and
$\sigma(Y) = p_0$, where p_0 is the stress exerted by the embedded grain in the absence
of any residual stresses. The integration gives

$$p_0 = (\tau\lambda Y/\ell^2)/(2d^2/\ell^2 - 1) \tag{A2}$$

The strain in the grain (measured relative to the strain endured if sliding
were to be prevented [17]) at the debond length Y is

$$u/Y = \tfrac{1}{2}(p_0/E)(2d^2/\ell^2 - 1). \tag{A3}$$

where the factor two is because the strain has a linear gradient along y.

Eliminating Y from Eqs. A2 and A3 gives

$$p_0(u) = (2rE\lambda u/\ell^2)^{1/2}/(2d^2/\ell^2 - 1). \qquad (A4)$$

Now suppose that the friction is Coulombic, i.e. due to residual internal stresses. Then we may write immediately, $r = \mu\sigma_R^-$. In addition, we must replace p_0 by $p_0 + \sigma_R$, to allow for the residual opening force exerted by the embedded grain on the matrix at zero crack-wall displacement [17]. With Eq. 2, these modifications lead to our final constitutive relation for debonding,

$$p(u) = \{(2\mu\sigma_R E\lambda/\ell^2)^{1/2}/(2d^2/\ell^2 - 1)\}u^{1/2} - \sigma_R \qquad (A5)$$

as per Eq. 3 in the text.

ACKNOWLEDGMENTS

REFERENCES

[1] H. Hubner & W. Jillek, *J. Mater. Sci.* 12 117 (1977).

[2] R.W. Steinbrech, R. Knehans & W. Schaarwachter, *J. Mater. Sci.* 18 265 (1983).

[3] R.F. Cook, B.R. Lawn & C.J. Fairbanks, *J. Amer. Ceram. Soc.* 68 604 (1985).

[4] C.J. Fairbanks, B.R. Lawn, R.F. Cook, Y-W. Mai, *Fracture Mechanics of Ceramics*, Vol 8, p. 23. (Edited by R.C. Bradt, A.G. Evans, D.P.H. Hasselman and F.F. Lange) Plenum, New York (1986).

[5] F. Duerler, R. Knehans & R.W. Steinbrech, *J. de Physique* C1 617 (1986).

[6] H. Wieninger, K. Kromp & R.F. Pabst, *J. Mater. Sci.* 21 411 (1986).

[7] P.L. Swanson, C.J. Fairbanks, B.R. Lawn, Y-W. Mai & B.J. Hockey, *J. Amer. Ceram. Soc.* 70 279 (1987).

[8] Y-W. Mai & B.R. Lawn, *J. Amer. Ceram. Soc.* 70 289 (1987).

[9] R.F. Cook, C.J. Fairbanks, B.R. Lawn & Y-W. Mai, *J. Mater. Res.* 2 345 (1987).

[10] P.L. Swanson, *Advances in Ceramics*, Vol. 22. American Ceramic Society, Columbus, Ohio (1988), p.135.

[11] Y-W. Mai, *Materials Forum*. 11 232 (1988).

[12] R.W. Steinbrech & O. Schmenkel, *J. Amer. Ceram. Soc.* 71 C-271 (1988).

[13] Y-W. Mai & B.R. Lawn, *Ann. Rev. Mat. Sci.* 16 415 (1986).

[14] R. Ballarini, S.P. Shah & L.M. Keer, *Eng. Fract. Mech.* 20 433 (1984).

[15] R.W. Rice, R.C. Pohanka & W.M. McDonough, *J. Amer. Ceram. Soc.* 63 703 (1980).

[16] M.V. Swain, *J. Mater. Sci.* 5 1313 (1986).

[17] D.B. Marshall & A.G. Evans, _Materials Forum_ 11 304 (1988).

[18] A.G. Evans, A.H. Heuer & D.L. Porter, _Fracture 1977_, Vol. 1, p. 529. (Edited by D.M.R. Taplin) University of Waterloo Press, Waterloo (1977).

[19] B.R. Lawn & T.R. Wilshaw, _Fracture of Brittle Solids_, Ch. 2. Cambridge University Press, London (1975).

[20] H. Tada, P.C. Paris & G.R. Irwin, _Stress Analysis of Cracks Handbook_. Paris Productions, St. Louis, Missouri (1985).

[21] J.R. Rice, _Treatise on Fracture_ (Edited by H. Liebowitz), Vol. II, Ch. 3. Academic Press, New York (1968).

[22] D.B. Marshall & B.R. Lawn, _J. Mater. Sci._ 14 2001 (1979).

[23] D.B. Marshall, B.R. Lawn & P. Chantikul, _J. Mater. Sci._ 14 2225 (1979).

[24] B.R. Lawn, A.G. Evans & D.B. Marshall, _J. Amer. Ceram. Soc._ 63 574 (1980).

[25] C.A. Handwerker, J.M. Dynys, R.M. Cannon & R.L. Coble, _J. Amer. Ceram. Soc._, in press.

[26] J.F. Shackelford & W.D. Scott, _J. Amer. Ceram. Soc._ 51 688 (1968).

[27] J.E. Blendell & R.L. Coble, _J. Amer. Ceram. Soc._ 65 174 (1982).

[28] A. Reichl & R.W. Steinbrech, _J. Amer. Ceram. Soc._ 71 C-299 (1988).

[29] R.J. Charles & R.R. Shaw, General Electric Report No. 62-RL-3081M.

[30] T. Chantikul, S.J. Bennison & B.R. Lawn, in preparation.

[31] S. Lathabai & B.R. Lawn, _J. Mater. Sci._, in press.

[32] S.J. Cho, B.J. Hockey, B.R. Lawn & S.J. Bennison, _J. Amer. Ceram. Soc._, in press.

FIGURE CAPTIONS

1. Schematic geometry of bridged interface, in rectangular "lattice" representation of microstructure: (a) projection normal to crack plane; (b) profile view along crack plane. Shaded areas denote bridging grains. Characteristic dimensions l, grain size, d, bridge spacing. (The factor 2 in our definition of the bridge separation is so that later in Fig. 4 we may conveniently delineate the region between no-bridging and bridging simply by c = d.)

2. Stages of frictional grain detachment from matrix at separating interface. (a) Initial debonding stage, with progression of shear crack up the grain-matrix walls to 2y = 2Y at separation 2u. (b) Subsequent sliding pullout to disengagement at 2u = 2u*. Long grain dimension L is limiting value that 2Y or 2u* may attain.

3. Schematic plot of p(u) closure function, Eq. 5. Area under the composite, solid curve is a measure of the energy absorbed by the debonding-pullout bridging process.

4. Growth of penny-like crack in bridging field; (a) side view, (b) projection view. Crack experiences only matrix tensile stresses up to first intersection with bridges at c = d. Thereafter, internal stresses rapidly average out to zero across crack plane, and frictional closure forces dominate.

5. Coordinate system for crack-interface bridging. C denotes crack tip, Z the edge of the bridging zone at $c = d$.

6. Plot of $\sigma_m(P)$ for selected alumina material of grain size $\ell = 20\ \mu m$. Points with standard deviation error bars are experimental data from reference [3]. Solid curve is best fit of bridging theory to these points. Dashed curve at extreme left is corresponding hypothetical curve for same material with matrix tensile stresses present but with no bridging tractions $(T = T_0 - T'_\mu)$; central dashed curve corresponds to same material but with no bridging or internal stresses $(T = T_0)$.

7. Deconvoluted toughness $T(c)$ function, Eq. 22, for selected alumina, corresponding to data fit in Fig. 6. The falloff in the function below T_0 prior to first bridge intersection at $c = d$ is indicative of the initially deleterious effect of (tensile) matrix internal stresses. Thereafter the crack becomes dominated by the beneficial influence of frictional grain pullout tractions, whence the curve rises above T_0 again to its saturation value T_* at $c = c_*$.

8. Plots of $\sigma_a(c)$, Eq. 25, for selected alumina, using the parametric determinations from Figs. 6 and 7. Curves are for indentation loads P covering the data range in Fig. 6: a, 0.2 N; b, 1 N; c, 2 N; d, 10 N; e, 100 N; f, 1000 N.

9. Plots of $\sigma_m(P)$ for alumina materials of grain size $\ell = 3$ and 25 μm. Points with standard deviation error bars are experimental data from reference [3]. Solid curves are predictions of bridging theory appropriate to these grain sizes, using best-fit parameters from the reference alumina material ($\ell = 20$ μm) from Fig. 6. (Reference $\sigma_m(P)$ curve included here as dashed curve for comparison.)

10. Strength vs grain size for polycrystalline alumina. Data points from Ref. [29], means and standard deviations of inert bend strengths for specimens with "natural" flaws (as-fired "Lucalox®" specimens). Solid line from bridging theory, predicted plateau strengths for natural flaws, using best-fit parameters from the reference alumina material. (Arrow on data point at $\ell = 66$ μm indicates a material with exceptionally broad grain size distribution [29].)

11. Comparison of T(c) data obtained by Steinbrech & Schmenkel [12] (shaded areas) on a nominally pure alumina of grain size $\ell = 13$ μm using surface cracks (SC) in four-point bend and single-edge-notched-beam (SENB) and specimens with small-scale flaws with theoretically-predicted curve from present analysis.

(a)
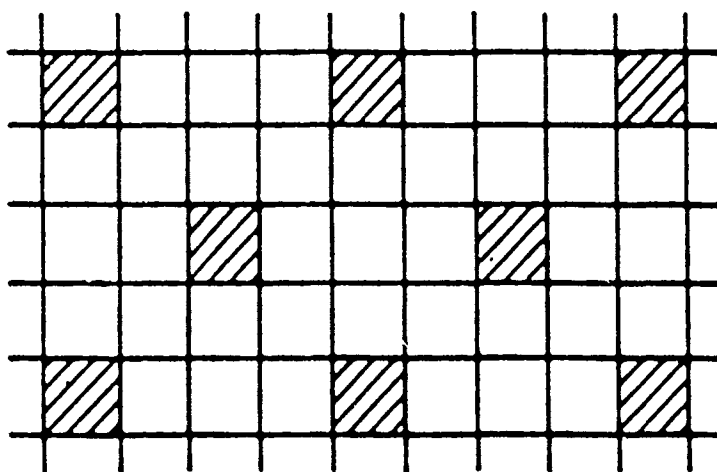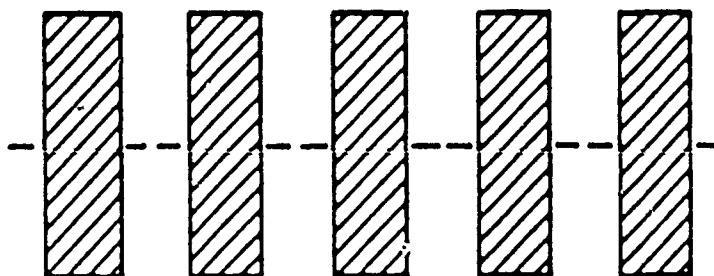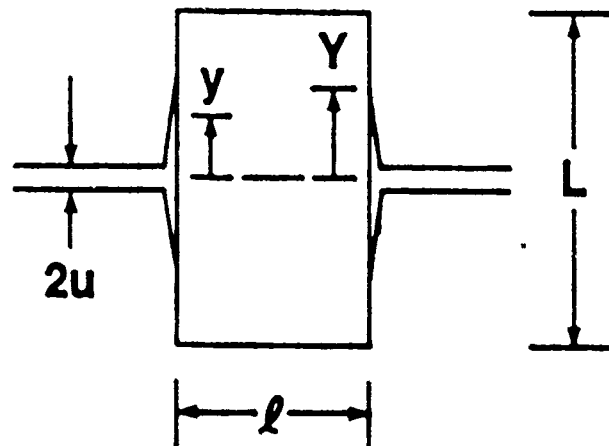
(b)

(a) Debonding

(b) Pullout
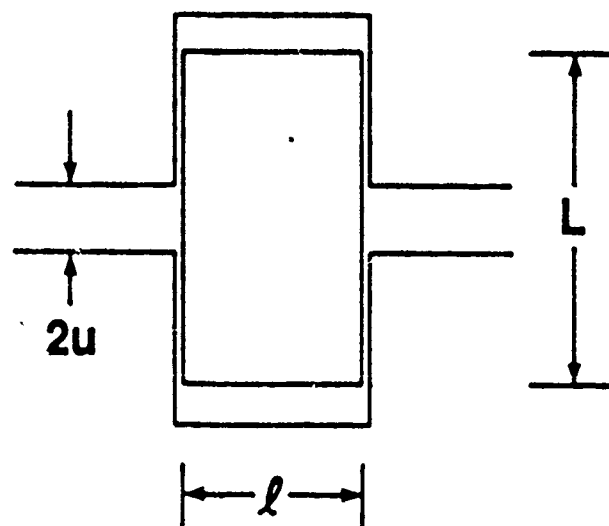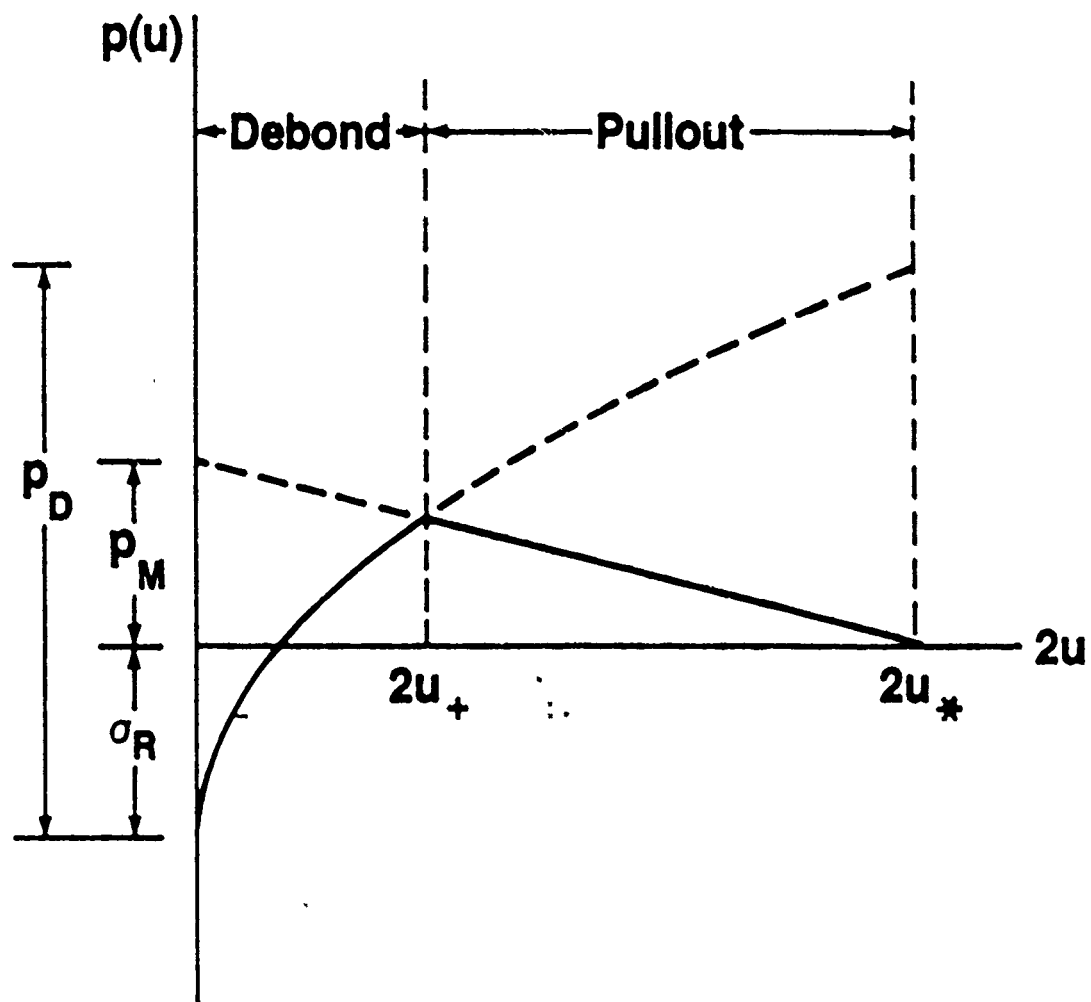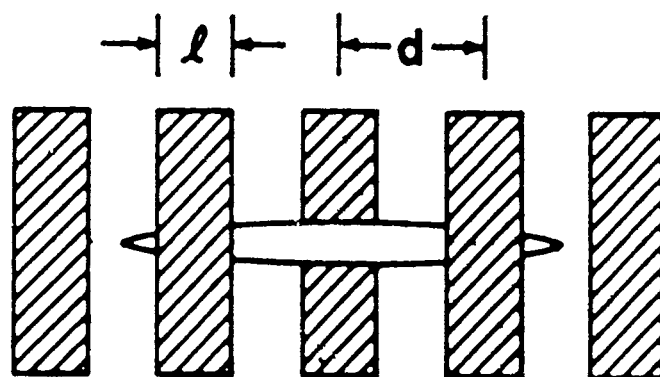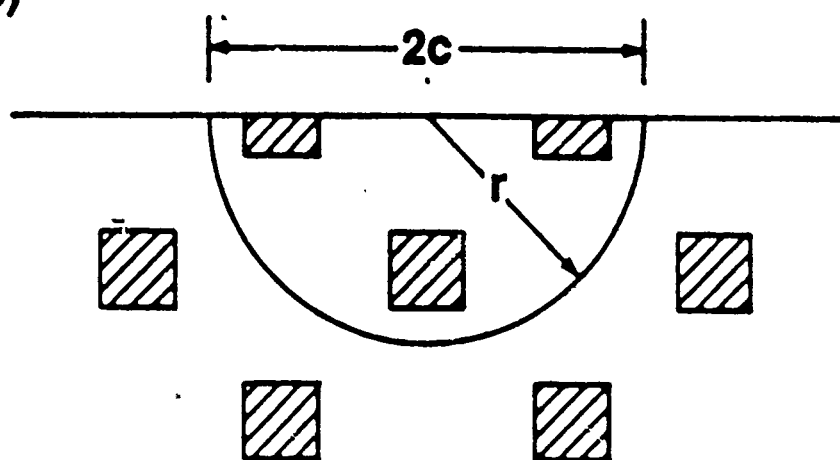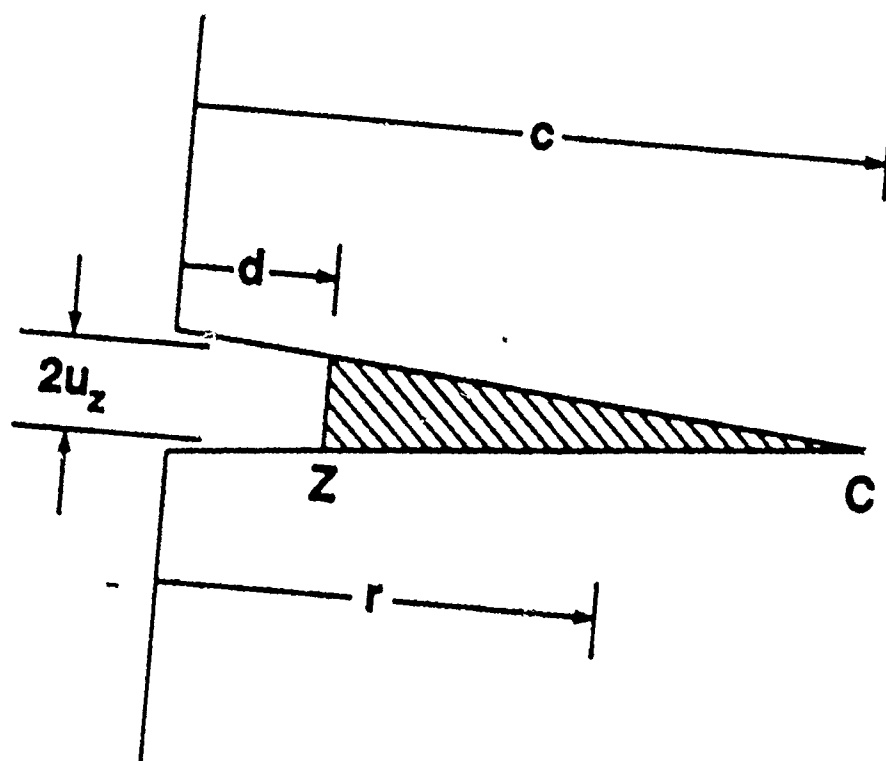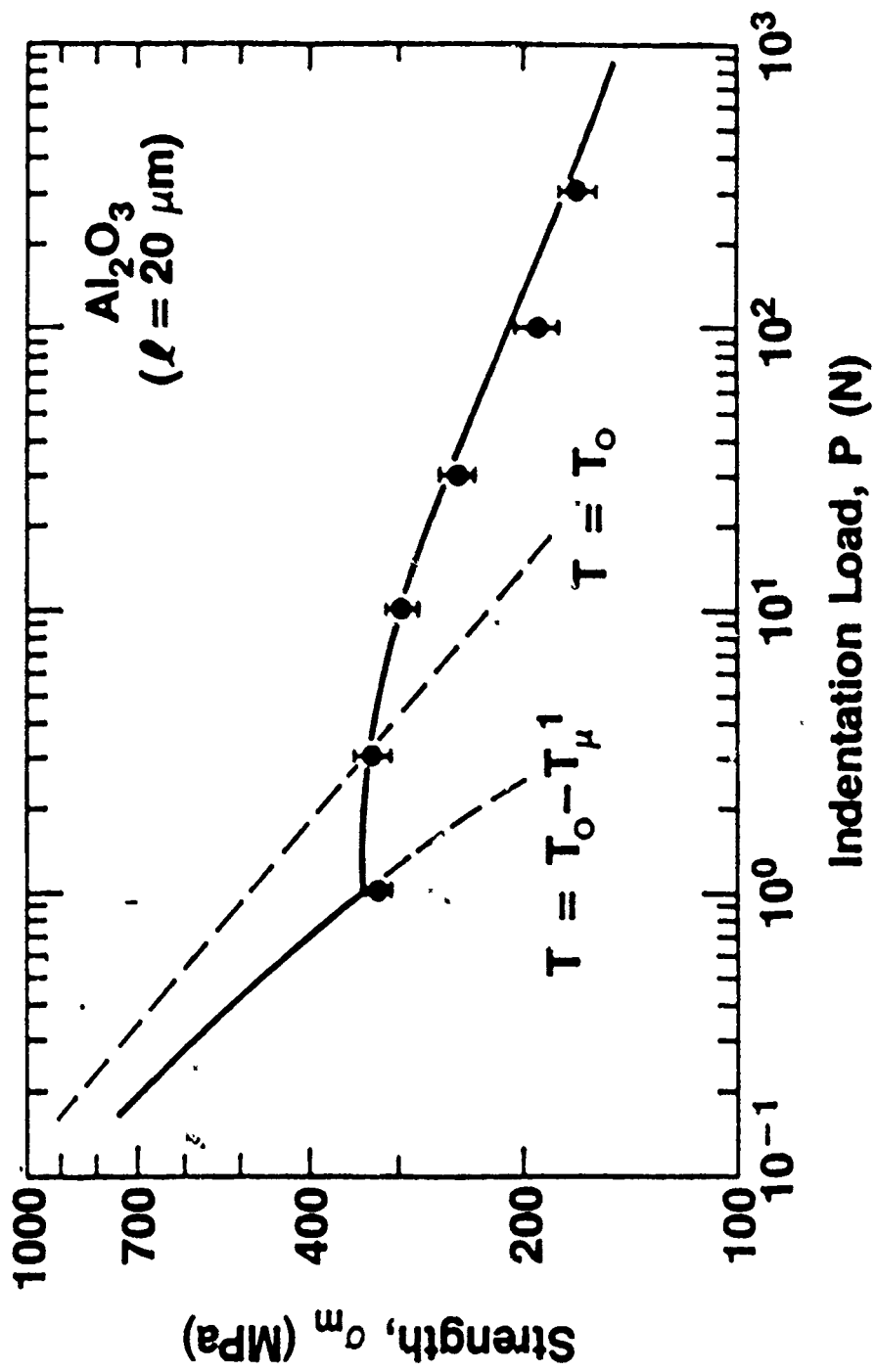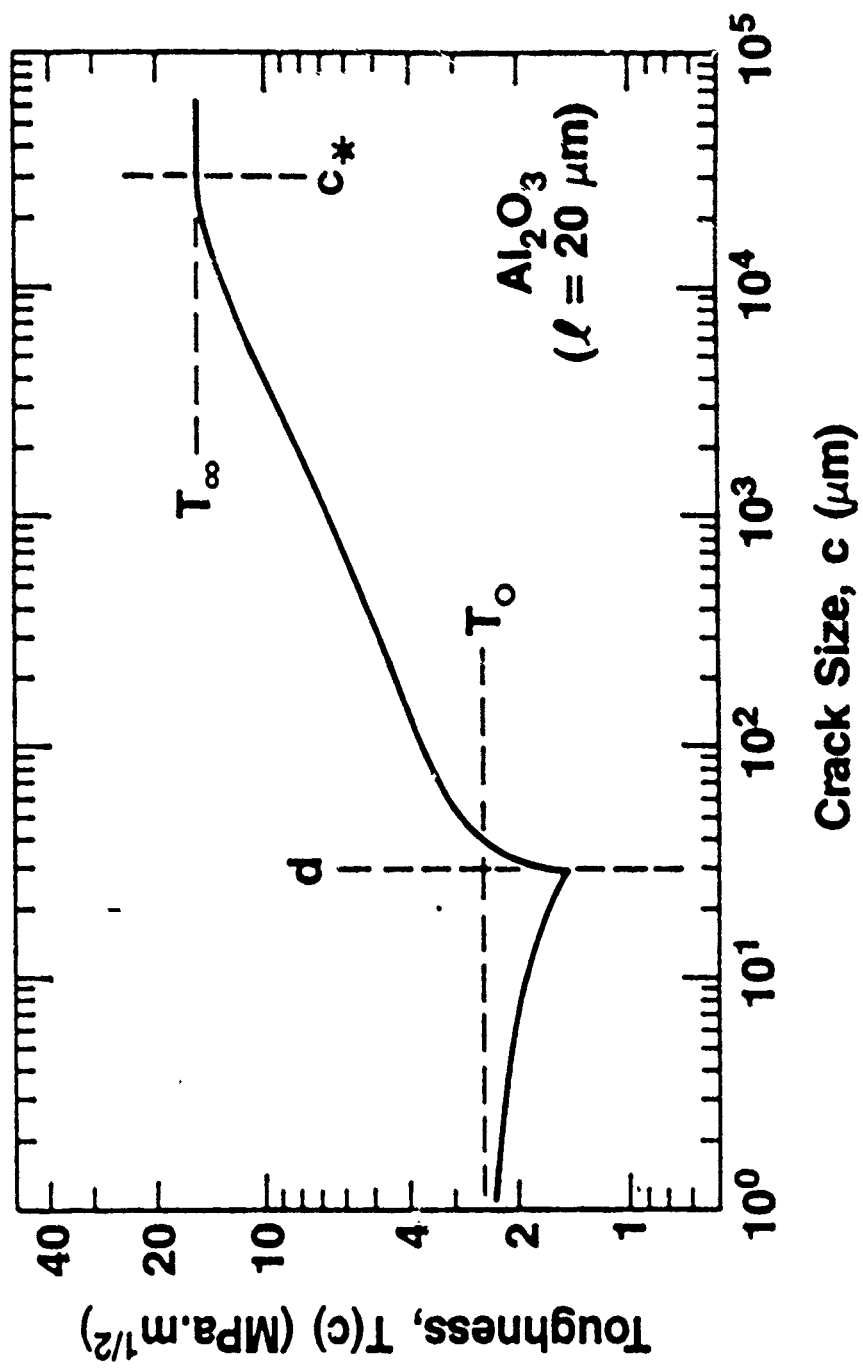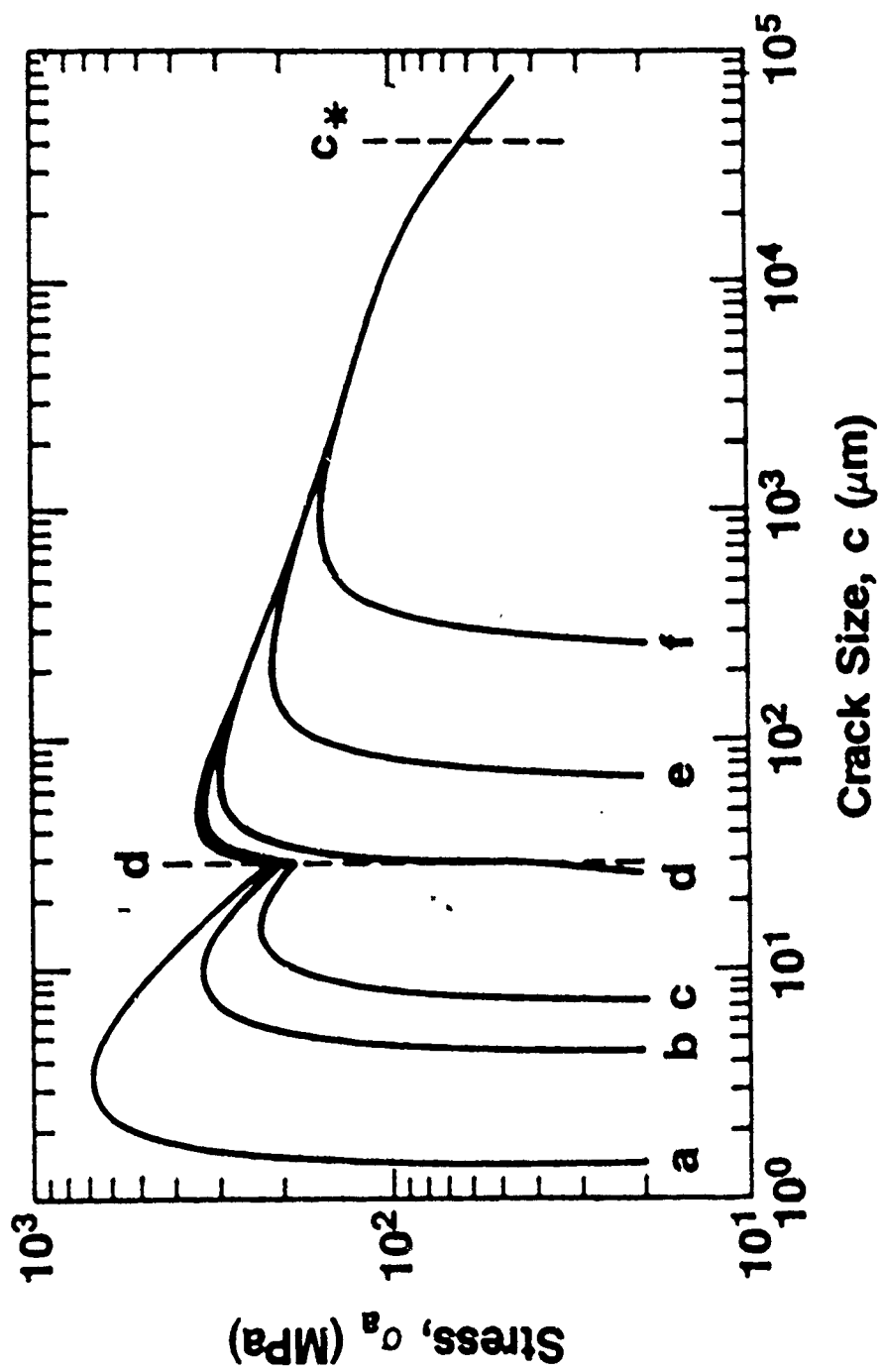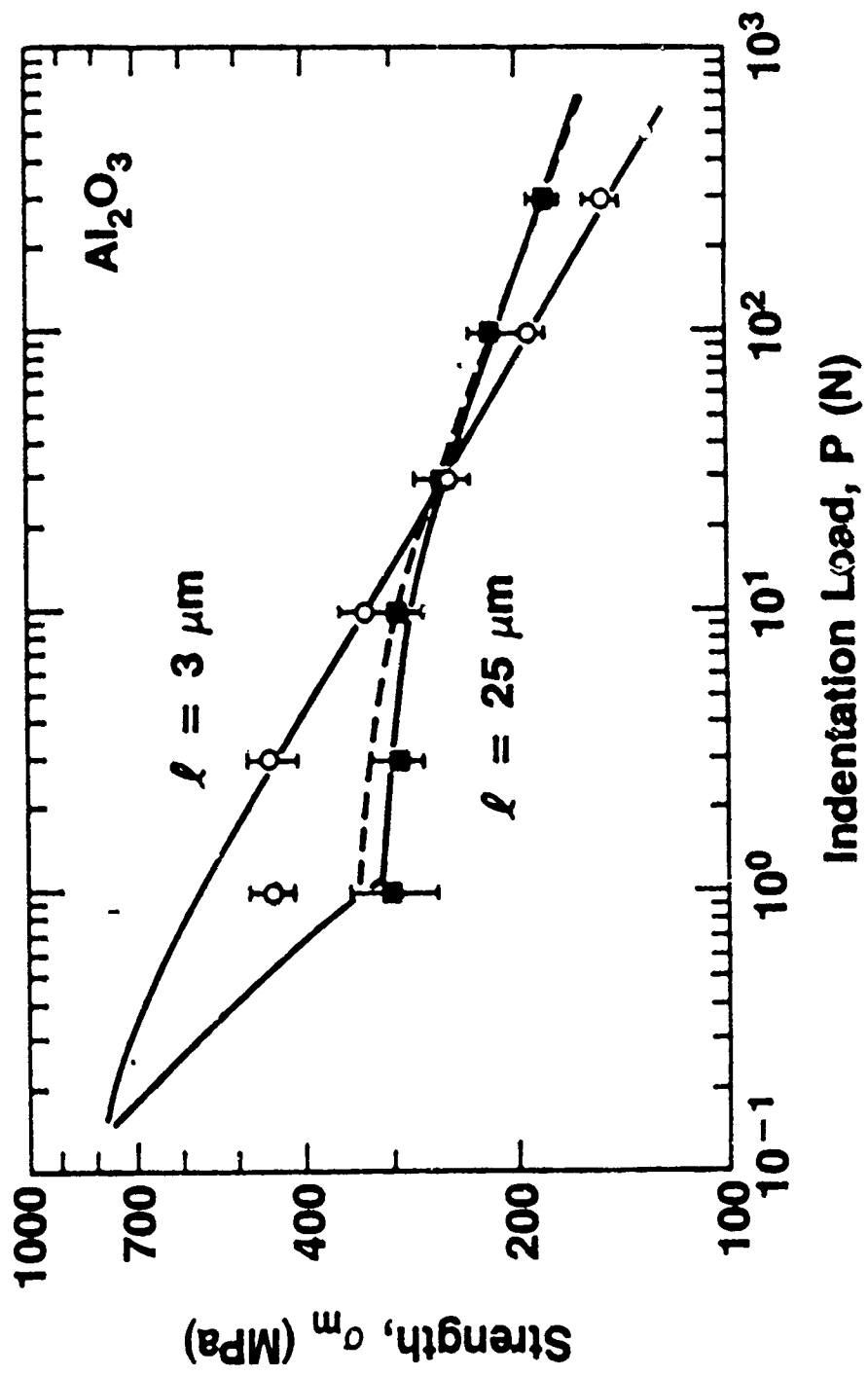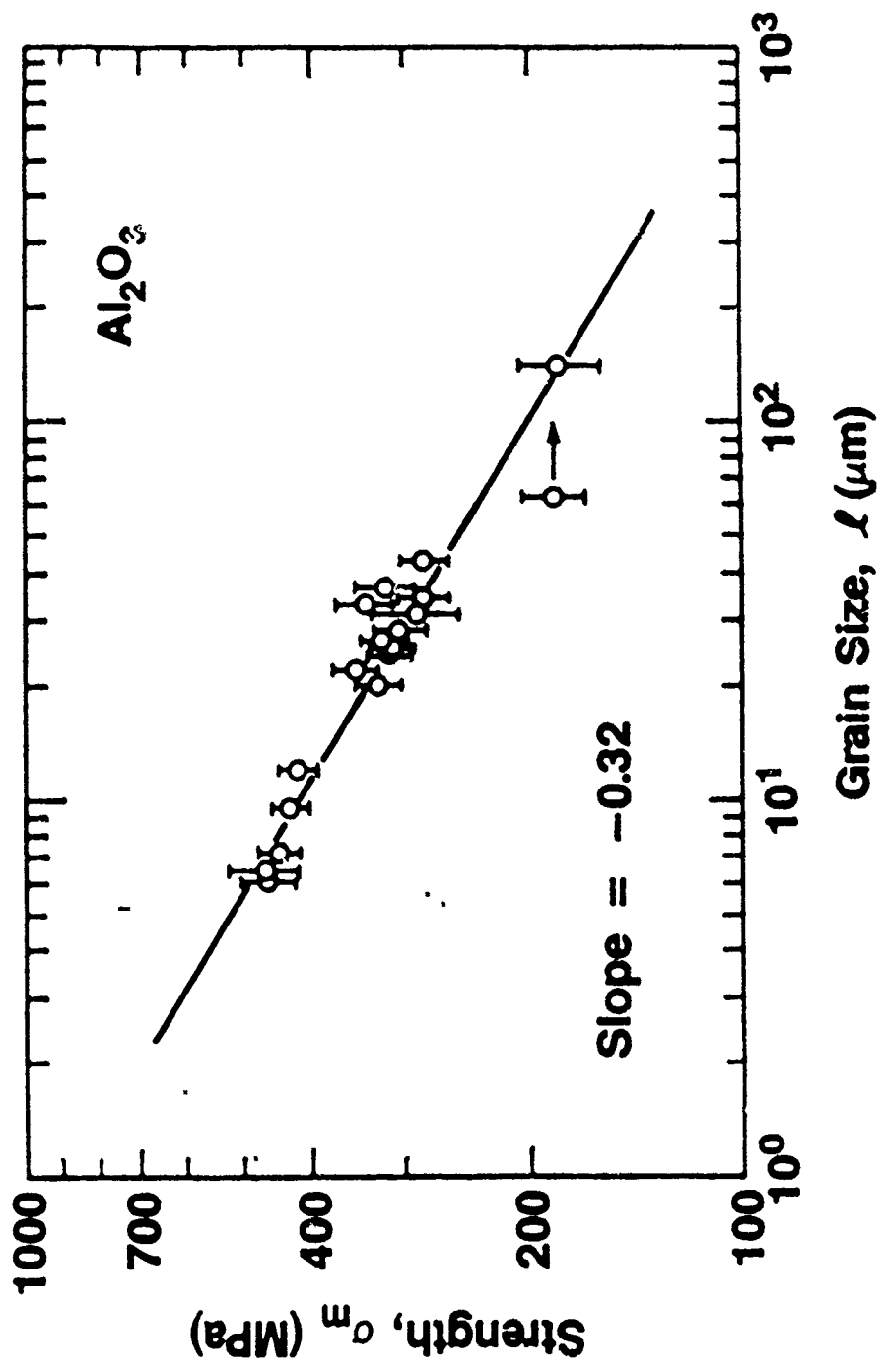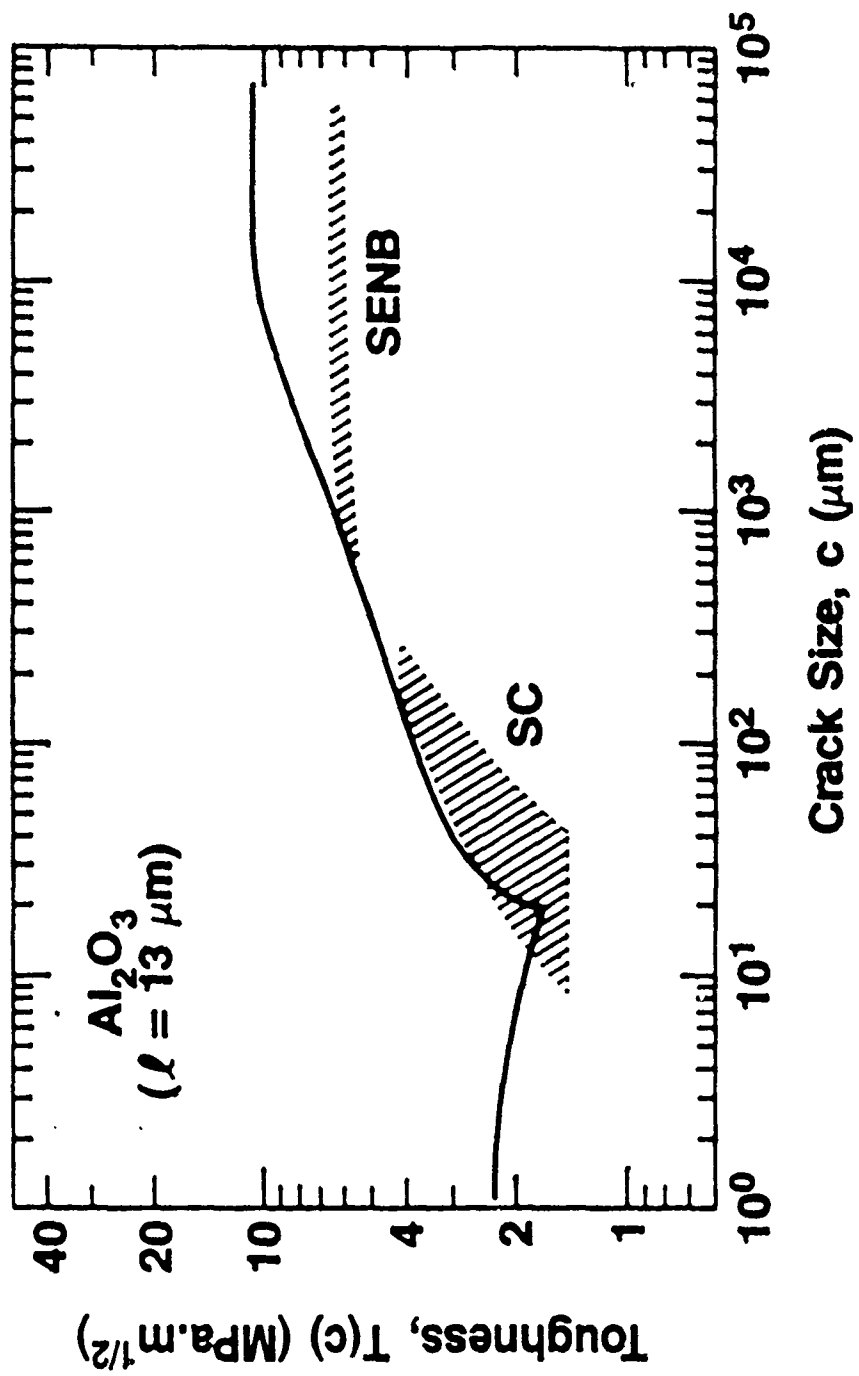
2

3

(a)

(b)

Figure showing Strength, σ_m (MPa) versus Indentation Load, P (N) for Al_2O_3 ($\ell = 20\ \mu m$). Curves labeled $T = T_o$, $T = T_o - T_\mu^1$.

7

Crack Size, c (μm)

Toughness, T(c) (MPa·m$^{1/2}$)

Al_2O_3
($\ell = 20$ μm)

$c*$

T_∞

T_o

d

Stress, σ_a (MPa) vs. Crack Size, c (µm)

Toughness, T(c) (MPa.m$^{1/2}$) vs Crack Size, c (μm)

Al_2O_3
($\ell = 13$ μm)

SENB

SC

12. "Fatigue Limits in Noncyclic Loading of Ceramics With Crack-Resistance Curves"

S. Lathabai and B.R. Lawn

J. Mater. Sci., in press.

ABSTRACT

Fatigue properties in the noncyclic loading of ceramics with R-curves are studied. Particular attention is directed to the potential role of R-curves in the enhancement of fatigue limits. A numerical algorithm for solving the appropriate differential equations of rate-dependent failure is developed. Our formalism specifically incorporates a crack-size dependent toughness function, based on grain-localised interfacial bridging, and a hyperbolic-sine velocity function, representative of a fundamental activation process. In a case study, dynamic fatigue (constant stressing rate) and static fatigue (constant applied stress) data for a coarse-grained alumina with a pronounced R-curve are analysed. With foreknowledge of the toughness parameters, the intrinsic crack-tip velocity function is deconvoluted. This intrinsic function is distinguished from the usual "apparent", or "shielded", (and demonstrably nonunique) function determined directly from the external load. It is confirmed that the R-curve, by virtue of its stablising influence on the crack growth, significantly enhances the fatigue limit, and confers the quality of "flaw tolerance" on fatigue lifetimes.

1

1. INTRODUCTION

Brittle solids are susceptible to delayed failure induced by "slow" growth of flaws to critical dimensions [1]. In the ceramics community such delayed failure is referred to as "fatigue", even for noncyclic loading conditions, e.g. constant stress ("static" fatigue) or constant stressing rate ("dynamic" fatigue). Experimental data are usually represented as linear plots on appropriate (logarithmic-coordinate) fatigue diagrams (applied stress vs failure time, or failure stress vs stressing rate), the slopes of which determine a fatigue "susceptibility". Embodied in most analytical treatments of these plots are certain idealisations concerning the fracture mechanics, e.g. that the strength-controlling flaws are free of any residual driving forces and that the material has a single-valued toughness, such that the (inverse) susceptibility is directly identifiable with the exponent in a power-law crack velocity relation [2,3]. Characteristic features of such treatments are: (i) an implied uniqueness of the crack velocity vs mechanical energy release rate (v-G) function for a given material-environment system; (ii) a critical dependence of the ensuing lifetime characteristics on the initial flaw size.

An important shortcoming of the conventional log-linear analysis of time-to-failure behaviour in ceramics is the lack of provision for a fatigue limit. The existence of a bounding applied stress, σ_{lim} say, below which a component effectively has infinite lifetime is an attractive prospect in engineering design. Efforts to detect such lower bounds as deviations from linear response in the long-lifetime domain of fatigue diagrams have been few, due partly to the notorious scatter in strength-related data and partly to self-

2

imposed short-term restrictions on data accumulation. This despite a well established precedent for analogous fatigue limits in the metals literature [4]. A study by Cook [5] on sapphire, using indentation flaws to reduce the scatter and extend the range of constant stressing rate data, is one exception. That author attributes the observation of an asymptotic lower limit in the sapphire strength to a threshold in the underlying crack velocity function, i.e. to the existence of a zero velocity state at (positive) nonzero applied load. Cook used a power-law velocity function in stress intensity factor K with cutoff to describe this threshold; we shall assert that the velocity function is written more justifiably as a hyperbolic sine in $G - 2\gamma$, where γ is a thermodynamic surface energy. Direct measurements of rate-dependent crack growth in large-scale crack specimens of other brittle materials [6,7] suggest that velocity thresholds, and thence fatigue limits, might be more prevalent in ceramics than previously suspected. In any event, it seems apparent that anything we could do to the material system to augment this threshold would surely stand to improve lifetime characteristics.

There is a way in which improvement of this kind might be achieved, and that is to make use of the crack-stabilising effect of R-curve (or T-curve) behaviour, i.e. a systematically increasing crack resistance R (or, equivalently, toughness T), with extension [15]. R-curve behaviour arises because of the shielding of the crack by some microstructure-associated energy-dissipative process in the region immediately surrounding the tip. It is now appreciated that many nontransforming ceramics exhibit such behaviour [8-16]. It has been argued on qualitative grounds that the restraining influence of shielding should extend to rate dependent crack growth [17], and there is some experimental evidence in support of this contention in zirconia

3

material systems [18]. However, the possibility of using shielding to improve lower-limit strength levels does not seem to have attracted much attention in the literature.

In the present paper we explore this last possibility. As a case study, we examine a material with pronounced R-curve behaviour, a coarse-grained alumina of a kind that has been investigated extensively in inert-environment (equilibrium) indentation-strength studies [10,12,14,15]. The R-curve behaviour in polycrystalline alumina is due to persistent grain-localised bridging at the interface behind the (intergranularly) propagating crack tip. In developing a fatigue formalism we proceed in a manner similar to that described in earlier indentation-flaw fatigue studies [19-23] for materials with single-valued toughnesses, but with proper refinements. Now, we incorporate specific information on the R-curve (evaluated from control, inert-environment indentation-strength tests [15] on the same material) into a general hyperbolic sine v-G function to establish a starting differential equation. A numerical algorithm is thereby set up to obtain lifetime solutions for prescribed time-dependent applied load states (constant stressing rate, constant stress). The algorithm is used to fit dynamic and static fatigue data on our alumina, and thence to determine unknown parameters in the v-G function.

More general implications of the analysis are then discussed: (i) We confirm that the R-curve, because of its stablising influence on the crack growth, strongly enhances the fatigue limit. Indeed, we argue that a fatigue limit may even be apparent in materials that exhibit no natural threshold in the v-G relation. (ii) We stress that the calibrated crack velocity function is the intrinsic v-G relation for the material-environment system, i.e. the

4

fundamental relation that expressly determines the crack-tip motion. This relation is to be distinguished from the "engineering" v-G_a relation that would normally be obtained by monitoring the external load on the system. It is suggested that the intrinsic velocity relation may not be readily obtained in traditional large-crack tests, because of a history-dependence of the shielding component in G. Consequently, contrary to conventional expectation, the apparent, v-G_a relation will generally not be unique. (iii) We show that the fatigue lifetimes are not strongly dependent on initial flaw size; the quality of flaw tolerance in the strength characteristics for materials with R-curves [24] extends to fatigue properties.

Finally, the versatility of the procedure is indicated; once the velocity equation is calibrated, the algorithm may be used for a priori predictions of the fatigue response in other, potentially more complex (e.g. cyclic) loading modes.

2. FRACTURE MECHANICS

In this section we outline the theoretical basis for determining failure lifetimes for ceramics with threshold crack velocity functions and with rising R-curves. We focus specifically on nontransforming materials whose R-curve is attributable to crack-interface bridging, although it is emphasised that the logical procedure for the analysis will be the same for other crack resistance processes. We start by writing expressions for the crack-size dependence of the mechanical energy release rate G(c), or the stress intensity factor K(c), incorporating the microstructural features that account for the toughness

5

variation. Then we combine these expressions with the crack velocity relation v(G) to introduce a criterion for rate-dependent extension. Given the time dependence of the applied stress, $\sigma_a(t)$, a differential equation for the crack growth evolution can be constructed. The aim of the exercise is to evaluate this differential equation to determine the failure time, i.e. the time to take the initial strength-controlling flaw to a critical dimension for unlimited unstable propagation. Our analysis will be directed to controlled indentation flaws, but we stress at the outset that the formulation in this section is applicable to all flaw types.

2.1 Crack Driving Force and the R-Curve

Consider first the mechanical driving force acting on the crack tip. As we shall argue in the next subsection, it is useful to express this driving force ultimately as a mechanical energy release rate G. For the special case of crack propagation in the absence of any environmental effects, the fundamental, Griffith condition for crack extension is expressible in terms of the energy release rate $G_a(c)$ at the crack tip,

$$G_a = 2\gamma_0, \qquad \text{(equilibrium)} \qquad (1)$$

where γ_0 is the fracture surface energy in inert atmospheres. In specifying γ_0 it is important to identify the mode of fracture: for our case study in Sect. 3 below we shall be concerned primarily with a polycrystalline material that shows essentially intergranular fracture, so that γ_0 must ultimately be relatable to a grain boundary energy.

To make full use of the superposability of linear stress fields it is

6

convenient to formulate the problem in terms of stress intensity factor notation K. Accordingly, we seek an expression for $K_*(c)$, the net K-field experienced at the crack tip, and convert to $G_*(c)$ using the plane-strain transformation relation

$$G_* = K_*^2/E' \qquad (2)$$

where $E' = E/(1 - \nu^2)$, with E Young's modulus and ν Poisson's ratio [25]. The net stress intensity factor will generally be made up of three components:

$$K_*(c) = K_a(c) + K_r(c) + K_\mu(c). \qquad (3)$$

(i) $K_a(c)$ is the familiar contribution from the externally applied loading system. In most traditional treatments this is the only component that is considered. (ii) $K_r(c)$ is the contribution from any residual local stress fields associated with the formation of the crack. This is certainly an important term for the indentation flaws to be considered later, and may also be a significant factor in many naturally occurring flaw types. (iii) $K_\mu(c)$ is the contribution from the microstructural elements that are responsible for the R-curve. It is usually (not necessarily always) negative (closure field). The second and third terms in Eq. 3 together effectively shield the crack tip field from the remote loading: it is only when these two terms are zero that we may revert to the simplistic identification of K_a with K_* that is implicit in most fatigue analyses for ceramic materials.

We need to specify the form of $K_\mu(c)$ for materials that exhibit R-curve behaviour by virtue of a crack-interface bridging mechanism. In the most recent analysis [15], the bridging restraint is modelled in terms of a "tail-dominated" stress-separation constitutive relation for interlocking grains on

7

either side of the crack interface. The interlocking is assumed to be governed by internal, matrix thermal expansion mismatch stresses, which "clamp" the bridging grains as the opposite crack walls separate. The bridges break by first debonding along the grain boundaries, and then sliding at these constrained boundaries until separation is complete. Coulomb friction at the grain-matrix interface during the latter, pullout stage accounts for the bulk of the energy dissipation responsible for the rising R-curve.

Suppose that our bridged crack system has essentially penny-like geometry, Fig. 1, as is pertinent to many flaw types and especially to indentation flaws. The solutions for the microstructural stress intensity factor may be derived in the pullout-dominated limit of a linearly diminishing constitutive relation between closure-stress p and (half) crack-opening displacement u [15];

$$p(u) = p_M(1 - u/u_m), \qquad (0 \le u \le u_m) \qquad (4)$$

where p_M is the maximum resistance stress (at u = 0) and u_m is (half) the wall-wall displacement at grain-matrix disengagement (at p = 0). These last two parameters may be written more explicitly for rectangular, equiaxed microstructures as [15]

$$p_M = (4\mu\sigma_R u_m \ell/d^2)(2d^2/\ell^2 - 1) \qquad (5a)$$

$$u_m = \epsilon_\ell \ell/2 \qquad (5b)$$

with ℓ mean grain diameter, d bridge spacing, μ coefficient of sliding friction, σ_R magnitude of the internal stress, and ϵ_ℓ bridge rupture strain.

The solutions may be subdivided into three domains [15]:

(i) __Precursor Tensile Zone__ (c < ɛ). Within this small-crack region no bridges are intersected, and the crack experiences only matrix tensile stresses $+\sigma_R$. There is a net driving force,

$$K_\mu(c) = \psi\sigma_R c^{1/2},\tag{6}$$

where ψ is a geometry-dependent coefficient appropriate to penny cracks.

(ii) __Bridging Zone__ (c ≳ d, 0 ≤ u ≤ u_m). The crack intersects bridges, and thereby has a positive component due to the persistent matrix tensile stresses and a countervailing component due to the integrated effect of the bridging tractions in Eq. 4. In the approximation of "small shielding" (appropriate to ceramics with modest toughening [15]) we derive

$$K_\mu(c) = \psi\sigma_R c^{1/2}[1 - (1 - d^2/c^2)^{1/2}] - (E'p_M/K_*)[u_z(1 - u_z/2u_m)]\tag{7}$$

where u_z is (half) the crack-opening displacement at the stationary edge of the closure zone, i.e. location Z at r = d in Fig. 2. The quantity $u_z(c)$ is determined separately from the Sneddon approximation for the crack profile equation at tip field K_*,

$$u_z(c) = (\psi K_*/E')[(c^2 - d^2)/c]^{1/2}.\tag{8}$$

(iii) __Saturation Zone__ (c >> d, u ≥ u_m). Ultimately, the first-intersected bridge at Z is pulled out and the bridging zone translates along with the crack. In this large-bridging domain only the second, closure term in Eq. 7 is significant, and this reduces to

$$K_\mu(c) = - E'p_M u_m/2K_*.\tag{9}$$

9

We note that K_μ depends on K_* in Eqs. 7-9, so that Eq. 3 becomes an implicit function for the crack-tip stress intensity factor.

2.2 Crack Extension Condition and the Velocity Function

Now consider the v-G relation that defines the fundamental kinetic condition for crack growth. We reiterate that the proper mechanical energy release rate in this relation is that experienced at the crack tip, i.e. G_*. We alluded in Sect. 1 to the shortcomings of the commonly used power-law function. The sole justification for retention of the empirical power-law function in traditional reliability formalisms has been the closed-form integrability of the ensuing fatigue lifetime differential equation [1-3]. However, with the introduction of the complex R-curve phenomenology into the $G_*(c)$ and $K_*(c)$ relations (Sect. 2.1), closed-form solutions are no longer feasible; there is thus nothing to be lost by introducing a physically-based, if more complex, velocity function, in particular one that provides for a threshold.

Accordingly, we resort to a hyperbolic sine function, based on the underlying notion of stress-enhanced thermal activation over atomically localised energy barriers [5,26-28]:

$$v(G_*) = v_0 \sinh[(G_* - 2\gamma_1)/2\Gamma], \qquad (2\gamma_1 \leq G_* \leq 2\gamma_0) \qquad (10a)$$

$$v(G_*) = 0, \qquad (2\gamma_1 > G_*) \qquad (10b)$$

$$v(G_*) = v_T, \qquad (2\gamma_0 < G_*) \qquad (10c)$$

where γ_1 is the fracture surface energy in the presence of the reactive

10

environment (i.e. lowered from γ_0), v_0 and Γ are intercept and slope (susceptibility) parameters, and v_T is a terminal velocity ($\approx 10^3$ m.s^{-1}). Again, the value of γ_1 is that corresponding to intergranular fracture. The velocity function $v(G_*)$ is sketched in Fig. 3. Note the provision in Eq. 10a for a threshold. The insistence that the velocity be zero at $G_* < 2\gamma_1$ in Eq. 10b is consistent with the practical experience that cracks generally do not heal in polycrystalline materials. At $G_* > 2\gamma_0$ the crack is able to propagate even in the absence of reactive environment (cf. Eq. 1), and rapidly attains dynamic velocities. Within these two cutoff extremes the velocity closely approximates an exponential dependence on G_*.

2.3 Differential Equation for "Static" and "Dynamic" Fatigue of Indentation Flaws

Finally, we develop the formalism for crack systems in time-dependent applied stress fields, $\sigma_a = \sigma_a(t)$, as pertains to strength considerations. For uniform stresses we may immediately write

$$K_a(c) = \psi \sigma_a c^{1/2} \qquad (11)$$

for the applied stress intensity factor in Eq. 3. The applied stress states $\sigma_a(t)$ of specific interest to us here are those of so-called "static fatigue"

$$\sigma_a = \text{const.}, \qquad (12a)$$

and "dynamic fatigue"

$$\dot{\sigma}_a = \sigma_a/t = \text{const.} \qquad (12b)$$

11

Also of specific interest here are indentation flaws. This flaw type is distinguished by a residual contact field [29]

$$K_r(c) = \chi P / c^{3/2} \qquad (13)$$

with P the contact load and χ an elastic-plastic coefficient [14,29].

Writing $v = dc/dt$, Eq. 10 may be combined with Eqs. 2-9 and 11-13 into a differential equation for $c(t)$ at fixed load P and stress σ_a or stress rate $\dot{\sigma}_a$. This composite differential equation has to be solved for the time to grow the crack from an initial equilibrium state to final instability, i.e. the "time to failure". Usually (but not always - see Sect. 4), the initial crack size c_i is calculated from Eqs. 2-9 by setting $G_*(c_i) = 2\gamma_1$ (zero velocity) at $K_a = 0$; likewise, the final crack size c_f is determined as the configuration $G_*(c_f) = 2\gamma_0$ (dynamic velocity) at which the system achieves uninterrupted propagation (see Sect. 3).

It is pointed out that Eqs. 11-13 are special cases, and that our formalism in Sects. 2.1 and 2.2 is readily extendable to any general loading configuration, $K_a[\sigma_a(t)]$, and to any residual stress state for the strength-controlling flaw, $K_r(c)$.

2.4 Numerical algorithm for solution of fatigue differential equation

We have indicated that the general differential equation for kinetic crack growth in materials with R-curves has no closed-form solution. It is necessary to resort to numerical analysis. Consequently, a suitably expanded version of an earlier computer algorithm [19,20] for determining static and dynamic fatigue times is employed. The algorithm increments c and t in Eq. 10

in a Runge-Kutta stepwise integration procedure, readjusting $\sigma_a(t)$ (where necessary, e.g. dynamic fatigue), hence $G_a(c,t)$ (after iterative solution of implicit expression for K_a, Eq. 3 - see Sect. 2.1), at each step.

Special attention to the stepping procedure in this algorithm is in order, owing to the typically enormous range of crack velocities embraced in the evolution to failure; a fixed increment in time runs the very clear risk of stalling the evaluation in the regions of slow growth and, conversely, of blowing it up in the regions of fast growth. It is necessary to adopt a stepping strategy that provides a reasonable compromise between accuracy and time of computation. Consequently, our algorithm incorporates computational elements that allow for automatic readjustment of the increments, according to the instantaneous velocity. One of these elements involves an inversion of the underlying differential equation, $dc/dt = v(c,t)$: at low velocities (i.e. relative to v_0 - see Fig. 2), the equation retains its normal form - _time_ is incremented, and the corresponding crack step determined from $dc = v(c,t)dt$; conversely, at high velocities, we rewrite the equation as $dt/dc = 1/v(c,t)$ - now _crack size_ is incremented, and the Runge-Kutta routine suitably modified to determine the time step $dt = dc/v(c,t)$.

Another critical element in our algorithm is a provision to allow for intermediate, "pop-in" instabilities in the crack evolution. Such pre-failure jump-arrest events are indeed characteristic of materials with R-curves [12,13,30]. Consequently, a routine for predetermining all the unstable crack sizes, by solving Eq. 1 at $dG_a/dc > 0$ in conjunction with Eqs. 2-9, is used to ensure that the program is not stopped before the final, true failure instability is attained.

Once the R-curve and crack velocity parameters are specified, we may

13

predetermine the fatigue characteristics for a given material-environment system: static fatigue curves directly as the times to failure t_f at specified applied stresses σ_a; dynamic fatigue curves as the fatigue strengths $\sigma_f = \dot{\sigma}_a t_f$ at specified stressing rates $\dot{\sigma}_a$.

3. RESULTS

3.1 Experimental Procedure

Let us now demonstrate the formalism by analysing indentation-strength data on a commercial polycrystalline alumina ceramic, nominally pure (< 0.1 % additive) with grain size $\ell \simeq 23$ μm. [1] The material is ostensibly the same as used in preceding studies [10,12,15,23], but was obtained from a new batch. The intergranular-fracture, crack-interface bridging mechanism considered in Sect. 2.1 has been identified in this material [12], and the associated R-curve characteristics documented [15]. Dynamic fatigue test results in water have also been reported [23]. However, to avoid possible discrepancies from batch-to-batch variations, we obtain an entirely fresh set of data here.

Accordingly, specimens were tested in the form of discs, approximately 22 mm diameter and 2 mm thickness. Controlled Vickers indentation flaws were introduced at the centres of the prospective tensile faces of each specimen. The indentations were immediately covered with silicone oil, for inert strength tests, or with water, for fatigue tests. A biaxial loading fixture, with a flat circular punch of diameter 4 mm on three-point support of diameter

---

[1]   Vistal grade Al_2O_3, Coors Ceramic Co., Golden, CO

14

19 mm, was used to break the specimens, and the surface tensile stress σ_a computed from thin plate formulae [10]. For the determination of inert strengths $(\sigma_a = \sigma_m)$, the contact loads covered a broad range (P = 3-300 N), and the breaks made at fast stressing rates (> 10^4 MPa.s^{-1}). For the fatigue tests, a single, intermediate load (P = 30 N) was used. Dynamic fatigue strengths $(\sigma_a = \sigma_f)$ were determined over sever.. decades of constant stressing rates $(\dot{\sigma}_a = 10^{-3}\text{-}10^{+4}$ MPa.s$^{-1})$, using a piezoelectric load cell [23] to extend the tests as far as practicable into the short-duration region (< 20 ms); static fatigue times to failure (t_f) were determined at prescribed applied stresses $(\sigma_a = $ const.) (ramp time < 6 s).

In all tests the broken specimens were examined to verify the indentation site as the origin of failure. Exceptions were excluded from the data pool.

3.2   Inert Strength Data and the R-curve Parameters

The inert strength data, $\sigma_m(P)$, are shown in Fig. 4. These strength data tend strongly away from the conventional $P^{-1/3}$ dependence for materials with a single-valued toughness, toward a plateau at low P. The plateau is a measure of the flaw tolerance associated with R-curve behaviour [13-15]. A bridging parameter adjustment routine, iterating on Eqs. 2-9 [15], is used to obtain the best-fit solid curve in this diagram. Assuming E' = 413 GPa, ψ = 1.24 and χ = 0.018 for the alumina [15], we obtain our fit with the following parameter values: γ_0 = 5.6 J.m^{-2} (grain boundary), ϵ_ℓ = 0.120, μ = 1.80, σ_R = 155 MPa and d = 35 μm. This set of parameters determines the R-curve. [2]

---

[2]   These parameters are similar to those in determined Ref. [15], except that γ_0 is about 15% lower, suggesting that our new batch of material may have slightly weaker grain boundaries.

It is instructive to insert Eqs. 3-9 into Eq. 2, and thence to evaluate

the critical function $G_*(c)$ corresponding to the inert strength data point at

$P = 30$ N, $\sigma_m = 220$ MPa, in Fig. 4. This function is plotted as the upper

curve in Fig. 5. We note the principal minimum at $G_* = 2\gamma_0$, representing the

configuration at failure.

3.3 Fatigue Data and the Crack Velocity Parameters

The dynamic and static fatigue results for our alumina are plotted in

Figs. 6 and 7, respectively. There is a strong asymptotic tendency to a

fatigue stress limit, σ_{lim}, in the long-time regions of both these plots.

This tendency is most apparent in Fig. 7, reflecting a bias in the static

testing methodology toward longer test durations; indeed, the data in Fig. 7

seem to lie almost exclusively in the fatigue-limit domain. At short times

the data must saturate at the inert strength level; only in the dynamic data

of Fig. 6 is the test duration short enough to indicate that this upper limit

is in fact being approached.

The solid curves are best fits to the data, obtained using the R-curve

parameters evaluated above (Sect. 3.1) and adjusting the crack velocity

parameters in Eq. 10. The procedure adopted for determining the velocity

parameters involves two steps:

(i) The surface energy term, γ_1, is evaluated from an estimate of the

asymptotic fatigue limit, $\sigma_{lim} = 129$ MPa, in Figs. 6 and 7. First we

determine the critical function $G_*(c)$ appropriate to σ_{lim}, at indentation load

$P = 30$ N, in exactly the same way as done previously for the inert strength

16

σ_m, i.e. upper curve in Fig. 5. The new function is plotted as the lower

curve in the same figure. Since the fatigue limit represents the applied

stress level below which the crack at some point in its evolution ceases all

growth, the principal minimum in this lower curve necessarily defines the

threshold state $G_*(c) = 2\gamma_1$ (i.e. $v = 0$ in Eq. 10); hence from Fig. 5 we

obtain $\gamma_1 = 1.20$ J.m^{-2}.

(ii) The parameters v_0 and Γ are now adjusted to give the best fit to the

fatigue data points. The computer does this by selecting the combination of

parameters that minimises the variance between computed and measured data

points at the experimental values of $\dot{\sigma}_a$ (dynamic fatigue) and σ_a (static

fatigue). In making these adjustments, it is useful to recognise that v_0

reflects more strongly in the intercepts, Γ likewise more strongly in the

slopes, of the fatigue plots. This procedure yields $v_0 = 7.0$ μm.s^{-1}, $\Gamma =$

0.325 J.m^{-2}.

The intrinsic v-G_* function corresponding to the above parameter

calibration is plotted in accordance with Eq. 10 for our polycrystalline

alumina in water as the solid curve in Fig. 8. Also included in Fig. 8, as

the dashed curve, is the analogous function for single crystal sapphire in

water, obtained by similarly deconvoluting fatigue data from Ref. [23]

(requiring $K_\mu = 0$, but retaining the hyperbolic -ine velocity function over

the Cook cutoff power-law [5]). The curve for the polycrystalline material

falls distinctly to the left of that for the single crystal. This is in

accord with the fact that the fracture in the former is intergranular (cf. γ_0

value 5.6 J.m^{-2} for our alumina with 11.0 J.m^{-2} for sapphire, as reflected in

the upper bounds to the two curves in Fig. 8).

4. **DISCUSSION**

We have developed a formalism for studying (noncyclic) fatigue limits in ceramic materials with R-curves. Introducing a microstructural closure stress intensity factor based on crack-interface bridging, and a threshold crack veloc ty function based essentially on activation kinetics, we have described a numerical algorithm that solves the ensuing fracture-mechanics differential equations for time-dependent failure. As an illustrative case study, dynamic and static fatigue limits for an alumina-water system with controlled (indentation) flaws have been quantified, and the intrinsic v-G, curve thereby deconvoluted. Once the R-curve and velocity parameters have been calibrated from the fatigue data, the algorithm becomes a powerful tool for analysing and predicting various elements of the limiting failure conditions. We shall explore some of these elements in the discussion below.

It might be contended that the present study does little more than reinforce an existing suspicion that fatigue limits are possible in ceramics: all that is necessary is a threshold in the crack velocity function. The novel aspect here is our focus on the role of the R-curve; in particular, on how the additional crack stability afforded by the microstructural crack resistance may enhance these fatigue limits. Indeed, it can be argued that a fatigue limit may be achieved in an R-curve material without any velocity threshold at all. To demonstrate, we use our algorithm to compute the hypothetical fatigue responses for our alumina using the deconvoluted v-G,

18

function in Fig. 8, but with the threshold artificially reduced to $\gamma_1 = 0$
(i.e. as represented by the extrapolated, dashed line in Fig. 3, using a curve
of the same Γ but with suitably adjusted intercept $v_0 = 1.0 \ \mu m.s^{-1}$ in Eq. 10).
The resulting modified fatigue relations are included as the dashed curves in
Figs. 6 and 7. We see that the prospective fatigue limit σ_{lim} is lowered, but
not to zero. Physically, the existence of this limit is possible because the
bridging closure term, $-K_\mu$ in Eq. 3, can negate the applied loading term, $+K_A$
(plus K_r, where applicable), giving rise to a balance state $G_* = 0$ in Eq. 2.
In terms of the construction of Fig. 5, the requirement for attaining such a
balance state is that the minimum in the $G_*(c)$ curve should intersect the c-
axis at nonzero σ_a.

However "good" we might regard the data fits in Figs. 6 and 7, we would
not suggest that we have proved the validity of the fracture mechanics
relations in Sect. 2. In particular, we certainly would not assert that the
results confirm the fundamental correctness of the hyperbolic form of the
intrinsic v-G_* function in Eq. 10. Nevertheless, we may feel confident that
the deconvoluted curves in Fig. 8 do faithfully represent the more important
quantitative features of this intrinsic function, including the surface energy
levels that define the thresholds.

In this context of velocity functions, we submit that caution needs to be
exercised in the interpretation of results from conventional large-crack
tests, because of the shielding effects associated with R-curve behaviour. In
an actual experiment one monitors the applied mechanical energy release rate
G_a, not the energy rate G_* experienced at the crack tip. Thus the apparent
velocity relation, v-G_a, will generally differ from the intrinsic relation, v-
G_*, and, moreover, will be history dependent. An important factor is the

19

starting location along the R-curve; larger starting cracks will experience greater shielding, resulting in displacements of the v-G_a curves to the right on a velocity diagram. Similar displacements may be anticipated at slower loading rates. As an illustration, we show in Fig. 9 hypothetical v-G_a curves for our indentation-flaw, alumina-water system, generated from our algorithm for three designated P-$\dot{\sigma}_a$ combinations. We reiterate, these are the curves that would be obtained experimentally if one were to evaluate $G_a = K_A^2/E' = \psi^2\sigma_a^2c/E'$ (Eqs. 2, 3 and 11, $K_r = 0 = K_\mu$) from direct monitoring of the applied load and the crack size. As foreshadowed, the displacements become more pronounced with increasing load and decreasing stress rate. Such a history dependence could account for the reports of progressive run-to-run v-G data shifts in the literature [31-33].

Another distinguishing feature of R-curve behaviour is the "flaw tolerance" referred to in Sects. 1 and 3.2 [24]. Again, we use the algorithm to demonstrate the point, by computing hypothetical dynamic fatigue strength σ_f vs initial flaw size c_i at prescribed constant stressing rates for our alumina-water system. The results of such computations for natural flaws (i.e. $K_r = 0$ in Eq. 3) are plotted in Fig. 10. The strength values remain relatively constant up to initial flaw sizes of several tens of micrometres. Such insensitivity is attributable to the stabilising influence of the (negative) $K_\mu(c)$ function on the crack driving force, as reflected for instance in the strongly diminishing $G_a(c)$ function to the left of the minimum in Fig. 5.

This stabilising influence may be demonstrated more explicitly by plotting out the complete evolutionary path to failure. It is a trivial matter to extract this path directly from the algorithm. Thus in Fig. 11 we

20

plot three $\sigma_A(c)$ functions (solid curves) at constant $\dot\sigma_A$ for our dynamic
fatigue, indentation-flaw (P = 30 N), alumina-water system (cf. Fig. 6). The
final instability configurations c_f (arrowed) in these curves occur at
relatively large crack sizes (cf. initial sizes c_i, at $\sigma_A = 0$), the more so
the slower the stressing rate; indeed, at the slowest rate represented the
crack undergoes several hundred micrometres of precursor stable extension.
For comparison, we include in Fig. 11 corresponding, bounding quasi-
equilibrium functions, computed using $G_* = 2\gamma_0$ (upper dashed curve) or $G_* =$
$2\gamma_1$ (lower dashed curve) in place of the v-G_* relations in Eq. 10 as a
condition for extension in the algorithm. We note the tendency for the
fatigue curves at the extremes of the stressing-rate range to approach these
quasi-equilibrium limits: at fast rates the failure stress approaches the
inert strength, confirming that the crack spends most of its pre-failure life
close to $G_* = 2\gamma_0$; conversely, at slow rates the failure stress approaches
the fatigue limit, indicating a pre-failure life perpetually close to $G_* =$
$2\gamma_1$.

In conclusion, we have described a procedure for analysing specific
fatigue (constant stress and constant stressing rate) and material-environment
(alumina-water) systems. There would appear to be no restriction on the
general flexibility of the algorithm. In principle, any stressing state (e.g.
complex, cyclic loading), velocity function (e.g. air or other reactive
environment), or even R-curve mechanism (e.g. transformation toughening),
could be handled by suitable modifications to individual elements in the
formulation.

ACKNOWLEDGEMENTS

REFERENCES

1. S.M. Wiederhorn, p. 613 in Fracture Mechanics of Ceramics, Vol. 2. Edited by R.C. Bradt, D.P.H. Hasselman and F.F. Lange. Plenum, New York (1974).

2. A.G. Evans and S.M. Wiederhorn, Int. J. Fract. 10 379 (1974).

3. S.M. Wiederhorn and J.E. Ritter Jr., p. 202 in Fracture Mechanics Applied to Brittle Materials. Edited by S.W. Freiman. ASTM Spec. Tech. Publ. No. 678, ASTM, Philadelphia, PA (1979).

4. H.H. Johnson and P.C. Paris, Engin. Fract. Mech. 1 3 (1968).

5. R.F. Cook, J. Mater. Res. 1 852 (1986).

6. T.A. Michalske, p. 277 in Fracture Mechanics of Ceramics, Vol. 5. Edited by R.C. Bradt, D.P.H. Hasselman and F.F. Lange. Plenum, New York (1983).

7. B.R. Lawn, D.H. Roach and R.M. Thomson, J. Mater. Sci. 22 4036 (1987).

8. H. Hubner and W. Jillek, J Mater. Sci. 12 117 (1977).

9. R.W. Steinbrech, R. Knehans, and W. Schaarwachter, J. Mater. Sci. 18 265 (1983).

10. R.F. Cook, B.R. Lawn and C.J. Fairbanks, J.Amer. Ceram. Soc. 68 604 (1985).

11. C.J. Fairbanks, B.R. Lawn, R.F. Cook and Y-W. Mai, p. 23 in Fracture Mechanics of Ceramics, Vol 8. Edited by R.C. Bradt, A.G. Evans, D.P.H. Hasselman and F.F. Lange. Plenum, New York (1986).

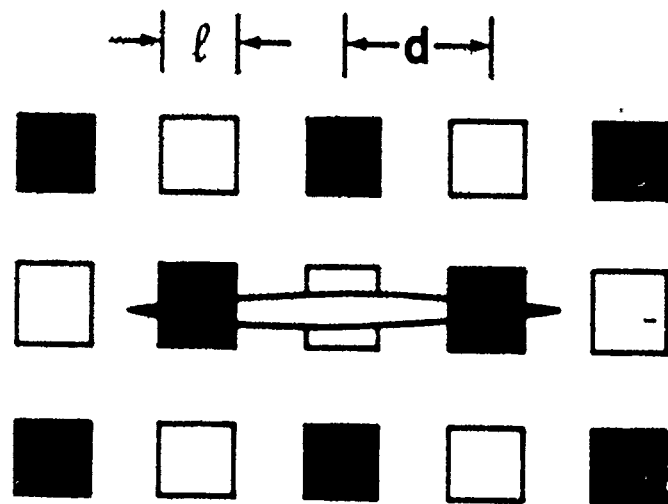12. P.L. Swanson, C.J. Fairbanks, B.R. Lawn, Y.W. Mai and B.J. Hockey, J. Amer. Ceram. Soc. 70 279 (1987).

13. Y-W. Mai and B.R. Lawn, J. Amer. Ceram. Soc. 70 289 (1987).

14. R.F. Cook, C.J. Fairbanks, B.R. Lawn and Y-W. Mai, J. Mater. Res. 2 345 (1987).

15. S.J. Bennison and B.R. Lawn , Acta Metall., submitted.

16. M. Sakai and R.C. Bradt, J. Ceram. Soc. Japan 96 801 (1988).

17. B.R. Lawn, J. Amer. Ceram. Soc. 66 83 (1983).

18. P.F. Becher, T.N. Tiegs, J.C. Ogle and W.H. Warwick, p. 61-73 in Fracture Mechanics of Ceramics, Vol. 7. Edited by R.C. Bradt, A.G. Evans, D.P.H. Hasselman and F.F. Lange. Plenum, New York (1986).

19. D.B. Marshall and B.R. Lawn, J. Am. Ceram. Soc. 63 532 (1980).

20. P. Chantikul, B.R. Lawn, and D.B. Marshall, J. Amer. Ceram. Soc. 64 322 (1981).

21. B.R. Lawn, D.B. Marshall, G.R. Anstis and T.P. Dabbs, J. Mater. Sci. 16 2846 (1981).

22. E.R. Fuller, B.R. Lawn and R.F. Cook, J. Amer. Ceram. Soc. 66 314 (1983).

23. R.F. Cook, B.R. Lawn and C.J. Fairbanks, J. Amer. Ceram. Soc. 68 616 (1985).

24. S.J. Bennison and B.R. Lawn, J. Mater. Sci., in press.

25. B.R. Lawn and T.R. Wilshaw, Fracture of Brittle Solids. Cambridge University Press, London, 1975, Ch. 3.

26. B.R. Lawn and T.R. Wilshaw, Fracture of Brittle Solids. Cambridge University Press, London, 1975, Ch. 8.

27. B.R. Lawn, J. Mater. Sci. 10 469 (1975).

28. B.R. Lawn and S. Lathabai, Mater. Forum 11 313 (1988).

29. D.B. Marshall and B.R. Lawn, J. Mater. Sci. 14 2001 (1979).

30. Y-W. Mai and B.R. Lawn, Ann. Rev. Mat. Sci. 16 415 (1986).

31. S.W. Freiman, K.R. McKinney, and H.L. Smith, p. 659 in Fracture Mechanics of Ceramics, Vol. 2. Edited by R.C. Bradt, D.P.H. Hasselman and F.F. Lange. Plenum, New York (1974).

32. B.J. Pletka and S.M. Wiederhorn, J. Mater. Sci. 17 1247 (1982).

33. P.L. Swanson, p. 299 in Fracture Mechanics of Ceramics, Vol. 8. Edited by R.C. Bradt, A.G. Evans, D.P.H. Hasselman and F.F. Lange. Plenum, New York (1986).

1. Growth of penny-like crack in bridging field; (a) side view, (b) projection view. (Open squares are out-of-plane bridging grains.)

2. Coordinate system for crack-interface bridging. C denotes crack tip. Z edge of the bridging zone.

3. Schematic $v(G_*)$ function in Eq. 10, plotted logarithmically on v axis and linearly on G_* axis.

4. Inert strength vs Vickers indentation load for polycrystalline alumina. Data points means and standard deviations (minimum ten specimens per point) in strength values. Solid curve is best fit obtained by adjusting parameters in bridging model.

5. Plot of $G_*(c)$ for polycrystalline alumina, Vickers indentation flaw ($P = 30$ N) evaluated at constant $\sigma_a = \sigma_m = 220$ MPa (inert strength) and $\sigma_a = \sigma_{11m} = 130$ MPa (fatigue limit).

6. Dynamic fatigue plot for polycrystalline alumina in water, for Vickers indentations at $P = 30$ N. Data points means and standard deviations (minimum ten specimens per point) in strength values. σ_m is inert strength level, σ_{11m} is fatigue limit. Solid curve is best fit obtained by adjusting crack velocity parameters. Dashed curve is equivalent fatigue response for material without crack velocity threshold (Sect. 4).

7. Static fatigue plot for polycrystalline alumina in water, for Vickers indentations at $P = 30$ N. Arrows at right designate interrupted tests, overlapping data for ten specimens. Arrows at left designate breakages during ramp loading to maximum applied stress, six specimens. Other data points are results of individual tests. σ_m is inert strength level, σ_{lim} is fatigue limit. Solid curve is best fit obtained by adjusting crack velocity parameters. Dashed curve is equivalent fatigue response for material _without_ velocity threshold.

8. Plot of the _intrinsic_ crack-tip velocity function, v-G_*, for polycrystalline alumina (solid curve) in water, as det nined from fits to fatigue data. Also included is corresponding function for single-crystal sapphire (dashed curve), using data from Ref. [23].

9. _Apparent_ velocity function, v-G_a, for polycrystalline alumina in water. Dashed curve (a) represents baseline zero-shielding limit ($K_r = 0 = K_\mu$), i.e. "true" crack-tip velocity function (v-G_*) from Fig. 8. Solid curves are for nonzero shielding, Vickers indentation flaws (loads P), dynamic fatigue (constant stressing rates $\dot{\sigma}_a$): (a) $P = 3$ N, $\dot{\sigma}_a = 10^{+3}$ MPa.s^{-1}; (b) $P = 30$ N, $\dot{\sigma}_a = 10^{+3}$ MPa.s^{-1}; (c) $P = 30$ N, $\dot{\sigma}_a = 10^{-1}$ MPa.s^{-1}. (Note expanded G scale relative to Fig. 8.)

10. Plot of dynamic fatigue strength σ_f as function of starting size c_i of _natural_ flaws ($K_r = 0$) for alumina-water system, at specified stressing rates: (a) $\dot{\sigma}_a = 10^{+4}$ MPa.s^{-1}; (b) $\dot{\sigma}_a = 10^{+1}$ MPa.s^{-1}; (c) $\dot{\sigma}_a = 10^{-2}$ MPa.s^{-1}.

11. Plot of fatigue $\sigma_a(c)$ function for Vickers indentation flaws, $P = 30$ N, in alumina-water system, at prescribed stressing rates (solid curves): (a) $\dot{\sigma}_a = 10^{+4}$ MPa.s^{-1}; (b) $\dot{\sigma}_a = 10^{+1}$ MPa.s^{-1}; (c) $\dot{\sigma}_a = 10^{-2}$ MPa.s^{-1}. Also included are comparative quasi-equilibrium plots for inert strength limit (upper dashed curve) and fatigue limit (lower dashed curve).
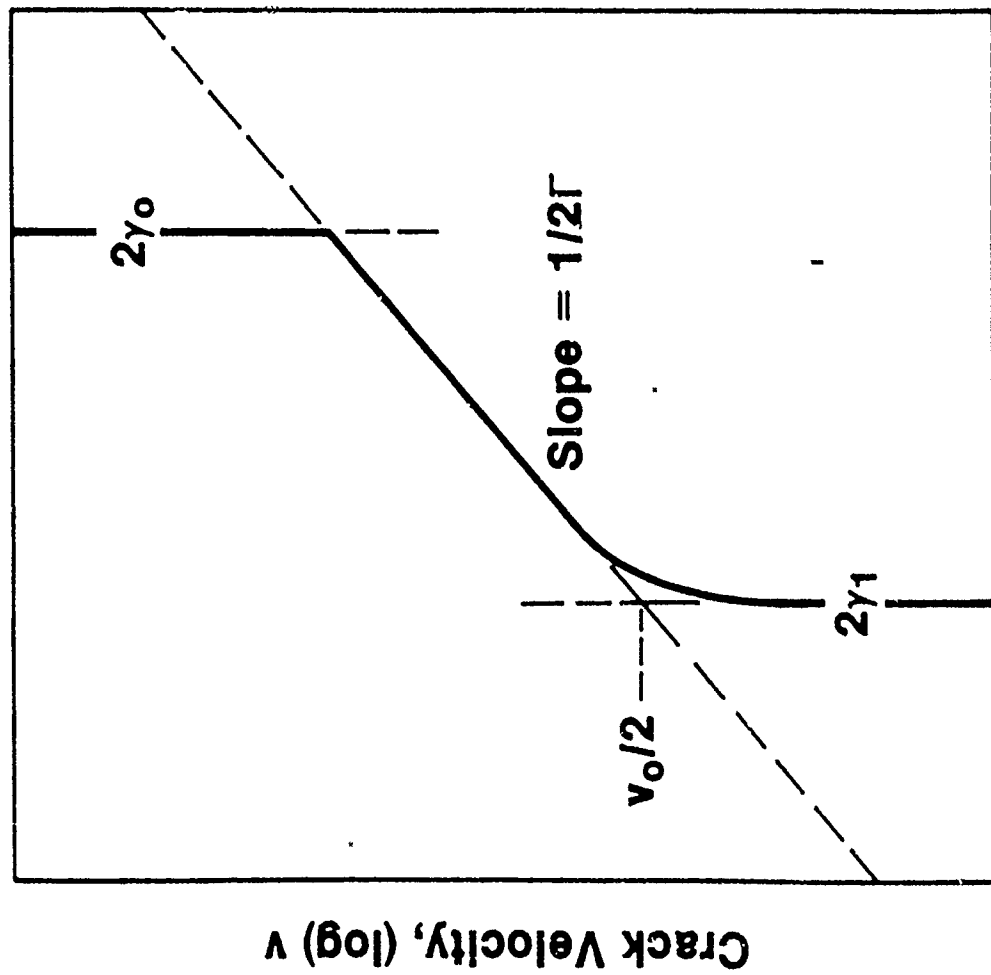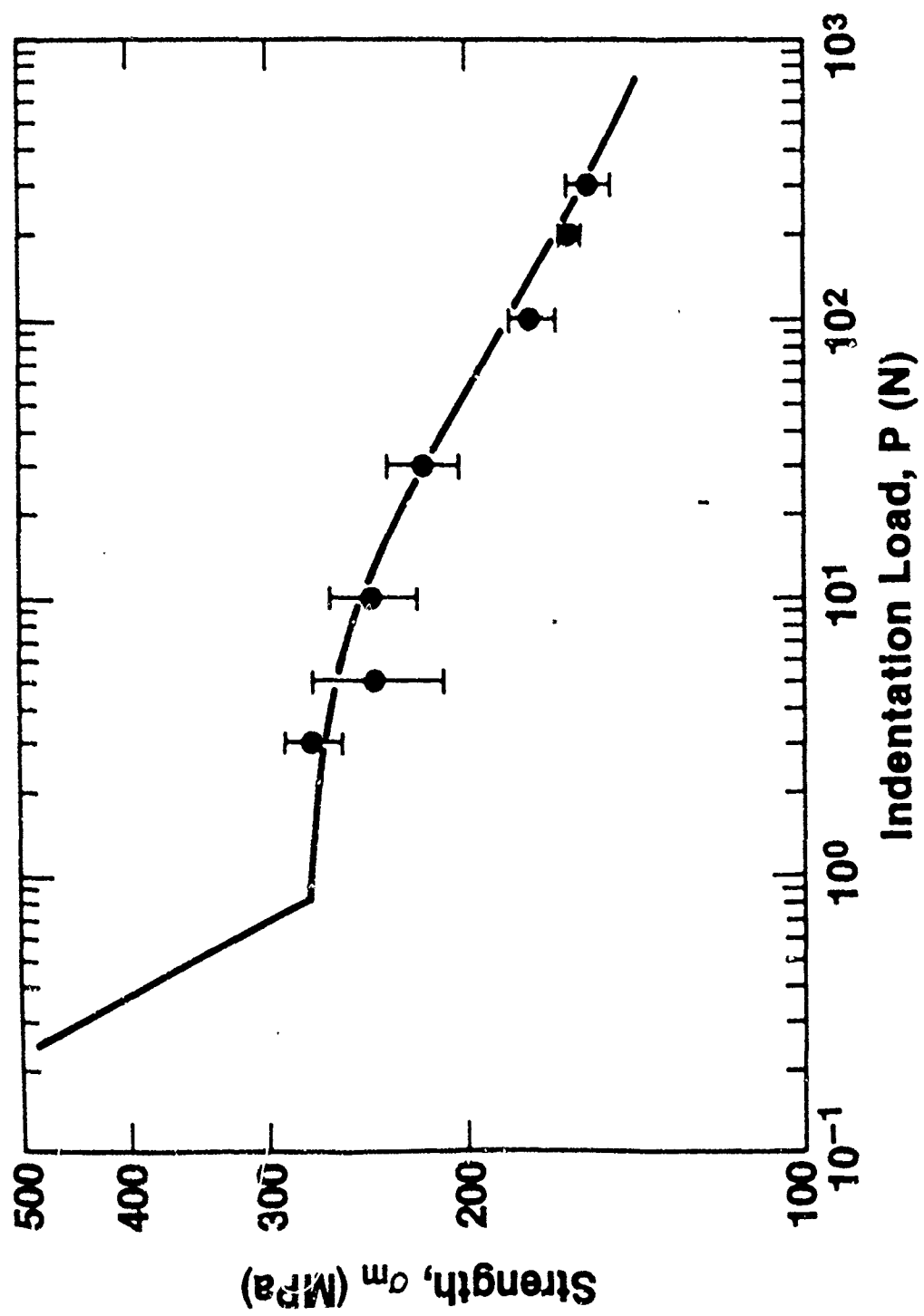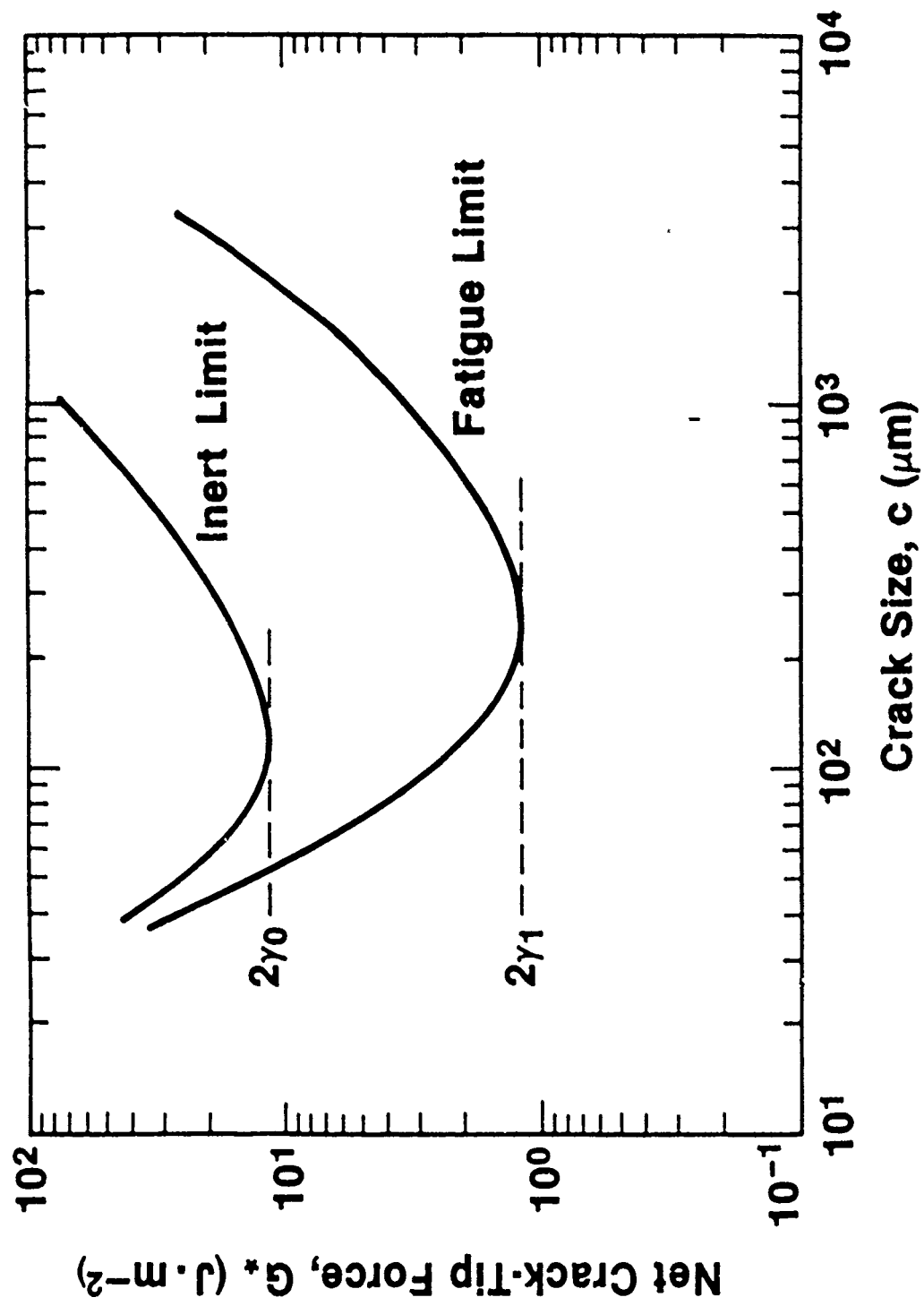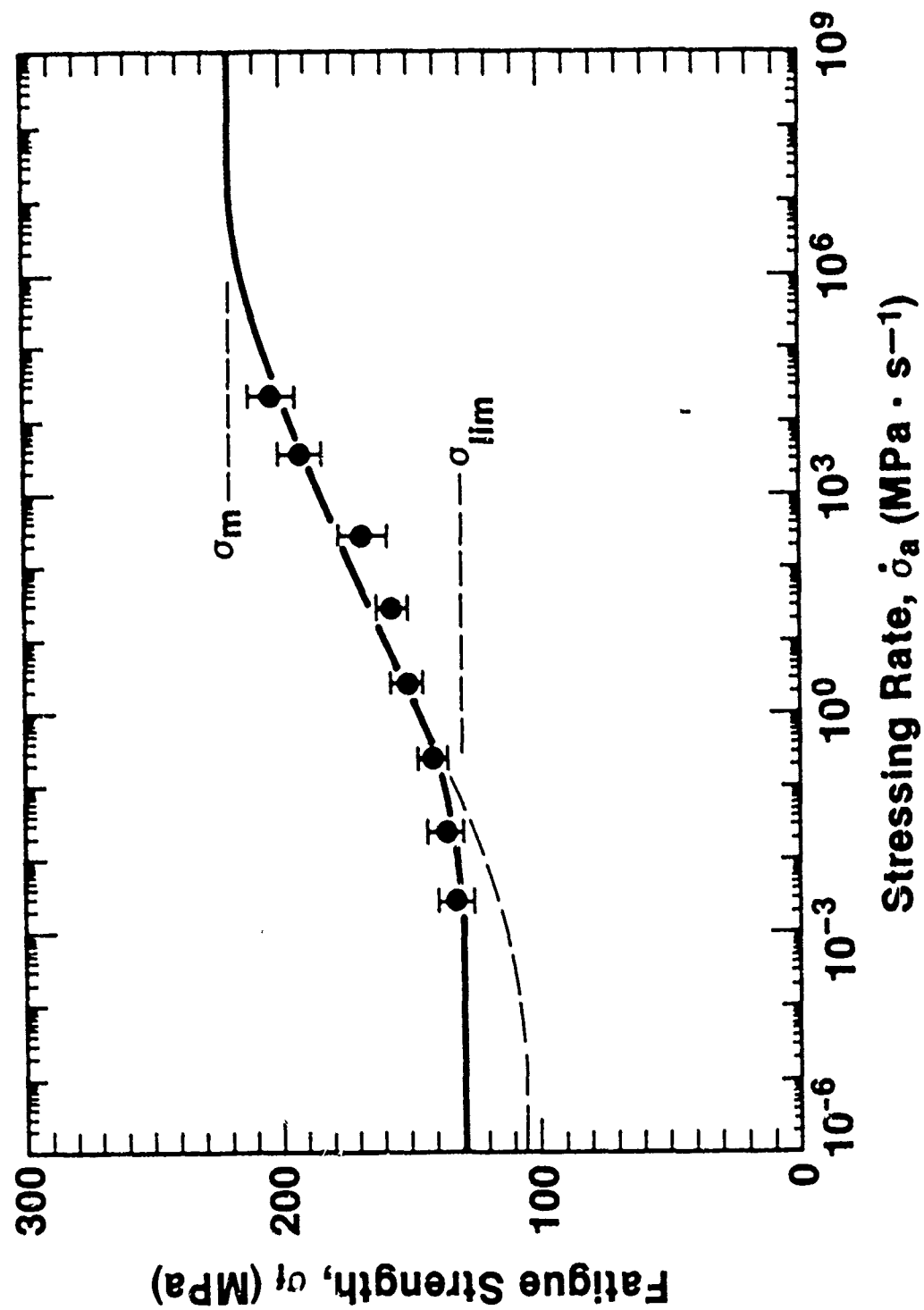
(a)

ℓ d

(b)

2c

2

Figure: Plot of Crack Velocity, (log) v versus Net Crack-Tip Force, G_*. The curve shows a plateau at $2\gamma_0$, a descending region labeled Slope = $1/2\Gamma$, with $v_0/2$ marked, leveling off toward $2\gamma_1$.

Fatigue Strength, σ_f (MPa)

Stressing Rate, $\dot{\sigma}_a$ (MPa · s^{-1})

σ_m

σ_{lim}

Figure showing Applied Stress, σ_a (MPa) versus Time to Failure, t_f (s). The y-axis ranges from 0 to 300 MPa. The x-axis is logarithmic from 10^{-6} to 10^9 s. Curves labeled σ_m and σ_{lim} are indicated.

Initial Flaw Size, c_i (μm)

Fatigue Strength, σ_f (MPa)

Crack Size, c (µm)

Applied Stress, σ_a (MPa)

13. "Cyclic Fatigue Behavior of an Alumina Ceramic With Crack-Resistance Curves"

    S. Lathabai, Y-W. Mai and B.R. Lawn

    J. Am. Ceram. Soc. 72 1760 (1989).

Cyclic Fatigue Behavior of an Alumina Ceramic with Crack-Resistance Characteristics

Srinivasarao Lathabal,*,* Yiu-Wing Mai,* and Brian R. Lawn*

Ceramics Division, National Institute of Standards and Technology, Gaithersburg, Maryland 20899

The behavior under cyclic tension–tension loading of an alumina ceramic with pronounced crack-bridging (R-curve) characteristics is studied. Tests on disk specimens with indentation cracks reveal no failures below the static fatigue limit. Theoretical predictions of the stress–lifetime response, based on the premise that environmentally assisted slow crack growth is the sole factor determining lifetime, are consistent (within experimental scatter) with the data. The results indicate that there is no significant cyclic degradation from potential damage to the bridges, at least in the short-crack region pertinent to strength properties. [Key words: fatigue, crack growth, alumina, R-curve.]

IT IS well-known that the mechanical properties of metals and polymers are susceptible to degradation under repeated loading, i.e., "cyclic fatigue." Ceramics have generally been perceived as immune to such damage on account of their lack of crack-tip plasticity. Literature studies of cyclic fatigue in ceramics are sparse and inconclusive. Some early work on alumina[1-5] report reduced lifetimes in cyclic relative to static loading. However, analysis of some of these data (specifically data

in Refs. 1 and 4) suggests that, within the range of experimental scatter, this reduction can be accounted for in large part by the integrated effect of environmentally enhanced slow crack growth.[6] Subsequently, cyclic fatigue studies have been reported on silicon nitride[6-10] and silicon carbide.[11] Again, these studies demonstrate no definitive evidence of true cyclic damage. Indeed, Matsuo *et al.*[8] imply that the fatigue failure times for their silicon nitride are in accord with slow crack growth alone.

Most recently, cyclic fatigue crack propagation has been unequivocally demonstrated,[12,13] in a transformation-toughened magnesia–zirconia ceramic (grain size of 50 μm), using tension–tension loading of compact-tension specimens with "long" cracks (i.e., millimeter-scale, large compared with the microstructure). That work demonstrated crack growth in cyclic loading at stress intensities significantly below those required to generate environmentally assisted crack

growth in sustained constant loading, with the extent of the shift in the attendant crack velocity curves depending on the degree of aging of the material. The fatigue effect in that material was attributed, at least in part, to crack-resistance (R-curve) behavior due to shielding by phase transformation, although the detailed micromechanisms remain obscure.

However, it is now established that a wide range of nontransforming ceramics such as aluminas can also exhibit R-curve characteristics, albeit via a different shielding mechanism. In these materials the predominant mechanism of R-curve behavior is persistent grain-localized bridging at the interface behind the crack tip.[12-21] Key to the efficacy of the bridges as toughening agents is the presence of internal thermal expansion mismatch stresses which "clamp" interlocking grains into the alumina "matrix" on either side of the crack interface behind the advancing crack tip. The R curve confers the quality of "flaw tolerance"[22] and, because of its stabilizing influence on crack growth, strongly enhances the "static fatigue" limit.[23] However, there is no direct information on what effect *repeated* loading and unloading might have on the bridging mechanism. In this context we may note that aluminas with more pronounced R curves show a demonstrably greater susceptibility to wear in repetitive abrasion; this increased susceptibility is attributable to cumulative augmentation of tensile internal stresses from the contact damage processes, leading to grain-boundary microfracture.[24] On these grounds we might reasonably expect analogous cumulative damage to the bridges in the repeated loading of propagating cracks, leading to a degradation in the toughness and strength properties. By reducing the crack-tip shielding, such degradation could give rise to cyclic fatigue.

Related effects on the fracture properties of alumina have been described in compression tests on specimens with large notches.[25] There, "fatigue" cracks were observed to initiate from the notches much more effectively in repeated than in sustained loading. As in the interpretation of the wear results referred to above, the enhanced initiation is attributed to grain-boundary microcracking, but driven now by notch-concentrated tensile stresses associated with irreversibilities in the compression stress–strain cycle.[26]

Our objective in the present study was to investigate the effect of cyclic loading on the behavior of a coarse-grained alumina ceramic that shows particularly strong R-curve behavior, specifically in the short-crack region relevant to strength properties. We present results from tension–tension cyclic loading of specimens with controlled indentation

flaws in biaxial flexure in water. Extensive indentation-flaw studies on the selected alumina have been previously documented: in inert-strength tests to determine the R-curve parameters[21] and in constant-stressing-rate tests in water to determine crack velocity parameters.[23] We use these "calibrated" parameters in a computer algorithm, tacitly assuming total reversibility of the bridging constitutive law during the loading–unloading cycle, to obtain a lifetime prediction for comparison with the data. The existence of a true cyclic enhancement of fatigue should then be apparent as a systematic tendency for the experimental data to fall below the predicted stress–lifetime curve.

EXPERIMENTAL PROCEDURE

The material used in this study was a commercial polycrystalline alumina ceramic, nominally pure (<0.1% additive) with a mean grain size of 23 μm.[1] The specimens were in the form of disks, approximately 22 mm in diameter and 2 mm thick.

Controlled Vickers indentation flaws, at a load 30 N were placed at the centers of the prospective tensile faces of each specimen. The specimens were mounted into a biaxial loading fixture, with a flat circular punch of diameter 4 mm on a three-point support of diameter 19 mm. The tensile stresses in the loaded specimen surfaces were computed from thin-plate formulas. This is identical to the indentation–strength configuration used previously[23] to obtain lifetime data at *static* applied stresses, which we will adopt here as a convenient baseline for comparing cyclic loading data.

The cyclic load tests were conducted in sinusoidal tension–tension on a servo-hydraulic fatigue testing machine.[1] The minimum tensile stress in each series of tests was maintained at 20 MPa, but the maximum stress was adjusted to coincide with the constant stress levels applied in the static loading tests (covering a practical range of 1 to 10^6 s in lifetime[23]). At least five specimens were tested at each selected peak stress, at frequencies of 1 and 50 Hz, in water. The time/cycles to failure were recorded in each case. In all tests the broken specimens were examined to verify that the failure initiated at the indentation site; exceptions were excluded from the data pool.

RESULTS

Consider first the static fatigue test results in Fig. 1, from Lathabai and Lawn.[23] The solid curve represents an a priori prediction of the static fatigue response, obtained numerically using a computer algorithm[23] based on a combined R-curve and crack-velocity-curve analysis (Appendix). the parameters used in this analysis were "calibrated" from the inert strength and constant stressing rate data for our alumina in previous experiments.[23] The data points are individual experimen-

tal breaks; left arrows designate specimens that broke during the loading ramp, right arrows designate long-term "survivors." It is seen that the data scatter uniformly about the theoretical curve, which coincides with the fatigue limit (130±10 MPa) over most of the practical stress range. Any additional fatigue effect in cyclic loading should therefore be manifest as failure stresses *below* this static limit.

The results for individual breaks in cyclic loading tests are plotted in Fig. 2 for the two experimental frequencies used. Arrows at right again designate long-term survivors. The data show a strong similarity in form and spread to those of Fig. 1. The solid curve in Fig. 2 is the integrated theoretical prediction for sinusoidal cyclic loading from the computer algorithm, presuming slow crack growth to be the *sole* source of fatigue and bridge displacements during the unloading to be reversible (Appendix). The level of agreement between theoretical prediction and experimental data is comparable with that in Fig. 1. In accordance with the assumptions above, the effect of cycling is simply to translate the fatigue curve to longer lifetimes, as seen by comparing the solid (cyclic) curve with the dashed (static) curve. The data in Fig. 2 do not fall below the static fatigue limit, indicating that any subsidiary mechanical damage mechanism, if present, plays an insignificant role in the degradation process.

Further indication as to a fatigue effect can be obtained by investigating the role of frequency. It is difficult to see any distinction between 1 and 50 Hz data points, within the scatter, in Fig. 2. Accordingly, we replot the data on cumulative probability diagrams in Fig. 3. The stress range in Fig. 2 is narrowly confined about the fatigue limit, so we include all data in the probability plots so as to increase the statistical sample. Whereas there seems to be a significant shift in the number of *cycles* to failure, no such shift is apparent in the *time* to failure. This is further support for the exclusive role of slow crack growth in the fatigue response.

DISCUSSION

The preliminary results above are confined to one alumina material, and to "short" initial cracks. Nevertheless, the study suggests that we may draw a rather strong general conclusion: that, contrary to the concerns expressed earlier, the micromechanisms responsible for the R curve in nontransforming ceramics *are not necessarily deleterious to the cyclic fatigue response.* We shall return to this important conclusion below.

To account *quantitatively* for the null effect of cyclic loading on the integrity of the bridges for our indentation flaws, it is necessary to resort once more to numerical algorithm. The algorithm contains complete (stepwise) information on the crack evolution for indentation flaws in our alumina–water system. Accordingly, we
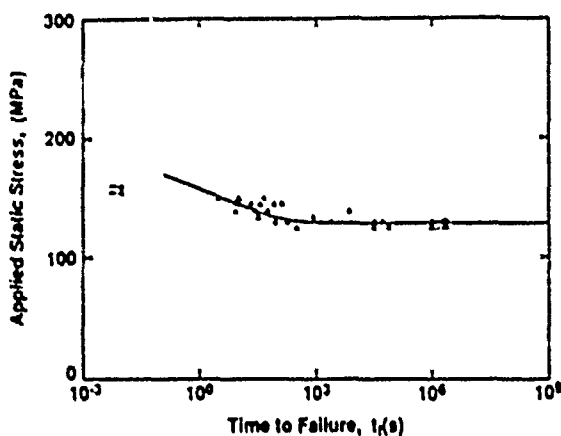
Fig. 1. Static fatigue plot for polycrystalline alumina in water, for Vickers indentations at $P=30$ N. Data points are results of individual tests. Arrows at right designate interrupted tests; at left breakages during ramp loading to maximum applied stress. Solid curve is theoretical prediction. Data from Lathabai and Lawn.[3]
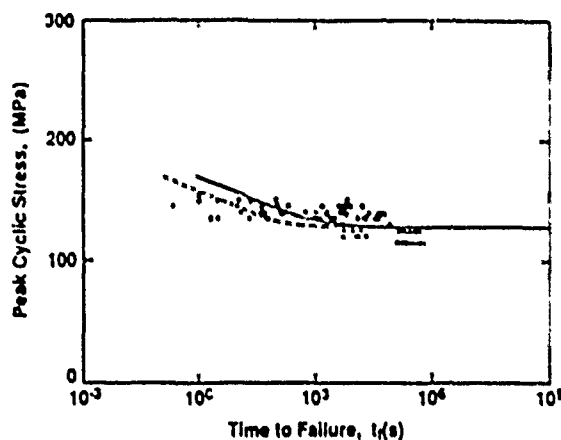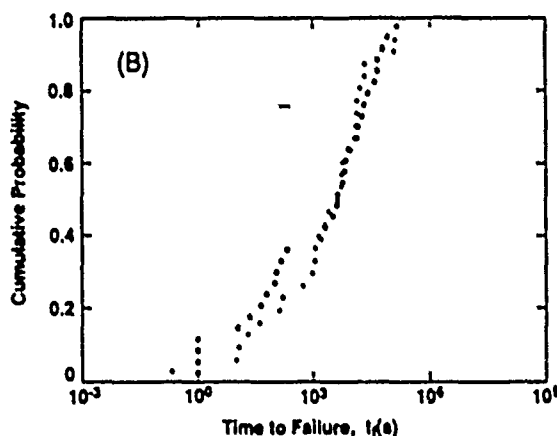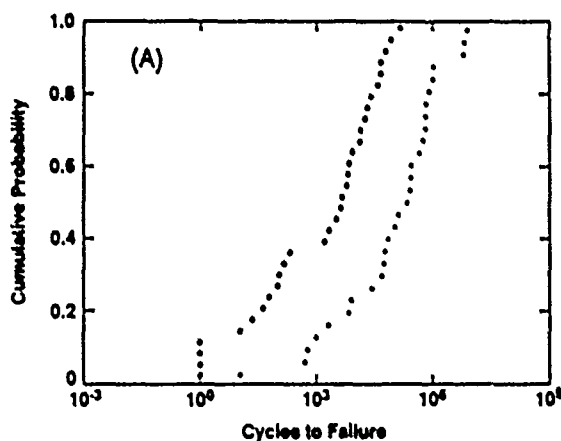

Fig. 2. Cyclic fatigue plot for polycrystalline alumina in water, for Vickers indentations at $P=30$ N. Data points are results of individual tests: open symbols are for 1 Hz, closed symbols, 50 Hz. Solid curve is prediction assuming only slow crack growth. Static fatigue curve from Fig. 1 included for comparison.

Cumulative probability plots for (A) cycles and (B) time to failure for data in Fig. 2. Open symbols are for 1 Hz, closed symbols 50 Hz.

evaluate $2u_z=0.66$ μm for the crack-opening displacement at the first-intersected bridge, Fig. 4, at failure (corresponding to an instability point part way up the R curve) for *static* applied stresses close to the fatigue limit. This displacement may be compared with $2u_M=2.76$ μm for complete disengagement of the interlocking bridging grains (which would be obtained if the crack were al-
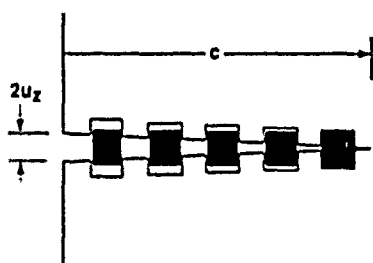
lowed to reach the upper plateau of the R curve), from previous inert strength data.[3] Thus, the ratio $u_z/u_M=0.24$ is a measure of the critical "pullout strain" for the bridging grains for our indentation cracks. It seems reasonable to suppose that, for ordinary flaws, the grains are in little danger of being effectively "dislocated" from the matrix at this strain.

This estimate is for static loading. In *repeated* loading one might expect irreversibility in the grain–matrix frictional sliding characteristics to contribute adversely to the fatigue response, by permanently degrading the bridges. We envisage two ways this degradation could occur: first, by reducing the frictional resistance at the grain–matrix interface; second, by damaging the surface of the interlocking grains, thereby enhancing transgranular fracture. The indication from our experimental results is that this kind of degradation does not occur to any significant extent, at least for indentation flaws.

In the present study we have considered only *short* cracks. Should we expect

the same null behavior for *long* cracks? The mechanisms referred to in the preceding paragraph will surely have a greater effect as the cracks grow farther up the R curve. In extreme cases, beyond the bounds of the R-curve plateau, the interlocking grains will disengage from the matrix ($u_z>u_M$), such that the bridging zone translates with the crack.[19] There is then additional potential for damage, e.g., from the wedging action of dislodged grains and associated debris at the closed interface. There is some evidence for deleterious fatigue effects in a recent study of long-crack (≈ 10 mm) specimens of alumina (10-μm grain size),[26] although the authors in that study did not consider the R-curve bridging mechanism and made no attempt at a direct identification of the underlying fatigue mechanisms. The link between short and long cracks in the analysis of fatigue is an important area for further study. Our results would indicate dangers in extrapolating from one crack-size region to the other, e.g., in using fatigue data from long-crack specimens to

Fig. 4. Schematic showing crack-opening displacement u_z at edge of bridging zone. At $u_z=u_M$, grains disengage from matrix.

predict strength behavior.

The present results have important implications. Ceramics processors might seek to tailor microstructures for optimum R-curve properties.[?] However, there is always the concern that such optimization at one extreme of crack size could lead to deleterious behavior at the other. We mentioned the inverse relation between long-crack toughness and wear properties earlier. The present results suggest that similar grounds for concern with regard to a potential correlation between R-curve and cyclic-loading strength properties could prove to be unwarranted.

APPENDIX

The algorithm used to compute lifetimes for alumina with R-curve characteristics combines the following fracture mechanics elements:[19,22,23]

(i) Fracture mechanics relations and R curve: First, a relation is written for the net driving force on a crack in a material with crack-interface bridging. The stress-intensity factor K_* at the tip of crack length c is given by

$$K_*(c) = K_a(c) + K_r(c) + K_\mu(c) \qquad (A\text{-}1)$$

where $K_a(c) = \psi\sigma_a c^{1/2}$ relates to the applied stress (ψ a geometry constant), $K_r = \chi P/c^{3/2}$ to the contact residual stress at indentation load P (χ a contact constant), and K_μ to the bridging. All the parameters except those in K_μ, which determines the shape of the R curve, are known from indentation studies.

(ii) Constitutive relation: To compute K_μ, one needs the underlying relation between the bridging stress p and crack-opening displacement $2u$ for grain–matrix pullout,

$$p(u) = p_m(1 - u/u_M) \qquad (A\text{-}2)$$

where p_m, maximum pullout stress at $u = 0$, and u_M, (half) pullout displacement at $p = 0$, are expressible in terms of such microstructure parameters as grain size and shape, internal thermal expansion stresses, grain–matrix friction, bridge rupture strain, etc.[23] All these microstructure parameters have been determined for our alumina from inert strength data.[23] In the approximation of "weak toughening," the bridging stress intensity factor is determined from[19]

$$K_\mu(c) = [E/K_*(c)]\int_0^{z_M} p(u)\,du \qquad (A\text{-}3)$$

where E is Young's modulus. The upper limit, $u_\mu(c)$, is (half) the displacement at the edge of the bridging zone, calculable from an expression for the crack profile.[19] This formula is used in conjunction with Eq. (A-1) for both loading and unloading half-cycles, implying full reversibility in the bridge-sliding response.

(iii) Crack velocity relation: The velocity function used is a hyperbolic sine,[23] based on the underlying notion of stress-enhanced thermal activation over atomically localized energy barriers.

$$v(G_*) = v_0 \sinh\left[(G_* - 2\gamma_i)/2\Gamma\right]$$
$$(2\gamma_i \le G_* \le 2\gamma_0) \qquad (A\text{-}4a)$$
$$v(G_*) = 0 \qquad (2\gamma_i > G_*) \qquad (A\text{-}4b)$$

where γ_0 and γ_i are surface energies in vacuum and reactive environment, respectively, and v_0 and Γ are adjustable parameters. Note the provision in Eq. (A-4) for a threshold, consistent with the existence of a natural static fatigue limit.[23] To connect Eqs. (A-1) and (A-4), we use the familiar relation $G_* = K_*^2/E$. The adjustable parameters in Eq. (A-4) have been evaluated from constant stressing rate data.[23]

(iv) Fatigue and lifetime relations: The time to failure can be computed numerically for any time-dependent applied stress function, $\sigma_a = \sigma_a(t)$.

$$\sigma_a = const \qquad (static) \qquad (A\text{-}5a)$$
$$\sigma_a = \sigma_M + \sigma_0 \sin(2\pi v t) \qquad (cyclic)$$
$$(A\text{-}5b)$$

with v the cyclic frequency, σ_M and σ_0 the mean and half-amplitude stresses.

The computer algorithm starts with the indentation flaw in its immediate, postindentation state, and grows the crack stepwise in accordance with Eqs. (A-1) to (A-5) until an instability condition $dG_*/dc > 0$ is attained (with care to ensure that the program is allowed to continue if this instability leads to a metastable arrest configuration[23]).

REFERENCES

[1] L. S. Williams, "Stress Endurance of Sintered Alumina," *Trans. Br. Ceram. Soc.*, 55 [5] 287–312 (1956).

[2] R. Sedlacek and F. A. Halden, "Static and Cyclic Fatigue of Alumina," pp. 211–20 in Structural Ceramics and Testing of Brittle Materials. Edited by S. J. Acquaviva and S. A. Bortz. Gordon and Breach, New York, 1967.

[3] B. K. Sarkar and T. G. T. Glinn, "Fatigue Behavior of High Alumina Ceramics," *Trans. Br. Ceram. Soc.*, 69, 199–203 (1970).

[4] D. A. Krohn and D. P. H. Hasselman, "Static and Cyclic Fatigue Behavior of a Polycrystalline Alumina," *J. Am. Ceram. Soc.*, 55 [4] 208–11 (1972).

[5] F. Guiu, "Cyclic Fatigue of Polycrystalline Alumina in Direct Push-Pull," *J. Mater. Sci. Lett.*, 13 [6] 1357–61 (1978).

[6] A. G. Evans and E. R. Fuller, "Crack Propagation in Ceramic Materials Under Cyclic Loading Conditions," *Metall. Trans.*, 5 [1] 27–33 (1974).

[7] A. G. Evans, "Fatigue in Ceramics," *Int. J. Fract.*, 16 [6] 485–98 (1980).

[8] Y. Matsuo, Y. Hattori, Y. Katayama, and I. Fukura, "Cyclic Fatigue Behavior of Ceramics," pp. 515–22 in Progress in Nitrogen Ceramics. Edited by F. L. Riley. Martinus Nijhoff, The Hague, the Netherlands, 1983.

[9] T. Kawakubo and K. Komeya, "Static and Cyclic Fatigue Behavior of a Sintered Silicon Nitride at Room Temperature," *J. Am. Ceram. Soc.*, 70 [6] 400–405 (1987).

[10] M. Masuda, T. Soma, M. Matsui, and I. Oda, "Cyclic Fatigue of Sintered Si_3N_4," *Ceram. Eng. Sci. Proc.*, 9 [9–10] 137–82 (1988).

[11] S. Horibe and M. Sumita, "Fatigue Behavior of Sintered SiC. Temperature Dependence and Effect of Doping with Aluminum," *J. Mater. Sci.*, 23, 3305–13 (1988).

[12] R. H. Dauskardt, W. Yu, and R. O. Ritchie, "Fatigue Crack Propagation in Transformation-Toughened Zirconia Ceramic," *J. Am. Ceram. Soc.*, 70 [10] C-248–C-252 (1987).

[13] R. H. Dauskardt, D. B. Marshall, and R. O. Ritchie, "Cyclic Fatigue Crack Propagation in Ceramics: Behavior in Overaged and Partially-Stabilized MgO-Zirconia", to be published in Fracture Mechanics/Structural Ceramics. Materials Research Society, Philadelphia, PA.

[14] H. Hubner and W. Jillek, "Subcritical Crack Extension and Crack Resistance in Polycrystalline Alumina," *J. Mater. Sci.*, 12, 117–25 (1977).

[15] R. W. Steinbrech, R. Knehans, and W. Schaarwachter, "Increase of Crack Resistance During Slow Crack Growth in Alumina Bend Specimens," *J. Mater. Sci.*, 18, 265–70 (1983).

[16] R. Knehans and R. W. Steinbrech, "Effect of Grain Size on the Crack Resistance Curves of Al_2O_3 Bend Specimens", pp. 613–19 in Science of Ceramics, Vol. 12. Edited by P. Vincenzi. Ceramurgica, Imola, Italy, 1984.

[17] C. J. Fairbanks, B. R. Lawn, R. F. Cook, and Y.-W. Mai, "Microstructure and the Strength of Ceramics"; pp. 23–37 in Fracture Mechanics of Ceramics, Vol. 8. Edited by R. C. Bradt, A. G. Evans, D. P. H. Hasselman, and F. F. Lange. Plenum, New York, 1986.

[18] P. L. Swanson, C. J. Fairbanks, B. R. Lawn, Y.-W. Mai, and B. J. Hockey, "Crack-Interface Grain Bridging as a Fracture Resistance Mechanism in Ceramics: I. Experimental Study on Alumina," *J. Am. Ceram. Soc.*, 70 [4] 279–89 (1987).

[19] Y.-W. Mai and B. R. Lawn, "Crack-Interface Grain Bridging as a Fracture Resistance Mechanism in Ceramics: II. Theoretical Fracture Mechanics Model," *J. Am. Ceram. Soc.*, 70 [4] 289–94 (1987).

[20] R. F. Cook, C. J. Fairbanks, B. R. Lawn, and Y.-W. Mai, "Crack Resistance by Interfacial Bridging: Its Role in Determining Strength Characteristics," *J. Mater. Res.*, 2 [3] 345–56 (1987).

[21] S. J. Bennison and B. R. Lawn, "Role of Interfacial Grain-Bridging Sliding Friction in the Crack-Resistance and Strength Properties of Nontransforming Ceramics", to be published in *Acta Metall.*

[22] S. J. Bennison and B. R. Lawn, "Flaw Tolerance in Ceramics with Rising Crack Resistance Characteristics", to be published in *J. Mater. Sci.*

[23] S. Lathabai and B. R. Lawn. "Fatigue Limits in Noncyclic Loading of Ceramics with Crack-Resistance Curves", to be published in *J. Mater. Sci.*

[24] S. J. Cho, B. J. Hockey, B. R. Lawn, and S. J. Bennison, "Grain-Size and R-Curve Effects in the Abrasive Wear of Alumina," *J. Am. Ceram. Soc.*, 72 [7] 1249–52 (1989).

[25] L. Ewart and S. Suresh, "Dynamic Fatigue Crack Growth in Polycrystalline Alumina Under Cyclic Compression," *J. Mater. Sci. Lett.*, 5, 774–78 (1986).

[26] M. J. Reece, F. Guiu, and M. F. R. Sammur, "Cyclic Fatigue Crack Propagation in Alumina Under Direct Tension-Compression Loading," *J. Am. Ceram. Soc.*, 72 [2] 348–52 (1989). □

14. "Grain-size and R-Curve Effects in the Abrasive Wear of Alumina"

S-J. Cho, B.J. Hockey, B.R. Lawn and S.J. Bennison

J. Am. Ceram. Soc. 72 1249 (1989).

15. "A History in the Role of MgO in the Sintering of α-Al_2O_3"

S.J. Bennison and M.P. Harmer

Ceramics Transactions, American Ceramic Society, Vol. 7, 1989.

Grain-Size and *R*-Curve Effects in the Abrasive Wear of Alumina

Seong-Jai Cho,[1] Bernard J. Hockey,* Brian R. Lawn,* and Stephen J. Bennison*[3]

Ceramics Division, National Institute of Standards and Technology, Gaithersburg, Maryland   20899

Results of sliding wear tests on three alumina ceramics with different grain sizes are discussed in the light of crack-resistance (R-curve, or T-curve) characteristics. The degree of wear increases abruptly after a critical sliding period, reflecting a transition from deformation-controlled to fracture-controlled surface removal. This transition occurs at earlier sliding times for the aluminas with the coarser-grained microstructures, indicative of an inherent size effect in the wear process. A simplistic fracture mechanics model, incorporating the role of internal thermal expansion mismatch stresses in the crack-resistance characteristic, is developed. The results suggest an inverse relation between wear resistance and large-crack toughness for ceramics with pronounced R-curve behavior. [Key words: alumina, R curve, wear, brittle materials, grain size.]

T HE brittleness of ceramics can lead to rapid wear by microfracture in severe local-contact conditions. Erosion by particle impact[1] and surface removal by machining[2] are two documented cases in point. Theoretical treatments of contact fracture mechanics[3] indicate that the associated wear rates should be greatest for materials with the least toughness, T.[3] The experimental erosion evidence,[1] embracing a broad range of brittle ceramics, lends some support to this contention. However, the growing realization that the toughness of a given material can be a sensitive function of the crack size (*T*-curve, or *R*-curve behavior),[4-8] de-

pending strongly on the microstructural makeup, has led to some contradictory conclusions. Indeed, from machining tests on alumina ceramics that differ only in microstructure, it appears that the machining rate actually *increases* with the toughness,[2] at least with the toughness measured in traditional large-crack test specimens. Accordingly, when specifying toughness parameters for ceramic materials in the context of wear properties, it has become necessary to make due allowance for the microstructural scale of the fracture process.

In this work we present some new data on microfracture-associated abrasive wear of alumina ceramics in which grain-size effects are apparent. We show that it is necessary to consider specific details of material removal in relation to the underlying mechanisms that determine the *T*-curve behavior. We also show that the resistance to fracture-associated surface removal in these materials is least for alumina materials with the greatest large-scale toughness, i.e., in the coarser-grained materials. Following an earlier hypothesis by Rice and co-workers,[9,10] we argue that this seemingly contradictory relation between wear resistance and traditional toughness parameters is linked to the presence of residual stresses in individual grains, and that the influence of these stresses on the contact-fracture process is manifest as a microstructural size effect.

Accordingly, alumina specimens for wear testing were prepared by hot-pressing. The starting material was ultra-high-purity alumina powder[4] doped with magnesia solute additive. Aluminas with three grain sizes, $\ell = 4$, 8, and 20 μm (as measured by a lineal intercept method[11]), were fabricated by suitable adjustment of the hot-pressing cycle.

The corresponding wear data are shown in Fig. 1. (These data represent just part of a broader, systematic study in our laboratories of wear transition behavior in ceramics, to be presented elsewhere.[13]) The test geometry for the data in Fig. 1 is that of a rotating sphere (silicon nitride, 12-mm diameter, 450-N applied load, 100 rpm) on three flat specimens (alumina). The three specimens are aligned with their surface normals in tetrahedral coordination relative to the rotation axis of the sphere and are mounted onto a bearing assembly to ensure equal distribution of the applied load. All tests were run at room temperature with purified paraffin oil as a lubricant. Wear is quantified by the ensuing scar diameter on the alumina specimen surfaces. Figure 1 shows that the scar diameter increases monotonically with sliding time. In the initial stages, this increase is relatively slight, indicative of a deformation-controlled removal process, and is independent of grain size. At a certain critical sliding time, however, the scar diameter for each material increases abruptly; moreover, the larger the grain
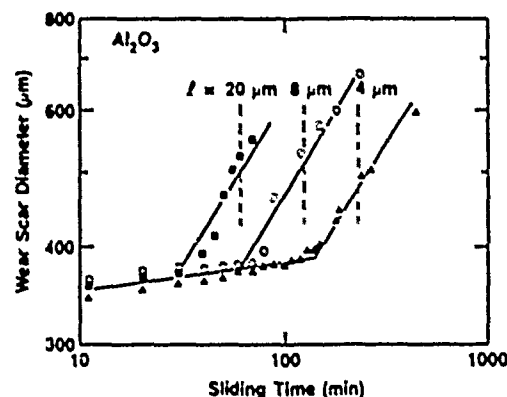
Fig. 1.   Wear data for nominally "pure" alumina ceramics of three grain sizes, ℓ. Room-temperature data for rotating silicon nitride sphere, 12 mm in diameter, 450-N load, on flat specimen, paraffin oil lubricant. Note initial slow, steady increase of scar diameter with sliding time, followed by abrupt transition to severe wear at critical sliding time. Sliding time for onset of transition diminishes significantly for the larger grain-size materials. Vertical dashed lines are theoretical predictions of the transition times.
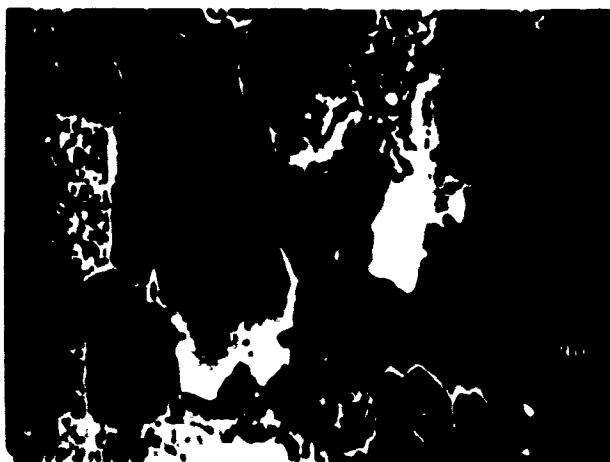
Fig. 2. Scanning electron micrograph of the wear surface of 4-µm-grain-size alumina after transition. Note extensive cracking at the grain boundaries.

size, the earlier this transition occurs. The coarser material is clearly more susceptible to severe surface degradation.

Examination of the specimen surfaces indicates that the abrupt transition to severe wear is associated with the onset of grain-localized microfracture. The scanning electron micrograph in Fig. 2 illustrates the appearance of the wear surface of the 4-µm-grain-size alumina after the transition. Before the transition, the damage shows only smooth scratches, typical of a deformation-controlled wear process. In Fig. 2, on the other hand, we see additional, severe damage in the form of extensive cracking along the grain boundaries, with dislodgement of individual grains and associated wear debris.

Transmission electron microscopy provides further clues to the transition mechanism. Figure 3 shows micrographs of foils (prepared by thinning from below the test surface) of the same alumina as in Fig. 2 outside and inside the worn area

just after the onset of transition. The pristine material in Fig. 3(A) shows a relatively "clean," i.e., dislocation-free, microstructure. Note the presence of void-like defects (inherent porosity after hot-pressing) at many of the triple points of the grain-boundary structure. The worn material in Fig. 3(B) shows severe accumulation of dislocation pileups and twins with strong crystallographic features, characteristic of abrasion damage in ceramics. At the same time, the triple-point defect structure has apparently evolved into an interconnected grain-boundary microcracking pattern. Note also the presence of diffraction bend contours, indicative of substantial damage-induced residual stress in the foil.

To explain the results, we need to elaborate on the nature of the toughness versus crack-size function (the T curve) for alumina. In Fig. 4 we plot this functional dependence for the three grain sizes investigated in Fig. 1, using computations

from an independent study of the toughness properties of alumina ceramics. The underlying basis of these plots is a model for increasing crack resistance, in which the grain-boundary crack is initially unimpeded over facet dimensions, but that as extension proceeds the interface is increasingly bridged by restraining, interlocking grains. There is strong physical justification for this model from direct observations of crack growth in alumina and other ceramics. Key to the bridging process is the presence of internal (thermal expansion mismatch) stresses in the noncubic alumina matrix; at small crack size, c, the microcracks tend to propagate preferentially in regions where these internal stresses are tensile, effectively reducing the intrinsic, grain-boundary toughness. At large c, the compressive component of the internal stress leads to increased crack restraint via a dominating influence on Coulombic frictional tractions that resist pullout of bridging grains. From the fact that the final toughness exceeds the initial toughness in the plots of Fig. 4, we see that the deleterious effect of the internal stresses at low c is more than outweighed by the countervailing influence of the bridging elements at large c. Now the magnitude of the internal stresses $\sigma_r \approx E\Delta\alpha\Delta T$, where E is Young's modulus, $\Delta\alpha$ is the differential expansion coefficient, and ΔT is the quench temperature range) is *independent of the grain size*. The tendency for the curves in Fig. 4 to cross each other is therefore associated with an inherent spatial scaling effect, determined ultimately by the crack extension distance between restraining bridges. the bridging distance is in turn proportional to the grain size. Thus, in the region of greatest pertinence to wear processes (i.e., small c), the resistance to crack extension for any given material tends to its minimum value; moreover, this minimum is
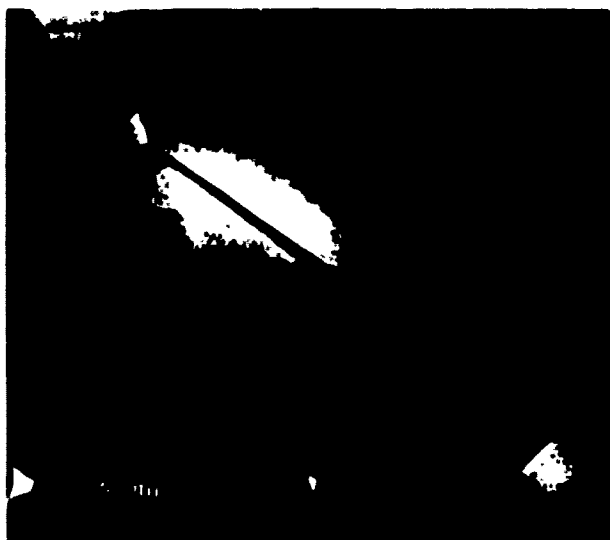

Fig. 3. Transmission electron micrograph of same alumina in Fig. 2 (A) outside and (B) inside wear scar. Accumulation of severe contact-damage stresses are responsible for propagating the flaws (represent triple-point defects evident in (A) or subsequent damage-induced defects) to form grain-boundary microcracking pattern.
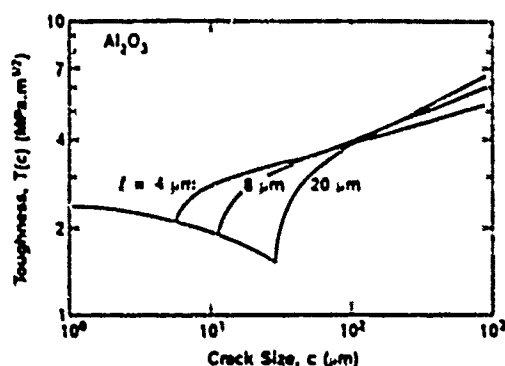
Fig. 4. Toughness versus crack-size function (*T* curve) for the three grain-size aluminas investigated in Fig. 1. Curves calculated from toughness model based on a crack-interface bridging mechanism, from Ref. 14. Note tendency for curves to cross each other.

Fig. 5. Schematic of idealized grain structure, dimension ℓ, with (triple-point) boundary flaws, dimension c_0. Flaws were subjected to tensile components of internal stresses σ_I and damage stresses σ_D.

strongest in those materials with the maximum large-crack toughness. These trends are in essential agreement with those reported by Rice and co-workers.[9,10]

With this background, we may develop a simplistic fracture mechanics description of the wear results. We suppose that there are grain-boundary flaws in the alumina, on the microscale, from which extended microcracking can generate. These flaws may either be prepresent, e.g., the triple-point defects mentioned, or be generated by the damage process itself, e.g., from stress concentrations at the (pileup) deformation elements in Fig. 3(B). We do not attempt to distinguish fine details of the flaw geometry here, assuming only that the size of these flaws scales with the grain diameter. We now assert that the critical condition for the onset of local microfracture in the wear experiment is one in which the damage-induced tensile field causes the larger flaws to become unstable. This assertion is given credence by the well-known phenomenon of *spontaneous* microfracture in ceramics at a critical grain size under the action of the *internal* (thermal expansion mismatch) tensile field alone.[15] We envision the damage stresses as *augmenting* the preexisting stresses, effectively lowering the grain (flaw) size at which the critical state is achieved.

To quantify this description, consider the driving forces on the flaws in the grain configuration in Fig. 5. We take the initial flaw size to be proportional to the grain dimension, $c_0=\beta\ell$, where β is a scaling coefficient. Then we may write the equilibrium condition for the flaws in terms of superposed stress-intensity factors

$$K_I+K_D=T_0 \qquad (1)$$

where T_0 is the intrinsic grain-boundary toughness and the subscripts I and D relate to the internal and damage-induced tensile stresses σ_I and σ_D, respectively. Neglecting gradients in the stress distributions over the flaw dimensions, the equilibrium requirement may be expanded in the form[16]

$$\psi\sigma_I(\beta\ell)^{1/2}+\psi\sigma_D(\beta\ell)^{1/2}=T_0 \qquad (2)$$

where ψ is a crack-geometry coefficient $(2/\pi^{1/2})$ for penny-shaped cracks. The equilibrium in Eq. (2) is unstable and may be achieved at either critical ℓ or critical σ_D.

Critical ℓ ($=\ell_c$ corresponds to spontaneous microfracture at $\sigma_D=0$: this relation provides us with a convenient bounding condition for Eq. (2):

$$\psi\sigma_I(\beta\ell_c)^{1/2}=T_0 \qquad (3)$$

For alumina ceramics, independent, approximate estimates of the grain-boundary toughness, critical grain size, and intensity of internal stresses give $T_0\approx2.1$ MPa·m$^{1/2}$ (Ref. 17), $\ell_c\approx400$ μm (Ref. 15), and $\sigma_I\approx100$ MPa (Ref. 18), respectively. From Eq. (3) we estimate that $\beta\approx0.8$, corresponding reasonably to an initial flaw size on the order of the grain diameter. Substituting Eq. (3) into Eq. (2) allows us to determine the critical σ_D condition as a normalized function of grain size, thereby circumventing any uncertainty in this estimate of β arising from sensitivity of Eq. (3) to T_0, ℓ_c, and σ_I:

$$\sigma_D(\ell)=\sigma_I[(\ell_c/\ell)^{1/2}-1] \qquad (4)$$

We note that Eq. (4) has something of a Hall-Petch ($\ell^{-1/2}$) relation, but with the spontaneous microfracture condition as a natural upper limit.

Equation (4) may now be used to determine the magnitudes of the damage-induced stress necessary to cause wear-associated grain spalling. Table I shows the calculated values for the grain sizes pertinent to the data in Fig. 1. Note that these stresses are substantial, characteristic of the severe deformation levels that attend typical point-contact (indentation) events[13,19,20] in brittle solids. These critical stresses diminish with increasing grain size, consistent with the observation in Fig. 1 that less sliding time is required to induce the transition in the coarser aluminas. If we postulate that the damage stresses accumulate at a constant rate, $\dot\sigma_D=\sigma_D/t$, in the wear process (a postulate supported by the steady, grain-size-independent increase in scar diameter in
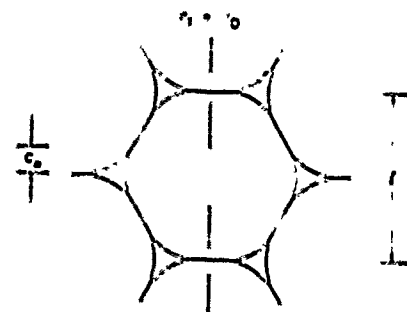
the initial stages of wear in Fig. 1), then we may make quantitative predictions of the trends for the transition regions. The vertical dashed lines in Fig. 1 correspond to such predictions for a stress-accumulation rate $\dot\sigma_D\approx5$ MPa·s^{-1}.

Our simplistic model is able to account for the major grain-size-related transition effects in wear data in alumina ceramics. The implications concerning optimization of microstructures for maximum wear resistance are clear enough here—refine the grain size and, if possible, avoid internal stresses. We reiterate that such measures may run entirely counter to the requirements for maximum large-crack toughness (Fig. 4), so that ultimate material design may involve subtle compromise.

Table I. Wear-Damage-Induced Stress Levels Required to Cause Grain-Boundary Microfracture in Alumina Ceramics

Grain size, ℓ (μm)	Wear-damage stress, σ_D (MPa)
400	0*
20	347
8	607
4	900

*Spontaneous microfracture limit

REFERENCES

[1] S. M. Wiederhorn and B. J. Hockey, "Effect of Material Parameters on the Erosion Resistance of Ceramics," *J. Mater. Sci.*, 18 [3] 766-80 (1983).

[2] D. B. Marshall, B. R. Lawn, and R. F. Cook, "Microstructural Effects on Grinding of Alumina and Glass-Ceramics," *J. Am. Ceram. Soc.*, 70 [6] C-139-C-140 (1987).

[3] A. W. Ruff and S. M. Wiederhorn Treatise on Materials Science and Technology, Vol. 16, Ch. 2 Edited by C. M. Preece. Academic Press, New York, 1978

[4] R. F. Cook and B. R. Lawn, and C. J. Fairbanks

"Microstructure-Strength Properties in Ceramics. I. Effect of Crack Size on Toughness," *J. Am. Ceram. Soc.*, **68** [11] 604–15 (1985).

[P. L. Swanson, C. J. Fairbanks, B. R. Lawn, Y. W. Mai, and B. J. Hockey, "Crack-Interface Grain Bridging as a Fracture Resistance Mechanism in Ceramics: I. Experimental Study on Alumina," *J. Am. Ceram. Soc.*, **70** [4] 279–89 (1987).

Y. W. Mai and B. R. Lawn, "Crack-Interface Grain Bridging as a Fracture Resistance Mechanism in Ceramics: II. Theoretical Fracture Mechanics Model," *J. Am. Ceram. Soc.*, **70** [4] 289–94 (1987).

R. Steinbrech, R. Knehans, and W. Schaarwächter, "Increase of Crack Resistance During Slow Crack Growth in Al₂O₃ Bend Specimens," *J. Mater. Sci.*, **18** [10] 265–70 (1983).

A. Reichl and R. W. Steinbrech, "Determination of Crack-Bridging Forces in Alumina," *J. Am. Ceram. Soc.*, **71** [6] C-299–C-301 (1988).

R. W. Rice, "Micromechanics of Microstructural Aspects of Ceramic Wear," *Ceram. Eng. Sci. Proc.*, **6** [7–8] 940–58 (1985).

C. Cm. Wu, R. W. Rice, D. Johnson, and B. A. Platt, "Grain-Size Dependence of Wear in Ceramics," *Ceram. Eng. Sci. Proc.*, **6** [7–8] 995–1011 (1985).

J. C. Wurst and J. A. Nelson, "Lineal Intercept Technique for Measuring Grain Size in Two-Phase Polycrystalline Ceramics," *J. Am. Ceram. Soc.*, **55** [2] 109 (1972).

S.-J. Cho, Y. Wang, B. J. Hockey, and S. M. Hsu, unpublished work.

B. J. Hockey, "Plastic Deformation of Aluminum Oxide by Indentation and Abrasion," *J. Am. Ceram. Soc.*, **54** [5] 223–31 (1971).

S. J. Bennison and B. R. Lawn, "Role of Interfacial Grain-Bridging Sliding Friction in the Crack-Resistance and Strength Properties of Nontransforming Ceramics," to be published in *Acta Metall.*

F. F. Lange, "Fracture Mechanics and Microstructural Design", pp. 799–819 in Fracture Mechanics of Ceramics, Vol. 4. Edited by R. C. Bradt, D. P. H. Hasselman, and F. F. Lange. Plenum, New York, 1978.

B. R. Lawn and T. R. Wilshaw, Fracture of Brittle Solids, Ch. 2. Cambridge University Press, London, UK, 1975.

C. A. Handwerker, J. M. Dynys, R. M. Cannon, and R. L. Coble, unpublished work.

J. E. Blendell and R. L. Coble, "Measurement of Stress Due to Thermal Expansion Anisotropy in Al₂O₃," *J. Am. Ceram. Soc.*, **65** [3] 174–78 (1982).

B. J. Hockey, "Use of the Hardness Test in the Study of the Plastic Deformation of Single Crystals", pp. 21–50 in The Science of Hardness Testing and its Research Applications. Edited by J. H. Westbrook and H. Conrad. American Society for Metals, Metals Park, OH, 1973.

H. M. Chan and B. R. Lawn, "Indentation Deformation and Fracture of Sapphire," *J. Am. Ceram. Soc.*, **71** [1] 29–35 (1988). ☐

A HISTORY OF THE ROLE OF MgO IN THE SINTERING OF α-Al₂O₃

Stephen J. Bennison and Martin P. Harmer
Department of Materials Science and Engineering
Whitaker Laboratory #5
Lehigh University
Bethlehem, PA 18015

ABSTRACT

This article traces the historical development of the understanding of the role of MgO in the sintering of α-Al₂O₃ beginning with the pioneering work of Robert L. Coble - the inventor of the Lucalox® process [1,2]. Considerable controversy has surrounded this topic and many varied interpretations of the role of MgO have been proposed over the last 27 years. Nonetheless, steady progress has been made during this period and the role of MgO is understood, at least phenomenologically, to be the control of grain boundary motion through a reduction in grain boundary mobility. The main obstacles that have hampered progress over the years are identified and the critical experiments and theoretical contributions that have helped overcome these obstacles are discussed in detail. Remaining challenges concerning the detailed atomic mechanisms responsible for the function of MgO are also identified.

I. INTRODUCTION

Since the discovery of the Lucalox® process by Coble [1,2] in 1961, a steady succession of papers have been published addressing the role of magnesia in the sintering of alumina. The majority of these are presented chronologically in Table 1 and are conveniently classified into two groups depending on whether the work was concerned mainly with sintering per se, or with analytical/diffusion type studies relevant to the problem. The total number of papers published addressing the issue of the role of MgO in the sintering of Al₂O₃ is approximately 60, which corresponds to an average publication rate of approximately 2 papers per year over the past 27 years.

We present in this contribution a historical account of the development of our understanding of the role of MgO in the sintering of alumina, beginning at the time of Coble's discovery. We spend more time on the most influential experiments and/or theoretical contributions and also at times deviate slightly from the strict chronological order to develop the subject matter as logically as possible. Following the main review we present a summary of the state of our understanding and identify the unresolved issues concerning this subject.

Table 1. A chronology of papers directly addressing the role of MgO in the sintering of Al_2O_3 published during the past 27 years.

Date	Sintering Studies	Analytical Studies
1961	Coble[1]	
1962	Coble[2], St. Pierre & Gatti[3], Coble & Burke[4], Coble[6], Bruch[7]	
1963	Johnson & Cutler[8]	
1964	Jorgensen & Westbrook[9]	
1965	Jorgensen[10]	
1967	Warman & Budworth[11]	
1968	Brook[12]	Roy & Coble[14]
1969	Brook[13]	
1970	Budworth[15], Haroun & Budworth[16]	Tong & Williams[17]
1972	Prendergast, Budworth & Brett[18]	Marcus & Fine[19]
1973	Mocellin & Kingery[20]	
1974	Jorgensen[21]	Taylor, Coad & Brook[22]
1975	Peelan[23]	Johnson & Stein[24]
1977		Johnson[25]
1978	Johnson & Coble[28]	Cannon & Coble[29]
1979	Harmer, Roberts & Brook[30], Heuer[31], Monohan & Halloran[32]	
1980	Harmer & Brook[33], Bannister[34], Heuer[35], Burke, Lay & Prochazka[36]	Clarke[37]
1981	Harmer & Brook[38], Yan[40]	Franken & Gehring[39]
1982	Brook[42], Glaeser & Chen[44]	Monty & Ledigou[41] Dynys[43]
1983	Handwerker[46], Bennison & Harmer[47], Bennison & Harmer[49] Harmer, Bennison & Narayan[50]	Bennison & Harmer[48]
1984	Harmer[51], Lynch[52]	
1985	Bennison & Harmer[53], Bennison & Harmer[54], Brook, Gilbart, Shaw & Eisele[58]	Baik, Fowler, Blakely & Raj[55]
1986	Berry & Harmer[59], Shaw & Brook[60]	Baik[61]
1987	Zhao & Harmer[62], Kaysser, Sprissler, Handwerker & Blendell[63], Wang & Harmer[64], Shaw[65]	Jardine, Mukhopadhyay & Blakely[66] Baik and White[67]
1988	Bateman, Bennison and Harmer[68], Handwerker, Dynys, Cannon and Coble[69]	Mukhopadhyay, Jardine Blakely & Baik[70]
Total #	47	17

II. HISTORICAL REVIEW

II.i) Late 1950's - Early 1960's: The Discovery Period

The invention of Lucalox® [1] resulted from an ongoing research effort at the General Electric Company laboratories in the late 1950's, aimed at the development of containment tubes suitable for use in high-pressure sodium vapor discharge lamps. Trials with single crystal sapphire tubes had demonstrated the suitability of Al_2O_3, however, the cost factor and shape limitations associated with the use of sapphire made it necessary to attempt the fabrication of tubes from polycrystalline material. The primary difficulty with the use of sintered material was its inherent opacity due to the presence of porosity, other second phases and grain boundary cracks. The main obstacle, therefore, in the development of a translucent polycrystalline alumina, was the removal or the prevention of these microstructural features during sintering.

The first attempts concentrated on the use of complex firing schedules and the use of special firing atmospheres. A translucent material was fabricated by St. Pierre and Gatti [3] from high purity (~99.9 %) alumina by way of a two-stage firing employing a hydrogen atmosphere. Coble however, found that the process would not work in the absence of magnesia vapor, which was provided accidentally in the firings of St. Pierre and Gatti by the furnace refractories. Coble subsequently identified magnesia as the critical additive in the sintering of alumina to high density. He showed that doping with 0.25 wt. % magnesia enabled alumina to be sintered to a low porosity, translucent state, after firing at high temperatures (~1900°C) in a hydrogen atmosphere (see figure 1).

II.ii) Initial Theories - Coble and Burke [1,4]

Coble observed that magnesia additions had a dramatic effect on the microstructure of sintered alumina (see figure 2). Undoped alumina developed abnormal grains which produced very non-uniform microstructures with many pores trapped within the large abnormal grains. With magnesia additions, abnormal grain growth was inhibited and the resultant microstructures were very uniform and dense and the pores remained attached to the grain boundaries. (Burke had demonstrated previously [5] the importance of keeping the pores attached to the grain boundaries in order to achieve high densities during sintering).

In nineteen sixty-one, Coble [1] analyzed the kinetics of densification and grain growth for undoped and MgO-doped alumina and postulated mechanisms for the function of magnesia as a sintering additive. He observed that additions of 0.25 wt. % MgO to high-purity Linde A alumina increased the rate of densification during isothermal sintering at 1675°C. However, the MgO was found to have no influence on the rate of normal grain growth during sintering. He hypothesized that densification was controlled

---

[1]   The trade name for transLUCent ALuminum OXide

by lattice diffusion of aluminum ions while oxygen was transported along the grain boundaries.

Initially Coble offered four possible explanations for how MgO might inhibit abnormal grain growth in alumina. First, there was the second phase pinning theory which asserted that magnesia, in excess of the solubility limit, could form precipitates of $MgAl_2O_4$ spinel which could pin the grain boundaries and inhibit abnormal grain growth. Second, the solid-solution pinning model proposed that MgO could absorb preferentially at the grain boundaries and inhibit abnormal grain growth by decreasing the grain boundary mobility. Third, it was speculated that magnesia could change the grain growth inhibiting effect of the pores by altering pore shapes. This would result from an alteration of the surface energy to grain boundary energy ratio. And fourth, the solid-solution theory assumed that a minimum amount of time was required to nucleate abnormal grain growth after reaching a critical density. It was argued that magnesia enhanced the densification rate relative to the rate of normal grain growth so that there was insufficient time for the formation of abnormal growth nuclei.

Given these four possibilities, Coble favored the solid-solution theory since each of the other mechanisms predict that the rate of normal grain growth should be inhibited by magnesia additions. Coble concluded ..

"In controlling the sinterability of alumina to theoretical density, it appears that magnesia does not "inhibit" discontinuous grain growth but instead increases the sintering rate such that discontinuous growth nuclei do not have time to form."

No detailed atomic mechanism was invoked to support this interpretation at the time.

A few years later in 1963, Coble and Burke [4] reviewed the matter again. They ruled out the second-phase pinning theory once more but this time based upon micrographic evidence that indicated there was insufficient second phase present for this mechanism to operate. They further concluded the solid-solution theory to be the most plausible description of the role of MgO. They did however, reconsider the solid-solution pinning model and argued that this mechanism should not be totally ruled out just because MgO was found to have no effect on the average rate of normal grain growth during sintering. They argued that solute pinning could limit the maximum grain boundary velocity of an abnormally growing grain, so suppressing the spread of abnormal grains, without influencing the grain boundary velocity of the normally growing grains whose growth rates would continue to be controlled by the attached pores. It was finally concluded..

"Under certain conditions any of these processes might operate, and other, independent measurements are necessary to decide between them."

The effect of firing atmosphere also came under study by Coble at this time [6]. He showed that the atmosphere had to be soluble in alumina in order to sinter MgO-doped material to theoretical density. Where insoluble gases were used, shrinkage was found to be terminated when the gas pressure in the closed pores balanced the driving pressure for shrinkage resulting

from the surface energy. Thus, MgO-doped alumina could be sintered to theoretical density at high temperatures in hydrogen, oxygen or vacuum but not in air, nitrogen, helium or argon.

II.iii) 1964: Jorgensen and Westbrook [9,10]

In 1964 Jorgensen and Westbrook [9] published a classic paper in which they presented indirect evidence for magnesium segregation to the grain boundaries in alumina. In one set of experiments they measured the microhardness profiles across grain boundaries in undoped, MgO-doped and alumina doped with a variety of other additives. They observed a strong peak in the microhardness profile at the grain boundary in the magnesia-doped alumina and presented this as evidence for grain boundary segregation (see figure 3). They also observed an increase in the alumina lattice parameter with increasing grain size, which was taken as further evidence of grain boundary segregation. It was noted, however, that the cooling rate had a strong influence on the magnitude of the observed lattice parameter changes. They further examined a range of different additives and were able to correlate the effectiveness of the dopant as a sintering aid with the degree of segregation inferred from the degree of grain boundary hardening. Nickel oxide was found to behave similarly to magnesia in controlling microstructure development and also showed apparent segregation. An autoradiograph of sintered alumina doped with a [63]Ni isotope gave clear direct evidence of grain boundary segregation of nickel. Given the similarities between the two dopants, this was taken as a strong indication that magnesia would also segregate strongly to grain boundaries in alumina.

Jorgensen [10] subsequently repeated earlier experiments of Johnson and Cutler [8], on the effect of MgO on the initial stage sintering kinetics of alumina, together with Coble's experiments on the effect of MgO on the kinetics of densification and grain growth. He confirmed the finding of Johnson and Cutler that magnesia additions decreased the densification rate during initial stage sintering. During the later stages of sintering he found that magnesia additions increased the densification rate (as observed by Coble) but he also noted a decrease in the average rate of normal grain growth, which was contrary to the observations of Coble. Jorgensen attributed this discrepancy to the fact that Coble had fired the undoped and magnesia-doped samples adjacent to one another in the furnace. He argued that magnesia could have transferred to the undoped samples unknowingly by vapor transport. [2] Jorgensen's data indicated that the densification rate of alumina was enhanced indirectly due to the retardation of grain growth by the magnesia. [3] He proposed that the

---

[2] Bruch [7] had shown that the surfaces of MgO-doped Al_2O_3 generally contained abnormal grains which resulted from magnesia loss at the surface by evaporation.

[3] The sintering models developed by Coble [1] predict that the densification rate varies with the reciprocal of the grain size to the third or fourth power for control by bulk diffusion or grain boundary diffusion respectively.

magnesia inhibited grain growth by a solute pinning mechanism. The direct effect of the additive on densification was assessed by comparing densification rates at _constant_ grain size. The analysis revealed that magnesia additions decreased the densification process directly either by lowering the lattice or grain boundary diffusion coefficient, or the solid - vapor surface energy. Jorgensen used a defect chemistry approach to interpret the results invoking that the incorporation of Mg^{2+} impurity ions promoted the formation of oxygen vacancies $(V_O^{\cdot\cdot})$ as the compensating defect for Mg_{Al}'. This in turn, it was argued, would suppress the concentration of aluminum ion vacancies (V_{Al}''') through the equilibrium reaction for Schottky defects. Thus, with the sintering rate $\dot{\rho} \propto D_l^{Al} \propto [V_{Al}'''] \propto [Mg_{Al}']^{-2/3}$ the effect of MgO on the densification rate could be explained. These findings ran contrary to the solid-solution model proposed by Coble from which one would have expected magnesia to increase the densification rate.

II.iv) 1964 - 1972: Solute-Pinning theory Gains Acceptance

Following the work of Jorgensen and Westbrook the solute-pinning theory became widely accepted. Warman and Budworth [11] were amongst those who accepted the proposition of solute-pinning. They also drew attention to the importance of the volatility of the additive; a high degree of volatility was argued to be necessary to obtain a uniform distribution of the additive during firing. They further confirmed that alumina could be doped with magnesia via vapor phase transport. Warman and Budworth [11] investigated the effect of a variety of additives on the sintering of alumina and showed that the criteria of ionic size, cation valence and additive volatility could account for the success or failure of a particular compound as a sintering aid. In a review article, Budworth [15] published criteria for the selection of sintering aids for alumina that function via the control of grain growth; he argued that grain boundary "films" offered the most viable mechanism responsible for such behavior.

Haroun and Budworth [16] conducted further studies of the effect of MgO, ZnO and NiO on grain growth in alumina. They concluded that, at a dopant level of 0.25 wt. %, the additive was present as discrete precipitates and a grain boundary film. They noted that a minimum amount of additive, approximately 0.05 wt. %, was necessary to control grain growth; this level corresponds to a film thickness of approximately 0.5 nm for a grain size of 3 μm. The observation suggested that the minimum amount of grain boundary phase required was the amount necessary to produce monolayer coverage of the grain boundary interfaces. Prendergast, Budworth and Brett [18] determined the optimum conditions for producing dense fine grained MgO-doped alumina. They discovered it was important, from a practical point of view, to prefire the powder compacts (~1,000 - 1,200°C) prior to sintering to aid the distribution of the additive.

Mocellin and Kingery [20] studied the effects of second phases (pores and spinel precipitates) and atmosphere on the microstructure development and grain growth kinetics in alumina. It was demonstrated that grain growth was controlled by pore drag throughout the majority of sintering for both undoped and MgO-doped material but at very high densities (>98%) motion of spinel particles for the MgO-doped material controlled grain

growth. All the kinetic data collected could be fitted with a cubic growth law. They concluded therefore, that kinetic measurements alone were incapable of distinguishing between the different possible ate controlling mechanisms.

To this point no direct evidence had been obtained to show that magnesia did segregate to grain boundaries as would be requ ad if a solute-pinning mechanism was responsible for the function of MgO. There was also some reason to doubt the solute-pinning mechanism because none of the samples studied thus far had been single phase and, therefore, it had been impossible to unequivocally rule out a second-phase pinning mechanism. [4]

In 1970 Tong and Williams [17] conducted the first direct microchemical analysis of solute segregation to grain boundaries in MgO-doped alumina. The technique of spark source mass spectrometry was employed in which material is removed from a region approximately 0.3 μm deep by striking a spark onto the surface of interest; the vaporized material is then analyzed using a mass spectrometer. A comparison was made between the bulk and grain boundary chemistry by comparing the analyses of a polished section and an intergranular fracture surface. A factor of 8 increase in magnesia concentration at grain boundaries was reported together with a factor of 13 increase in calcia concentration. Unfortunately no details were provided of the composition or thermal history of the alumina studied so no conclusions relevant to the role of magnesia in the sintering of alumina could be made. This work led to a succession of studies carried out in the 1970's of grain boundary chemistry using more sophisticated surface analysis techniques. We shall see that the results of these studies raised significant doubt as to whether MgO did segregate to grain boundaries in Al_2O_3 and thus whether it could inhibit grain growth by a solid-solution pinning mechanism.

II.v) 1972 - 1975: Search For Grain Boundary Segregation

Marcus and Fine [19] used the technique of Auger electron spectroscopy (AES) to characterize grain boundary chemistry in alumina. A piece of Lucalox® was fractured in the high vacuum chamber of the instrument and the intergranular fracture surface analyzed. No magnesia was detected in this study but, surprisingly, strong calcium segregation was observed. The bulk calcium levels were on the order of 10 - 15 ppm, whereas the concentration at the grain boundaries was of the order of 2 - 5 %, corresponding to an enrichment of some several thousand. The calcium concentration profile away from the grain boundary was determined with the aid of ion sputtering; the calcium was found to be confined to the first few monolayers at the grain boundary. It was postulated that calcium segregates more strongly than magnesium because of its larger ionic radius and correspondingly

---

[4] Roy and Coble [14] determined the solubility of MgO in Al_2O_3 as a function of composition and atmosphere by lattice parameter measurements. It was found that the solubility limit was much less (e.g 250 ppm at 1,630°C and 1,350 ppm at 1,850°C in vacuum) than the concentrations commonly used during sintering (typically 2,500 ppm).

larger lattice strain misfit.

Taylor, Coad and Brook [22] carried out a similar study using x-ray photoelectron spectroscopy (XPS) which can detect lower concentrations of magnesium than AES. In this work magnesium was found to be enriched at the grain boundary by a factor of two over the bulk levels. Strong calcium segregation was confirmed.

Johnson and Stein [24] conducted a detailed study of grain boundary segregation in an alumina doped with approximately 1,000 ppm MgO. A scanning Auger microprobe (SAM) was used in this work which has superior lateral resolution (~5 μm) compared to the instruments used to this date. The study showed that most of the magnesia on the intergranular fracture surface was confined to a $MgAl_2O_4$ spinel second phase. Analysis of areas not containing spinel precipitates indicated that magnesia was not segregated to grain boundaries in significant amounts. Johnson and Stein also demonstrated that spinel precipitates are preferentially removed during ion sputtering and concluded that concentration profiling using this technique yields an apparent profile which is an artifact. They further confirmed segregation of calcium to concentrations of several thousand times the bulk level but found the degree of segregation to be very sensitive to the thermal history of the specimens.

This latter finding supports a key point made by Kingery [26] in a review article which reads...

"a large fraction of the grain boundary solute segregation observed at temperatures below an equilibrium temperature forms on cooling."

This point was also recognized by Jorgensen [21] who agreed that many of the observations of segregation over wide regions from a grain boundary (including his own earlier work [9]) were probably the result of segregation induced by slow cooling. This gave further reason to be cautious of any result which showed magnesia segregation in alumina, because most samples studied were from a commercial source where typically materials are allowed to cool slowly from the firing temperature. [5]

By 1975 considerable doubt had been raised as to the validity of the solute-pinning theory because of the inability to detect magnesium segregation in alumina. Several papers were then published which served to refocus attention on the solid solution model.

---

[5] This problem arose during further work in the 1980's. Franken and Gehring [39] investigated a series of aluminas doped with MgO solute. Segregation of MgO to grain boundaries was reported. However, it was subsequently demonstrated [48] that the cooling rate used by Franken and Gehring (200°C/hr.) was sufficient to induce segregation and/or precipitation of $MgAl_2O_4$.

II.vi) 1975 - 1979: Revival of The Solid Solution Theory

Peelan [23] studied the evolution of the microstructure of alumina as a function of MgO additions both below and above the solubility limit. The host alumina used was very pure with a total cation concentration of less than 100 ppm; this allowed the effect of very small additions of MgO (down to 50 ppm) on microstructure development to be determined. Figure 4 shows Peelan's findings on the evolution of density and grain size, as a function of MgO content, for a fixed firing schedule. The most notable feature of the data is that both the density and grain size were observed to pass through a maximum at the solubility limit of MgO in Al_2O_3 (~300 ppm for this study which compares favorably with the 250 ppm limit determined by Roy and Coble [14] for this temperature). It was clear from this data that very small amounts of magnesia, below the solubility limit, were effective in aiding the sintering of alumina.

Peelan rejected the solute-pinning theory for three reasons. First, MgO enhanced normal grain growth in the solid solution regime (he argued that previous studies that indicated MgO additions retarded grain growth had been conducted with MgO concentrations above the solubility limit). Second, AES analysis revealed no segregation of magnesium. And third, CaO, a known segregant, did not prevent abnormal grain growth in alumina.

The essential action of MgO was, therefore, proposed to be a direct enhancement of the densification rate. In support of this proposal work by Rao and Cutler [27] was cited which showed that Fe^{2+} ions increased the sintering rate of alumina. He argued in favor of a cation Frenkel defect model, in which both lower valence and higher valence dopants could increase the aluminum ion diffusion coefficient either by raising the concentration of aluminum interstitials (in the case of the lower valence additive) or aluminum vacancies (in the case of the higher valence additive). Peelan proposed that the normal rate of grain growth was controlled by the volume fraction and size of the pores, and that the grain growth rate was dependent on the rate of pore removal. The enhanced grain growth rate via doping was therefore a result of the direct increase of the densification rate yielding smaller, more mobile, pores at a given grain size. A direct effect of the MgO on the pore mobility was not completely ruled out.

Johnson and Coble [28] conducted a further critical test of the second phase and solid solution models. In their experiments an undoped pellet of alumina was sintered in close proximity to a pre-equilibrated compact of spinel and alumina. The experiment was ingeniously designed to allow transfer of MgO from the spinel/alumina compact to the undoped pellet in concentrations not exceeding the solubility limit. This produced a pellet of alumina with a dense fine grained MgO-doped outer surface, and a core, devoid of MgO, consisting of abnormal grains and entrapped porosity. This experiment established without doubt that a second phase was not necessary for MgO to function successfully as a sintering aid for alumina. AES analysis of grain boundary chemistry confirmed Ca segregation at boundaries of both normal, and abnormal grains, in the MgO-doped, and undoped regions of the specimen respectively; no evidence for Mg segregation was found. Johnson and Coble also concluded, much as Peelan did, that Ca segregation

did not suppress abnormal grain growth and that the solid-solution model was a reasonable description of the function of MgO.

The earlier findings of Johnson and Cutler [8] and Jorgensen [10] on initial stage sintering were dismissed as being inapplicable to the problem since they were carried out at low temperatures and fine grain sizes as compared to the high temperature, large grain size conditions under which Lucalox® is fabricated. Also the findings of creep studies [29] which showed that diffusional creep rates of alumina are enhanced on doping with MgO and other divalent cations were cited in support of the solid-solution model. Johnson and Coble did, however, add the following qualifying note after arguing for the solid-solution model...

"Since the definitive experiment« (pore removal in the absence of grain growth and grain growth in the absence of porosity) have not been attempted for doped and undoped alumina, no direct evidence can be presented for this model."

At this point opinion was firmly returning towards the solid-solution model.

Harmer, Roberts and Brook [30] studied the effect of MgO solute on the densification and grain growth in alumina during fast-firing. They observed that MgO, in solid solution, enhanced both densification and normal grain growth after firing for a few minutes at 1850°C. It was proposed that MgO additions promoted densification through a modification of point defect concentrations. Enhanced densification was argued to give smaller, more mobile pores, at a given grain size, thereby preventing pore-grain boundary separation and abnormal grain growth.

Harmer and Brook [33] used hot-pressing dilatometry to quantitatively show MgO solute additions enhance the aluminum ion lattice diffusion coefficient and proposed two plausible defect chemistry models to explain this observation. They also presented an expression showing that the conditions for pore-grain boundary separation were less likely to be fulfilled if the ratio of the pore mobility to the grain boundary mobility (M_p/M_b) were increased. Assuming the pore moved by surface diffusion, the mobility ratio was given as:

$$M_p/M_b \propto (\delta_s D_s/r^4)(1/M_b) \qquad \dots\dots\dots (1)$$

were $\delta_s D_s$ is the surface diffusivity and r is the pore radius. It was argued that the essential action of the MgO was to increase the pore mobility indirectly through decreasing the pore size (viz increasing the densification rate) at a given grain size. This explanation was preferred over any effect on $\delta_s D_s$ or M_b, because of the strong power dependence of M_p on pore radius, r.

Heuer [31] objected to the solid-solution theory and argued strongly in favor of MgO increasing the pore mobility directly by raising the surface diffusivity. He did not accept that the solid-solution theory gave an adequate explanation for the inhibition of abnormal grain growth by MgO. Heuer was also concerned by the fact that several papers had reported that MgO inhibited densification in alumina. Bannister [34] commented on Heuer's note, correcting a mathematical error, and offered some indirect evidence in support of Heuer's proposal. Heuer [35] acknowledged the comment and argued further against the solid-solution theory by disagreeing with the point defect interpretation given by others. At this time however, Heuer had no experimental results to support his proposition.

Monty and Ledigou [41] responded to Heuer's note and used the method of multiple scratch smoothing to measure the effect of MgO on surface diffusion in sapphire. The method involved measuring the decay in amplitude of a periodic wave etched into the surface of a sapphire crystal. They observed, contrary to Heuer's prediction, that MgO decreased the rate of amplitude decay, hence the surface diffusivity, by a factor of ten at 1600°C. These findings were therefore contrary to the predictions made by Heuer.

Brook [42] accepted that MgO lowered surface diffusion in alumina and offered an explanation for the role of MgO based upon the combined effect on surface diffusion and lattice diffusion. He refocused attention on the effect of the additive on the ratio of the relative densification rate $(\dot{\rho}/\rho)$ to the relative grain growth rate $(\dot{G}/G)$. Following the treatment of Yan [40] of simultaneous densification and grain growth, he derived the following expression for the ratio:

$$(\dot{\rho}G/\rho\dot{G}) = (D_l/D_s)(\gamma_s/\gamma_b)G(1-\rho)^{4/3} \qquad \ldots\ldots\ldots (2)$$

assuming densification was controlled by lattice diffusion and grain growth was controlled by surface-diffusion-controlled pore drag. Brook deduced that MgO would increase the ratio by a factor of 30 at 1600°C based upon the independent measurements of Monty and Ledigou (MgO decreases $\delta_s D_s$ by a factor of 10) and Harmer and Brook (MgO increases D_l^{Al} by a factor of 3). Assuming that densification was controlled by lattice diffusion and that grain growth was controlled by surface-diffusion-controlled pore drag. This adjustment was predicted to cause a significant fattening of the grain size-density trajectory followed during sintering (figure 5). The treatment presented by Brook amounted to a modified version of the original solid-solution theory proposed by Coble [1]. No experimental measurements of grain size-density trajectories comparing undoped and MgO-doped alumina were available at that time to test Brook's hypothesis.

Burke, Lay and Prochazka [36] had previous to this measured the trajectories of specific surface area (SSA) versus density for undoped and 500 ppm MgO-doped alumina; this measurement also provided an estimate of the effect of the additive on the relative densification rate - relative

coarsening rate ratio. Their results, reproduced in figure 6, showed no effect of MgO on the SSA - ρ trajectory for alumina. They concluded that MgO had no effect on surface diffusion or pore mobility in alumina. These findings were skeptically received because of the low temperatures used in the study (1000 - 1500°C) and the attendant low solubility of MgO in alumina over this temperature range. Burke et al. suggested that the role of MgO was to lower the grain boundary mobility, M_b. They presented observations of abnormal grain growth at the free surface of an alumina specimen, where MgO was believed to have been lost by evaporation, and observations of fine normal grains within the bulk of the (MgO doped) specimen. They estimated that the remaining MgO in the bulk had decreased M_b by up to a factor of one hundred. No atomic mechanism was invoked and no explanation given for the lack of evidence for magnesium segregation to grain boundaries in alumina.

Dynys [43] conducted an extensive review of the surface diffusion literature for alumina. From a ranking of the reported diffusivities he concluded that, in general, the cleaner the experiment (i.e the higher the specimen purity), the lower the reported surface diffusivity. Dynys also conducted grain boundary grooving experiments in aluminas doped with a range of additives from which he concluded that MgO most likely enhanced surface diffusion in alumina. He also pointed out that facetting can lead to serious errors in determining surface diffusivities in experiments where the kinetics of shape changes driven by capillarity are studied. Monty and Ledigou [41] observed facetting in their experiments which created some concern at the time about the validity of their findings on the effect of MgO on surface diffusion in sapphire.

In summary, two opposing theories were advanced to explain the role of MgO in the sintering of Al_2O_3 based on an alteration of the surface diffusion coefficient. One theory was that MgO increased pore mobility by increasing $\delta_s D_s$, so avoiding pore-grain boundary breakaway and abnormal grain growth, whereas the other theory proposed that MgO decreased $\delta_s D_s$ and consequently promoted densification relative to grain growth. The experimental measurements, however, were inconclusive at this stage, because of problems with either the experimental technique itself or the range of experimental conditions over which the measurements were made.

II.viii) 1983: Critical Experiments to Measure Grain Boundary Mobility

It is clear from the previous discussions that further progress could not be made without obtaining much needed critical experimental data. A crucial test was to design an experiment that could determine, unambiguously, whether MgO solute affected the grain boundary mobility of alumina. Several workers had attempted to examine this influence but the results were always inconclusive because of the interference from ever-present pores and/or second phases [1,7,9,10,16,18,20,23,32,44,45].

Bennison and Harmer [47] utilized hot-pressing to fabricate test specimens suitable for conducting controlled experiments on grain growth. However, hot-pressed alumina was found to swell during subsequent grain growth anneals conducted in air [48]. The cause of this was determined to be a gas forming reaction between trace carbon and/or sulphur impurities at

grain boundaries with oxygen from the ambient. The swelling was prevented by annealing in atmospheres of low oxygen content or by pretreating the starting powders in flowing oxygen to burn off the carbon and sulphur contaminants beforehand [53]. By preventing swelling, grain growth kinetics were successfully measured in fully dense, hot-pressed, alumina as a function of MgO solute additions. It was found that MgO doping (Mg/Al = 250 ppm) decreased the grain growth rate in one fully dense alumina by a factor of five at 1600°C and led to more uniform grain shapes. This was the first direct proof that MgO solute could retard grain growth in alumina. The samples were believed to be single phase at the time of the study and a grain growth mechanism based on a solute drag effect involving solute partitioning of segregated ions (trace calcium contamination and added magnesium) between different boundary types was proposed.

Table 2. A comparison of rate constants, K (cubic kinetics), for grain growth at 1600°C in dense aluminas of varying purities.

Source	K value ($m^3 \cdot s^{-1}$)	
	Undoped	MgO Doped
High-Purity (99.98) (unintentional liquid phase present) [47]	1.74×10^{-19}	3.90×10^{-20}
Ultra-High-Purity (99.995) (single phase) [54]	5.17×10^{-19}	1.04×10^{-20}

It was subsequently revealed by transmission electron microscopy, however, that the samples used were sufficiently impure (~99.98 % Al_2O_3) to contain a small amount of an amorphous phase at certain grain boundaries which was presumably liquid at the firing temperature. Accordingly, the study was repeated using an ultra-high purity alumina (~99.995 % Al_2O_3) in which there was little chance of forming amorphous phases [54]. In these ultra-high purity samples 250 ppm MgO was found to decrease the grain boundary mobility by a factor of fifty at 1600°C; an order of magnitude more than in the less pure system. The grain structures of both undoped and doped samples were very uniform in the ultra-high purity work suggesting that no amorphous phases were present in these specimens (it was asserted that the elongated lath-like grains commonly observed in less-pure aluminas signalled the presence of a liquid phase at the grain boundaries). The degree of grain growth inhibition was correlated with powder purity and MgO-doping; Table 2 gives the observed trend which is supported with a recent study by Kaysser et al. [61].

It was further proposed that compensating lattice defects played a role in the grain growth inhibition mechanism. Results of a study by Lynch [52]

on the kinetics of grain in codoped aluminas had shown that the inhibiting effect of MgO could be cancelled by an equimolar addition of ZrO_2 and was cited in support of this mechanism. A compensating defect mechanism had been proposed earlier by Roy and Coble [14] to explain the enhanced solubility of Mg and Ti in Al_2O_3.

Based upon their findings, Bennison and Harmer concluded that the dominant role of MgO in the sintering of alumina was to reduce the grain boundary mobility; the most plausible atomistic mechanism was believed to be a solid-solution pinning mechanism.

II.ix) 1984: Microstructure Development Maps [51]

In 1984, Harmer introduced a new type of microstructure development map to describe sintering which proved to be a valuable aid in deconvoluting the function of solid-solution sintering additives [51]. The diagram combined the grain size density diagrams developed by Yan [40] with the pore-grain boundary separation diagrams (originally plotted in pores size - grain size space) developed by Brook [13]. The maps-were used to illustrate the effect of using solid solution additives to alter diffusion parameters (D_l, $\delta_s D_s$, M_b, etc.) in sintering. The maps proved their use when demonstrating conflicting effects of certain additives on microstructure development. Consider, for example, the case of altering the surface diffusivity; Figure 8 shows the predicted effect of raising the surface diffusivity in alumina by a factor of ten. This produces a beneficial effect on the pore separation region (recall from equation 1 that raising $\delta_s D_s$ promotes pore - boundary contact) by moving the conditions for separation to larger grain sizes. This is offset, however, by the detrimental effect on the grain size - density trajectory, which is a function of the $\dot{\rho}G/\rho\dot{G}$ ratio (recall from equation 2 that $\dot{\rho}G/\rho\dot{G} \propto 1/\delta_s D_s$). [6] Overall, therefore, raising the surface diffusivity alone was not predicted to be helpful to sintering. By a similar argument, lowering the surface diffusivity was predicted to be beneficial to the ratio but detrimental to pore-grain boundary separation; lowering the surface diffusivity alone was also predicted to be unhelpful to sintering. Thus, the earlier explanations for the role of MgO in the sintering of alumina, based solely on an alteration of the surface diffusivity, did not appear to be justified. Harmer went on to use the map to explain the effect of MgO in terms of its combined influence on M_b (lowered by 5 at 1600°C) and D_l (increased by 3 at 1600°C).

II.x) Critical Experiments on the $\dot{\rho}G/\rho\dot{G}$ Ratio

By now it was generally agreed that MgO decreased M_b significantly in alumina by a solid solution mechanism. At this point Berry and Harmer [57] grouped the various explanations for the role of MgO into four general categories, viz: i) MgO raises the lattice diffusion coefficient, D_l, and/or the grain boundary diffusion coefficient, D_b, which raises the $\dot{\rho}G/\rho\dot{G}$

---

[6] Note the steepening of the trajectory leads to a kinetic limit to densification.

ratio and so flattens the grain size-density trajectory (i.e smaller pores at a given grain size). ii) MgO raises $\delta_s D_s$ (hence the pore mobility) and lowers the $\dot{\rho}G/\rho\dot{G}$ ratio which changes the G-ρ trajectory to give larger grains (and pores) at a given density. iii) MgO lowers $\delta_s D_s$ which raises the $\dot{\rho}G/\rho\dot{G}$ ratio to give smaller grains at a given density, and iv) MgO lowers M_b which may not affect the trajectory but will suppress pore - grain boundary separation.

Explanations 1 - 3 are based upon a change in the relative densification rate-relative coarsening rate ratio which is manifest in a change in the grain size-density trajectory. Accordingly, a critical test of these proposals was to measure the effect of MgO additions on the trajectory. Berry and Harmer [59] measured this influence at 1600°C and found it to be negligible (figure 9). They were also able to isolate the separate effects of MgO and densification from their kinetic measurements. MgO solute was found to increase the densification rate directly, by a factor of 3, through an increase in the grain boundary diffusion coefficient. MgO solute was also found to increase the grain growth rate, by a factor of 2.5, through an increase in the surface diffusivity. Since the additive increased both the densification and grain growth rates similarly, its effect on the ratio, and hence the trajectory, was minimal.

In order to explain the role of MgO the following expression was derived as a figure of merit for the resistance to pore - boundary separation:

$$(1/G^2)_\rho \delta_s D_s / M_b \qquad \dots\dots\dots (3)$$

An independent study of grain growth in fully dense samples conducted on the same powder [52] revealed that MgO solute decreased M_b by a factor of 25 under the same conditions. Combined with the observed increase in $\delta_s D_s$ and flattening of the trajectory (grain size for MgO-doped samples 1.8 times less than undoped samples at a given density) resulted in an increase in the figure of merit by a factor of 112. Furthermore, since the additive acted most strongly through the M_b term, it was concluded that the dominant role of the MgO was to reduce grain boundary mobility. The net effect of doping was displayed on a microstructure development map (figure 10). It can be seen from figure 10 that the main change resulting from doping is that the separation region is moved to higher grain sizes (the grain size of the tip of the separation region is $\propto (\delta_s D_s / M_b)^{1/2}$) and the trajectory avoids entering the region.

Brook et al. [58] also independently measured the effect of MgO on the relative densification rate-relative coarsening rate ratio using hot-pressing dilatometry. They also found that MgO doping had little effect on the ratio. Shaw and Brook [60] studied the specific surface area-density trajectories for alumina which also are sensitive to variations in the ratio. Again it was found that the additive had little effect on the ratio. They also measured the specific grain boundary area versus density trajectory in a carefully conducted ceramographic study. Figure 11 shows their result. It was found that the specific grain boundary area was increased at a given density by MgO doping and concluded that a solid-

solution pinning effect was the only additive function evidenced by their findings.

II.xi) Relevance of Solute-Pinning to Inhomogeneity

By the mid 1980's it had become evident that the most important function of MgO solute additions was to decrease the grain boundary mobility. An important consequence of this action was to minimize the probability for the occurrence of pore-grain boundary separation.

It had been assumed that pore-boundary separation was the primary cause of abnormal grain growth in alumina. Burke [56] proposed in the 1960's that variations in grain boundary mobility due to chemical inhomogeneity could also trigger abnormal grain growth. Mistler and Coble [57] demonstrated that structural inhomogeneity in the green state resulted in density fluctuations in the final body and proposed that enhanced grain boundary motion in high density regions could further trigger abnormal grain growth. Bennison and Harmer [49,50] confirmed these ideas that inhomogeneity can lead to abnormal grain growth by following a series of microstructural changes in the sintering of alumina. It was found in one powder studied that inhomogeneous densification was the principal cause of abnormal grain growth rather than pore-boundary separation. Locally dense regions were observed to form in the microstructure at a relatively early stage of sintering. These dense regions formed a site for the initiation of abnormal grain growth due to the lack of restraining pores. MgO was found to suppress grain boundary motion within the dense regions so preventing abnormal grain growth development. Therefore, a second major benefit of the solute pinning action of MgO was to stabilize the microstructure against the consequences of inhomogeneous densification.

Shaw and Brook [60] also recognized this fact and observed during their measurement of specific grain boundary area-density trajectory (figure 11) that MgO preserved grain boundary area in locally densified regions of the microstructure. They described the function of the additive as a microstructural stabilizer, i.e. one which acts to restrain such processes as abnormal grain growth by the pinning of otherwise mobile boundaries.

If conditions of boundary controlled grain growth could be achieved by doping a non-uniform distribution of porosity would, therefore, not cause correspondingly non-uniform (potentially abnormal) grain growth. Zhao and Harmer [62] realized such a result by sintering ultra-high purity alumina doped with 250 ppm MgO; the grain growth rate during sintering (with a high fraction of pores present) was observed to be the same as that for fully dense samples prepared by hot-pressing. This arises because MgO solute lowers M_b by an exceptional amount in very pure powders. The density at which pores no longer influence boundary velocity is much lower (~87 % theoretical) than for less pure powders. Where MgO additions were seen to enhance grain growth [57] less pure powders where employed were grain growth was controlled by pore motion to much higher densities (>99 %).

The combination of using ultra-high purity powders and MgO doping has been shown to be especially effective in guarding against inhomogeneous microstructure development. The same benefits have also been demonstrated

in two phase systems where non-uniform distribution of a second phase poses a similar threat to microstructural stability [62].

A further feature related to inhomogeneity concerns the sintering of alumina in the presence of a small quantity of a liquid phase. Practical alumina ceramics frequently contain a small quantity of an amorphous phase at the grain boundaries resulting from a reaction between trace contaminants. This often leads to the growth of elongated, flat sided i.e. facetted, abnormal grains. MgO additions can prevent the development of such abnormal grains and produce uniform microstructures.

Kaysser et al. [63] carried out a model study of grain growth in alumina in which controlled amounts of anorthite glassy phase were deliberately added. Large spheres of alumina were also included to seed abnormal grain growth. It was found that the growth rates of matrix grains decreased in the order: undoped $Al_2O_3 \rightarrow Al_2O_3$ + anorthite $\rightarrow Al_2O_3$ + anorthite + MgO $\rightarrow Al_2O_3$ + MgO, thus confirming earlier findings where accidental contamination led to the presence of a liquid phase during firing [47,51,54]. These differences in mobility between clean grain boundaries and intergranular films were proposed as a cause of abnormal grain growth where the glass in inhomogeneously distributed on a coarse scale (following the ideas of Burke [56]). Important observations of facetting behavior as function of composition were also made by Kaysser et al. [63]. Specifically, basal facetting and anisotropic growth of the abnormal seed grains was observed for all compositions except for alumina doped with MgO alone. The growth of such facets was observed to be slower than matrix grain boundaries. It was further concluded that abnormal grain growth in systems containing small amounts of liquid can be caused by anisotropic growth of grain boundaries comprised entirely of intergranular liquid films.

Bateman et al. [68] conducted a TEM investigation of undoped and MgO-doped alumina contaminated with a small amount of an amorphous phase in an attempt to correlate the extent of grain boundary motion with the presence or absence of an intergranular phase and determine the function of MgO. The amorphous phase was found as thin intergranular films wetting the long facets of incipient abnormal grains in both undoped and MgO-doped material (figure 12). The long facets were identified as basal type (0001) as in the case of Kaysser et al. [63]. No glass phase was detected at the ends of the elongated grains and it was postulated that the ends were not wet by the amorphous phase. [7] In this system the glass was non-uniformly distributed on a scale less than the grain size. It was argued that the rapid growth of the elongated grains in the undoped alumina on subsequent annealing was due to the large mobility difference between boundary types, i.e. between the flat, slow moving intergranular films, and the clean, fast moving end segments. The function of MgO was suggested to be the reduction in the difference in boundary mobility between these boundary types; it was speculated that the solute additions would give a drag effect on the clean end boundaries. The broad function of MgO appeared to be as a microstructural stabilizer based upon a solute-pinning mechanism. It is

---

[7] Shaw [65] has recently presented direct evidence for the non-uniform wetting of grains of alumina by a silicate-based liquid phase.

clear however, that the exact atomic mechanism, particularly where liquid phases are present, is very sensitive to the system chemistry.

II.xii) Anisotropy of Interfacial Properties

In this final section of the historical review we describe some recent measurements of the effect of MgO on the interfacial properties of alumina.

Handwerker [46], and Handwerker et al. [69], measured the effect of MgO doping on the distribution of dihedral angles formed at the root of grain boundary grooves on polished and thermally etched surfaces of alumina. MgO was observed to narrow the distribution of angles without substantially affecting the mean value (117°). The dihedral angle is a measure of the ratio of the free surface energy to the grain boundary energy so MgO additions reduced the spread in this ratio. This was argued to contribute towards the effectiveness of the additive in preventing pore-grain boundary separation. Generally, MgO doping would also reduce local variations in the driving force for sintering and grain growth so promoting the development of more uniform structures during sintering.

Wang et al. [64] have also measured the relative anisotropy in free surface energy of alumina as function of MgO content through the study of equilibrium pore shapes in sapphire. MgO additions led to more uniform shapes indicating the additive reduced the anisotropy in free surface energy. This result, taken with Handwerker's, suggests that MgO decreases both the grain boundary energy anisotropy as well as the free surface energy anisotropy.

Baik et al. [55,61,67,70] recently carried out a state of the art AES study of the segregation of Mg and Ca to free surfaces in sapphire. Strong segregation of Mg to several different surfaces of sapphire was observed. Baik and White [67] also studied Ca segregation to free surfaces, although in this case the degree of segregation was found to be strongly dependent on the surface orientation. Baik noted that Mg segregates as strongly to free surfaces as Ca; the negative findings of the 1970's on grain boundary segregation of Mg were attributed to the poor sensitivity of the technique to Mg. The observations of free surface segregation suggest that Mg may segregate to grain boundaries also, and that a solute-drag mechanism may explain the role of MgO as a grain growth inhibitor. Again assuming these results indicate the segregation behavior in the case of grain boundaries, the observations of anisotropic Ca segregation may explain the ineffectiveness of CaO as a grain growth inhibitor.

III. SUMMARY AND FUTURE DIRECTIONS

The following general conclusions can be drawn from the past research on the role of MgO in the sintering of Al_2O_3. First, MgO additions affect all of the parameters controlling the sintering of alumina (i.e. D_l, $\delta_b D_b$, $\delta_s D_s$, M_b and γ_s/γ_b) to some extent. Generally the additive affects all these parameters in a favorable way which accounts, to some degree, for the potency of the additive in controlling microstructure evolution. Second, alumina responds to MgO doping by different degrees, depending on the

background impurity level and type. For example MgO has been observed to directly increase densification in some powders and directly decrease densification in others. Surface diffusion seems to be generally increased slightly by MgO doping whereas the grain boundary mobility always is decreased. Thirdly, we conclude that the single most important effect of MgO doping is its ability to significantly reduce the grain boundary mobility, despite the presence of varying background impurities, through a solid solution pinning mechanism. The consequences of the pinning action of MgO solute are a reduced tendency for pore-grain boundary separation, protection against abnormal grain growth arising from inhomogeneous densification and/or non-uniform liquid phase distribution, and in some cases, an indirect enhancement of densification processes.

Concerning future work, it is apparent we have come a long way in understanding the phenomenology of this classic additive effect. However, we still do not understand the detailed atomic mechanism through which MgO solute acts as a grain growth inhibitor in alumina. Without such fundamental information we do not possess the capability of a priori additive selection.

At the core of the problem is our lack of understanding of the fundamental grain growth mechanisms in ionic solids, and our lack of experimental information concerning grain boundaries in alumina. We need to know the grain boundary mobility as a function of MgO content and temperature. Segregation profiles would also be required and may now be accessible with the recent improvements in surface analysis techniques. However, the chemical characterization of MgO doped Al_2O_3 remains one of the most difficult obstacles to the complete understanding of the role of MgO. In less pure systems, knowledge of the grain growth mechanisms where amorphous intergranular films are involved is needed. From a practical viewpoint, more information concerning the role of MgO during liquid phase sintering is needed.

We now have a relatively simple experimental methodology for studying the effects of solutes on grain boundary motion in alumina [54]. It is timely to carry out systematic studies with other dopants of different ionic radii and valencies to investigate the role of strain misfit concepts, point defects and compensation effects.

ACKNOWLEDGMENTS

REFERENCES

1) R.L. Coble, "Sintering of Crystalline Solids - II. Experimental Test of Diffusion Models in Porous Compacts," J. App. Phys., 32[5] 793 - 99 (1961).

2) R.L. Coble, "Transparent Alumina and Method of Preparation," U.S. Patent # 3,026,210 March (1962).

3) P.D.S. St. Pierre and A. Gatti, "Process for Producing Transparent Polycrystalline Al_2O_3," U.S. Patent # 3,026,177 March (1962).

4) R.L. Coble and J.E. Burke, "Sintering in Ceramics," Progr. Ceram. Sci., 3 197 - 251 (1963).

5) J.E. Burke, "The Role of Grain Boundaries in Sintering," J. Am. Ceram. Soc., 40[3] 80 - 85 (1957).

6) R.L. Coble, "Sintering of Alumina: Effect of Atmospheres," J. Am. Ceram. Soc., 45[3] 123 - 27 (1962).

7) C.A. Bruch, "Sintering Kinetics for the High Density Alumina Process," Am. Ceram. Soc. Bull., 41[12] 799 - 806 (1962).

8) D.L. Johnson and I.B. Cutler, "Diffusion Sintering: II, Initial Sintering Kinetics for Alumina," J. Am. Ceram. Soc., 46[11] 545 - 50 (1963).

9) P.J. Jorgensen and J.H. Westbrook, "Role of Solute Segregation at Grain Boundaries During Final Stage Sintering of Alumina," J. Am. Ceram. Soc., 47[7] 332 - 38 (1964).

10) P.J. Jorgensen, "Modification of Sintering Kinetics by Solute Segregation in Al_2O_3," J. Am. Ceram. Soc., 48[4] 207 - 10 (1965).

11) M.O. Warman and D.W. Budworth, "Criteria for the Selection of Additives to Enable the Sintering of Alumina to Proceed to Theoretical Density," Trans. Brit. Ceram. Soc., 6[6] 253 - 64 (1967).

12) R.J. Brook, "The Impurity Drag Effect and Grain Growth Kinetics," Scripta Metall., 2[7] 375 - 78 (1968).

13) R.J. Brook, "Pore-Grain Boundary Interactions," J. Am. Ceram. Soc., 52[1] 56 - 67 (1969).

14) S.K. Roy and R.L. Coble, "Solubilities of Magnesia, Titania and Magnesium Titanate in Aluminum Oxide," J. Am. Ceram. Soc., 5[1] 1 - 6 (1968).

15) D.W. Budworth, "The Selection of Grain-Growth Control Additives for the Sintering of Ceramics," Mineralogical Magazine, 37[291] 833 - 38 (1970).

16) N.A. Haroun and D.W. Budworth, "Effects of Additions of MgO, ZnO and NiO on Grain Growth in Dense Alumina," Trans. Brit. Ceram. Soc., 69[] 73 - 79 (1970).

17) S.S.C. Tong and J.P. Williams, "Chemical Analysis of Grain Boundary Impurities in Polycrystalline Ceramic Materials by Spark Source Mass Spectrometry," J. Am. Ceram. Soc., 53[1] 58 - 59 (1970).

18) I.D. Prendergast, D.W. Budworth and N.H. Brett, "Densification and Grain Size Control in Alumina," Trans. Brit. Ceram. Soc., 71[1] 31 - 36 (1972).

19) H.L. Marcus and M.E. Fine, "Grain Boundary Segregation in MgO-Doped Al_2O_3," J. Am. Ceram. Soc., 55[11] 568 - 70 (1972).

20) A. Mocellin and W.D. Kingery, "Microstructural Changes During Heat Treatment of Sintered Alumina," J. Am. Ceram. Soc., 56[6] 309 - 14 (1973).

21) P.J. Jorgensen, "Grain Boundary Phenomena in Ceramic Materials," p. 205 in Proceedings of the 4th. Bolton Landing Conference, "Grain Boundaries in Engineering Materials," J.L. Walter, J.J. Westbrook and D.A. Woodford eds., Claitor's Publishing Division, Baton Rouge LA (1974).

22) R.I. Taylor, J.P. Coad and R.J. Brook, "Grain boundary Segregation in Al_2O_3" J. Am. Ceram. Soc., 57[12] 539 - 40 (1974).

23) J.G.J. Peelan, "Influence of MgO on the Evolution of the Microstructure of Al_2O_3," Mater. Sci. Res., 10 443 - 53 (1975).

24) W.C. Johnson and D.F. Stein, "Additive and Impurity Distribution at Grain Boundaries in Sintered Alumina," J. Am. Ceram. Soc., 58[11 - 12] 485 - 88 (1975).

25) W.C. Johnson, "Grain Boundary Segregation in Ceramics," Metall. Trans. A, 8A[9] 1413 - 22 (1977).

26) W.D. Kingery, "Plausible Concepts Necessary and Sufficient for Interpretation of Ceramic Grain Boundary Phenomena: II. Solute Segregation, Grain Boundary Diffusion and General Discussion," J. Am. Ceram. Soc., 57[2] 74 - 83 (1974).

27) W.R. Rao and I.B. Cutler, "Effect of Iron Oxide on the Sintering Kinetics of Al_2O_3," J. Am. Ceram. Soc., 56[11] 588 - 93 (1973).

28) W.C. Johnson and R.L. Coble, "A Test of the Second Phase and Impurity Segregation Models for MgO Enhanced Densification of Sintered Alumina," J. Am. Ceram. Soc., 61[3-4] 110 - 14 (1978).

29) R.M. Cannon and R.L. Coble, "Review of Diffusional Creep of Alumina," p. 61 in Deformation of Ceramic Materials, R.C. Bradt and R.E. Tressler eds., Plenum Press, New York NY (1975).

30) M.P. Harmer, E.W. Roberts and R.J. Brook, "Rapid Sintering of Pure and Doped α-Al_2O_3," Trans. Brit. Ceram. Soc., 78[1] 22 - 25 (1979).

31) A.H. Heuer, "The Role of MgO in the Sintering of Alumina," J. Am. Ceram. Soc., 62[5-6] 317 - 18 (1979).

32) R.D. Monohan and J.W. Halloran, "Single-Crystal Boundary Migration in Hot-Pressed Aluminum Oxide," J. Am. Ceram. Soc., 62[11-12] 564 - 67 (1979).

33) M.P. Harmer and R.J. Brook, "The Effect of MgO Additions on the Kinetics of Hot-Pressing in Al_2O_3," J. Mater. Sci., 15 3017 - 24 (1980).

34) M.J. Bannister, "Comment on the Role of MgO in the Sintering of Alumina," J. Am. Ceram. Soc., 63[3-4] 229 - 30 (1980).

35) A.H. Heuer, "Reply," J. Am. Ceram. Soc., 63[3-4] 230 - 31 (1980).

36) J.E. Burke, K. Lay and S. Prochazka, "The Effect of MgO on the Mobilities of Grain Boundaries and Pores in Aluminum Oxide," Mater. Sci. Res., 13 417 - 25 (1980).

37) D.R. Clarke, "Grain Boundary Segregation in an MgO-Doped Al_2O_3," J. Am. Ceram. Soc., 63[5-6] 339 - 41 (1980).

38) M.P. Harmer and R.J. Brook, "Fast Firing: Microstructural Benefits," Trans. J. Brit. Ceram. Soc., 80 147 (1981).

39) P.E.C. Franken and A.P. Gehring, "Grain Boundary Analysis of MgO-Doped Al_2O_3," J. Mater. Sci., 16[] 384 (1981).

40) M.F. Yan, "Microstructural Control in the Processing of Electronic Ceramics," Mater. Sci. Eng., 48 53 - 72 (1981).

41) C. Monty and J. LeDigou, "Effect of MgO on Surface Diffusion in Alumina," High Temperature, High Pressure, 14 709 - 16 (1982).

42) R.J. Brook, "Fabrication Principles for the Production of Ceramics with Superior Mechanical Properties," Proc. Brit. Ceram. Soc., 32 7 - 24 (1982).

43) J.M. Dynys, "Sintering Mechanisms and Surface Diffusion for Aluminum Oxide," Sc.D. Dissertation, Mass. Inst. Tech., Cambridge MA (1982).

44) A.M. Glaeser and J.C. Chen, "Technique for Measuring Grain Boundary Mobility: Application to MgO-Doped Al_2O_3," J. Am. Ceram. Soc., 65[7] C98 - C99 (1982).

45) M.F. Yan, R.M. Cannon and H.K. Bowen, "Grain Boundary Migration in Ceramics," p. 276 in Ceramic Microstructures '76, R.M. Fulrath and J.A.

Pask eds., Westview press, Boulder CO (1977).

46) C.A. Handwerker, "Sintering and Grain Growth of MgO," Sc.D. Thesis, Mass. Inst. Tech., Cambridge MA (1983).

47) S.J. Bennison and M.P. Harmer, "Effect of MgO Solute on the Kinetics of Grain Growth in Al_2O_3," J. Am. Ceram. Soc., 66[5] C90 - C92 (1983).

48) S.J. Bennison and M.P. Harmer, "Grain Growth and Cavity Formation in MgO-Doped Al_2O_3," p. 171 in Advances in Ceramics, vol. 6, "Character of Grain Boundaries," M.F. Yan and A.H. Heuer eds., The American Ceramic Society, Columbus OH (1983).

49) S.J. Bennison and M.P. Harmer, "Microstructural Studies of Abnormal Grain growth Development in Al_2O_3," p. 929 in Ceramic Powders, P. Vincenzini ed., Elsevier Scientific Publishing Co., Amsterdam, The Netherlands, (1983).

50) M.P. Harmer, S.J. Bennison and C. Narayan, "Microstructural Characterization of Abnormal Grain Growth Development in Al_2O_3," Mater. Sci. Res., 15 309 (1983).

51) M.P. Harmer, "Use of Solid Solution Sintering Additives in Ceramic Processing," p. 679 in Advances in Ceramics, vol. 10, Structure and Properties of MgO and Al_2O_3 Ceramics, W.D. Kingery ed., The American Ceramic Society, Columbus OH (1984).

52) M.J. Lynch, "Sintering and Grain Growth Studies on Al_2O_3 doped with MgO and/or ZrO_2," M.S. Thesis, Lehigh University, Bethlehem PA (1984).

53) S.J. Bennison and M.P.Harmer, "Swelling of Hot-Pressed Al_2O_3," J. Am. Ceram. Soc., 68[11] 591 - 97 (1985).

54) S.J. Bennison and M.P. Harmer, "Grain Growth Kinetics for Alumina in the Absence of a Liquid Phase," J. Am. Ceram. Soc., 68[1] C22 - 24 (1985).

55) S. Baik, D.E. Fowler, J.M. Blakely and R. Raj, "Segregation of Mg to the (0001) Surface of Doped Sapphire," J. Am. Ceram. Soc., 68[5] 281 - 86 (1985).

56) J.E. Burke, "Grain Growth," in Ceramic Microstructures '66, R.M. Fulrath and J.A. Pask eds., Wiley-Interscience, New York NY (1967).

57) R.E. Mistler and R.L. Coble, "Microstructural Variation due to Fabrication," J. Am. Ceram. Soc., 51[4] 237 (1968).

58) R.J. Brook, E. Gilbart, N.J. Shaw and U. Eisele, "Solid Solution Additives and the Sintering of Ceramics," Powder Metallurgy 28[2] 105 - 107 (1985).

59) K.A. Berry and M.P. Harmer, "Effect of MgO Solute on Microstructure Development in Al_2O_3," J. Am. Ceram. Soc., 69[2] 143 - 49 (1986).

60) N.J. Shaw and R.J. Brook, "Structure and Grain Coarsening During the Sintering of Alumina," J. Am. Ceram. Soc., 69[2] 107 - 110 (1986).

61) S. Baik, "Segregation of Mg to the (0001) Surface of Doped Sapphire: Quantification of AES Results," J. Am. Ceram. Soc., 69[5] C101 - 103 (1986).

62) J. Zhao and M.P. Harmer, "Sintering of Ultra-High Purity Alumina Doped Simultaneously with MgO and FeO," J. Am. Ceram. Soc., 70[12] 860 - 66 (1987).

63) W.A. Kaysser, M. Sprissler, C.A. Handwerker and J.E. Blendell, "Effect of Liquid Phase on the Morphology of Grain Growth in Alumina," J. Am. Ceram. Soc., 70[5] 339 - 43 (1987).

64) Z. Wang, unpublished research, Lehigh University (1988).

65) T.M. Shaw, "Which Grain Boundaries are Penetrated by Liquid?" Paper# 48-B-97, presented at the 89th Annual Meeting of The American Ceramic Society (1987).

66) A.P. Jardine, S.M. Mukhopadhyay and J.M. Blakely, "Mg Implantation and Characterization of Sapphire Surfaces," Mater. Res. Soc. Symp. Proc., 74 365 - 73 (1987).

67) S. Baik and C.L. White, "Anisotropic Calcium Segregation to the Surface of Al_2O_3," J. Am. Ceram. Soc., 70[9] 682 - 88 (1987).

68) C.A. Bateman, S.J. Bennison and M.P. Harmer, "A Mechanism for the Role of MgO in the Sintering of Al_2O_3 Containing Small Amounts of a Liquid Phase," in press, J. Am. Ceram. Soc. (1989).

69) C.A. Handwerker, J.M. Dynys, R.M. Cannon and R.L. Coble, "Dihedral Angles in MgO and Al_2O_3," submitted to J. Am. Ceram. Soc., (1988).

70) S.M. Mukhopadhyay, A.P. Jardine, J.M. Blakely and S. Baik, "Segregation of Magnesium and Calcium to the (10$\bar{1}$0) Prismatic Surface of Magnesium Implanted Sapphire," J. Am. Ceram. Soc., 71[5] 358 - 62 (1988).

FIGURE CAPTIONS

Figure 1. Translucent polycrystalline Al_2O_3 tube for use in a sodium vapor lamp; the tube was fabricated via the Lucalox® process.

Figure 2. Microstructures of sintered Al_2O_3: a) undoped material, note pore-grain boundary separation and abnormal grain growth, and b) MgO-doped material, note high density and equiaxed grain structure.

Figure 3. Variation of microhardness on traversing a grain boundary in MgO-doped alumina. (After Jorgensen and Westbrook [9]).

Figure 4. a) Final density and b) final grain size, for a series of sintered aluminas as a function of MgO concentration. (After Peelan [23], courtesy of Plenum Publishing Co.).

Figure 5. Predicted effect of raising the densification rate/coarsening rate ratio by a factor of thirty on microstructure evolution during the sintering of Al_2O_3. (After Brook [42], courtesy of The British Ceramic Society).

Figure 6. Specific surface area-density trajectory for undoped and MgO-doped Al_2O_3; note the MgO addition has a negligible effect on the trajectory. (After Burke et al. [36], courtesy of Plenum Publishing Co.).

Figure 7. Microstructures of a) dense undoped alumina, and b) dense MgO-doped alumina. Note the MgO addition has led to a more uniform grain structure and retarded grain growth in these samples. (After Bennison and Harmer [47]).

Figure 8. Microstructure development map showing the predicted effect of increasing the surface diffusivity by a factor of ten, via MgO doping, on both the grain size-density trajectory and the conditions for pore-grain boundary separation. While this increase favors pore-boundary contact, the steepened trajectory results in a kinetic limit to densification. (After Harmer [51]).

Figure 9. Measured effect of MgO doping on the grain-size density trajectory during sintering of alumina at 1600°C. (After Berry and Harmer [59]).
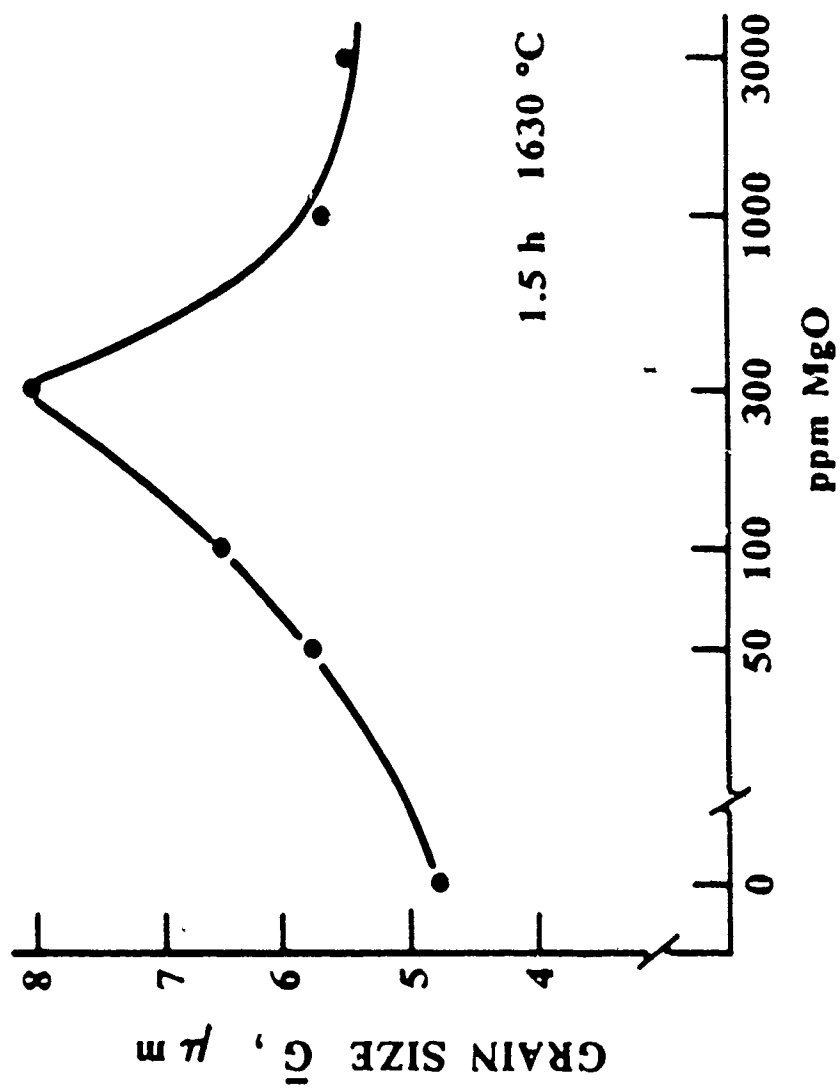
Figure 10.   Predicted effect of simultaneously increasing lattice
             diffusion by a factor of 3, increasing surface diffusivity
             by a factor of 2.5 and decreasing grain boundary mobility
             by a factor of 25, via doping with MgO solute, on
             microstructure development in alumina. (After Berry and
             Harmer [59]).

Figure 11.   Variation in the specific grain boundary area-density
             trajectory during sintering on MgO doping. Note the
             additive increases the grain boundary area at a given
             density, viz: smaller grain size at a given density. (After
             Shaw and Brook [60]).

Figure 12.   Transmission electron micrographs of a) undoped, and b)
             MgO-doped, Al_2O_3 containing trace amounts of an amorphous
             intergranular phase. Note the MgO additions have led to a
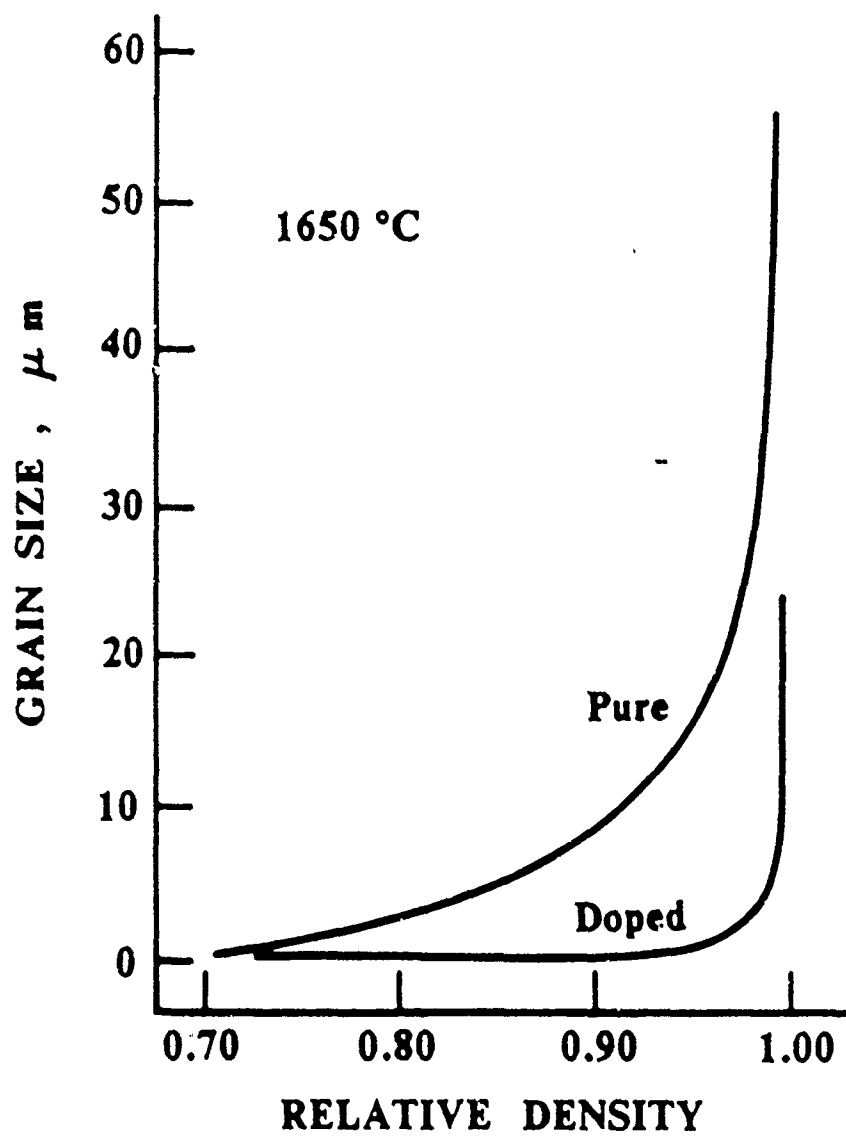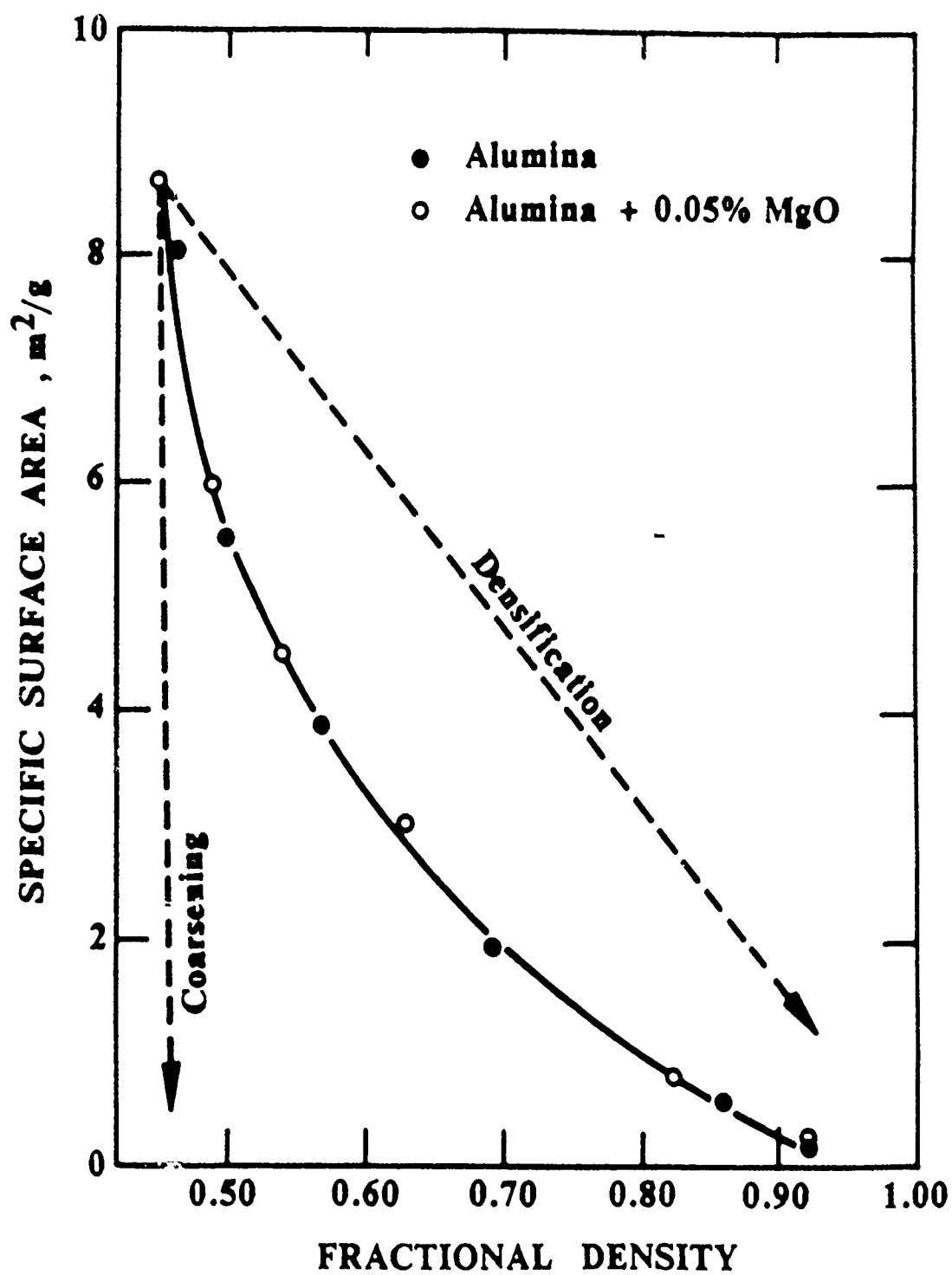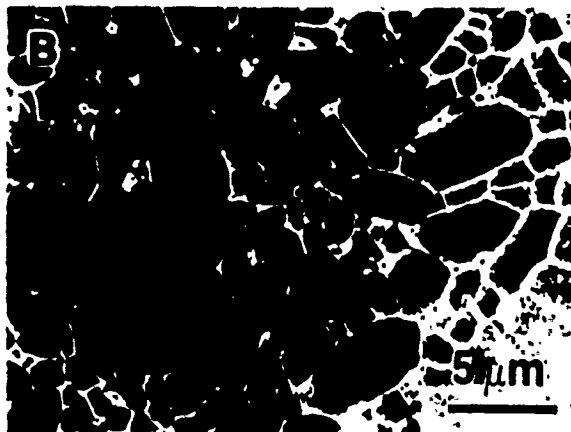   finer, more uniform, grain structure. (After Bateman et al.
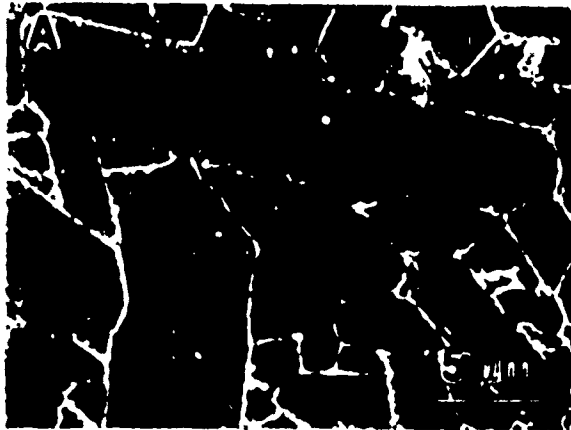   [68]).

4 cm

1

20 μm

20 μm

DISTANCE FROM BOUNDARY , micron

HARDNESS , kg/mm²

DENSITY vs ppm MgO

Theoretical Density

B

A

A: 1.5 h 1630 C
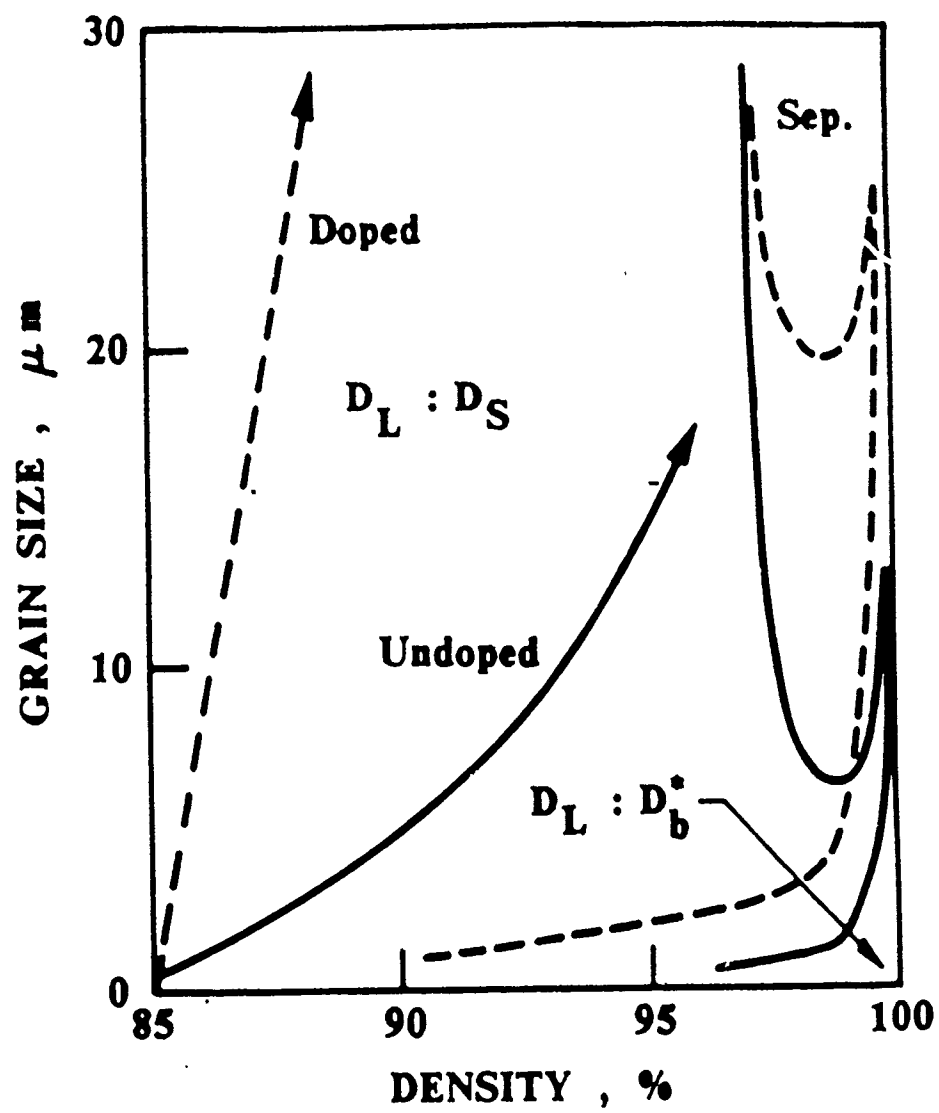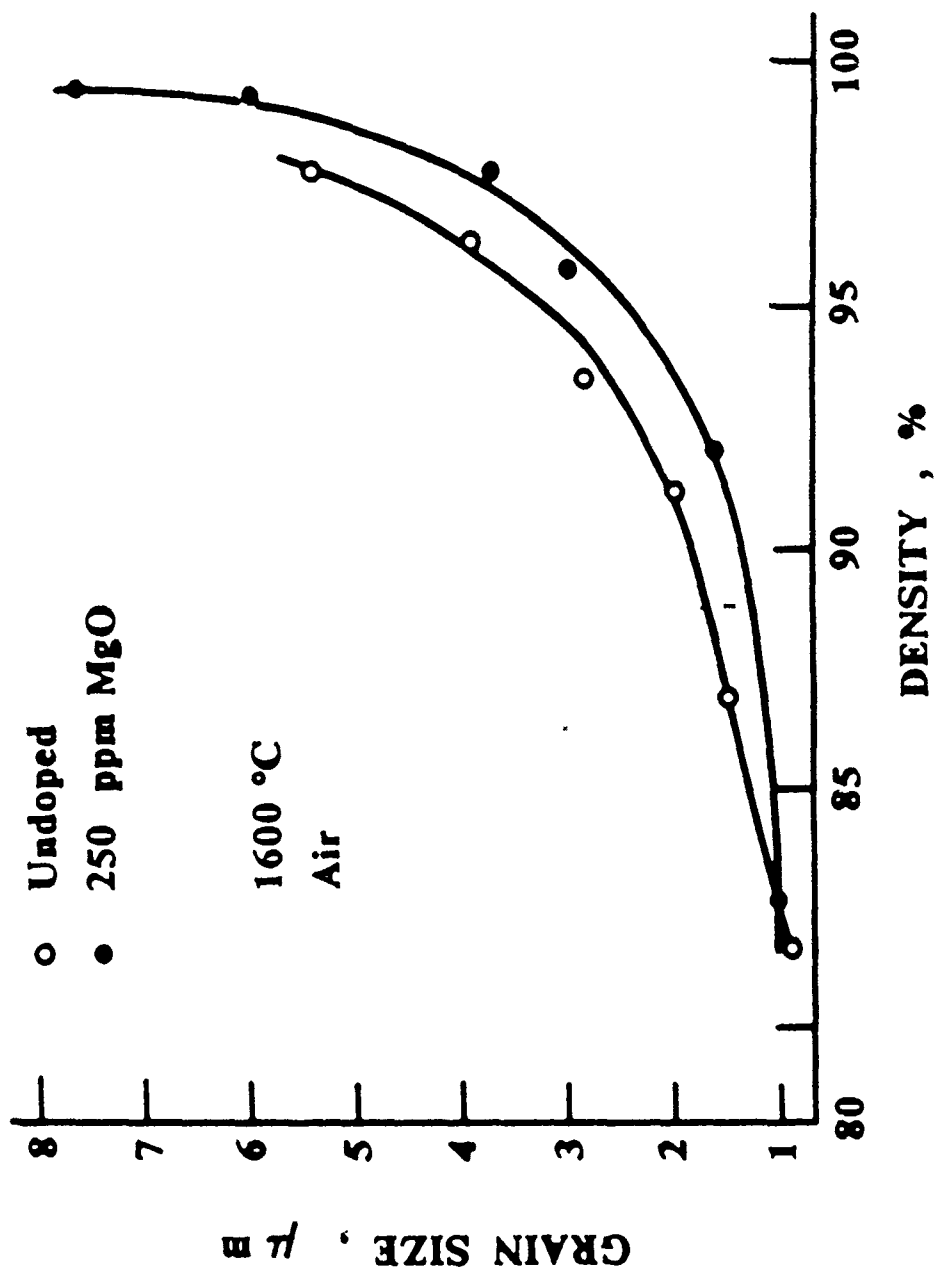B: 1.5 h 1630 C
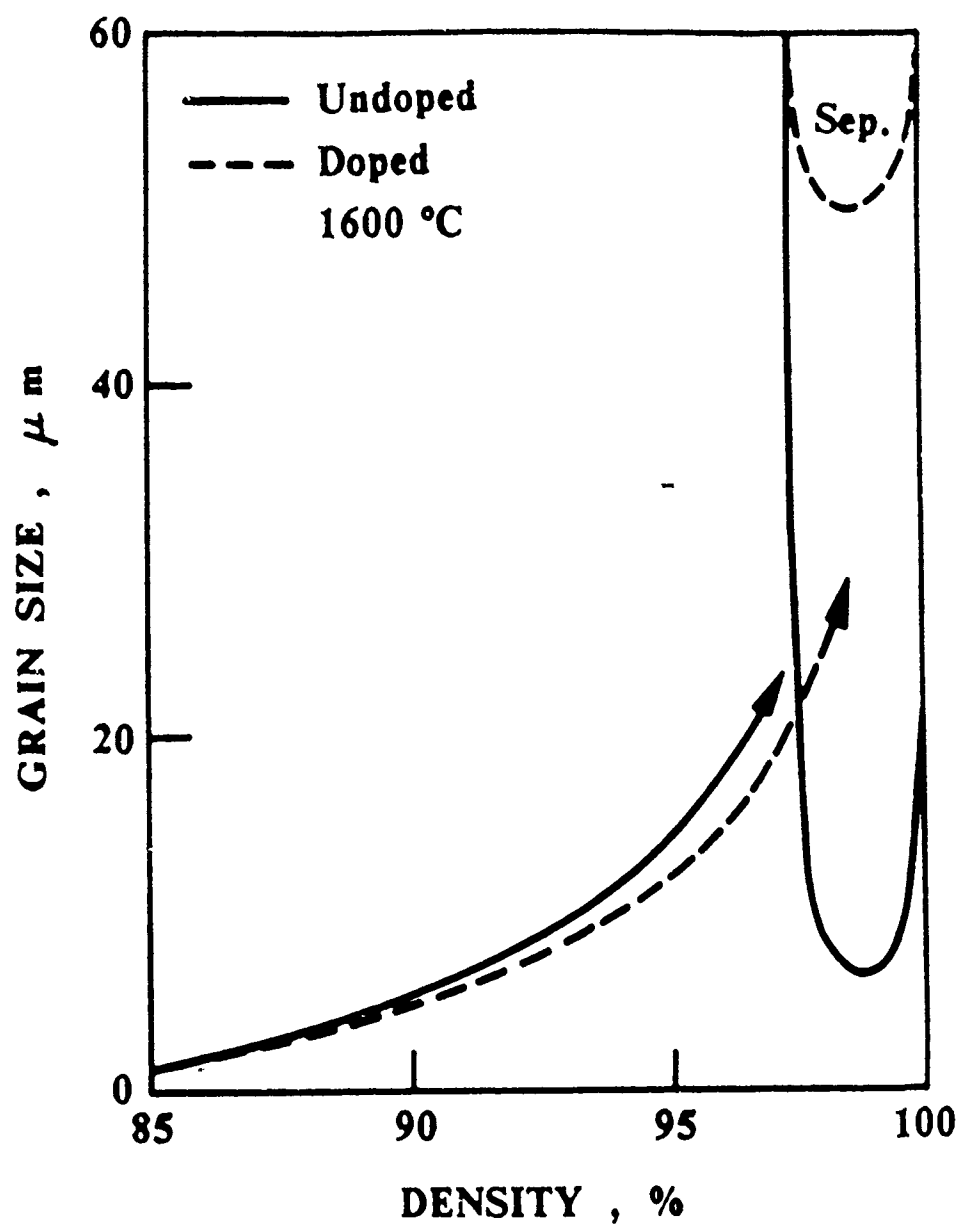   +10 h 1850 C

GRAIN SIZE $\bar{G}$, μm

ppm MgO

1.5 h 1630 °C

5μm
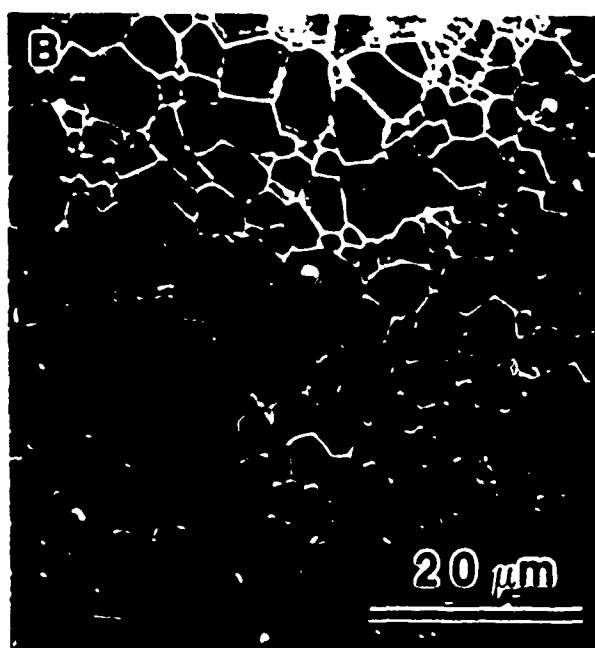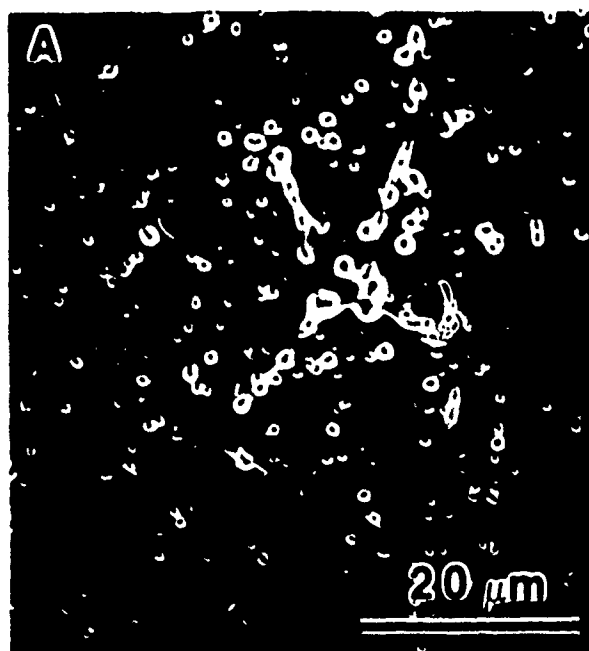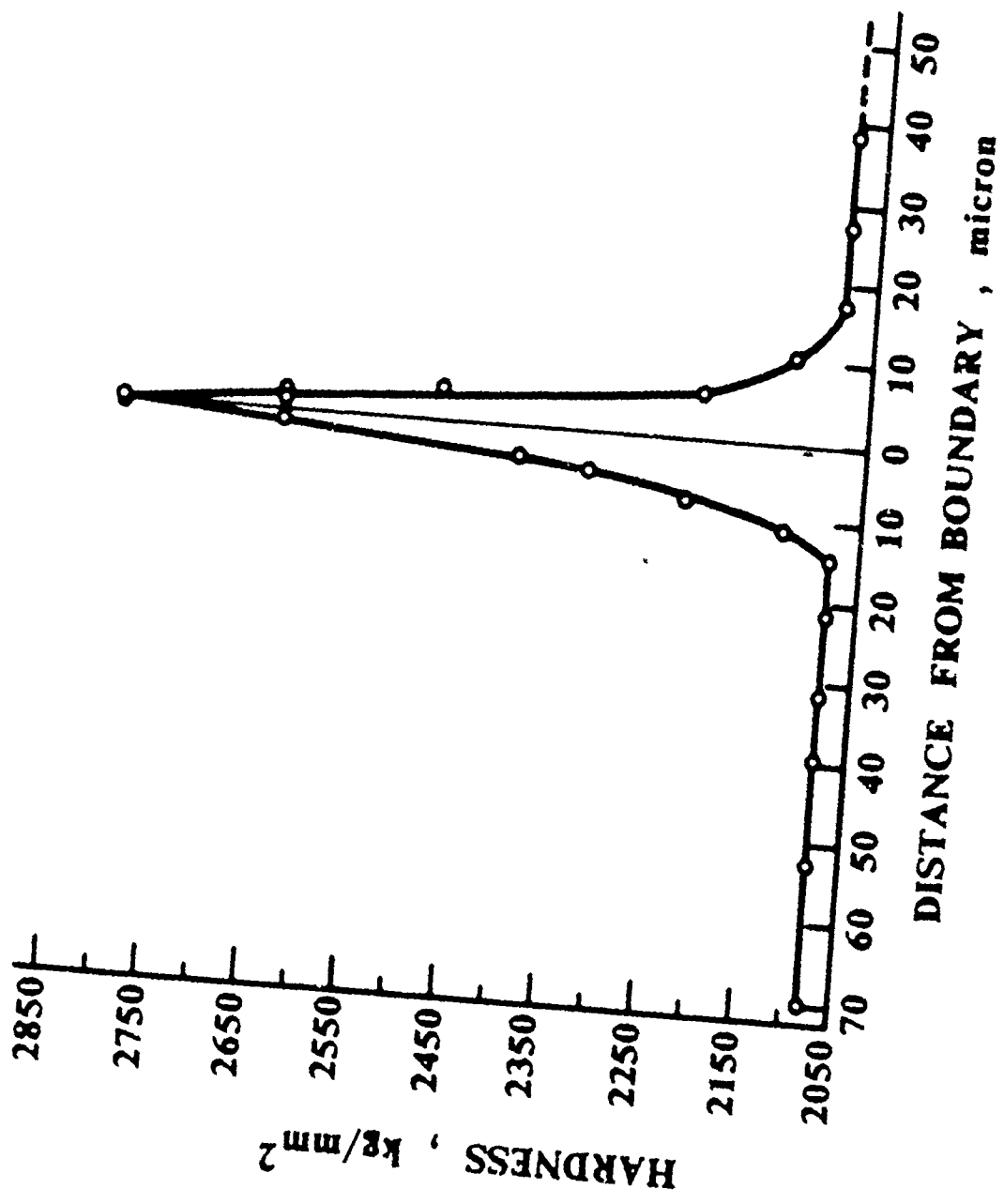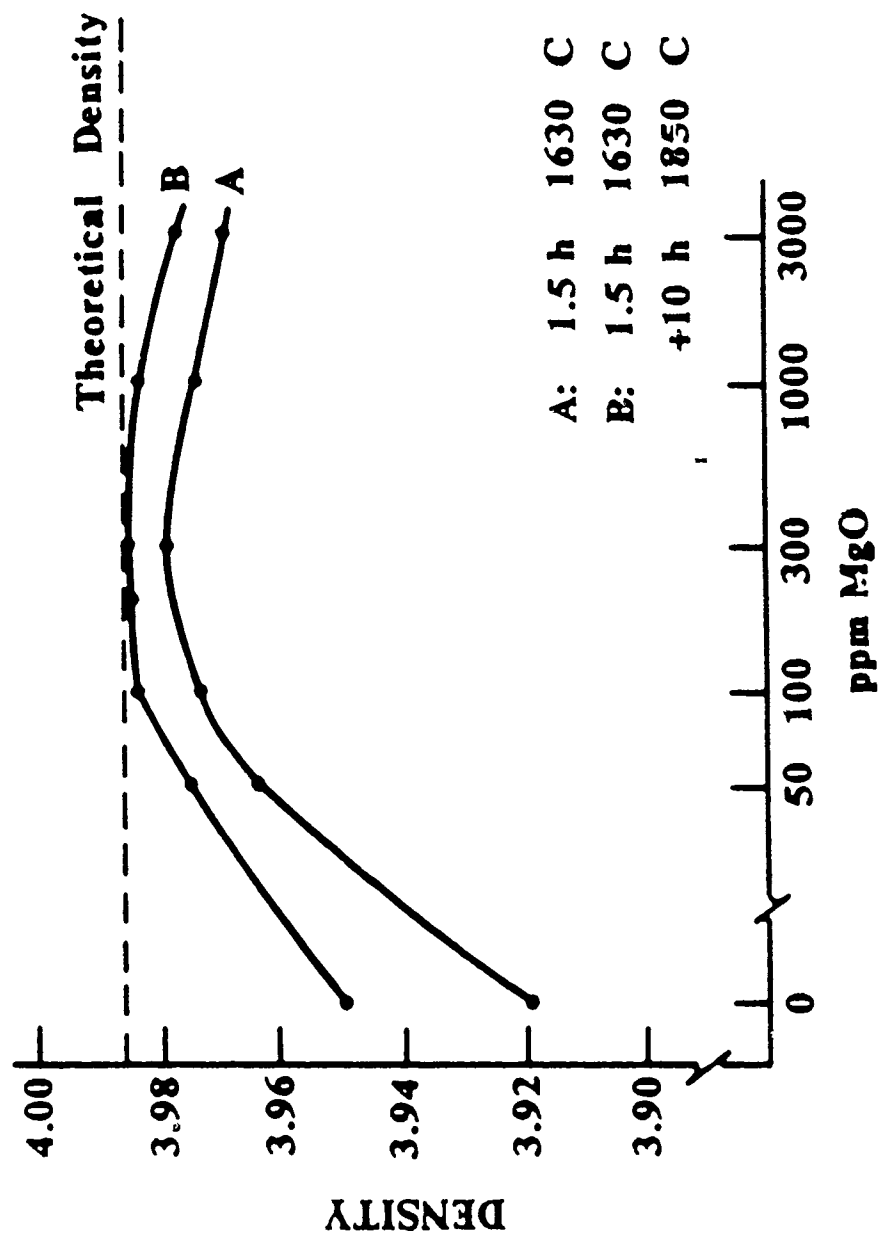
A6Z Al_2O_3

A6Z Al_2O_3 + 100 ppm MgO